Excited-state structure and energy-transfer dynamics in various photosynthetic antenna complexes: hole-burning and modeling studies

by

Mahboobe Jassas

B.S., Arak University, 2005
M.S., University of Tabriz, 2008

AN ABSTRACT OF A DISSERTATION

submitted in partial fulfillment of the requirements for the degree

DOCTOR OF PHILOSOPHY

Department of Chemistry
College of Arts and Sciences

KANSAS STATE UNIVERSITY
Manhattan, Kansas

2020

Abstract

Natural photosynthesis has been an inspiration for solving humankind's urgent demand for replacing fossil energy sources with renewable forms of energy. Knowledge of the molecular mechanisms that lies behind photosynthetic processes is essential for designing novel devices capable of producing solar fuel. Great efforts are being made to understand the first steps of photosynthesis, in particular light-harvesting and excitation energy transfer (EET). In this work, to overcome the static disorder in protein complexes and provide insight into both inhomogeneous and homogeneous line broadening, as well as the excitonic structure and dynamics in various photosynthetic proteins, we use site-selective frequency-domain hole burning (HB) spectroscopy. Complexes studied in detail include: i) wild type (WT) CP29 and CP47 antenna complexes of Photosystem II (PSII), and ii) chlorosome-baseplate proteins of two different green bacteria families (*Cb. tepidum and Cfx. aurantiacus*). Experimental and modeling results obtained for these complexes shed more light on their excitonic structure and EET dynamics. Simultaneous modeling of various types of optical spectra is based on a non-Markovian reduced density matrix approach. For example, we demonstrate that improved simultaneous fits of absorption, emission, circularly polarized luminescence, circular dichroism, and nonresonant hole-burned spectra, provide new information on the excitonic structure of intact and destabilized CP47 complexes and their lowest energy state(s). Regarding the reconstituted wild-type CP29 protein antenna we show that, depending on the laser excitation frequency, reconstituted complexes display two (independent) low-E states (i.e., the ***A*** and ***B*** traps) with different HB and emission spectra. We argue that with two subpopulations identified, only the major one corresponds to the native folding of CP29, whereas the minor conformation occurs only in reconstituted complexes. The lowest energy state of the major subpopulation is mostly delocalized over the *a*611, *a*612, *a*615 Chl trimer, and that of the minor one is localized on Chl *a*604. Studies of the *Cb. tepidum and Cfx. aurantiacus* baseplates reveal that in both complexes excitation energy is transferred to a localized low-energy trap state near 818 nm with similar rates, most likely via exciton hopping. These data are consistent with the model in which baseplate *CsmA* proteins are arranged as dimers containing two Bchl *a* molecules sandwiched between the hydrophobic protein regions.

Excited-state structure and energy-transfer dynamics in various photosynthetic antenna complexes: hole-burning and modeling studies

by

Mahboobe Jassas

B.S., Arak University, 2005
M.S., University of Tabriz, 2008

A DISSERTATION

submitted in partial fulfillment of the requirements for the degree

DOCTOR OF PHILOSOPHY

Department of Chemistry
College of Arts and Sciences

KANSAS STATE UNIVERSITY
Manhattan, Kansas

2020

Approved by:

Major Professor
Ryszard Jankowiak

Copyright

Abstract

Natural photosynthesis has been an inspiration for solving humankind's urgent demand for replacing fossil energy sources with renewable forms of energy. Knowledge of the molecular mechanisms that lies behind photosynthetic processes is essential for designing novel devices capable of producing solar fuel. Great efforts are being made to understand the first steps of photosynthesis, in particular light-harvesting and excitation energy transfer (EET). In this work, to overcome the static disorder in protein complexes and provide insight into both inhomogeneous and homogeneous line broadening, as well as the excitonic structure and dynamics in various photosynthetic proteins, we use site-selective frequency-domain hole burning (HB) spectroscopy. Complexes studied in detail include: i) wild type (WT) CP29 and CP47 antenna complexes of Photosystem II (PSII), and ii) chlorosome-baseplate proteins of two different green bacteria families (*Cb. tepidum and Cfx. aurantiacus*). Experimental and modeling results obtained for these complexes shed more light on their excitonic structure and EET dynamics. Simultaneous modeling of various types of optical spectra is based on a non-Markovian reduced density matrix approach. For example, we demonstrate that improved simultaneous fits of absorption, emission, circularly polarized luminescence, circular dichroism, and nonresonant hole-burned spectra, provide new information on the excitonic structure of intact and destabilized CP47 complexes and their lowest energy state(s). Regarding the reconstituted wild-type CP29 protein antenna we show that, depending on the laser excitation frequency, reconstituted complexes display two (independent) low-E states (i.e., the ***A*** and ***B*** traps) with different HB and emission spectra. We argue that with two subpopulations identified, only the major one corresponds to the native folding of CP29, whereas the minor conformation occurs only in reconstituted complexes. The lowest energy state of the major subpopulation is mostly delocalized over the *a*611, *a*612, *a*615 Chl trimer, and that of the minor one is localized on Chl *a*604. Studies of the *Cb. tepidum and Cfx. aurantiacus* baseplates reveal that in both complexes excitation energy is transferred to a localized low-energy trap state near 818 nm with similar rates, most likely via exciton hopping. These data are consistent with the model in which baseplate *CsmA* proteins are arranged as dimers containing two Bchl *a* molecules sandwiched between the hydrophobic protein regions.

Table of Contents

List of Figures

List of Tables

List of Abbreviations

α	Debye-Waller factor
BChl	bacteriochlorophyll
Car	carotenoid
Cb.	*Chlorobaculum*
CD	circular dichroism
Cfx.	*Chloroflexus*
Chl	chlorophyll
CP29	Chlorophyll Protein bonding of 29 kDa
CP47	Chlorophyll Protein bonding of 47 kDa
CPL	circularly polarized Luminescence
CW	continuous wave
EET	excitation energy transfer
el-ph	electron-phonon
FMO	Fenna-Matthews-Olson
FWHM	full-width at half-maximum
GSB	green sulfur bacteria
HB	hole burning/burned
LD	liniear dichroism
NRHB	nonresonant hole burned
PHB	photochemical hole burning
PSB	phonon side band
PSI	Photosystem I

PSII	Photosystem II
SDF	site distribution function
SHB	spectral hole burning
TrEsp	transition charges from electrostatic potential
TLS	two-level system
ZPH	zero-phonon hole
ZPL	zero-phonon line

Acknowledgements

The list of people whom I am indebted for the completion of my Ph.D. Would far exceed the number that I can list here. First and foremost, I would like to express my sincerest thanks to my supervisor Prof. Ryszard Jankowiak. His support and guidance provided many excellent opportunities and experiences during my graduate studies. I'm very grateful that he and Majka were such loving hosts over the years, providing a warm atmosphere that you could say that you are not far away from your family!

It is my pleasure to thank my Graduate Committee members, Profs. Viktor Chikan, Daniel Higgins, and Michal Zolkiewski for their valuable time and suggestions. I would also like to sincerely thank Prof. Don Gruenbacher for being the chairperson of my graduate committee.

Other thanks belong to former group members, Dr. Jinhai Chen, for sharing his lab experiences, and especially Dr. Kell, whom I still have his help after four years he left the KSU. I thank Dr.Tonu Reinot for his support in theoretical and modeling studies and many helpful comments in his emails. Special thanks to the current group member, Dr. Anton Khmelnitskiy, for being very helpful during the experiments and for his comments on presentations.

I must thank members of the Chemistry Department that provide pleasant environment. The ladies in the office for answering questions and organizing department functions, Michael Hinton for valuable feedback and guidance in teaching undergraduate labs; Tobe Eggers, Jim Hodgson, and Ron Jackson for technical supports in our lab over the years.

Finally, I would like to thank my beloved husband, Hamid. He has been a huge support, always picked me up when I did not think I could do it anymore, and never stopped me from chasing my dreams in spite of his own, and I am eternally grateful.

Dedication

To Hamid

Preface

The research presented in this dissertation was performed in the Department of Chemistry, Kansas State University (KSU), from August 2014 to May 2020. Chapter 3 was collaboration between KSU and Istituto di Biologia e Biotecnologia Agraria, (Milano, Italy), Chapter 4 was collaboration between KSU and Clark University, (Worcester, Massachusetts) and Chapter 5 was collaboration between KSU and Washington University in St. Louis (St. Louis, MO), where all institutions provided samples for the experimental measurements.

Chapter 1 - Introduction

Overview of Photosynthesis

During the last several decades, finding an alternative source for fossil fuels has drawn much attention. The investigations for clean and renewable energy sources lead to notice molecular mechanisms of photosynthesis and establishing the basis for the development of new routes towards biological energy sources. Generally, photosynthesis, the most crucial process for providing all food and most energy resources on Earth, occurs in bacteria, algae, and plants.[1] Photosynthetic organisms employ light-harvesting complexes to capture solar energy and transfer the excitation energy to reaction centers, where the energy is transformed to a charge separated state that is stored for use in cellular metabolism and function. This process is categorized into two types, oxygenic and anoxygenic photosynthesis.

1.1 Oxygenic Photosynthesis

During oxygenic photosynthesis, which occurs in higher plants, cyanobacteria and algae, CO_2 is reduced, and water becomes oxidized. Ultimately, oxygen is produced along with carbohydrates. The equation is written as follows:

$$6CO_2 + 12\ H_2O + \text{Light Energy} \rightarrow C_6H_{12}O_6 + 6O_2 + 6\ H_2O \qquad (1.1)$$

The initial reactions of photosynthesis take place by three protein complexes embedded in the thylakoid membrane of the chloroplast. These complexes are Photosystem II (PSII), the cytochrome b_6f complex ($Cytb_6f$), and photosystem I (PSI), which are electronically connected in series. The light-harvesting systems of PSII and PSI collect the light energy and transfer the excitation energy to the reaction center (RC) chlorophylls to create a charge separation across the membrane, and the Cyt b_6f complex mediates electron transfer between the reaction centers.[2] Plant PSII, the "engine of life," is largely organized in supercomplexes and catalyzes the splitting of

water into oxygen, which is essential for the survival of life on Earth.[3] The PSII core complex contains the RC and two core light-harvesting antenna so-called CP43 and CP47, which enclosed by additional antenna proteins that enhance the effective absorption cross-section of the RC. These antenna proteins are the major light-harvesting complex II (LHCII) and the minor light-harvesting complexes CP29, CP26 and, CP24, which connect LHCII and the core complex and, compared to LHCII occur at a lower amount in the chloroplast. In chapters two and three of this dissertation, the core and minor antenna complexes of PSII, CP47 and CP29 respectively, have been studied, and in the following, their structure briefly explained.

1.1.1 Structure of CP29 and CP47 subunits

CP29 is located between the outmost antenna LHCII and the inner antenna CP47 in the core complex;[4] therefore, it is in a good position to regulate the energy flow towards the RC. The X-ray structure of the CP29 complex that contains nine chlorophyll *a* (Chl *a*), four chlorophyll *b* (Chl *b*), and three carotenoids,[5] demonstrated in Figure 1.1 (frame A). These 13 Chls arranged in the protein matrix embedded in the lipid bilayer are responsible for the light-harvesting process through their low energy π-π^* transitions, known as Q_y .[6] CP47, the light-harvesting antenna of the Photosystem II core complex (PSII-cc), see Figure 1.1-frame B, is a challenging protein to study, as it is more difficult to separate from the PSII-cc.[7] CP47 binds 16 Chls *a* which are located in symmetry-related positions and at least 2β-carotene molecules. Additionally, the Chlorophylls are roughly distributed in two layers near the stromal and luminal sides of thaylakoid membrane, with their planes oriented perpendicular to the membrane.[8]

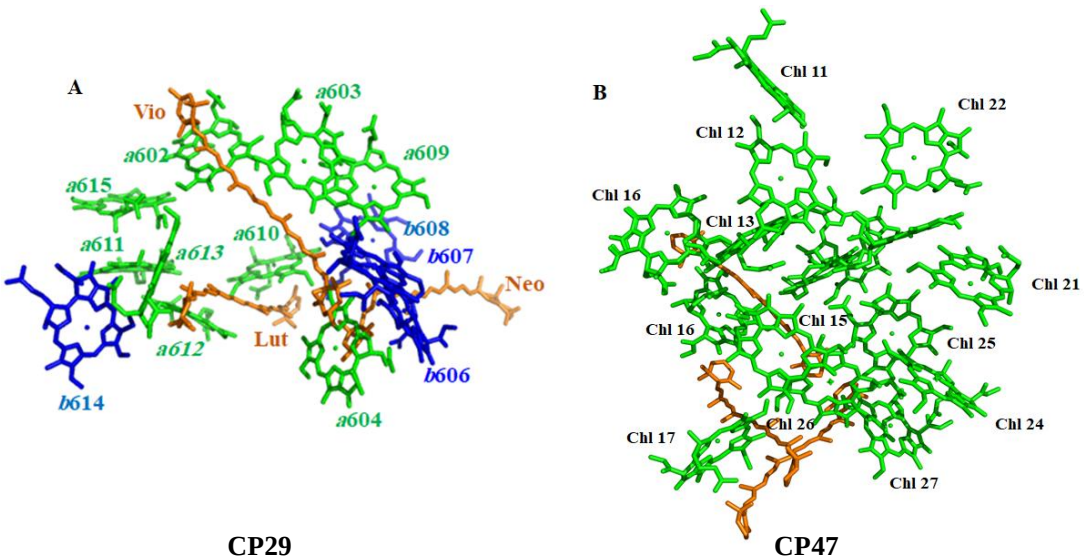

CP29 **CP47**

Figure 1.1 Frames A and B show the arrangement of Chls in CP29 and CP47, respectively.[5] Chl *a*, Chl *b* and carotenoids are green, blue, and orange respectively.

1.2 Anoxygenic Photosynthesis

Anoxygenic photosynthesis, which typically occurs in bacteria, uses electron donors other than water, and no oxygen is produced. The byproduct depends on the electron donor, e.g., many bacteria use the hydrogen sulfide, producing solid sulfur as a byproduct. The various anoxygenic photosynthesis reaction can be described as the following:

$$CO_2 + 2\ H_2A + \text{Light Energy} \rightarrow CH_2O + 2A + H_2O \qquad (1.2)$$

H_2A represents the potential electron donor. The key focus in chapters 4 and 5 is on two thermophilic green photosynthetic bacteria, which are green sulfur bacterium *Chlorobaculum* (*Cb.*) *tepidum* and filamentous anoxygenic phototropic bacterium (FAP) *Chloroflexus* (*Cfx.*) *aurantiacus*.

1.2.1 Photosynthesis apparatus of Green bacteria

To capture the light energy, the green bacteria employ chlorosome, the highly efficient and the largest natural photosynthetic light-harvesting antenna, which it is substantial for

understanding the ability of these bacteria to survive at low-light conditions. Although the peripheral light-harvesting antenna structures in these two bacteria are remarkably similar,[9,10] the structure of the reaction centers, as well as their membrane-associated antenna complexes, are quite different.[10] That is, both families contain chlorosome-baseplate complexes, while *Cb. tepidum* contains Fenna-Matthews-Olson complex (FMO) and reaction center (RC) type I, the *Cfx. aurantiacus* include B808-866 light-harvesting core antenna and RC type II. The schematic structure of *Cb.tepidum* and *Cfx. aurantiacus* are shown in Figure 2, frame A and B, respectively.[11]

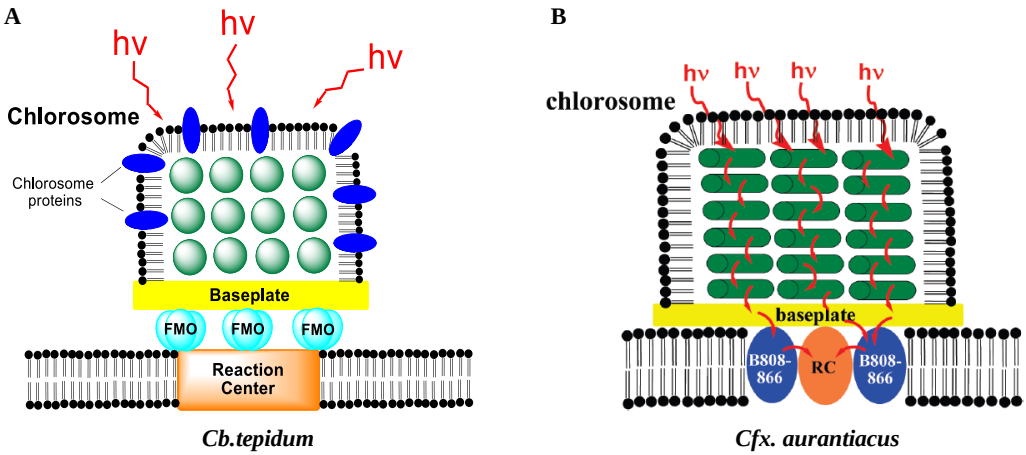

Figure 1.2 The schematic structure of *Cb.tepidum* and *Cfx. aurantiacus* in frames A and B, respectively.[11]

Most of the incoming light energy is collected by an atypically large light-harvesting antenna-chlorosome. Then the excitation energy is gathered from the interior of the chlorosome by a baseplate complex that is attached to its side facing the cytoplasmic membrane. The baseplate acts as the mediator of excitation energy transfer (EET) from the chlorosomal body towards the FMO antenna in *Cb. tepidum* and subsequently to the reaction center (RC), and to the integral membrane light-harvesting B808-866 core antenna/RC system in *Cfx. aurantiacus*, which does not contain the FMO protein.[12] The structure and function of the individual components of the photosynthetic apparatus are described below.

1.2.1.1 Chlorosome

The main pigments in chlorosomes, BChl *c* (*Cfx. aurantiacus* ~95% and *Cb. tepidum* 99%,[13] respectively) self-aggregate without any assistance from the peptides in hydrophobic environment.[14,15] From cryo-electron microscopy and NMR studies, it was proposed that BChls are organized into enveloped in an ellipsoidal (rod-shaped) structure,[16,17] but the exact arrangement of BChls within chlorosomes is still in controversy. Chlorosomes contain about 10000[14] up to 250000[15] BChl *c* pigments, but lipid, protein, quinone and small amount of BChl *a* are also present.[18] Compared to other light-harvesting antenna, chlorosomes are unique concerning their efficiency and size. The size and the thickness of chlorosomes depends on growth conditions; the size becomes larger under low-light conditions[19-21] Typically, the chlorosome from *Cfx. aurantiacus* are approximately 100 nm long, 20-40 nm wide and 10-20 nm high.[21,22] The chlorosome from the sulfur bacteria can be considerably large with length from 70 to 180 nm and width from 30 to 60 nm.[21,23] Each chlorosome may contain 10-30 rod elements, the rod elements of sulfur bacteria chlorosome are 10 nm in diameter,[23] whereas the rod elements of *Cfx. aurantiacus* chlorosomes are only 5.2-6 nm in diameter.[22]

1.2.1.2 Baseplate

Chlorosomes connect to the cytoplasmic membrane[24] through a crystalline baseplate which contains Bchl *a* and acts as a mediator to transfer energy from the chlorosome to the reaction centers in the membrane. In contrast to the Bchl *c* aggregate, the baseplate is a pigment-protein complex, where the relative positions and fine spectral properties of individual pigments are controlled by protein scaffold. The B798 (absorbance band at 798 nm) light-harvesting baseplate of *Cfx. aurantiacus* consists of Bchl *a*, β-carotene, and three major proteins namelly, CsmA, CsmM and CsmN with molecular massess 5.7, 11, and 18 kDa respectively.[15,25] CsmA protein,

the smallest and most abundant, binds one BChl *a* molecule and one or two carotenoid molecules per monomer.[15,26,27] The molar ratio of chlorosome to BChl *a* in *Cfx. aurantiacus* is about typically 25/1[25] and in tepidum is about 90/1.[28]

1.2.1.3 Fenna-Matthews-Olson (FMO) Protein

FMO, a water-soluble protein which naturally appears as a trimer, binds eight BChl a molecules. For a long time, it was believed that the FMO binds seven BChl a molecules; however, recent experiments identified the eighth BChl *a* in the structure.[29,30] FMO proteins are located between the chlorosomes and cytoplasmic membrane, where they are in close contact with both baseplate and RC. Most likely, two FMO trimers are attached to a single RC complex.[31,32]

1.2.1.4 B808-B860 Antenna

The B808-866 light-harvesting core antenna complex is a protein-pigment complex associated with two spectral types of BChl *a* (B808 and B866) in cytoplasmic membranes. The B808-866 complex efficiently absorbs light energy and funnel it ~ 43 ps to the reaction center.[15]

1.2.1.5 Reaction Center (RC)

The reaction center (RC) is located at the very bottom of the energy funnel. Its function is to convert the excitation energy into a more stable energy of chemical bonds. The RC of green sulfur bacteria is conceptually similar to the RC of PSI of cyanobacteria and higher plants[31] which, contains iron-sulfur centers as electron acceptors, so-called type 1 RC.[33,34] In contrast the RC of anoxygenic phototrophic (FAP) containing quinone acceptor molecule which resemble RC from purple bacteria.[35] However, X-ray structural data are not available for the RC of *Cfx. aurantiacus* and *Cb. tepidum* and the proposals for molecular structure and interaction between cofactors are primarily based on the results of spectroscopic measurements.

1.3 Laser-Based Spectroscopy Techniques

Since the primary processes of photosynthesis, light-harvesting, are intimately connected with the absorption of visible and near-infrared light, they can be investigated by time - and frequency-resolved laser spectroscopy methods. In the time-domain spectroscopies, e.g., two-dimensional electronic spectroscopy (2DES),[36,37] photon echo,[38] and pump-probe,[39] excitation sources have a short pulse with a broad bandwidth in frequency. The optical spectra of photosynthetic pigment-protein complexes usually show broad absorption bands, i.e., their homogeneously broadened bands are buries under largely inhomogeneous broadened spectra.[40] Therefore, to unravel the optical and dynamic properties of such hidden species, a frequency-domain spectroscopy technique utilizes continuous wave (CW) lasers with narrow bandwidth as opposed to the time-domain method is applicable. In frequency-domain measurements, a selected domain within the disordered sample is probed by the narrow-band lasers, so-called site-or energy-selective spectroscopies, and provides information on lineshapes and dynamic processes.[41-43] Hole-burning (HB)spectroscopy is one of the powerful techniques that overcome the inhomogeneity and provide more information about dynamic of the pigment-protein complexes. Below, the principle of HB spectroscopy and the experimental set-up utilized in this work are addressed.

1.3.1 Inhomogeneous (Static) and Homogeneous (Dynamic) Disorder

Broadening mechanisms can be categorized as inhomogeneous and homogeneous, based on the slower or faster relaxation processes timescale compared to excited-state lifetime, respectively. Inhomogeneous broadening (Γ_{inh}) caused by the slightly different environment of the individual chromophores in a disordered matrix. As shown schematically in the Figure 1.3A, sites 1,2, and 3, experience different environments in the disordered host which affects the

transition energy of the molecules.[41,44,45] The inhomogeneous disorder is assumed to have Gaussian profile with an inhomogeneous width Γ_{inh}.

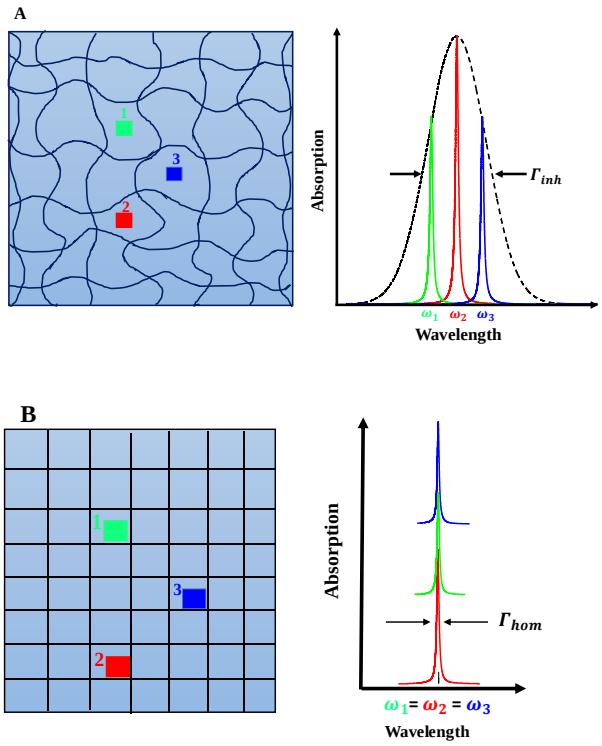

Figure 1.3 Frame A-left: Schematic of several sites dispersed in different local matrix. Right: inhomogenously broadened absorption profile. Frame B-left: show several sites dispersed in perfect crystal. Right: Absorption lines are homogenously broadened. $\boldsymbol{\Gamma_{hom}}$ is the homogenous line width.

In a perfect crystal all sites have the same energy transition and no static disorder exists, see figure 1.3B.[41] The sharp bands (zero-phonon line, *vide infra*) corresponding to the absorption of the "guest" molecules are buried in the inhomogeneously broadened lined band. These narrow spectra have homogenous broadening (Γ_{hom}), which is the same for every chemically identical molecule in the ensemble at given temperature. The line shape of a homogeneously broadened electronic transition is Lorentzian (it is the Fourier-transform of an exponential decay function), and determined by total dephasing time T_2:[41,46]

$$\Gamma_{hom} = (\pi T_2 c)^{-1} \tag{1.3}$$

Where c is the speed of light in $cm\ s^{-1}$ and T_2 defined as

$$\frac{1}{T_2} = \pi c \Gamma_{hom} = \frac{1}{2T_1} + \frac{1}{T_2'} \tag{1.4}$$

Where T_1 is the lifetime of the electronically excited state and T_2' is the pure dephasing time which results from interaction of excited state with bath phonons which lead to a decay of the phase coherence of the superposition state initially created by photon.[41]

Total absorption band includes a distribution of energetically inequivalent sites (site-distribution function, SDF) and their coupling to an environment in which the molecules reside. That is, Figure 1.3A describes (0-0)-absorption band at low temperature (~5 K) for the weak electron-phonon coupling. The total absorption bandwidth is described by $\Gamma_{inh} + S\omega_m$, where S is Huang-Rhys factor and ω_m is the mean phono frequency, see Figure 1.4. the sharp band with Lorentzian line shape is called a zero-phonon line (ZPL) and corresponds to a pure electronic transition with a bandwidth of $\Gamma_{hom.}$[47] Building on each ZPL is a broad phonon wing so-called phonon-side band (PSB) which located to higher and lower-energy side of ZPL in absorption and emission, respectively. ω_m, the mean phonon frequency is the difference between the peak position of ZPL and PSB.

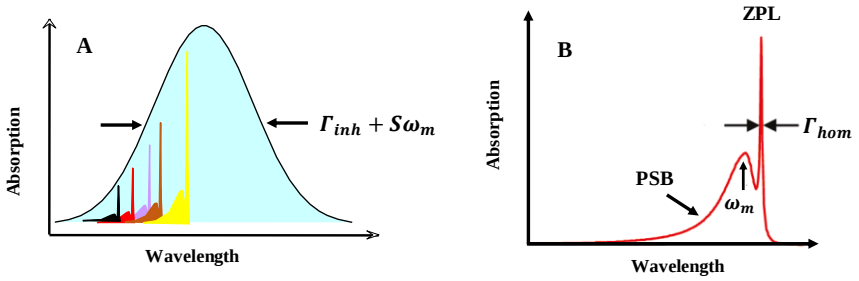

Figure 1.4 Frame A: Schematic of inhomogenously broadened absorption band and, Frame B: show ZPL and PSB. The mean phonon frequency, $\boldsymbol{\omega_m}$ is the difference between the peak position of ZPL and PSB which determined with Franc-Condon principle.

The dimensionless Huang-Rhys factor *S*, i.e., the strength of electron-phonon coupling is related to the Franc-Condon (FC) factors.[48-50] The FC for the ZPL is defined as:

$$FC_{00} = \left| < 1,0 \mid 0,0 > \right|^2 = e^{-S} \tag{1.5}$$

To evaluate the value of *S*, the Debye-Waller factor, α can be obtained by estimating the integral intensity of the ZPL (I_{ZPL}) and the PSB (I_{PSB}):

$$\alpha = \frac{I_{ZPL}}{(I_{ZPL}+I_{PSB})} \tag{1.6}$$

As shown in Figure 1.5, the relative intensities of the ZPL and PSB depend upon the strength of the electron-phonon (el-ph) coupling. At the low-temperature limit (~0 K) α define as:

$$\alpha = e^{-S} \tag{1.7}$$

where *S* (T= 0 K) given by[51]

$$S = \sum_{\xi} \frac{M_{\xi}\omega_{\xi}}{2\hbar} (\Delta q_{\xi})^2 \tag{1.8}$$

Where M_{ξ} and ω_{ξ} are the reduced mass and frequency of the phonon mode ξ, respectively. Δq_{ξ} is the displacement of the minima of the potential energy surfaces of the ξ^{th} bath mode of the ground and excited electronic states with respect to each other, the more this displacement, the larger is S). That is, for molecules that upon electronic excitation undergo large geometry changes, the electron-phonon coupling is strong, and corresponding *S* is large. In the absorption/fluorescence spectrum, a strong coupling producing a weak ZPL and an intense PSB, whereas weak coupling (small *S*) is reflected in an intense ZPL and a weak PSB. For very strong coupling ($S \geq 10$), no ZPL is observed since they are FC forbidden.[41]

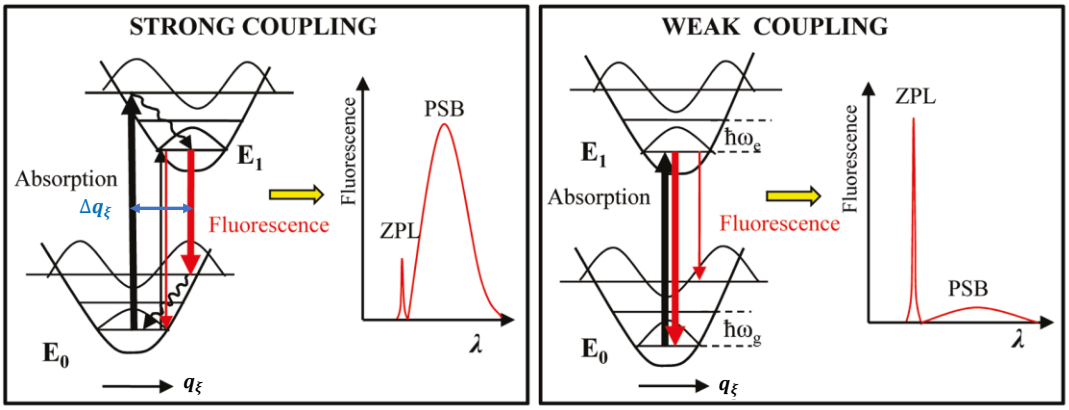

Figure 1.5 Diagram of potential curves in the case of linear el-ph coupling ($\hbar\omega_g = \hbar\omega_e$) for both strong and weak coupling are illustrated. Optical transitions in accordance with the FC principle are shown as vertical.[41]

1.3.2 Principles of Hole Burning Spectroscopy

Hole-burning (HB) spectroscopy, a frequency-domain, site-elective technique, carried out under liquid helium temperature (~5 K), whereby an ensemble of molecules in a disordered matrix illuminated at a given wavelength with a narrow-band laser beam. The sample is cooled to a low temperature to decrease thermal broadening effect, e.g. dephasing. A diagram of the HB experimental setup is shown in Figure 1.6. The sample is settled on a holder inside of the cryostat, which is aligned with the beam path of the Fourier transform infrared spectrometer (FTIR). A tungsten bulb utilized as a white light source for the probe. The probe hit the beam splitter, which sends part of the signal to either stationary or movable mirror. Both mirrors reflect the light back to the beam splitter, where they recombine and interrogate the sample. The resultant detected by a photodiode and the preburn spectrum is measured. The white light is turned off to burn the sample by laser. To strike the sample by laser the shutter is opened, and the intensity of the laser is controlled by a stabilizer and neutral density filter.

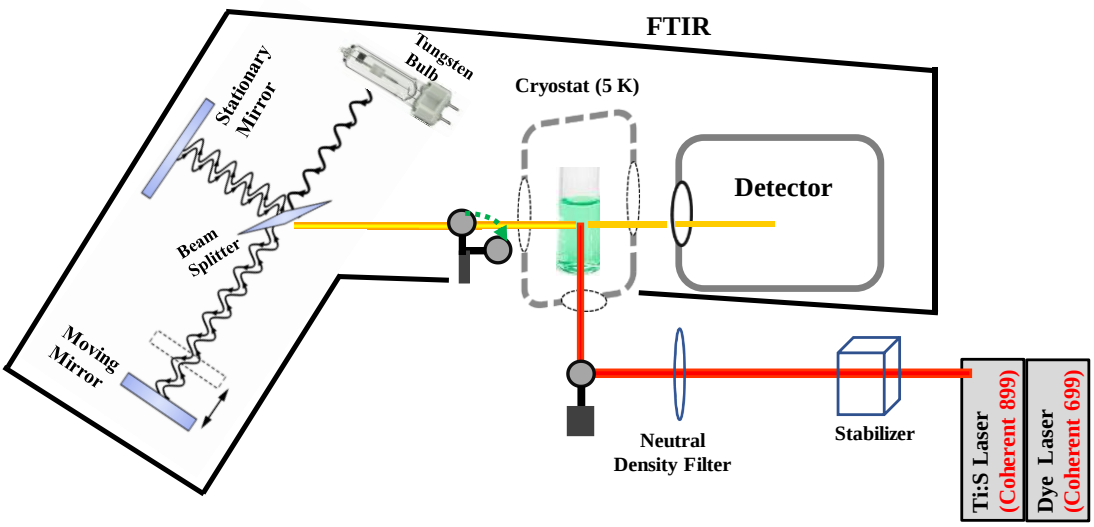

Figure 1.6 Schematic of the experimental setup for the low-temperature absorption and HB measurement. First, the preburn is measured by white light, then the sample is illuminated by the laser, and finally, the FTIR measures the postburn absorption.

After laser exciting the sample for a particular time, the shutter is closed, and again white light is turned on, and the post-burn is measured to explore the changes induced by burning. The HB spectra are measured as the difference in absorption before and after excitation by the laser (post-burn minus preburn).

Figure 1.7 shows absorption or preburn (curve a-black) and post-burn (curve b, blue) spectra, which burning at λ_b = 683 nm. The green curve in frame B shows the HB spectrum resulting from the difference of post-burn and preburn. The HB spectra reveal a sharp zero-phonon hole (ZPH) resonant with the laser wavelength and two PSB holes (PSBHs) [41,44,45] so-called real-PSBH and pseudo-PSBH. The real-PSBH resulting from a bleach of molecules excited via their ZPL appears at higher energy than ZPH. Whereas, the pseudo-PSBH is observed the lower energy than the ZPH resulting from bleach of pigments via their PSBs.

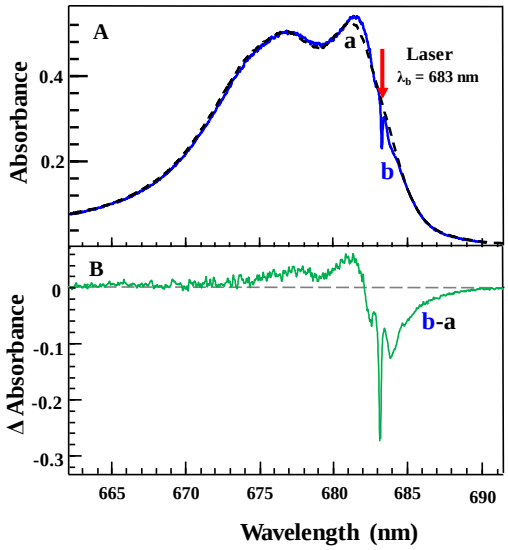

Figure 1.7 Fram A: Illustrates preburn (curve a-black) and post-burn (curve b, blue) spectra which burning at $\boldsymbol{\lambda_b}$ = 683 nm, and Frame B shows: the resulting HB spectrum (b-a, green).

Hole-burning mechanisms can be divided into two categories: persistent HB and transient HB (THB). Within the first category, as long as the temperature is maintained, the absorbance changes are preserved after excitation, HB spectra exhibit persistent holes. For measuring the transient HB (population bottleneck), absorption is measured while the laser is on and burning the sample and then when the shutter is closed the absorption is measured, the THB resulting from absorption of laser on minuses absorption of laser off. Generation of THB spectra requires a long-lived state, usually a triplet state or charge separation state, which populated from the excited singlet state.[41] In this case, the pigment's ground state is depopulated for the lifetime of the long-lived state and the spectral hole will be observed only for the duration of this lifetime on the order of $\mu s - ms$.[41,52,53]

Additionally, the HB mechanism can be classified as photochemical and nonphotochemical.[41,43,54] Photochemical HB (PHB) occurs when the pigment undergoes some photoinduced transformation, such as photo-oxidation and tautomerization. The product of the reaction usually absorbs far from

the original excitation wavelength. In the case of nonphotochemical spectral hole-burning (NPHB), the pigment molecule does not experience a chemical reaction. Instead, upon excitation rearrangement of the pigment's local environment occurs to result in the change in the interactions between the pigment and its surrounding.[41,55-57] Figure 1.8 illustrates the mechanism of NPHB of a single site by configurational tunneling between the two-level system (TLS) of the gust and host.[41] Upon optical excitation of the chromophore, the pigment in the ground state (conformation A) absorbs a resonant photon and photon-assisted tunneling can occur in the excited state (yellow arrow). After tunneling, the pigment returns to the new ground state. If the barriers between environment configurations are higher in the ground electronic state than in the excited electronic state of the pigment molecules, the system gets permanently trapped in the new configuration as long as low temperature is maintained and persistent hole results.

Both PHB and NRHB result in the formation of persistent holes, meaning that the holes are preserved long after the initial excitation is turned off.

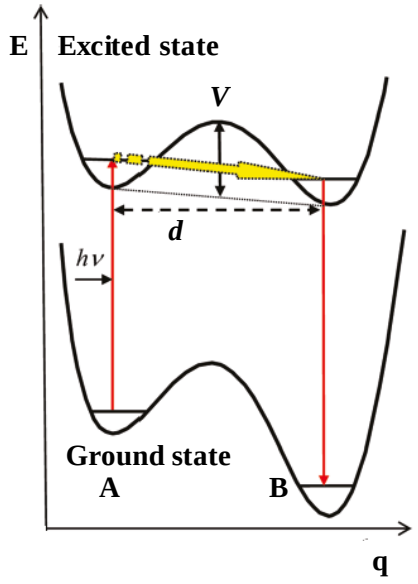

Figure 1.8. TLS with ground and excited state of pigment shows the photon-assisted tunneling mechanism of NPHB. The barrier between conformations A and B is lower in the excited state.

Red arrows represent the excitation and relaxation, while the yellow indicated tunneling in the excited states.[41]

HB spectroscopy can be used to reveal inhomogeneous broadening parameters, that is, the shape and width of the SDF. For this purpose, the zero-phonon action (ZPA) spectroscopy utilizes in which HB spectra are measured for constant low fluence doses at many excitation wavelengths across the absorption band. The ZPA spectrum is then obtained as a plot of resonant hole depth versus excitation wavelengths, and the fwhm of the envelope of the ZPH is approximately Γ_{inh}.[41,58] Another information provided by HB spectroscopy is excitation energy transfer (EET) time by the width of the ZPH. Information on the dynamic of the excited state of the system is contained in the homogeneous linewidth Γ_{hom} is usually a factor of 10^3- 10^5 times smaller than the SDF width Γ_{inh}, if el-ph coupling is ignored, the only remaining contribution to the hole spectrum will be ZPH, a convolution of ZPL with itself. For a Lorentzian ZPL line shape, the width of the ZPH, in the shallow hole limit, will be twice of the ZPL:[41]

$$\Gamma_{hole} = 2\Gamma_{hom} \tag{1.9}$$

Energy transfer will produce lifetime broadening, that is for low-fluence

$$\Gamma_{ZPH} = 2\Gamma_{hom} = \frac{1}{\pi c T_1} + \frac{2}{\pi c T_2^*} + \frac{1}{\pi c \tau_{EET}} \approx \frac{1}{\pi c \tau_{EET}} \tag{1.10}$$

T_1 is the fluorescence lifetime, T_2^* is the pure dephasing time which is very large at low-temperature in comparison with T_1. τ_{EET} *is the* EET time and is dominant in eq. 1.10 since it is on order of femtoseconds to picoseconds.

1.4 Light harvesting Antenna in Action: Excitation Energy Transfer

A detailed analysis of the light-harvesting antenna can be obtained by combining the structural information with optical spectroscopy and theoretical studies. A realistic theory has to describe the pigment-pigment interaction and coupling between each pigment with the protein

(bath). The theory is started by defining the Hamiltonian which is comprised of the system ($\hat{H}_s$), bath ($\hat{H}_B$), and system-bath interaction parts ($\hat{H}_{SB}$), respectively.

$$\hat{H}_{tot} = \hat{H}_s + \hat{H}_B + \hat{H}_{SB} \tag{1.11}$$

The Hamiltonian of the system can be expressed as $\hat{H}_s = \hat{H}_\varepsilon + \hat{H}_v$, with

$$\hat{H}_\varepsilon = \sum_n E_m |m><m| \tag{1.12}$$

The transition energies E_m are called "site energies" since they depend on the local protein environment of the pigments and defined as the optical transition energies at the equilibrium position of nuclei in the electronic ground state. A microscopic calculation of site energies is complicated since they can be affected by the complexity of different protein-chromophore interactions,[59,60] e.g., electrostatic interactions with charged amino acid side chains,[61] electrostatic interactions with neutral amino acid side chains and the protein backbone,[60] specific protein-chromophore interaction like H-bonding, and difference in the dielectric constant of the local environment. Thus, in most cases, the site energies are used as free parameters that are determined from the fitting of the theoretical to the experimental optical spectra. The second part of the system Hamiltonian:

$$\hat{H}_v = \sum_{m,n}^{m \neq n} V_{mn} |m><n| \tag{1.13}$$

V_{mn} denoting the interaction potential between sites m and n and leads to a non-radiative transfer of excitation energy between the pigments.[62] Finding the interaction potential between the pigments in photosynthesis complexes is assumed to be dominated by the Columb interaction and is calculated using the point-dipole approximation. This approximation becomes invalid in light-harvesting antenna complexes due to closely spaced chlorophylls (Chls), and the excitonic coupling has to be calculated by quantum chemical methods. In this work the Transition charges from electrostatic potentials (TrEsp) method[63] is used which the equation written as:[63]

$$V_{mn} = \frac{f}{4\pi\varepsilon_0} \sum_I^N \sum_J^N \frac{q_I^m(1,0) q_J^n(0,1)}{|\vec{r}_I - \vec{r}_J|} \tag{1.14}$$

Where f and ε_0 are screening factor and dielectric constant, respectively. The excitonic coupling result from the atomic transition charges $q_I^m(1,0)$ and $q_J^n(0,1)$ which these charges are determined for pigments *m* and *n* using time-dependent density functional theory[63-65] that fit the electrostatic potentials of the transition (or charge) densities to yield the appropriate vacuum dipole moments. The second part of the Hamiltonian, $\widehat{H}_B$, describes the vibrational dynamics of the bath (protein) by harmonic oscillators.

$$\widehat{H}_B = \sum_\xi \frac{\hbar\omega_\xi}{4} Q_\xi^2 + T_{nucl} \tag{1.15}$$

Where T_{nucl} denotes the kinetic energy of the nuclei. The coordinate Q_ξ can be expressed in terms of creation and annihilation operators of vibrational quanta, $Q_\xi = C_\xi + C_\xi^+$.[66] The last part of the Hamiltonian is a dynamical modulation of pigment transition energies induced by the protein (and pigment) vibrations that is described by the system-bath coupling

$$\widehat{H}_{SB} = \sum_m \sum_\xi \hbar\omega_\xi g_\xi^{(m)} Q_\xi |m><m| \tag{1.16}$$

Which assumes a linear modulation of the transition energy with the (dimensionless) vibrational coordinate Q_ξ and contains the (dimensionless) coupling constant $g_\xi^{(m)}$ that describes the coupling between a vibrational mode with frequency ω_ξ and the optical transition of the *m*th pigment and appear in the spectral density $J(\omega)$. Spectral density or phonon profile, $J(\omega)$, describes how the configuration of nuclei of the protein changes upon electronic excitation of the pigment.

$$J(\omega) = \sum_\xi g_\xi^2 \, \delta(\omega - \omega_\xi) = \sum_\xi s_\xi \, \delta(\omega - \omega_\xi) \tag{1.17}$$

s_ξ as defined above, is the dimensionless Huang-Rhys factor for each bath mode ξ and frequency ω_ξ indicating the strength of electron-phonon coupling.

A temperature-dependent phonon spectral density can be defined as

$$J(\omega;T) = \big(1 + n(\omega;T)\big)J(\omega) + n(-\omega;T)J(-\omega) \tag{1.18}$$

Where $n(\omega;T)$ is the temperature dependence of phonon described by Bose-Einstein distribution.[67]

$$n(\omega;T) = \frac{1}{e^{\hbar\omega/KT}-1} \tag{1.19}$$

Where K is the Boltzmann constant ($cm^{-1}\ K^{-1}$) and T is absolute temperature (K). $J(\omega;T)$ is zero for $\omega \leq 0$, and the second term on the right-hand side of Eq. (1.18) is only nonzero for negative wavenumbers which representing phonon annihilation events. The spectral density determines two important physical parameters, the total Huang-Rhys factor *S* and the optical reorganization energy E_λ [6668]

$$S = \int_0^\infty d\omega\, J(\omega) = \sum_\xi g_\xi^2 \tag{1.20}$$

$$E_\lambda = \hbar \int_0^\infty \omega\, J(\omega)\, d\omega \tag{1.21}$$

S also, can be defined as the average number of phonons coupled to an electronic transition and E_λ is the average energy needed to reorganize the nuclei after excitation. In practice, $J(\omega)$ can be approximated by a continuous function whose shape depends on the system under study. Due to lack of additional information usually the same spectral density is assumed for all similar chromophores in a system, although at present there is no way to validate this approximation. The spectral density is the key input parameter in Redfield theory and directly determines energy transfer rate constants and the shape of the phonon sideband.

1.4.1 Weakly and Strongly Coupled Pigments

In this section, the theories applicable to calculating energy transfer kinetics and optical spectra of photosynthesis pigment-protein complexes are reviewed. If the excitonic coupling between electronic excitations of the pigments is strong compared to the dynamic and static disorder ($V_{mn} \gg E_\lambda$), then delocalized electronic states are formed after light excitation. In this

case, the exciton relaxation between delocalized states is treated in the framework of multi-level Redfield theory. After light excitation in the weak coupling limit ($V_{mn} \ll E_\lambda$), localized states are created, and the excitation energy is transferred via incoherent hopping mechanism, and EET treated by Förster theory. In general, for photosynthetic pigment-protein complexes, neither limit applies in a strict sense, i.e., the situation where an aggregate of strongly coupled pigments couples weakly to another chromophore or aggregate, more sophisticated theories describing the intermediate cases have to be applied. An extension of Förster's theory, so-called generalized Förster theory has been considered in recent years[69-71] where the excitonic system divided into domains of strongly coupled pigments. Inter-domain excitation energy transfer is assumed to proceed via a hopping mechanism described by Förster theory, while intra-domain dynamics are treated with Redfield theory.[71,72] In practice, the domains for generalized Förster theory are determined by setting all coupling smaller than a critical value ($V_c \sim E_\lambda$) to zero.

1.4.1.1 Strongly Coupled pigments, Redfield Theory

If the excitonic coupling V_{mn} are large compared to the static and dynamic disorder, the excited state $|M>$ are delocalized. Each of these exciton states are linear combinations of localized excited stats $|m>$, that is

$$|M> = \sum_m c_m^M |m> \tag{1.22}$$

Where c_m^M are eigenvector coefficients which obtained by diagonalization of $\hat{H}_s = \sum_m E_m |m><m| + \sum_{m,n}^{m \neq n} V_{mn} |m><n|$.

$$\hat{H}_s |M> = E_M |M> \tag{1.23}$$

$|c_m^M|^2$ give the contribution of site m to state M and the eigenvalue E_M is corresponding to exciton-energies. Also, excited state transition dipoles are linear combination of the site dipole:

$$\vec{\mu}_M = \sum_m c_{mM} \vec{\mu}_m \tag{1.24}$$

The Multilevel Redfield theory, a second-order perturbative method, which is an example of Markovian (memoryless) theory, is used to describe energy relaxation in the limit of strong coupling. In this work, to simulate various optical spectra, a non-Markovian density matrix approach utilizing a Redfield rate equation to describe relaxation between exciton states is employed. It is noteworthy that in a Markovian theory for the equation of motion of a statistical density operator, $d\hat{\rho}(t)/dt$, depends only on the properties of the system at time t and not on properties at earlier times, i.e. there are no memory effects of the earlier behavior. The density matrix $\hat{\rho}(t)$ is a reduced statistical operator describing the electronic motion and in general, it is the reduction in degrees of freedom from the description of the dynamics of a large system to that of a small subsystem, which resulting in non-Markovian, or memory, effects.[68]

The homogenous absorption and fluorescence signals are given by, respectively,[73,74]

$$A(\omega) = \frac{4\pi^2 \omega n}{3\hbar c} \sum_M |\vec{\mu}_M|^2 D_M(\omega) \tag{1.25}$$

$$F(\omega) = \frac{4\omega^3 n^3}{3\hbar^2 c^3} \sum_M \left[\frac{e^{-\omega_M/kT}}{\sum_N e^{-\omega_N/kT}} \right] |\vec{\mu}_M|^2 D'_M(\omega) \tag{1.26}$$

with

$$|\vec{\mu}_M|^2 = \sum_{m,n} c_m^M c_n^M (\vec{\mu}_m \cdot \vec{\mu}_n) \tag{1.27}$$

Where $D_M(\omega)$ is the lineshape function for exciton state *M*. Similarly, the linear (LD) and circular dichroism (CD), and circularly polarized luminescence (CPL) expressed as:

LD (where is $\hat{n}$ the membrane normal vector), the intensity of LD spectra depends on the orientation angle between the transition dipole and the membrane normal $\hat{n}$.

$$LD(\omega) \propto \omega \sum_M (|\vec{\mu}_M|^2 - 3(\vec{\mu}_M \cdot \hat{n})^2) D_M(\omega) \tag{1.28}$$

and,

$$CD(\omega) \propto \omega \sum_M r_M D_M(\omega) \tag{1.29}$$

and CPL.

$$CPL(\omega) \propto \omega^3 \sum_M \left[\frac{e^{-\omega_M/kT}}{\sum_N e^{-\omega_N/kT}}\right] r_M D'_M(\omega) \tag{1.30}$$

respectively.

Note that for CD and CPL the exciton dipole strength ($|\vec{\mu}_M|^2$) is replaced with the excitonic rotational strength

$$r_M = \frac{\pi}{2}\sum_{m,n} c_m^M c_n^M \left(E_0^m \vec{R}_m - E_0^n \vec{R}_n\right) \cdot (\vec{\mu}_m \times \vec{\mu}_n) \sim \frac{\pi}{2}\sum_{m,n} c_m^M c_n^M \vec{R}_{mn} \cdot (\vec{\mu}_m \times \vec{\mu}_n) \tag{1.31}$$

A CPL spectrum is the fluorescence analog of CD. The positive component in CPL spectrum indicates that the I_L (absorption of left circularly-polarized light) is stronger than I_R (right circularly-polarized light). In the opposite case one will observe a negative CPL band.

The exciton line shape function which account for both diagonal and off-diagonal exciton-vibration coupling, is derived from the reduced density matrix as:[68]

$$D_M^{(\prime)}(\omega) = \int_{-\infty}^{\infty} e^{\pm 2\pi i(\omega - \tilde{\omega}_M)t + \mathrm{G}_M(t) - \mathrm{G}_M(0) - \pi\Gamma_M|t|} dt \tag{1.32}$$

where $\pm$ describes absorption (D_M) and emission (D'_M), respectively. Additionally, the Fourier transform of the spectral density (scaled for delocalization) describes the time-dependent function:

$$G_M(t) = \left[\sum_{m,n} |c_m^M|^2 |c_n^M|^2 e^{-R_{mn}/R_c}\right] \int_{-\infty}^{\infty} e^{-2\pi i\omega t} J_{ph}(\omega) d\omega \tag{1.33}$$

$$\tilde{\omega}_M = E_M + \sum_{N \neq M}\left[\sum_{m,n} c_m^M c_n^M c_m^N c_n^N e^{-R_{mn}/R_c}\right] C^{(Im)}(\omega_M - \omega_N) \tag{1.34}$$

The first term of Eq. 1.34 is the eigenvalue from Eq. (1.23) and the second term describes the energy shift due to el-ph coupling. Where R_c is the correlation radius of protein vibrations. In the limit of completely correlated/ uncorrelated fluctuation no exciton relaxation/maximum exciton relaxation rate ocuurs.[59,68] A value of 5 Å has been proposed by pump-probe spectra of PSII RC.[75]

Γ_M, exciton lifetime broadening which depends on the rates of exciton relaxation ($k_{M\to N}$)[68]

$$\Gamma_M = \sum_N k_{M\to N} \tag{1.35}$$

$$\Gamma_M = \sum_{N\neq M}\left[\sum_{m,n} c_m^M c_n^M c_m^N c_n^N e^{-R_{mn}/R_c}\right] C^{(Re)}(\omega_M - \omega_N) \tag{1.36}$$

The real and imaginary parts of the Fourier transfer of the energy gap correlation function can be described in terms of the spectral density, respectively, as:

$$C^{(Re)}(\omega) = \pi\omega^2\left[\big(1+n(\omega)\big)J_{ph}(\omega) + n(-\omega)J_{ph}(-\omega)\right] \tag{1.37}$$

$$C^{(Im)}(\omega) = \frac{1}{\pi}\mathfrak{p}\int_{-\infty}^{\infty}\frac{C^{(Re)}(\Omega)}{\omega-\Omega}d\Omega \tag{1.38}$$

Finally, the rates of exciton relaxation:[68]

$$k_{M\to N} = 2\pi\,\omega_{MN}^2 \sum_{m,n} c_m^M c_n^M c_m^N c_n^N e^{-R_{mn}/R_c} \times J(\omega_{MN}, T) \tag{1.39}$$

1.4.1.2 Weakly Coupled pigments, Förster Theory

If the excitonic coupling between pigment is weak compared to the dynamic and static disorder, a second order perturbation theory in the excitonic coupling is used to obtain a Förster type rate constant $k_{m\to n}$ for EET between pigment *m* and *n*.[62] the rate constant:

$$k_{m\to n} = 2\pi\,\frac{|V_{mn}|^2}{\hbar^2}\int_{-\infty}^{\infty} d\omega D_I^{(m)}(\omega)\, D_\alpha^{(n)}(\omega) \tag{1.40}$$

is given as an overlap integral of fluorescence lineshape function $D_I^{(m)}(\omega)$ of the donor and the absorption lineshape function $D_\alpha^{(n)}(\omega)$ of the acceptor. The equation describes radiationless energy transfer between excited state localized on individual pigments.

1.4.1.3 Weak Inter- and Strong Intra-Aggregate coupling- Generalized Förster Theory

In order to describe interdomain EET rate in generalized Förster theory ($k_{Ma\to Nb}$),[71,72] the standard Förster rate equation (1.40) is used to delocalized exciton states. That is,

$$k_{Ma\to Nb} = 2\pi \frac{|V_{Ma,Nb}|^2}{\hbar^2} \int_{-\infty}^{\infty} d\omega D_I^{(Ma)}(\omega)\, D_\alpha^{(Nb)}(\omega) \tag{1.41}$$

Where *Ma* indicates exciton state $|Ma\rangle$ of aggregate a. Exciton coupling $V_{Ma,Nb}$ between exciton state $|Ma\rangle$ and $|Nb\rangle$ is given as a sum of the point-dipole couplings $V_{ma,nb}$ between the individual pigments, weighted by the exciton coefficient $c_{ma}^{(Ma)}$ of pigment *m* in aggregate *a* and $c_{nb}^{(Nb)}$of pigment *n* in aggregate *b*:

$$V_{Ma,Nb} = \sum_{m_a,m_b} c_{m_a}^{(Ma)} c_{n_b}^{(Nb)} V_{m_a n_b} \tag{1.42}$$

The total rate of energy transfer from aggregate *a* to aggregate *b* depends on the thermally weighted interdomain EET rates[71,72]

$$k_{a\to b} = \sum_{Ma,Nb} \frac{e^{-E_{Ma}/KT}}{\sum_{Ka} e^{-E_{Ka}/KT}} k_{Ma\to Nb} \tag{1.43}$$

References

(1) Blankenship, R. E. *Molecular Mechanisms of Photosynthesis*; Blackwell Science: Oxford, **2002.**

(2) Kallas, T. in The Molecular Biology of Cyanobacteria, D. A. Bryant, Ed.; Kluwer Academic: Dordrecht, The Netherlands, 1994, pp. 259–317.

(3) Barber, J. Photosystem II: The Engine of Life. *Q Rev Biophys.* **2003**, *36*, 71-89.

(4) Wei, X.; Su, X.; Cao, P.; Liu, X.; Chang, W.; Li, M.; Zhang, X.; Liu, Z. Structure of Spinach Photosystem II−LHCII Supercomplex at 3.2 Å Resolution. *Nature* **2016**, *534*, 69−74.

(5) Pan, X.; Li, M.; Wan, T.; Wang, L.; Jia, C.; Hou, Z.; Zhao, X.; Zhang, J.; Chang, W. Structural Insights into Energy Regulation of Light-harvesting Complex CP29 from Spinach. *Nat. Struct. Mol. Biol*. **2011**, *18*, 309-315.

(6) Jurinovich, S.; Viani, L.; Prandi, I. G.; Renger, T.; Mennucci, B. Towards an ab Initio Description of the Optical Spectra of Light-Harvesting Antenna: Application to the CP29 Complex of Photosystem II. *Phys. Chem. Chem. Phys.* **2015**, *17*,14405-14416.

(7) Picorel, R.; Alfonso, M.; Seibert, M. Isolation and purification of CP43 and CP47 Photosystem II Proximal Antenna Complexes from Plants. In Photosynthesis Research Protocols; Methods in Molecular Biology Series; Walker, J. M., Ed.; Springer: New York, 2011; Vol 684, pp 105−112.

(8) Casazza, A. P.; Szczepaniak, M.; Müller, M. G.; Zucchelli, G.; Holzwarth, A. R. Energy Transfer Processes in the Isolated Core Antenna Complexes CP43 and CP47 of Photosystem II. *Biochimica et Biophysica Acta*, **2010**, *1797*, 1606–1616.

(9) Olson, J. M. Chlorophyll Organization in Green Photosynthetic Bacteria. *Biochim Biophys Acta*, **1980**, *594*, 33-51.

(10) Blankenship, R. E.; Brune, D. C.; Wittmershaus, B. P. in Light Energy Transduction in Photosynthesis: Higher Plants and Bacterial Models, S. E. Stevens, Jr. and D. A. Bryant, Eds.; American Society of Plant Physiologists, Rockville, MD, 1988; pp 32–46.

(11) Tang, K.-H.; Zhu, L.; Urban, V. S.; Collins, A. M.; Biswas, P.; Blankenship, R. E. Temperature and Ionic Strength Effects on the Chlorosome Light-Harvesting Antenna Complex. *Langmuir* **2011**, *27*, 4816–4828.

(12) Mimuroa, M.; Nozawab, T.; Tamai, N.; Nishimurad, Y.; Yamazakid, I. Presence and Significance of Minor Antenna Components in the Energy Transfer Sequence of the Green Photosynthetic Bacterium *Chloroflexus aurantiacus. FEBS Lett*. **1994**, *340*, 167-172.

(13) Prokhorenko, V. I.; Steensgaard, D. B.; Holzwarth, A. R. Exciton Dynamics in the Chlorosomal Antennae of the Green bacteria *Chloroflexus aurantiacus* and *Chlorobium tepidum. Biophysical Journal*. **2000**,*79*, 2105–2120.

(14) Olson, J. M. Chlorophyll Organization and Function in Green Photosynthetic Bacteria. *Photochem. Photobiol.***1998**, *67*, 61–75.

(15) Montaño, G. A.; Wu, H.-M.; Lin, S.; Brune, D. C.; Blankenship, R. E. Isolation and Characterization of the B798 Light-Harvesting Baseplate from the Chlorosomes of *Chloroflexus aurantiacus*. *Biochemistry* **2003**, *42*, 10246–10251.

(16) Oostergetel, G. T.; Reus, M.; Chew, A. G. M.; Bryant, D. A.; Boekema, E. J.; Holzwarth, A. R. Long-range Organization of Bacteriochlorophyll in Chlorosomes of *Chlorobium tepidum* Investigated by Cryo-Electron microscopy. *FEBS Lett.* **2007**, *581*, 5435−5439.

(17) Egawa, A.; Fujiwara, T.; Mizoguchi, T.; Kakitani, Y.; Koyama, Y.;Akutsu, H. Structure of the Light-Harvesting Bacteriochlorophyll c Assembly in Chlorosomes from *Chlorobium limicola* Determined by Solid-State NMR. *Proc. Natl. Acad. Sci. U.S.A.* **2007**, *104*, 790−795.

(18) Frigaard, N. U.; Takaichi, S.; Hirota, M.; Shimada, K.; Matsuura, K. Quinones in Chlorosomes of Green Sulfur Bacteria and their Role in the Redox-Dependent Fuorescence Studied in Chlorosome-Like Bacteriochlorophyll c Aggregates. *Arch. Microbiol.* **1997**, *167*, 343-349.

(19) Yakovlev, A. G.; Taisova, A. S.; Fetisova, Z. G. Light Control over the Size of an Antenna Unit Building Block as an Efficient Strategy for Light Harvesting in Photosynthesis. *FEBS Lett.* **2002**, *512*, 129–132.

(20) Borrego, C.M.; Gerola, P. D.; Miller, M.; Cox, R. P. Light Intensity Effects on Pigment Composition and Organization in the Green Sulfur Bacterium *Chlorobium tepidum*. *Photosynthesis Research*.**1999**, *59*, 159-166.

(21) Oelze, J.; Golecki, J. R. Membranes and Chlorosomes of Green Bacteria: Structure, Composition and Development. In *Anoxygenic Photosynthetic Bacteria*, EdS.; Blankenship, R.E.; Madigan, M. T.; Bauer, C. E., Kluwer: Dordrecht.1995, 259-278.

(22) Staehelin, L. A.; Golecki, J. R.; Fuller, R. C.; Drews, G. Visualization of the Supramolecular Architecture of Chlorosomes (Chlorobium Type Vesicles) in Freeze-Fractured Cells of *Chloroflexus aurantiacus*. *Arch Microbiol.* **1978**, *119*, 269–277.

(23) Staehelin, L. A.; Golecki, J. R.; Drews, G. Supramolecular Organization of Chlorosomes (Chlorobium Vesicles) and of their Membrane Attachment Sites in *Chlorobium limicola*. *Biochim. Biophys. Acta.* **1980**, *589*, 30-45.

(24) Pedersen, M.O.; Linnanto, J.; Frigaard, N. U.; Nielsen, N. C.; Miller, M. A model of the protein – pigment baseplate complex in chlorosomes of photosynthetic green bacteria. *Photosynth Res.***2010**, *104*, 233–243.

(25) Feick, R. G.; Fuller, R. C. Topography of the Photosynthetic Apparatus of *Chloroflexus aurantiacus*. *Biochemistry.* **1984**, *23*, 3693-3700.

(26) Sakuragi, Y.; Frigaard, N. U.; Shimada, K.; Matsuura, K. Association of Bacteriochlorophyll a with the CsmA Protein in Chlorosomes of the Photosynthetic Green Filamentous Bacterium *Chloroflexus aurantiacus*. *Biochimica et Biophysica Acta*. **1999**, *1413*, 172-180.

(27) Bryant, D. A.; Vassilieva, E. V.; Frigaard, N. U.; Li, H. Selective Protein Extraction from *Chlorobium tepidum* Chlorosomes Using Detergents. Evidence that CsmA forms Multimers and Binds Bacteriochlorophyll *a*. *Biochemistry*. **2002**, *41*,14403–14411.

(28) Pierson, B. K.; Castenholz, R. W. Taxonomy and physiology of filamentous anoxygenic phototrophs. In *Anoxygenic Photosynthetic Bacteria* (Edited by Blankenship, R.E.; Madigan, M. T.; Bauer, C. E.) Kluwer, Dordrecht. **1995**, 3147.

(29) Ben-Shem, A.; Frolow, F.; Nelson, N. Evolution of photosystem I-from Symmetry through Pseudo-Symmetry to Asymmetry. *FEBS Lett.* **2004,** *564*, 274–280.

(30) Tronrud, D. E.; Wen, J.; Gay, L.; Blankenship, R. E. The Structural Basis for the Difference in Absorbance Spectra for the FMO Antenna Protein from Various Green Sulfur Bacteria. *Photosynth Res*, **2009**, *100*, 79–87.

(31) Hauska, G.; Schoedl, T.; Remigy, H.; Tsiotis, G. The Reaction Center of Green Sulfur Bacteria. *Biochim Biophys Acta.* **2001**, *1507*, 260–277.

(32) Permentier, H. P.; Schmidt, K.A.; Kobayashi, M.; Akiyama, M.; Hager-Braun, C.; Neerken, S.; Miller, M.; Amesz, J. Composition and Optical Properties of Reaction Centre Core Complexes from the Green Sulfur Bacteria *Prosthecochloris aestuarii* and *Chlorobium tepidum*. *Photosynth Res.* **2000,** *64*, 27–39.

(33) Blankenship, R.E.; Olson, J.M.; Miller, M. Antenna Complexes from Green Photosynthetic bacteria, in: R.E. Blankenship, M.T. Madigan, C.E. Bauer (Eds.), Anoxygenic Photosynthetic Bacteria, Kluwer Academic Publishers, The Netherlands, 1995, 399–471.

(34) Li, Y. F.; Zhou, W.L.; Blankenship, R. E.; Allen, J.P. Crystal structure of the Bacteriochlorophyll *a* Protein from *Chlorobium tepidum*, *J. Mol. Biol.* **1997**, *271*, 456–471.

(35) Adams, P. G.; Cadby, A. J.; Robinson, B.; Tsukatani, Y.; Tank, M.; Wen, J.; Blankenship, R. E.; Bryant, D. A.; Hunter, C. N. Comparison of the Physical Characteristics of Chlorosomes from Three Different Phyla of Green Phototrophic Bacteria. *Biochimica et Biophysica Acta*, **2013**, *1827* ,1235–1244.

(36) Cho, M. Coherent Two-Dimensional Optical Spectroscopy. *Chem. Rev.* **2008**, *108*, 1331–1418.

(37) Abramavicius, D.; Pamieri, B.; Voronine, D. V.; Šanda, F.; Mukamel, S. Coherent Multidimensional Optical Spectroscopy of Excitons in Molecular Aggregates; Quasiparticle versus Supermolecule Perspectives. *Chem. Rev.* **2009**, *109*, 2350–2408.

(38) Read, E. R.; Lee, H.; Fleming, G. R. Photon Echo Studies of Photosynthetic Light Harvesting. *Photosynth Res*. **2009**, *101*, 233–243.

(39) Chauvet, A.; Jankowiak, R.; Kell, A.; Picorel, R.; Savikhin, S. Does the Singlet Minus Triplet Spectrum with Major Photobleaching Band Near 680-682 nm Represent an Intact Reaction Center of Photosystem II? *J. Phys. Chem. B* **2015**, *119*, 448–455.

(40) Purchase, R.; Völker, S. Spectral Hole Burning: Examples from Photosynthesis. *Photosynth Res*. **2009**, *101*, 245–266.

(41) Jankowiak, R.; Reppert, M.; Zazubovich, V.; Pieper, J.; Reinot, T. Site Selective and Single Complex Laser-Based Spectroscopies: A Window on Excited State Electronic Structure, Excitation Energy Transfer, and Electron-Phonon Coupling of Selected Photosynthetic Complexes. *Chem. Rev.* **2011**, 111, 4546–4598.

(42) Jankowiak, R.; Small, G. J. Hole-Burning Spectroscopy and Relaxation Dynamics of Amorphous Solids at Low Temperatures. *Science* **1987**, 237, 618–625.

(43) Jankowiak, R.; Hayes, J. M.; Small, G. J. Spectral Hole-Burning Spectroscopy in Amorphous Molecular Solids and Proteins. *Chem. Rev.* **1993**, 93, 1471–1502.

(44) *Persistent Spectral Hole-Burning: Science and Applications*; Moerner, W. E., Ed.; Topics in Current Physics, Volume 44; Springer-Verlag: Berlin, 1988.

(45) *Zero-Phonon Lines and Spectral Hole Burning in Spectroscopy and Photochemistry*; Sild, O., Haller, K., Eds.; Springer-Verlag: Berlin, 1988.

(46) Moerner, W. E. *Topics in Current Physics. Persistent Spectral Hole Burning: Science and Applications*; Springer-Verlag: New York, 1987; p 1.

(47) Rebane, K. K., *Impurity Spectra of Solids*, Plenum: New York, 1970, p 1.

(48) Franck, J. Elementary Processes of Photochemical Reactions. *Trans. Faraday Soc.* **1926**, 21, 536–542.

(49) Condon, E. A Theory of Intensity Distribution in Band Systems. *Phys. Rev.* **1926**, 28, 1182–1201.

(50) Parson, W. W. *Modern Optical Spectroscopy*; Springer-Verlag: Berlin, 2009, pp 163–170.

(51) Personov, R. I. *In Spectroscopy and Excitation Dynamics of Condensed Molecular Systems*; Agranovich, V. M., Hochstrasser, R. M., Eds.; Elsevier Science Ltd: Amsterdam, 1983; p 1.

(52) Kihara, S.; Hartzler, D. A.; Orf, G. S.; Blankenship, R. E.; Savikhin, S. The Fates of the Triplet Excitations in the Fenna–Matthews–Olson Complex. J. Phys. Chem. B **2015**, 119, 5765–5772.

(53) *The Photosynthetic Reaction Center: Volume II*; Deisenhofer, J., Norris, J. R., Eds.; Academic: San Diego, 1993.

(54) Jankowiak, R.; Hayes, J. M.; Small, G. J. Spectral Hole-Burning Spectroscopy in Amorphous Molecular Solids and Proteins. Chem. Rev. **1993**, 93, 1471–1502.

(55) Hayes, J. M.; Jankowiak, R.; Small, G. J. Two-Level-System Relaxation in Amorphous Solids as Probed by Nonphotochemical Hole-Burning in Electronic Transitions. *In Persistent Spectral Hole-Burning: Science and Applications*; Moerner, W. E., Ed.; Topics in Current Physics, Volume 44; Springer-Verlag: Berlin, 1988; pp 153–202.

(56) Shu, L.; Small, G. J. On the Mechanism of Nonphotochemical Hole Burning of Optical Transitions in Amorphous Solids. *Chem. Phys.* **1990**, 141, 447–455.

(57) Shu, L.; Small, G. J. Mechanism of Nonphotochemical Hole Burning: Cresyl Violet in Polyvinyl Alcohol Films. *J. Opt. Soc. Am. B* **1992**, 9, 724–732.

(58) Rätsep, M.; Pieper, J.; Irrgang, K. D.; Freiberg, A. Excitation Wavelength-Dependent Electron-Phonon and Electron-Vibrational Coupling in the CP29 Antenna Complex of Green Plants. *J. Phys. Chem. B* **2008,** *112*, 110-118.

(59) Adolphs, J.; Renger, T. How Proteins Trigger Excitation Energy Transfer in the FMO Complex of Green Sulfur Bacteria. *Biophys. J.* **2006**, 91, 2778–2797.

(60) Gudowska-Nowak, E.; Newton, M. D.; Fajer, J. Conformational and environmental effects on bacteriochlorophyll optical spectra: Correlations of calculated spectra with structural results. *J Phys Chem.***1990**, *94*, 5795–5801.

(61) Eccles, J.; Honig, B. Charged amino acids as spectroscopic determinants for chlorophyll in vivo. *Proc Natl Acad Sci USA*, **1983**, *80*, 4959–4962.

(62) Förster, T. Zwischenmolekulare Energiewanderung und Fluoreszenz. *Ann. Phys. (Berlin)* **1948**, *437*, 55–75.

(63) Madjet, M. E.; Abdurahman, A.; Renger, T. Intermolecular Coulomb Couplings from Ab Initio Electrostatic Potentials: Application to Optical Transitions of Strongly Coupled Pigments in Photosynthetic Antennae and Reaction Centers. *J. Phys. Chem. B* **2006**, *110*, 17268–17281.

(64) Müh, F.; Madjet, M. E.-A.; Renger, T. Structure-Based Identification of Energy Sinks in Plant Light-Harvesting Complex II. *J. Phys. Chem. B* **2010**, *114*, 13517–13535.

(65) Adolphs, J.; Müh, F.; Madjet, M. E.-A.; Schmidt am Busch, M.; Renger, T. Structure-Based Calculations of Optical Spectra of Photosystem I Suggest an Asymmetric Light-Harvesting Process. *J. Am. Chem. Soc.* **2010**, *132*, 3331–3343.

(66) May, V.; Kühn, O. *Charge and Energy Transfer Dynamics in Molecular Systems:* A theoretical introduction.; John Wiley & Sons: Berlin, 2000.

(67) Bose. Plancks Gesetz und Lichtquantenhypothese. *Z. Phys.* **1924**, 26, 178–181.

(68) Renger, T.; Marcus, R. A. On the Relation of Protein Dynamics and Exciton Relaxation in Pigment-Protein Complexes: An Estimation of the Spectral Density and a Theory for the Calculation of Optical Spectra. *J. Chem. Phys.* **2002**, 116, 9997–10019.

(69) Raszewski, G.; Saenger, W.; Renger, T. Theory of optical spectra of Photosystem II reaction centers: Location of the triplet state and the identity of the primary electron donor. *Biophys J.* **2005**, *88*, 986–998.

(70) Scholes, G. D.; Fleming, G. R. On the mechanism of light harvesting in photosynthetic purple bacteria: B800 to B850 energy transfer. *J Phys Chem B.* **2000**, *104*, 1854–1868.

(71) Renger, T.; Holzwarth, A. R. Theory of excitation energy transfer and optical spectra of photosynthetic systems. *In Biophysical techniques in photosynthesis II.*eds. Aartsma, T. J.; Matysik, J. Dordrecht, The Netherlands: Springer, 2008, pp. 421–443.

(72) Raszewski, G.; Renger, T. Light harvesting in Photosystem II core complexes is limited by the transfer to the trap: can the core complex turn into a photoprotective mode? *J. Am. Chem. Soc.* **2008**, *130*,4431–4446.

(73) Lax, M. The Franck-Condon Principle and Its Application to Crystals. *J. Chem. Phys.* **1952**, *20*, 1752–1760.

(74) Kubo, R.; Toyozawa, Y. Application of the Method of Generating Function to Radiative and Non-Radiative Transitions of a Trapped Electron in a Crystal. *Prog. Theor. Phys.* **1955**, *13*, 160–182.

(75) Renger, T.; Marcus, R. A. Photophysical Properties of PS-2 Reaction Centers and a Discrepancy in Exciton Relaxation Times. *J. Phys. Chem. B* **2002**, *106,* 1809–1819.

Chapter 2

Toward an Understanding of the Excitonic Structure of the CP47 Antenna Protein Complex of Photosystem II Revealed via Circularly Polarized Luminescence

Mahboobe Jassas[1,%], Tonu Reinot[1,%], Adam Kell[1] and Ryszard Jankowiak[1,2*]

[1]Department of Chemistry and [2]Department of Physics, Kansas State University, Manhattan, KS 66506, USA

[%]Contributed equally to this work

Reproduced from *the Journal of Physical Chemistry B* **2017**, 121, 4364-4378

Abstract

Identification of the lowest energy pigments in the photosynthetic CP47 antenna protein complex of Photosystem II (PSII) is essential for understanding its excitonic structure, as well as excitation energy pathways in the PSII core complex (PSII-cc). Unfortunately, there is no consensus concerning the nature of the low-energy state(s) nor chlorophyll (Chl) site energies in this important photosynthetic antenna. Although, we raised concerns regarding the estimations of Chl site energies obtained from modeling studies of various types of CP47 optical spectra [Reinot, T; et al., *Anal. Chem. Insights* **2016**, *11*, 35–48] recent new assignments imposed by the shape of the circularly polarized luminescence (CPL) spectrum [Hall, J; et al., *Biochim. Biophys. Acta* **2016**, *1857*, 1580–1593] necessitate our comments. We demonstrate that other combinations of low-energy Chls provide equally good or improved simultaneous fits of various optical spectra (absorption, emission, CPL, circular dichroism, and nonresonant hole-burned spectra), but more importantly, we expose the heterogeneous nature of the recently studied complexes and argue that the published composite nature of the CPL (contributed to by CPL_{685}, CPL_{691}, and CPL_{695}) does not represent an intact CP47 protein. A positive CPL_{695} is extracted for the intact protein, which when simultaneously fitted with multiple other optical spectra, provides new information on the excitonic structure of intact and destabilized CP47 complexes and their lowest energy state(s).

2.1 Introduction

2.1.1 CP47 complexes

Light absorbing chromophores in various photosynthetic complexes initiate a series of processes which drive many chemical reactions that support life on Earth.[1] CP47 is an important photosynthetic antenna complex, being part of the Photosystem II core complex (PSII-cc) with its primary function thought to be light energy absorption and transport of excitation energy to the reaction center. The CP47 complex is a challenging protein to study, as it is more difficult to separate from the PSII-cc than, for example, the accompanying CP43 antenna.[2,3] In addition, it is not known to what extent the absence and/or destabilization of the PsbH protein affects the site energies of chlorophylls (Chls) and the resulting emission spectra. It is also not clear whether all (or only some) Chl 29 have a H-bond between their 13'-keto and threonine (Thr5) of the PsbH protein. This is probably why different optical spectra have been reported over the years, which has led to disagreement about which spectra represent *intact* CP47 complexes and should be used in modeling studies.[4-6] As a result, there is still no agreement as to which Chl(s) contribute to the lowest energy exciton state(s) and what their corresponding site energies are.[7-11] While inter-pigment coupling matrix elements can be calculated from available X-ray structures,[12,13] the site energies are typically extracted from simultaneous fits of various experimental data.[7-9] Quantum chemical approaches can also be used,[14-17] but so far the calculated site energies cannot describe experimental data. As a result, the calculated values have to be largely modified by additional shifting to lower- and/or higher-energies, via fitting algorithms.[7-11] Nevertheless, it is anticipated that future higher-resolution structural data and more reliable experimental data will further aid in discarding unrealistic site energy sets obtained from the fitting algorithms, in particular when optical spectra of intact samples are analyzed (vide infra). The difficulties in finding Chl *a* site

energies in the CP47 complex are not surprising, as this protein can be easily destabilized. For example, as mentioned above, CP47 complexes may possess an intact PsbH subunit, which could be also absent or destabilized. In the latter case, the H-bond(s) between one of the CP47 Chls and the amino acid residues of PsbH and/or the H-bond(s) between Chls and water molecules (serving as axial ligands) could be broken or weakened.[6] Thus, the key problem concerning the uncertainties in pigment site energies is sample integrity and stability of the complex after isolation.

2.1.2 Further challenges facing determination of Chl a site energies in CP47

Furthermore, interrogation of CP47 complexes using a large excitation fluence at low-temperatures may also lead to modification of optical spectra; i.e., the latter can change the shapes of absorption, and, in particular, the shapes of emission and circularly polarized luminescence (CPL) spectra due to reversible hole-burning (HB) and/or irreversible photodamage phenomena.[4,5] While the effect of HB can be eliminated by sample annealing, one needs to be mindful of photodamage that is irreversible.[4,5] Another important obstacle in providing a unified description of the structure-function relationship in CP47 (or any other photosynthetic complex) is that different shapes of the phonon spectral density, $J_{\mathrm{ph}}(\omega)$, are used to describe its electronic structure.[5,8,10,11] In addition, there is insufficient experimental information on site-dependent inhomogeneities and site-dependent $J_{\mathrm{ph}}(\omega)$. Therefore, we argued recently that a single solution of pigment site energies based on modeling studies of typically measured optical spectra alone may not exist, and a larger number of experimental constraints is needed to narrow the possible choices; for example, the resulting Hamiltonian needs to be able to describe all frequency- and time-domain data. However, most importantly, the consensus (not available as of yet) must exist as to which spectra constitute an intact/stable complex and should be used in modeling studies.[11] To provide more insight we analyze and model multiple spectra obtained for both destabilized[10] (at least in

our view; vide infra) and intact[4] CP47 complexes to identify the most likely low-energy Chls in intact samples.

2.1.3 CPL spectra

We begin with a discussion of the recently published theoretical fits of the low-temperature CPL and circular dichroism (CD) spectra obtained at liquid helium temperatures for CP47, which, as argued by the authors of ref 10, offer a clear identification of the lowest energy exciton state of *intact* CP47. While we agree that the CPL spectrum has the advantage in that it is selective for the lowest energy state, the key questions are: *i)* does the interrogated lowest energy state(s) represent the intact, destabilized, or a *mixture* of intact and destabilized complexes, especially under experimental conditions used in ref 10; *ii)* which emission spectrum (whose reported maxima vary in the literature from 689-695 nm,[4,5,18-20] with a variable contribution of the so-called 685 nm, 691 nm, and 695 nm emissions[4]) originates from the lowest energy state of *intact/stable* CP47 and/or intact PSII-cc; and *iii)* how reliable is the identification of the low-energy Chls based on the fits of the CPL and CD spectra reported in ref 10, that is, is there a unique solution to account for the lowest energy pigment, i.e. Chl 11, as suggested in ref 10?

2.1.4 What is the assertion of this work?

We suggest that in contrast to the conclusions of ref 10, the CP47 complex studied by Hall et al. was likely structurally modified during or after the isolation procedure (i.e. the sample was heterogeneous), and for that reason its optical spectra cannot be considered to represent intact/stable complex, and as a result should not be directly used in modeling studies. The complex shape of the CPL curve is in perfect agreement with the variable 685 nm, 691 nm, and 695 nm contributions observed over the years in the CP47 emission spectra.[4] Although in the main part of this work we focus on intact CP47 complexes (again, in our opinion), for the sake of argument we

will also fit spectra reported by Hall et al.[10] using our algorithm (see Appendix A). However, by doing this, we will demonstrate that in contrast to their fit different sets of low-energy Chls provide improved or equally good fits of their optical spectra. In summary, we raise concerns about the recently proposed interpretation and innovative implications suggested for new understanding of the excitonic structure of isolated CP47 complex and the entire PSII-cc, and proposed regulation of energy transfer, as described in ref 10. An alternative view is proposed, emphasizing the new interpretation of the recently published CPL spectrum. Finally, the implications of our new assignments are also briefly discussed.

2.2 Methods

To test the key assertion of ref 10 we first model their optical spectra, focusing, as an example, on the newly measured CPL spectra. Our modeling approach is described in ref 11; in brief, the disorder is introduced into the diagonal matrix elements (i.e., E_0^n) by a Monte-Carlo approach with normal distributions centered at E_0^n (n labeling various pigments, i.e., n = 1-16) and with *fwhm* representing Γ_{inh}, which can be site-dependent or independent. Eigen decomposition of the interaction matrix provides eigen-coefficients (c_n^M) and eigenvalues (ω_M). Phonon and vibrational Huang-Rhys (S) factors are used as free or fixed parameters and are optimized simultaneously against the experimental spectra. We use experimentally determined phonon spectral density $J_{\text{ph}}(\omega)$[11] and vibrational spectral density $J_{\text{vib}}(\omega)$.[8] Intramolecular vibrational modes (J_{vib}) are dynamically localized[21] and only contribute to absorption, HB, linear dichroism (LD) and fluorescence spectra.[22]

For easy comparison, the Chls within the CP47 complex are divided into the same five excitonic domains of coupled Chls as in ref 10 with V_c = 30 cm^{-1}. In this case, the Poisson-TrEsp coupling matrix elements (based on the 1.9 Å crystal structure of PSII from cyanobacteria, PDB

ID: 3ARC[12]) are used in all modeling studies. Isolated Chls are placed in separate domains. We also use somewhat larger TrEsp V_{nm} values with V_c = 30 cm^{-1} which leads to three domains. We hasten to add that a division into well-defined domains is not straightforward and often impossible. However, two criteria for defining domains have been proposed,[23] both relating to circumstances which can cause localization of the excited state. That is, pigment *m* is considered in a domain if the following is true for the coupling constant of pigments *m* and *n*, where *n* is already assigned to a particular domain, i.e., 1) $|V_{nm}|$ is larger than the coupling cutoff V_c (which is on the order of the reorganization energy); and 2) $|V_{nm}| > (E_n - E_m)/6$ (with *E* representing each pigment's site energy). These criteria are simple approximations for the consideration of dynamic localization and localization due to large energetic separation. The latter is critical when inhomogeneous broadening is large or weakly coupled Chls have very different site energies. Thus, three cases (A, B, and C) could be considered. In Case A, the complex is divided into five domains as in ref 10 using Poisson-TrEsp V_{nm} and the domain cutoff of V_c = 30 cm^{-1} with excitons delocalized over an entire domain. In Case B we also put all intradomain V_{nm} values smaller than V_c = 30 cm^{-1} to zero. Finally, we also performed modeling study with TrEsp V_{nm} assuming that both intra- and interdomain $V_{nm} < V_c$ are set to zero (Case C). The results obtained for all cases are compared below. The intermediate case, which would explicitly consider disorder within the second criterion ($V_{nm} > (E_n - E_m)/6$) (taking into account the inhomogeneous broadening for all Chls in the Monte Carlo simulations), is beyond the scope of this work, as, in the first approximation, we anticipate that the resulting fits should lie somewhere between the above mentioned limiting cases.

In simulations, we used a non-Markovian reduced density matrix theory[24] with a Nelder-Mead Simplex algorithm for parameter optimization.[25] It is assumed that the phonon spectral

density (weighted phonon profile) can be described by a continuous function, which is chosen to be a lognormal distribution,[26]

$$J_{ph}(\omega) = \frac{S_{ph}}{\omega\sigma\sqrt{2\pi}} e^{-\frac{\left[\ln\left(\frac{\omega}{\omega_c}\right)\right]^2}{2\sigma^2}} \tag{2.1}$$

where ω_c is the cutoff frequency, σ is the standard deviation, and $J_{ph}(\omega \leq 0) = 0$. The real and imaginary parts of the Fourier transfer of the energy gap correlation function can be described in terms of the spectral density as

$$C^{(Re)}(\omega) = \pi\omega^2\left[\big(1 + n(\omega)\big)J_{ph}(\omega) + n(-\omega)J_{ph}(-\omega)\right] \tag{2.2}$$

$$C^{(Im)}(\omega) = \frac{1}{\pi}\mathfrak{p}\int_{-\infty}^{\infty}\frac{C^{(Re)}(\Omega)}{\omega-\Omega}d\Omega \tag{2.3}$$

with $n(\omega)$ the Bose-Einstein distribution and $\mathfrak{p}$ representing the Cauchy principal value. Eqs 2 and 3 are used in calculating the exciton lifetime broadening and energy shift, respectively, as

$$\Gamma_M = \sum_{N\neq M}\Big[\sum_{m,n} c_m^M c_n^M c_m^N c_n^N e^{-R_{mn}/R_c}\Big]C^{(Re)}(\omega_M - \omega_N) \tag{2.4}$$

$$\widetilde{\omega}_M = \omega_M + \sum_{N\neq M}\Big[\sum_{m,n} c_m^M c_n^M c_m^N c_n^N e^{-R_{mn}/R_c}\Big]C^{(Im)}(\omega_M - \omega_N) \tag{2.5}$$

with a correlation radius (R_c) of 5 Å.[27] Additionally, the Fourier transform of the spectral density (scaled for delocalization) describes the time-dependent function

$$G_M(t) = \Big[\sum_{m,n}|c_m^M|^2|c_n^M|^2 e^{-R_{mn}/R_c}\Big]\int_{-\infty}^{\infty} e^{-2\pi i\omega t} J_{ph}(\omega)d\omega \tag{2.6}$$

Finally, the exciton line shape function is given by

$$D_M^{(\prime)}(\omega) = \int_{-\infty}^{\infty} e^{\pm 2\pi i(\omega-\widetilde{\omega}_M)t + \mathrm{G}_M(t) - \mathrm{G}_M(0) - \pi\Gamma_M|t|}dt \tag{2.7}$$

where $\pm$ describes absorption (D_M) and emission (D_M'), respectively. This line shape is used in the simulations of all homogeneous optical spectra.

Absorption is calculated according to the equation given below,

$$A(\omega) \propto \omega \sum_M |\vec{\mu}_M|^2 D_M(\omega) \tag{2.8}$$

with

$$|\vec{\mu}_M|^2 = \sum_{m,n} c_m^M c_n^M (\vec{\mu}_m \cdot \vec{\mu}_n) \tag{2.9}$$

Nonresonant HB spectra are modeled in the following way. After diagonalization of the Frenkel Hamiltonian, a pre-burn absorption spectrum is calculated from Redfield theory. The occupation numbers (squared eigenvector coefficients) of the lowest energy exciton state are used to determine the pigments to be burned. This corresponds to the low-fluence approximation, where only pigments contributing to the lowest energy state are burned. For CP47, the post-burn site energy of the burned pigment is found from the pre-burn site-distribution function, while all other diagonal elements of the Hamiltonian are unchanged. The Hamiltonian is again diagonalized and a post-burn absorption spectrum is calculated. The resulting HB spectra is calculated as the pre-burn absorption subtracted from the post-burn absorption spectrum.

Additional spectra are calculated as CD,

$$CD(\omega) \propto \omega \sum_M r_M D_M(\omega) \tag{2.10}$$

LD (where is $\hat{n}$ the membrane normal vector),

$$LD(\omega) \propto \omega \sum_M (|\vec{\mu}_M|^2 - 3(\vec{\mu}_M \cdot \hat{n})^2) D_M(\omega) \tag{2.11}$$

Fluorescence,

$$F(\omega) \propto \omega^3 \sum_M \left[\frac{e^{-\omega_M/kT}}{\sum_N e^{-\omega_N/kT}}\right] |\vec{\mu}_M|^2 D'_M(\omega) \tag{2.12}$$

and CPL.

$$CPL(\omega) \propto \omega^3 \sum_M \left[\frac{e^{-\omega_M/kT}}{\sum_N e^{-\omega_N/kT}}\right] r_M D'_M(\omega) \quad (2.13)$$

Note that for CD and CPL the exciton dipole strength is replaced with the excitonic rotational strength

$$r_M = \frac{\pi}{2}\sum_{m,n} c_m^M c_n^M \left(E_0^m \vec{R}_m - E_0^n \vec{R}_n\right) \cdot (\vec{\mu}_m \times \vec{\mu}_n) \sim \frac{\pi}{2}\sum_{m,n} c_m^M c_n^M \vec{R}_{mn} \cdot (\vec{\mu}_m \times \vec{\mu}_n) \quad (2.14)$$

where the second formula on the right neglects the contribution from pigment site energies and, to a good approximation, the spectral shapes (of concern in this work) are not affected. A CPL spectrum is the fluorescence analog of CD. At low temperatures only the lowest energy state will emit, with a positive or negative signal determined by the rotational strength. Note that a localized state will have zero rotational strength (see Eq. 2.14). Note that the positive component in CPL spectrum indicates that the I_L (absorption of left circularly-polarized light) is stronger than I_R (right circularly-polarized light). In the opposite case one will observe a negative CPL band.

2.3 Results and Discussion

2.3.1 Low temperature CP47 emission spectra

First, we compare various CP47 fluorescence spectra adopted from ref 10. Curves a and b in Figure 2.1 (right frame) were obtained at identical conditions at 2 K after different stages of 514 nm illumination, i.e., with doses of 70 and 0.02 J/cm^2, respectively. Curve c represents the so-called 695 nm (5 K) emission, i.e., the F695 fluorescence of CP47 complexes measured in our laboratory,[4] suggested to represent fluorescence of an intact CP47 complex. The F695 emission is also observed in the PSII-cc.[28] Spectrum d is the difference between spectra a and b (d = a - b). As argued before typically measured CP47 emission spectra,[4,11] including spectra a and b in Figure 2.1, can be fitted by the 695 nm emission (i.e., curve c), and two other contributions with maxima at ~691 and ~685 nm by simply adjusting their relative intensities. Based on our extensive studies

over the years the smaller the amount of the so-called 685 nm and 691 nm emission, the more intact the sample is. Below, we refer to these contributions as F691 and F685 fluorescence bands, respectively. (The latter two contributions were previously labeled as FT1 and FT2, respectively[4]). Note that spectra a and b, as mentioned in ref 10, are also contaminated with CP29 and/or LHCII complexes exposed by the weak ~680 nm emission indicated by the red dashed arrow, further complicating a straightforward analysis. We suggested before that the most likely interpretation is that the typically studied CP47 samples contain emissions from two more subpopulations of complexes in addition to the F695 emission. The shape of the difference spectrum (d) supports our previous interpretation, i.e., the blue shift of spectrum (a) is largely caused by the nonphotochemical (persistent) HB[4] that leads to a bleach of the lowest energy state responsible for the 695 nm emission. This is why curve c′ (scaled and inverted curve c) fits well the negative lobe of the difference curve d, while the positive band near 685 nm increases. The presence of the latter emission band can be eliminated by sample annealing (i.e., the bleach of the lowest state can be erased), but in some samples the band exists before sample illumination due to permanent damage. Most of our destabilized CP47 samples showed similar spectra to curve b, though with relatively larger contribution from the 695 nm and smaller contribution from the ~685 nm band, suggesting again that broad emission spectra with variable maxima near 689-692 nm are a mixture of F695 band and additional emissions from two subpopulations of destabilized complexes characterized by the F691 and F685 bands. Most likely such complexes have weakened and/or broken H-bond(s), vide infra; though the nature of destabilization and/or conformational changes is not known. Thus, we conclude again that in our view only curve c represents emission from *intact/stable* CP47 complex.[4,5,11]

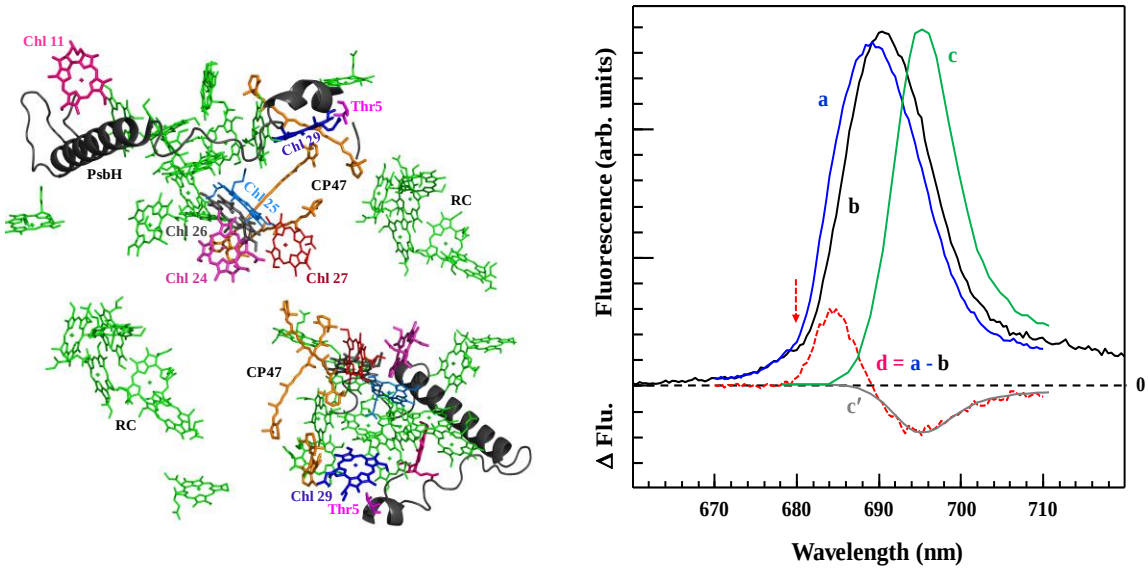

Figure 2.1 Left: Arrangement of CP47 Chls in relation to the RC pigments within the PSII-cc dimer based on the 1.9 Å resolution structure (PDB ID: 3ARC[12]). This structure is very similar to the recently obtained 3.2 Å resolution structure from spinach; PDB ID: 3JCU.[13] Each CP47 complex contains 16 Chls and 3 carotenoids (in orange). Location of the PsbH protein in relationship to CP47 is shown in black, and Thr5 that is shown in pink. Right frame: Curves a and b (from ref 10) are 2 K fluorescence spectra of CP47 obtained at different stages of 514 nm illumination (see text). Spectrum d is the difference between spectra a and b (d = a - b). Curve c represents the so-called 695 nm 5 K emission CP47 complexes adopted from ref 4. Curve c′ is inverted and scaled curve c.

Interestingly, differences between various low-temperature emission spectra reported in ref 10, including our unpublished emission spectra measured over many years, also exhibit an isosbestic point near 690 nm. The latter suggests that upon strong sample irradiation the ~695 nm emission band changes into ~685 nm band. That is, when the intensity of the ~695 nm band decreases the intensity of the ~685 nm increases. For relatively low irradiation intensities this process is reversible upon sample annealing to about 50-60 K, suggesting that the changes are largely due to a bleach of the lowest energy band responsible for the F695 emission. However, the situation is more complex, as the conversion F695 → F690 → F685 strongly depends on fluence ($f = I \cdot t$), where I is laser intensity and t is time of sample irradiation. This, in turn, suggests the energy landscape with multi-level system could lead to the observed phototransformations. In

general, the observed emission shift might be reversible if caused by nonphotochemical/photochemical HB (NPHB/PHB), or irreversible if photodamage occurs.[4] The change observed in the emission spectra due to NPHB, induced via variable blue-shift(s) of the post-burn site energy distribution of low-energy pigment(s), reveals very complex energy tier in the CP47 protein energy landscape. Various energy tiers have been observed in photosynthetic complexes, they typically occur on average near 5-20 cm^{-1}, ~30-70 cm^{-1}, and about 180-320 cm^{-1}.[29] However, multiple consecutive transformations cannot be excluded nor that the fluorescence shift is also contributed to by PHB (i.e., likely via proton transfer). That is, it is feasible that the lowest energy Chl(s) (which are largely responsible for the 695 nm emission band) with a strong H-bond to the surrounding protein could be significantly weakened by laser illumination leading to 691 nm emission maximum (F691). The weakening of the H-bond could be driven via light induced protein conformational changes (e.g., proton dynamics). Experimental data also suggest that for very large laser intensities small irreversible changes may also occur (e.g., the H-bond(s) could be broken) and the 685 nm emission could persist even after sample annealing to 150 K (thermal cycling to 150 K and lowering the temperature to 5 K). If this happens, the original emission spectrum cannot be fully recovered; such behavior was also observed previously for isolated CP47[30] and PSII-cc complexes,[28] and it is also consistent with the data of ref 31 where heterogeneity of CP47 complexes was revealed via observation of different fluorescence decay components. Possible candidates are Chl 26, which may have a strong putative H-bond between the ester group and His9, or Chl 29, which interacts directly with the PsbH protein and has a strong H-bond between its 13′-keto group and Thr5 of the PsbH protein. However, other changes in the vicinity of the low-energy Chls, e.g., protein conformational changes in the neighboring hydroxyl groups, cannot be excluded as they would also lead to modified Chl(s) site energies.

2.3.2 Experimental, simulated, and calculated CP47 CPL spectra

The authors describing the new CPL spectrum in ref 10 (an analogue of CD spectrum[10,32]) used a five domain model and correctly argued that Chl 29, isolated in its own domain, should not exhibit excitonic CD or CPL, as its contributions to all rotational strengths are zero. Therefore, the site energy of Chl 29 in ref 10 was placed at higher energy (i.e., at 14771 cm^{-1}; 677 nm), in contrast to the quantum chemically estimated value and their previous modeling studies,[9] which identified Chl 29 as the most likely low-energy pigment. Apparently, their algorithm could not find site energies that would describe the CPL and CD spectra, when the lowest energy band near 690 nm is contributed to by Chl 29. Therefore, a significant refinement of CP47 excitonic structure was proposed.[10] However, Chl 29 may still have the lowest energy and contribute to the lowest energy state; besides, we find that there are at least several solutions which provide good fits of both CPL and CD spectra (*vide infra*) with different parameters than those reported by Hall et al.,[10] though the good fits of the positive and negative lobs of the CPL curve are rare. Recall that we fit CPL spectrum of Hall et al.[10] below (and other optical spectra shown in the Appendix A) for completeness, although we do not think that such spectra represent intact CP47 complexes (vide infra). First, we show in Figure 2.2A that a significantly better fit of the experimental CPL (curve a) spectrum can be obtained using the same theory and all input parameters from ref 10 with our new algorithm for parameter optimization (see curve b; vibrations are dynamically localized and do not contribute to CPL, as in ref 10). Our calculated spectrum (green curve in Figure 2.2A) fits well the experimental CPL with the same five domains (Case A; vide supra), coupling constants (V_{nm}), spectral density, and Huang-Rhys factor (S = 0.6) as reported in ref 10. The main difference between our calculated CPL and that reported in ref 10 (see curve c in Figure 2.2B, calculated with identical parameters as those used in ref 10) is that we used three values of Γ_{inh} instead of two as

in ref 10. As a result, a better fit was obtained for both CPL and CD spectra (the latter is not shown for brevity) employing a different set of site energies and different values of Γ_{inh} for the two lowest energy Chls mostly contributing to the lowest energy state.

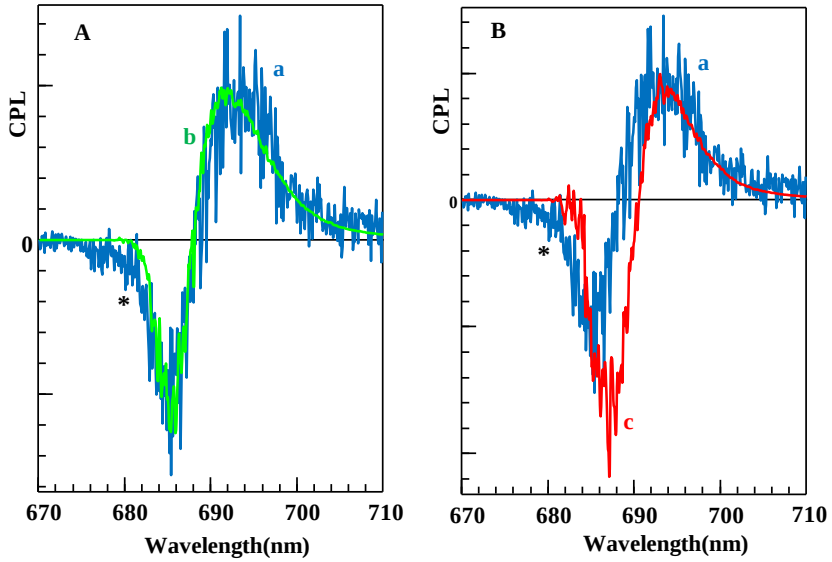

Figure 2.2 Curves a in frames A and B are experimental CPL spectra from ref 10. Spectra b (this work) and c (with parameters from ref 10) are the calculated CPL spectra; see text for more details.

That is, in contrast to ref 10, in our fit Chl 29 could still have the lowest site energy (14559 cm^{-1}), with Chl 11 and Chl 24 being the second and third lowest energy pigment 14580 and 14710 cm^{-1}, respectively. Thus, the Chl site energies reported recently for CP47[10] are not exclusive in any way (see also Figure A.1 in the Appendix A). Of course excitation is not delocalized on Chl 29, and, as a result, this Chl does not directly contribute to the excitonic CPL spectrum. This pigment, however, due to large disorder may still contribute to the lowest-energy state band emission spectrum and its site energy may indirectly influence the relative intensity of the positive and negative lobes of the CPL spectrum. Following this line of reasoning, Chl 29 (isolated in a single-pigment domain) cannot contribute to the CPL signal. However, as shown in the Appendix A, the shape of CPL is slightly dependent on the site energy of Chl 29. This observation, along

with the analysis of CP47 CPL in ref 10, show how static disorder can create complex CPL spectra (for example, two bands even at low temperatures). Spectral overlap of site distribution functions (SDFs) can lead to multiple low-energy states (localized and delocalized) in disorder averaged calculations. Specifically, Chl 29 can indirectly affect the CPL spectrum if its SDF is at low enough energy such that in some iterations of Monte Carlo disorder CP47 has a localized lowest energy state. This situation effectively suppresses the CPL signal (due to zero rotational strength) and only when Chl 29 is not the lowest energy state will CPL be observed.

In fact, this is why the intensity of the negative lobe in figure 2.2A fits better the experimental CPL spectrum. (For more details see Figure A.1 in the Appendix A). Our Γ_{inh} values for the three lowest energy Chls, i.e., Chl 29, Chl 11, and Chl 24 are 269 cm^{-1}, 290 cm^{-1}, and 140 cm^{-1}, respectively. For all remaining pigments in our fits Γ_{inh} was also 140 cm^{-1}. Hall et al.[10] argued that Chl 11 has the lowest site energy (14545 cm^{-1}) with Γ_{inh} = 255 cm^{-1}, while Chl 24 was the second lowest energy pigment at 14641 cm^{-1} with a Γ_{inh} value of 150 cm^{-1};[10] the site energy of Chl 29 was placed at 14771 cm^{-1} (677 nm). In their fits the Γ_{inh} =150 cm^{-1} was also used for all remaining pigments. Data in Figure 2.2A confirm that one set of site energies may describe both the negative and positive CPL lobes. To obtain such shape of the CPL spectrum it is necessary to assume that the two lowest energy Chls contributing to the CPL spectrum have significantly different Γ_{inh} values. Finally, we note that the fits of absorption and emission spectra using the same parameters as those to obtain the CPL and CD spectra in Figure 2.2 were not very good but quite similar to those reported in ref 10, again suggesting that the samples were heterogeneous.

Now, regarding the shape of the experimental CPL spectra (curves a in Figures 2.2), we believe that this CPL corresponds to a mixture of intact and destabilized complexes. If this is the case, there is no reason to fit the CPL spectrum in question with one set of site energies, as done

in Figure 2.2. That is, what if the positive and negative lobes originate from different emission spectra, i.e., emissions from different subpopulations of CP47 complexes? Previous work,[4,5,11] as well as data shown in Figure 2.1 (right frame) and Figure A.2 in the Appendix A, suggest that the typically studied CP47 complexes are heterogeneous. This can be easily demonstrated by a simple deconvolution of the experimental CPL spectrum (noisy curve a in Figure 2.3) from ref 10, as shown in Figure 2.3A, using simulated CPL spectra obtained from the often observed CP47 emission bands, i.e. the F685, F691, and F695. This is consistent with the fact that the maxima and band widths of the CP47 emission spectra reported in the literature varied from sample to sample.[4,5,10,18,33,34] Analysis of various CP47 fluorescence origin bands revealed that typical CP47 emission is contributed by one to three bands, i.e., F685, F691 and F695, with the single F695 band assigned to emission from the most intact complex.[4] In addition, a minor FT3 contribution near 680 nm (indicated by the asterisk in the figure 2.3A) was also observed in agreement with emission spectra reported in ref 10; see dashed arrow in Figure 2.1 (right frame). We argue, based on a deconvolution of many literature CP47 emission spectra,[4] as well as emission spectra from ref 10 obtained before and after illumination by 514 nm (see Figure A.2 in the Appendix A) that all fluorescence spectra can be describe with three bands of variable relative integrated intensity; such bands, as noted above, correspond to the F685, F691 and F695 emission. Note that the CPL spectrum shown in ref 10 even at the first stage of illumination had a negative component near 685 nm, proving that their sample already contained a fraction of permanently destabilized CP47 complexes, as discussed above. Finally, we note, that a single F695 contribution is only observed in intact complexes[4] and PSII-cc (at both 5 and 77 K),[28] and this component was *not* clearly revealed in ref 10 even at 80 K, suggesting again that the contribution from the F695 band in their samples was smaller than that of F691. Thus, if our supposition is correct, the CPL spectrum (curve

a) in Figure 2.3A originating from three equilibrated state(s), should by its nature enable a clear identification of the lowest energy exciton states. Successful analysis of this spectrum (based on literature data and fluorescence spectra shown in ref 10) would further support our earlier suggestion that the typically observed emissions are contributed by heterogeneous mixture of CP47 complexes.[4,5,35]

To demonstrate that this is indeed the case, we fitted (using Redfied theory[34]) all three experimentally obtained F685, F691, and F695 emission spectra from ref 4 (which inherently contain contributions from both delocalized and localized transitions). In order to generate the corresponding CPL spectra we subsequently subtracted vibronic contributions, as localized vibrations do not contribute to the CPL spectra.[10] Consequently, we obtained three new simulated CPL spectra, referred to below as CPL_{685}, CPL_{691}, and CPL_{695}. The task at hand is to demonstrate that these curves can directly describe the experimental CPL curve from ref 10. We assume, in agreement with experiment, that F685 (whose contribution strongly depends on sample quality) has negative CPL_{685} (curve e), while the F691 and F695 emissions have positive CPL_{691} and CPL_{695} spectra (see curves c and d in Figure 2.3A, respectively). Indeed, as expected, the sum (curve b; red) consisting of all three contributions (b = c + d + e) describes the experimental CPL spectrum very well. To generate curve b, the relative c, d, and e contributions were adjusted to fit the experiment. Interestingly, the relative contributions are nearly identical (see the stick spectrum in Figure 2.3B) to the relative contributions of the F685, F691, and F695 bands that fit the CP47 emission obtained after strong illumination,[10] i.e., the condition under which the emission and CPL spectra were obtained. (The fits of the emission spectra before and after illumination from ref 10 are shown in Figure A.2 of the Appendix A). Here we only note that the contribution from the F685 increases with the illumination dose. In our understanding, the latter proves that the CPL obtained

for the sample in question does not represent a “pure” intact CP47 complex, and such spectrum should not be modeled as intact CP47 complex. The asterisk indicates that this sample was also contaminated by other antenna complex(es), as already indicated in Figure 2.1 (right frame) and mentioned in ref 10, hence a small discrepancy at higher energies.

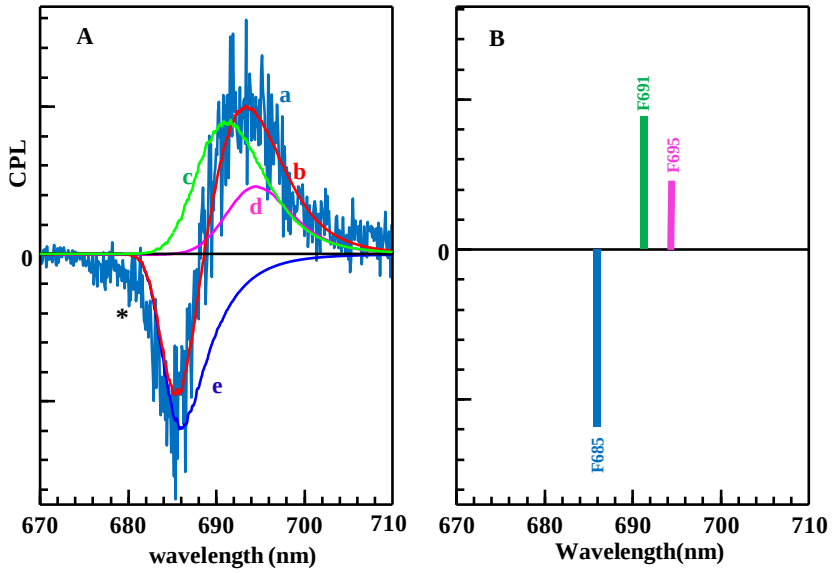

Figure 2.3 Curve a is the experimental CPL spectrum.[10] Spectra c, d, and e in frame A represent the calculated CPL based on the F691, F695, and F685 emission spectra, respectively (see text for details). Curve b (c + d + e) represent the resulting CPL expected for the heterogeneous CP47 sample. The asterisk indicates that this sample was also contaminated by other antenna complex(es) not included in the spectral decomposition. The stick spectrum in frame B shows that the relative contributions from F685, F691, and F695 emission bands to the simultaneously measured fluorescence and CPL are nearly identical.

Thus, based on this simple analysis, we suggest that *it is meaningless* to describe the spectra reported in ref 10 with one set of parameters, knowing that the spectra represent a heterogeneous sample. That is, data shown in Figure 2.3 imply that it is very unlikely that Chl 11 and Chl 24 (with very different Γ_{inh}) are the lowest energy pigments, as suggested in ref 10. We propose that only CPL_{695} represents intact CP47 complexes. Thus, a significant refinement of the CP47 excitonic structure (as described in ref 10) in our view is not necessary. We conclude that neither the parameter set obtained from fits of spectra reported in ref 10 nor our parameters used to obtain an

improved CPL fit (as shown in Figure 2.2A) should be used to describe the excitonic structure, population dynamics, and excitation energy pathway(s) of intact CP47 and/or the CP47 complex residing within the PSII-cc. This is why, we do not report our parameters used to obtain the CPL fit shown in Figure 2.2A (curve b).

Rather, one should describe CPL_{695} contribution for intact complexes and strive to obtain one set of parameters that could describe all intact CP47 spectra (with a single F695 emission spectrum and single low-energy exciton band consistent with HB.[4] Thus we strongly disagree with the statement from ref 10 that *"… emission from the intact low-energy state of CP47 seems more likely to peak at ~692-693 nm than at 695 nm"*. It has been well established via HB spectroscopy that the position of the lowest exciton state in intact complexes is near 693 nm, while the resulting emission peaks near 695 nm (F695 band). The majority of destabilized complexes (in most studied samples so far) were characterized by the 691 nm emission (F691 band) and the corresponding lowest exciton state near 689 nm,[4,5] with variable contributions from the F685 and F695 emission; see Figure A.3 in the Appendix A.

2.3.3 Simultaneous modeling of various optical spectra obtained for intact CP47 sample

In this subsection we present calculated steady-state absorption, emission, and non-resonant HB spectra from ref 4, along with newly extracted low-temperature (2 K) CPL_{695} (assigned above to the intact CP47 complex) and the recently obtained 2 K CD spectrum.[10] We included the CD spectrum in the simultaneous fits though this spectrum was obtained for a partly destabilized CP47 complexes. However, destabilization most likely affects the lowest energy pigment(s), while the entire shape of CD (very sensitive to all Chl site energies) should provide an additional constraint, in particular for the higher energy pigments. Based on the literature data[4,10]

and extensive modeling studies we consider below Chl 26, Chl 29, Chl 24, or Chl 11 as the best candidates for the low energy pigments. In this work, in comparison to our previous analyses,[8,11] we add two more spectra and use more advanced theory in our simulations, as described above. In addition, for a straightforward comparison with the data of Hall et al.,[10] we continue to do simulations based on the 1.9 Å resolution X-ray structure of CP47 (3ARC structure[12]), since the V_{nm} values based on the very recent structure of PSII supercomplexes from spinach (3.2 Å resolution; PDB ID: 3JCU[13]) showed very similar TrEsp coupling constants (see Tables A.1 and A.2 in the Appendix A). We note that the V_{nm} values calculated with the Poisson-TrEsp method exist only for the 3ARC structure.[9] However, in our modeling studies we use the experimentally determined $J_{ph}(\omega)$ for all pigments, and allow Γ_{inh} to vary independently for all Chls. LD spectra are not included in simultaneous fits, as they were never measured for intact samples (vide infra), and the two LD spectra reported in the literature were obtained for differently destabilized complexes, as witnessed by very different shapes of the LD and corresponding emission spectra,[19,36] see Figure 2.9 below. The search for realistic site energies is aided by Monte Carlo simulations using a Nelder-Mead optimization algorithm (*vide supra*). Our new assignments significantly differ from those of Hall et al.,[10] due primarily to differences in the experimental data simulated. Since the simultaneous fits of the absorption, emission, CPL, CD, and non-resonant HB spectra are more restrictive (in terms of possible site energies) than those of absorption/emission/HB spectra as done in ref 8 and/or low temperature absorption/emission/HB spectra and room-temperature CD obtained for a different sample,[11] we suggest that our new simultaneous fits of an expanded set of low-temperature spectra should represent more realistic site energies.

We focus below on spectra assigned to intact and destabilized CP47 complexes. The most critical are the shapes of fluorescence, CPL, and HB spectra, as their shapes strongly depend on sample heterogeneity and the nature and composition of the lowest-energy band(s). The shapes of absorption and CD spectra in the high-energy region are somewhat less critical, as destabilization affects mostly the low-energy pigments as mentioned above. We show in Figures 2.4 and 2.5 simultaneous fits of measured 5 K absorption, emission, HB, and 2 K CD, along with the extracted 2 K CPL_{695} spectrum, assigned to intact CP47 sample, obtained for two models in which Chl 26 (Model I) and Chl29 (Model II), respectively, are the lowest energy pigments. The fits shown in Figure 2.4 and 2.5 (five domains) were obtained with Poisson-TrEsp V_{nm} values from ref 9. For completeness we consider two cases . In Case A (Figures 2.4 and 2.5) all intradomain V_{nm} are included in calculations; in Case B, (see Figures A.5 and A.6 in the Appendix A) all intradomain $V_{nm} < V_c$ (30 cm^{-1}) are also put to zero. The corresponding site energies are given in Tables A.3 and A.4 in the Appendix A. For brevity, we discuss only the calculated spectra, exciton composition (focusing on the lowest energy exciton state(s)), the extracted site energies, inhomogeneous broadening, and Huang-Rhys factors. We emphasize that division into domains is important for discussion of EET dynamics (not addressed in this work), however, very similar fits of optical spectra (not shown) were obtained for one domain, i.e. when the small V_{nm} values were not neglected.

2.3.4 Model I (Chl 26), Case A

We begin with Chl 26 as the lowest-energy Chl for Cas*e* A. (For Case B, see the Appendix A). We consider Chl 26 first, as our previous simple excitonic calculations (no lifetime broadening effects) of absorption, emission, and non-resonant HB spectra,[8] based on the 2.9 Å resolution structure of the PSII-cc from cyanobacteria,[37] suggested that Chl 26 could be the lowest energy

pigment. In Case A (see Figure 2.4), Chl 26 as the lowest energy Chl (with site energy of 14479 cm^{-1}) contributes 91.6% to the lowest exciton state. The second Chl mostly contributing to the lowest energy state is Chl 27 (5.4%) with site energy of 14771 cm^{-1}. Chl 16 contributes 0.74%. Thus, the Lowest exciton state is weakly delocalized over 1.13 Chls. Site-energies and inhomogeneous broadenings are listed in Table A.3 in the Appendix A. Huang-Rhys factors are S_{ph} = 0.92, $S_{vib\text{-}em}$ = 0.6, $S_{vib\text{-}abs}$ = 0.4. Note that in this case the CPL (black solid line in Figure 2.4) is positive in agreement with the extracted CPL spectrum discussed above (solid grey band).

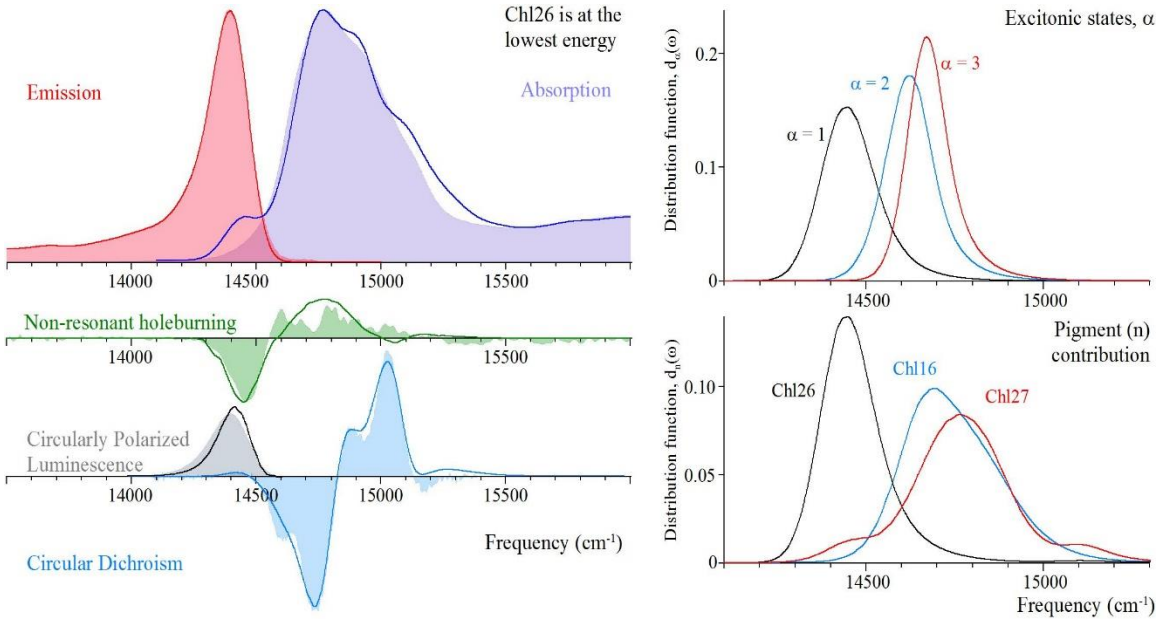

Figure 2.4 Left (Case A): Chl 26 is the lowest energy pigment. Best simultaneous fits (lines) of 5 K absorption (dark blue), emission (red), and low-fluence nonresonant HB (green), 2 K CPL_{695} (black) and CD (cyan) spectra compared to experiment (filled curves). Right: Contributions to 5 K absorption of the three lowest energy exciton states (top) and the three pigments (Chl 26, 27 and 16) which contribute most to the α = 1 exciton state (bottom). Fitting error = 3.33.

2.3.5 Model II (Chl 29), Case A

We do not assert that the fits in Figure 2.4 or A.5 (in the Appendix A) and the corresponding site energies shown in Table A.3 in the Appendix A, are the only solution, as reasonable fits can be obtained with Chl 29 as the lowest energy pigment (see Figures 2.5 and A.6 for Cases A and B,

respectively). The figures 5 and S6 were obtained for the Cases A and B, respectively. Filled bands are the same as in Figure 2.4; solid lines in the left frames are the calculated spectra. However, closer inspection of the CD spectra Figures 2.5 and A.6 show that there is no positive CD contribution near 14430 cm^{-1} observed in PSII-cc CD spectra.[38] Since such weak band is observed in Figures 2.4 and A.5 (with overall better fits) we one could suggest that Chl 26 is a better choice for low-energy pigment. Also the shape of CD in the very low energy region is not accounted for (vide infra).

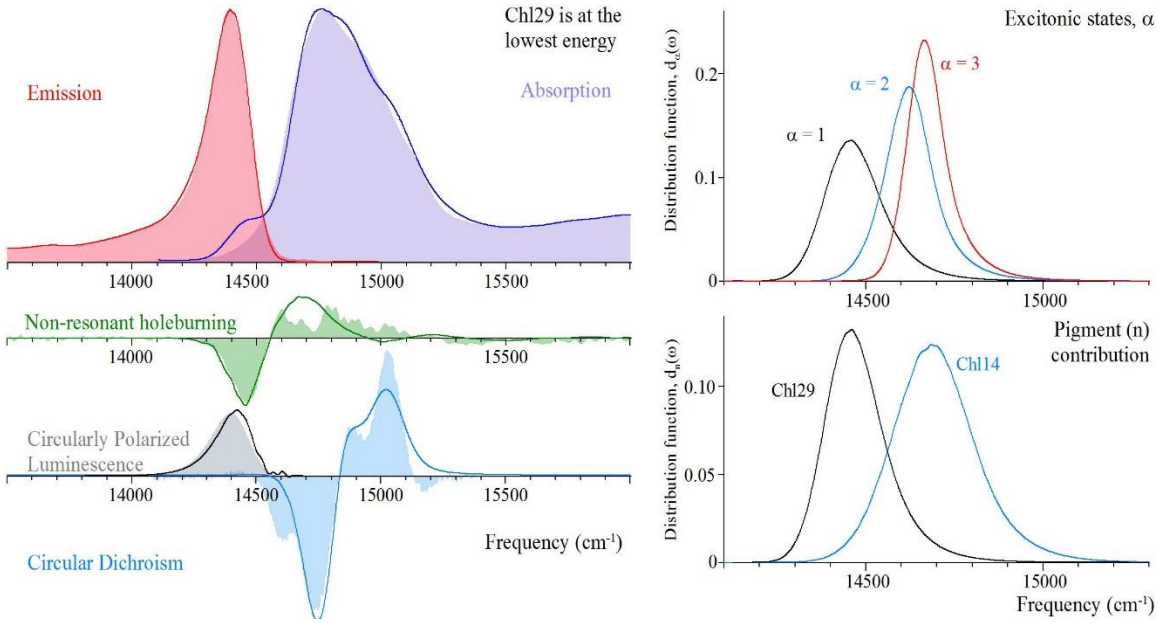

Figure 2.5 Left (Case A): Chl 29 is the lowest energy pigment. Best simultaneous fits (lines) of 5 K absorption (dark blue), emission (red), and low-fluence nonresonant HB (green), 2 K CPL_{695} (black) and CD (cyan) spectra compared to experiment (filled curves). Lowest energy pigments are Chls 29 and 14 with contribution to the lowest-energy exciton state of 95% and 3.5%, respectively. These two Chls, i.e., Chls 29 and 14, have $\boldsymbol{E_0^n}/\Gamma_{inh}$ of 14482/150 cm^{-1} and 14712/253 cm^{-1}, respectively. Right frame: see text. Fitting error =3.58.

Again, we do not assert that the corresponding site energies shown in Tables A.3 and A.4 in the Appendix A for Figures 2.4/A.5 and 2.5/A.6 are unique solutions, as Case C simulations (obtained with TrEsp V_{nm}, see Figure 2.6 and A.7 in the Appendix A) also provide reasonable fits. That is, the quality of the fits alone does not necessarily guarantee a unique outcome, as still a

number of parameters (e.g., spectral densities for various Chls), have not been established experimentally and could affect the fitted site energies. Additionally, the values of elucidated site energies from fits presented in Figures 2.4/A.5 and 2.5/A.6 somewhat depend on assumptions regarding Γ_{inh}. Therefore, more data for intact samples and further modeling studies are necessary before final conclusions are made. Unfortunately, mutational data do not help to distinguish which Chl (26 or 29) should have the lowest energy, as mutation experiments[39] did not exclude Chl 26 nor Chl 29 as the most red-shifted pigments.

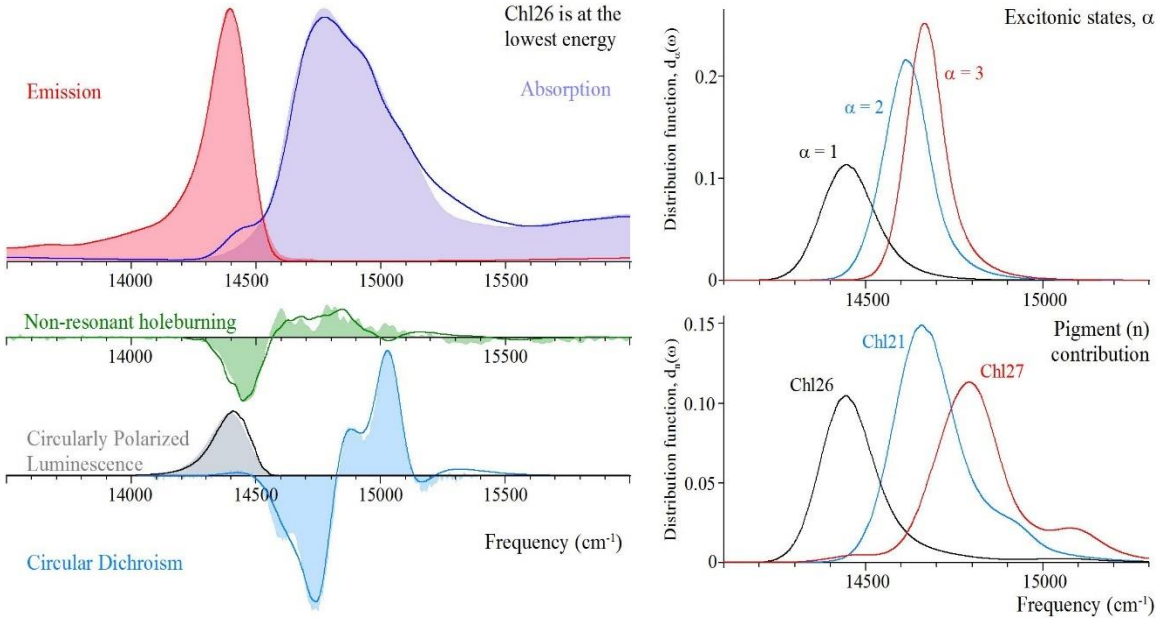

Figure 2.6 Case C (left frame): Chl 26 is the lowest energy pigment. The same experimental spectra as those in Figure 2.4 calculated with TrEsp V_{nm} parameters and assuming that all intradomain $V_{nm} < V_c$ (30 cm^{-1}) are set to zero (see text for details). In this case the Chls contributing mostly to the lowest-energy state ($\alpha = 1$) are Chl 26 (91.5%), Chl 27 (2.9%) and Chl 21 (1.1%). The lowest energy Chls (26, 21, and 29) have $\boldsymbol{E_0^n}/\Gamma_{inh}$ of 14490/155 cm^{-1}, 14721/191 cm^{-1}, and 14792/224 cm^{-1}, respectively. Right frames: see text. Fitting error = 2.33.

2.3.6 Model I (Chl 26), Case C

The solid curves in Figures 2.6 (and A.7 in the Appendix A) are the best fits for intact CP47 complexes we obtained so far. All fit parameters obtained for fits shown in Figures 2.6 and A.7 are summarized in Table A.5 in the Appendix A. Although similar fits were obtained for Chl 26

and Chl 29 as the lowest energy Chls with different sets of parameters, it appears that better fits are obtained when Chl 26 is the lowest energy pigment. In particular, the fits of the CPL_{695} and CD spectra is better in Figure 2.6 in comparison with data shown in Figure A.7 in the Appendix A. Of course these parameters must be further tested whether or not they can properly describe time-domain data, which are not available for intact CP47 complexes at this time.

Figures 2.4-2.6 show that reasonable simultaneous fits can be obtained for absorption, fluorescence, HB, CD, and CPL_{695} spectra and the resulting parameters differ. Low-temperature absorption, CD, and CPL_{695} spectra are better described in Figure 2.6 for Case C whih Chl 26 as the lowest energy Chl. Finally, based on our extensive modeling studies we found that Chls 24 and 11 can be rejected as low energy Chls based on the fits of the HB, CPL_{695} and CD spectra (data not shown). We are rather confident that spectra for *intact* proteins (characterized by F695 emission and CPL_{695} spectrum) cannot be properly fitted assuming Chl 11 (or Chl 24) as the lowest energy pigment. For example, Chl 24 must be a higher energy pigment, otherwise the CPL_{695} spectrum cannot be well fitted. We hasten to add that fitting simultaneously all five spectra, assuming the same Γ_{inh} did not provide very good fits.

2.3.7 What is a possible difference between intact and partly destabilized CP47 complexes?

This is very difficult to assert, nevertheless, below we try to provide some insight how sample preparation (sample integrity) and/or strong illumination could affect various optical spectra. In particular, why composite emission spectra (containing variable contribution from F685, F691 and F695) have been reported in the literature over the years. Thus, we focus on the long-standing debate, which spectra describe intact CP47 complexes and what we mean by destabilized CP47 proteins. Based on our extensive work with CP47 proteins over the years,[4] we

think that they are highly susceptible to disruption of Chl site energies, most likely Chl(s) contributing to the lowest exciton state, and/or modification of critical Chl-protein interactions. Although the changes due to photophysical (i.e., reversible NPHB) effects are rather well understood,[4] irreversible changes may also occur. For example, it is well known that the resulting emission of intact CP47 complexes, as a function of fluence at 5 K, shifts blue after various stages of illumination, following the shift (due to HB process) of the modified lowest energy excitonic band. However, as often observed in the literature,[4,5,18-20] some samples already exhibit blue shifted emission as a result of compromised sample integrity (i.e., irreversible modification). For example, we show below that it is enough to shift site energy of lowest energy Chl (for example, due to weakened strength of the putative H-bond, for example, between the low-energy Chl and one of the amino acids), to observe shift of the resulting emission from 695 nm (F695) to 691 nm (F691). Whether or not the putative H-bond(s) is intact, weakened, or broken cannot be assessed during sample preparation and purification. Also, very broad room-temperature spectra cannot provide much insight. This is why over the years our collaborators provided us with multiple CP47 samples whose emission maxima varied from 689-695 nm in agreement with data published by other groups.[4,5,18-20] Such samples also revealed variable positions of the lowest exciton state, in agreement with HB spectroscopy data.[4] Thus, based on our experience with CP47 proteins, we are convinced that quality of prepared CP47 complexes is rather random, and cannot be controlled by researchers during sample extraction, isolation, and purification. All samples studied in our laboratory over the years were prepared by the same very experienced scientist (Dr. R. Picorel from CSIC) during his stays at NREL (Golden, Colorado) in Dr. M. Seibert laboratory, and their samples also varied from preparation to preparation.

2.3.8 On possible spectral changes in destabilized CP47 complexes

Let us assume, for a qualitative assessment, that the set of the parameters obtained from the best fits of five optical spectra shown in Figure 2.6 (see Table A.5 in the SI) describes intact CP47 complexes reasonably well. Figure 2.7 illustrates the possible changes in optical spectra induced by a shift of just one Chl site energy mostly contributing to the lowest energy state. That is, in comparison with the calculated spectra shown in Figures 2.6 and A.7, only the site energy of the lowest energy Chl was shifted blue by 85 cm^{-1} for Chl 26 (left frame) and 93 cm^{-1} for Chl 29 (right frame). The above shifts are made arbitrarily to account for the blue-shifted F691 emission and experimental nonresonant HB spectra assigned to partly destabilized complexes. Recall that in these two cases the lowest energy exciton is mostly localized on Chl 26 (left frame) or Chl 29 (right frame).

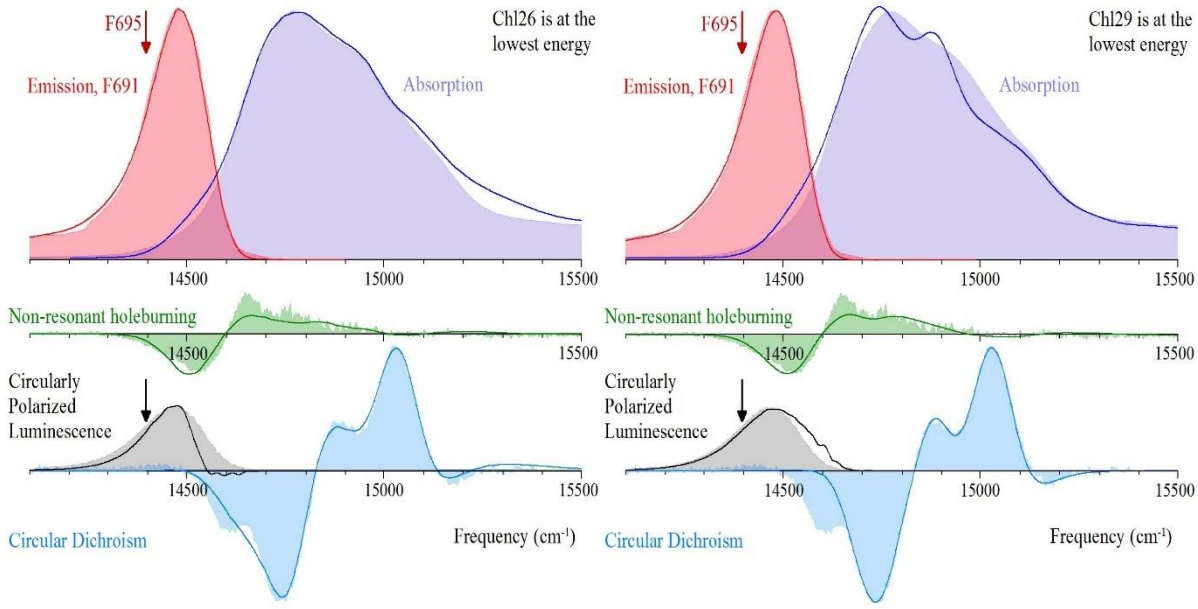

Figure 2.7 The calculated spectra are plotted as solid lines. Filled bands are the experimental spectra (see text). Left and right frames show calculated absorption (blue), F691 emission (red), low-fluence blue-shifted nonresonant HB (green), CPL_{691} (black), and CD (cyan) spectra after Chl 26 or Chl 29 are shifted blue by 85 and 93 cm^{-1}, respectively. (All remaining parameters are from fits shown in Figures 2.6 and A.7; see also Table A.5 in the Appendix A). We emphasize that no

additional fitting was performed. Red and black arrows indicated the maximum of F695 and CPL_{695} spectra, respectively.

The calculated spectra show qualitative agreement with experiment for both cases. CPL_{691} and CD spectra show better agreement with experiment for Chl 26 being the lowest energy Chl. The filled absorption was obtained for intact CP47 and is shown here for comparison. The red and black downward pointing arrows indicate the maxima of the F695 emission and CPL_{695} spectra assigned to the intact complexes (vide supra). Interestingly, when the site energy of Chl26 (or Chl 29) is shifted to higher energies by 85 cm^{-1} (or 93 cm^{-1}) possibly due to a weakened H-bond and/or some protein conformational changes, the resulting emission band shifts blue to ~691 nm (red solid line), in very good agreement with the experimental F691 fluorescence band (pink filled spectrum) observed in destabilized CP47 complexes. Note that this simple change also qualitatively describes all remaining spectra (without any further optimization), that is, the extracted CPL_{691} (solid grey band) and, in particular, the blue-shifted (experimental) nonresonant HB spectrum obtained for destabilized CP47 complexes.[4] Thus, it is likely that a putative H-bond between His9 and the ester group of Chl 26 exists, which could be significantly weakened due to some protein conformational changes. In turn, if Chl 29 is the lowest energy pigment, the putative H-bond between Chl 29 and the PsbH protein could also be affected, which would account for the experimentally measured blue-shifted fluorescence and HB spectra.[4] The fits also account for the shape of the CPL_{691} spectrum. Note, that the overall changes on absorption and CD are rather small, as the only change occurred to the lowest energy Chl.

We emphasize that in Figure 2.7 both Chl 26 and Chl 29 (now both at 14575 cm^{-1}) are still the lowest energy pigments, although their contributions to the lowest exciton states changed. For data shown in the left frame of Figure 2.7 Chls 26, 21, 27, 16 contribute to the lowest energy state 76.4, 6.2, 4.8, and 2.3%, respectively. For Chl 29 (right frame of Figure 2.7), the contributions to

the lowest exciton state are: Chl 29 (63.9%), Chl 14 (14.6%), Chl 11 (7.6%), and Chl 28 (7.5%). We emphasize again that the calculated spectra were not optimized. Finally, we note that in contrast to suggestion given in ref 10 the positive CPL_{691} is not necessarily characteristic of intact CP47, as CP47 complexes characterized by F691 (destabilized proteins in our evaluation) and F695 band (assigned to intact samples) have both positive CPL spectra, i.e. CPL_{691} and CPL_{695}, respectively, in perfect agreement with our simple analysis shown in Figure 2.3. Importantly, the calculated CD spectra in Figure 2.7 (partly destabilized complexes) do not have a weak positive band at low energies, a feature that was observed in the PSII-cc[38] and intact CP47 complexes (see Figures 2.4 and 2.6). Note that a simple destabilization of one putative H-bond for Chl contributing to the lowest energy exciton (Chl 26 or Chl 29), reveals significant changes to fluorescence, HB, and CPL spectra (see text) in qualitative agreement with experiment. Therefore, we propose that by referring to partly destabilized samples one could suggest that one of the H-bonds of low-energy Chl(s), e.g., Chl 26 (or Chl 29), could be weakened due to protein conformational changes.

However, we often observe additional emission near 685 nm (F685 band),[4,5] not necessarily formed via reversible HB process at low temperatures discussed above. The presence of such band may be irreversible. To account for the F685 fluorescence and even more blue-shifted nonresonant HB spectrum (for highly destabilized proteins) additional shifts of Chl site energies are required. This is not surprising as our unpublished data for site directed mutant (with a single point mutation near BChl *a* 3, i.e., the Y16F mutant of FMO complex (where Thr5 was replaced with phenylamine) revealed multiple changes to BChl site energies (unpublished data). The HB spectrum (see green filled curves in Figure 2.8) correspond to a difference between two large fluence HB spectra obtained for destabilized CP47, revealing continuous irreversible bleach of the photoconverted subpopulation of CP47 complexes. To qualitatively account for such HB spectra

(see Figure 2.8, left),Chl 26 would have to undergo an additional blue-shift (in comparison to data shown in Figure 2.7, left) by 195 cm^{-1} while the second lowest energy pigment, i.e., Chl 21, must shift blue by 30 cm^{-1}. The about 200 cm^{-1} shift is consistent with a broken H-bond; the latter could also affect the energy landscape leading to additional conformational changes. That is, intense sample irradiation may induce irreversible changes, in agreement with experimental observations, induced by extended irradiation. (Of course we cannot exclude that in this case other low energy pigments could be also affected and/or that the above shifts are related to distorted charge distributions leading to modified polarization state of the protein in a given conformation). Therefore, the data shown in the left frame of Figures 2.8 are only for illustrative purpose. In summary, although in general, illumination-induced spectral changes may be reversible upon sample annealing, for large irradiation doses the changes to absorption, emission, and HB spectra are permanent (i.e., they are irreversible[4]). This may suggest that one or more H-bonds could be broken (inducing irreversible conformational changes). For example, it is well known that a change in polarizability could shift Chl *a* site energy by -350 cm^{-1}.[40] This is why some samples showed F685 emission in the absence of HB process (for example, the CP47 sample studied in ref 4). Again, no fitting is performed; the latter modifications makes Chl 21 the lowest energy Chl at 14751 cm^{-1}. As a result, the lowest exciton state is highly delocalized over several pigments, i.e., Chl 21 (20.6%), Chl 15 (15.9%), Chl 26 (13%), and Chl 16 (12.7%). The calculated solid lines (including the above mentioned energy shifts of Chl 26 and Chl 21) are in qualitative agreement with experimental data given by filled pink, green, and grey spectra shown on the left side in Figure 2.8.

The most interesting finding, however, (see Figure 2.8, left frame) is that upon additional shift of two low energy Chls (Chl 26 and Chl 21), the CPL_{685} spectrum changes sign in perfect

agreement with the composite CPL spectrum shown in Figure 2.3 in agreement with experiment.[10] (A negative CPL with minimum near 683 nm was also observed in CP43 complex[22]). Thus, we conclude that this qualitative comparison is consistent with all experimental data obtained for destabilized CP47 complexes. Figure 2.8 (right) shows the same data (filled curves) with fits (solid lines) when Chl 29 undergoes additional shift by 205 cm^{-1} while Chl 11 and Chl 14 are blue shifted by 85 and 50 cm^{-1}, respectively. Now Chl 26 has the lowest site energy (14767 cm^{-1}). In this case the lowest state is highly delocalized (1.57) and mostly contributed by Chl 28 (24.2%), Chl 14 (23.8%), Chl 26 (16.7%), and Chl 15 (11.1%). Again, no fitting was made, the pigments were just shifted to illustrate that various spectra obtained over the years for CP47 complexes could be qualitatively explained.

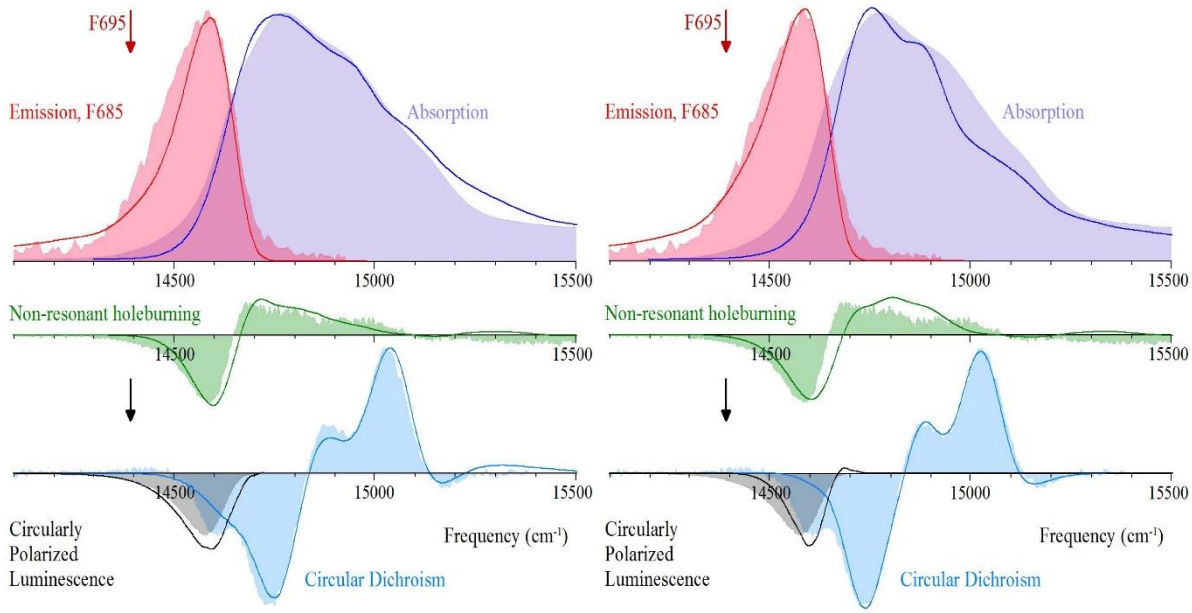

Figure 2.8 Calculated absorption (solid blue line), F685 emission (red), high-fluence difference between two consecutive nonresonant HB (green), CPL_{685} (black; note, the sign is now reversed), and CD (cyan) spectra, after Chl 26 and Chl 21 are shifted blue by 195 cm^{-1} and 30 cm^{-1}, respectively, in comparison with data shown in Figure 2.7 (left frame). The right frame shows resulting the calculated curves after Chl 29, 11, and 14 were shifted blue (see text for details). The red and black arrows indicate the maxima of the F695 emission and CPL_{695} spectra assigned to the intact complexes. The minimum of the nonresonant hole observed for the intact CP47 sample is located near 14430 cm^{-1}.[4]

We emphasize that solid lines shown in Figures 2.7 and 2.8 are just calculated spectra, i.e., no additional fitting was performed. Interestingly, data shown in Figure 2.6 and A.7 suggest both Models (I and II, with either Chl 26 or Chl 29 as the lowest energy Chl, respectively) can reasonably well describe the five spectra modelled in this work. In turn, Figures 2.7 and 2.8 also illustrate that optical spectra obtained for destabilized samples could be also qualitatively accounted for.

In summary, it appears that the 85 (or 93) cm^{-1} blue-shift of the site energy of Chl 26 (or Chl 29) well describes the F691 emission, HB, and CPL_{691} spectra; if this happens, one could argue that in destabilized CP47 complex Chl 26 (or Chl 29) undergoes site energy shift as mentioned above. For example, Chl 29 in destabilized proteins may not strongly interact with the PsbH protein, i.e., the H-bond between the 13^1-keto group of the pigment and the Thr5 residue of the protein could be weakened. To explain the F685 emission, nonresonant holes, and CPL_{685} spectra one would have to assume that Chl 29 (or any other close-lying low-energy Chl) undergo additional shift blue with other pigments affected. In this case the CPL_{685} is negative in agreement with experiment; now the lowest exciton is delocalized over several pigments. Although modeling of optical spectra shown above suggested that Chl 26 could also be the lowest energy pigment, such assignment, however, based on the angle between the Chl Q_y-transition and the membrane normal vector, is inconsistent with the LD spectra.[10] The transition dipole vector of the low-energy state is oriented somewhat perpendicularly to the membrane normal (> 35°)[10], as indicated by the negative LD signal at 690 nm, but the transition dipole of Chl 26 does not fit this criterion. However, this conclusion is premature as no reliable LD spectra are available for CP47 proteins. This is illustrated in Figure 2.9, which show two very different LD spectra, which, as revealed by the corresponding emission spectra, do not represent LD spectra for intact CP47 proteins. Why?

Because both emission spectra (see inset) contain different contributions from the F695, F691, and F685 emission bands (see a subsection below for more details). For that reason, we conclude, in agreement with earlier studies,[5,7-9,11] that the most likely candidate for the low-energy pigment is either Chl 26 or Chl 29, and, as a result, the recent refinement of the CP47 excitonic structure proposed by Hall et al.[10] is not warranted.

2.3.9 LD spectra

As mentioned above, spectra a and b in Figure 2.9 correspond to the 4 and 77 K LD spectra (obtained for oriented samples) digitized from refs 19 and 36. The different spectral shapes of spectra a and b are not solely due to different temperature, but mostly due to differences in sample composition. That is, it appears that the above two samples were mixtures of intact and destabilized complexes, as indicated by the corresponding emission spectra (a′ and b′) shown in the inset. Apparently LD represented by curve b was obtained for a more intact preparation, as the corresponding fluorescence spectrum is red shifted, due to larger contribution from F695 emission. Note that intact CP47 has an emission maximum near 695 nm at both 5 and 77 K.[4] Thus, curve a modeled in ref 10, with fluorescence maximum at 691 nm definitely does not reflect LD of intact CP47 complexes. It is interesting that the weak negative bands near 690 nm (curve a) and 693 nm (curve b) are consistent with our analysis presented above. Thus it is an open question whether the transition dipole vector of the low-energy state in intact CP47 must be oriented somewhat perpendicularly to the membrane normal (> 35°)[10], as suggested based on the negative LD signal at 690 nm (see curve b), as this CD was most likely obtained for very heterogeneous (a mixture of various CP47 subpopulations) sample. Thus the (so far published) LD spectra cannot be used as done in ref 10 to reject Chl 26 as the lowest energy pigment. Note that curve b has much weaker

negative band near 690 nm and larger contribution from intact proteins, as reflected by larger contribution from the F695 band.

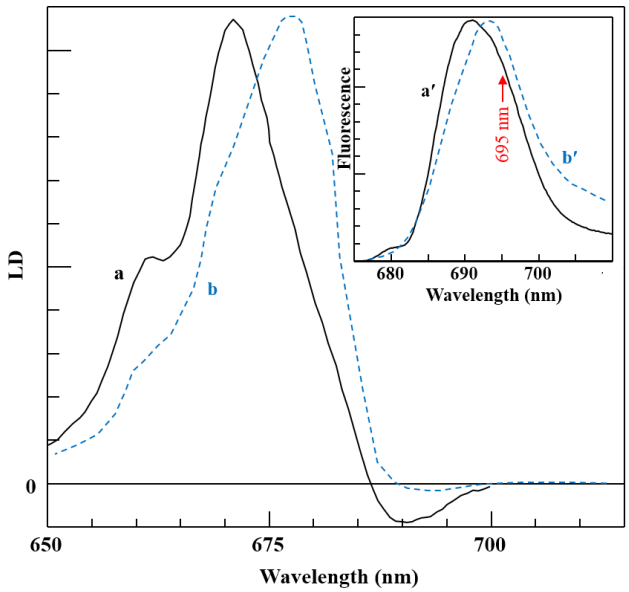

Figure 2.9 Spectra a and b are the 77 K and 4 K LD spectra from refs 19 and 36. The inset shows the corresponding fluorescence spectra a′ and b′.

2.3.10 Calculated low-energy part of the CD spectrum

Finally, we comment on the low-temperature (2 K) CD spectrum obtained for CP47 and reported in ref 10. Figure 2.10 shows that our calculated CD spectrum from Figure 2.6 (green curve b) has similar shape as the experimental CD spectrum (blue curve a) indicating that our parameters properly describe the lowest energy transition that has positive rotational strength. Such a positive band was also observed in the PSII-cc.[38] This is in perfect agreement with the lowest energy state observed for intact CP47, which is located near 692-693 nm.[4] A similar positive CD band, though somewhat weaker, is also observed in Figures 2.4 and A.5. The agreement with the experimental CD is not surprising, as the heterogeneous (destabilized) sample for which the CD was obtained, also has the contribution from the lowest 692-693 exciton state responsible for the 695 nm (F695) emission observed for intact complexes (see Figure 2.1). However, in the case of the destabilized

sample discussed by Hall et al.,[10] the ~689 nm state (see Figure A.3 in the SI) responsible for the F691 emission band is not clearly observed due to an overlap with the significantly stronger CD of the higher energy states. That is, the anticipated weak CD band (also with positive rotational strength) corresponding to the lowest energy exciton state of the major subpopulation of CP47 near 689 nm[10] is not clearly observed. Finally, stronger contribution near 683 nm in the experimental CD spectra used in our modeling studies (vide supra), in comparison with the CD reported by Kwa et al.[41] at 77 K, can also be qualitatively explained, as the sample studied by Hall et al.[10] had much larger subpopulation of CP47 with the 683 nm lowest absorption state (i.e., characterized by significantly increased F685 emission). Again, this reflects the difference in samples studied and supports our interpretation that typically studied CP47 complexes are a mixture of subpopulations with F685, F691, and F695 emission bands. F685 is largely induced by exposure to light at room temperature, and/or via an extended illumination at low temperatures via the HB process.[4,5] Thus, it is likely that our calculated CD with less resolved shoulder near 683 nm (see Figures 2.4. 2.6 and A.5) represents a more intact sample, supporting our analysis. This might be the reason why triplet-bottleneck spectra (i.e., transient holes with minimum near 684 nm) were only observed in destabilized complexes.[30] Finally, data shown in Figures 2.4, 2.6 and A.5 clearly show that Chl 11 does not have to be placed at the lowest energy to reproduce the positive CD and CPL observed experimentally at low energies.

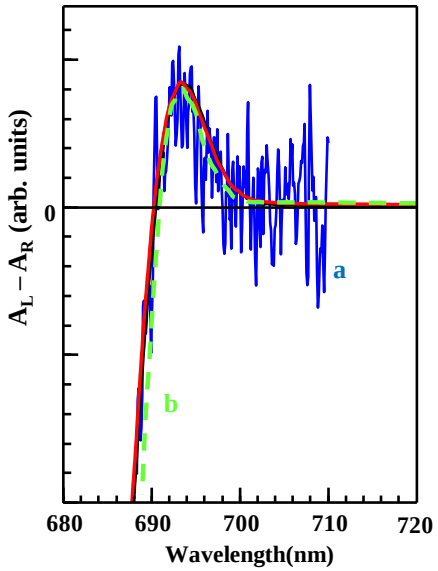

Figure 2.10 Spectra a and b are the experimental[10] and calculated CD spectra, respectively, plotted in the long-wavelength region to reveal the weak positive part of the CD curve with the maximum near the 693 nm. Curve b is from Figure 2.6, while the red curve is from Figure 2.4.

2.4 Conclusions

We argued that good simultaneous fits of absorption, emission, CPL, and CD spectra reported for the CP47 complex in ref 10 can be obtained for at least two different sets of parameters. However, we do not think that the excitonic structure of the CP47 protein can be properly revealed by describing spectra obtained for heterogeneous samples, as those studied in ref 10, which are contributed by three slightly modified subpopulations of CP47 complexes. Therefore, we question the fit parameters presented recently by Hall and co-workers,[10] which favoured Chl 11 as the lowest energy pigment. More importantly, we demonstrate that the spectra reported and calculated in ref 10, as well as the simulated spectra shown in Figures A.8-A.11 in the Appendix A, represent heterogeneous samples, and, as a result, do not represent parameters of intact CP47 complexes. Thus, the suggested new energy flow in the CP47 antenna protein complex, proposed in ref 10, where Chl 11 is the lowest energy pigment, is highly questionable. We provide unambiguous evidence that three different states contribute to the observed emission

and CPL spectrum obtained by Hall et al.[10] That is, their CPL spectrum is a composite spectrum, contributed to by three CPLs (i.e., the CPL_{685}, CPL_{691}, and CPL_{695}), in perfect agreement with previously published[4] and recent fluorescence spectra reported by Hall et al.[10] All these spectra have variable contributions from the so-called F685, F691, and F695 emission bands.

We suggest that the positive CPL_{695} represents the intact CP47 complexes. When the latter spectrum is simultaneously fitted with absorption, fluorescence, CD, and nonresonant HB spectra, a new information is revealed on the excitonic structure of intact complexes and the composition of the lowest energy state(s). We suggest again that the lowest energy exciton band is mostly contributed to by either Chl 26 or Chl 29 as also suggested in refs 5, 7-9 and 11. Therefore, the assignment of the lowest energy Chl in CP47 to Chl 11 proposed to be responsible for the F695 fluorescence band is incorrect. Identification of the low-energy Chl(s), and their suggested blue shift in destabilized subpopulations, afforded new insight into possible origin of the F691 and F685 emission bands and nonresonant HB spectra.

Thus, our findings can be summarized as follows: (*i*) the CPL and emission spectra reported in ref 10 clearly demonstrate that their samples were highly heterogeneous; (*ii*) the experimental CPL spectrum reported in ref 10 consists of three contributions, i.e. CPL_{695}, CPL_{691}, and CPL_{685}; (*iii*) only the positive CPL_{695} with a maximum near 695 nm (in agreement with nonresonant HB spectra[4]) and the 695 nm emission (F695) band (with *fwhm* ~195 cm^{-1}) represent intact CP47 complex; (*iv*) the blue shifted HB, $CPL_{691,}$ and F691 emission represent destabilized complexes in which the H-bond between one of the low energy Chl and nearby amino acids is weakened due to likely protein conformational changes; (*v*) the HB spectrum obtained as a difference between high burning fluences, CPL_{685} and F685 fluorescence originate mostly from the photoconverted complexes via the HB process and/or irreversible changes. That is, the F685 emission induced at

low temperatures is reversible, unless some H-bonds are broken due to large conformation changes, and in this case contribution from the F685 band is always observed in agreement with experiment; (*vi*) the blue-shifted emission spectra with variable maxima near 690-693 nm contain subpopulations of intact and destabilized complexes; and (*vii*) simultaneous fits of low-temperature absorption, emission, nonresonant HB, CD and CPL_{695} spectra provide best fits when either Chl 26 or Chl 29 mostly contributes to the lowest energy exciton state. These conclusions are based on extensive modeling studies of the optical spectra assigned to intact and destabilized CP47 proteins. Finally, we conclude that the shape of the recently measured CPL spectrum[10] helped to solve the long-standing controversy which spectra represent intact CP47 proteins.

Acknowledgments

This work was supported by the Chemical Sciences, Geosciences and Biosciences Division, Office of Basic Energy Sciences, Office of Science, U.S. Department of Energy (Grants No. DE-FG02-11ER16281 and DE-SC0006678 to R.J.). We acknowledge Drs J. Hall and E. Krausz for sharing with us their original spectra.

References

(1) Blankenship, R. E. *Molecular Mechanisms of Photosynthesis*; Blackwell Science: Oxford, 2002.

(2) Picorel, R.; Alfonso, M.; Seibert, M. Isolation of CP43 and CP47 Photosystem II Proximal Antenna Complexes from Plants. In *Methods in Molecular Biology*, Vol 274; Walker, J. M., Ed.; Humana: Totowa, New Jersey, 2004, 129–135.

(3) Picorel, R.; Alfonso, M.; Seibert, M. Isolation and purification of CP43 and CP47 photosystem II proximal antenna complexes from plants. In: Walker JM, ed. *Methods in Molecular Biology*. Vol 684. New York: Springer, 2011,105–112.

(4) Neupane, B.; Dang, N. C.; Acharya, K.; Reppert, M.; Zazubovich, V.; Picorel, R.; Seibert, M.; Jankowiak, R. Insight into the Electronic Structure of the CP47 Antenna Protein Complex of Photosystem II: Hole Burning and Fluorescence Study. *J. Am. Chem. Soc.* **2010**, *132*, 4214–4229.

(5) Acharya, K.; Neupane, B.; Reppert, M.; Feng, X.; Jankowiak, R. On the Unusual Temperature-Dependent Emission of the CP47 Antenna Protein Complex of Photosystem II. *J. Phys. Chem. Lett.* **2010**, *1*, 2310-2315.

(6) D'Haene, S. E.; Sobotka, R.; Bučinská, L.; Dekker, J. P.; Komenda, J. Interaction of the PsbH Subunit with a Chlorophyll Bound to Histidine 114 of CP47 is Responsible for the Red 77 K Fluorescence of Photosystem II. *Biochim. Biophys. Acta* **2015**, *1847*, 1327-1334.

(7) Raszewski, G.; Renger, T. Light Harvesting in Photosystem II Core Complexes is Limited by the Transfer to the Trap: Can the Core Complex Turn into a Photoprotective Mode? *J. Am. Chem. Soc.* **2008**, *130*, 4431–4446.

(8) Reppert, M.; Acharya, K.; Neupane, B.; Jankowiak, R. Lowest Electronic States of the CP47 Antenna Protein Complex of Photosystem II: Simulation of Optical Spectra and Revised Structural Assignments. *J. Phys. Chem. B* **2010**, *114*, 11884–11898.

(9) Shibata, Y.; Nishi, S.; Kawakami, K.; Shen, J.-R.; Renger, T. Photosystem II Does Not Possess a Simple Excitation Energy Funnel: Time-Resolved Fluorescence Spectroscopy Meets Theory. *J. Am. Chem. Soc.* **2013**, *135*, 6903–6914.

(10) Hall, J.; Renger, T.; Müh, F.; Picorel, R.; Krausz, E. The Lowest-Energy Chlorophyll of Photosystem II is Adjacent to the Peripheral Antenna: Emitting States of CP47 Assigned via Circularly Polarized Luminescence. *Biochim. Biophys. Acta* **2016**, *1857*, 1580–1593.

(11) Reinot, T.; Chen, J.; Kell, A.; Jassas, M.; Robben, K. C.; Zazubovich, V.; Jankowiak, R. On the Conflicting Estimations of Pigment Site Energies in Photosynthetic Complexes: A Case Study of the CP47 Complex. *Anal. Chem. Insights* **2016**, *11*, 35-48.

(12) Umena, Y.; Kawakami, K.; Shen, J.-R.; Kamiya, N. Crystal Structure of Oxygen-Evolving Photosystem II at a Resolution of 1.9 Å. *Nature* **2011**, *473*, 55–60.

(13) Wei, X.; Su, X.; Cao, P.; Liu, X.; Chang, W.; Li, M.; Liu, Z. Structure of Spinach Photosystem II–LHCII Supercomplex at 3.2 Å Resolution. *Nature* **2016**, *534*, 69–74.

(14) Müh, F.; Madjet, M. E.-A.; Adolphs, J.; Abdurahman, A.; Rabenstrin, B.; Ishikita, H.; Knapp, E.-W.; Renger, T. α-Helices Direct Excitation Energy Flow in the Fenna–Matthews–Olson Protein. *Proc. Natl. Acad. Sci. U.S.A.* **2007**, *104*, 16862–16867.

(15) Adolphs, J.; Müh, F.; Madjet, M. E.-A.; Renger, T. Calculation of Pigment Transition Energies in the FMO Protein. *Photosynth. Res.* **2008**, *95*, 197–209.

(16) Gao, J.; Shi, W.-J.; Ye, J.; Wang, X.; Hirao, H.; Zhao, Y. QM/MM Modeling of Environmental Effects on Electronic Transitions of the FMO Complex. *J. Phys. Chem. B* **2013**, *117*, 3488–3495.

(17) Cole, D. J.; Chin, A. W.; Hine, N. D. M.; Haynes, P. D.; Payne, M. C. Toward ab initio Optical Spectroscopy of the Fenna–Matthews–Olson Complex. *J. Phys. Chem. Lett.* **2013**, *4*, 4206–4212.

(18) Groot, M.-L.; Peterman, E. J. G.; van Stokkum, I. H. M.; Dekker, J. P.; van Grondelle, R. Triplet and Fluorescing States of the CP47 Antenna Complex of Photosystem II Studied as a Function of Temperature. *Biophys. J.* **1995**, *68*, 281–290.

(19) de Weerd, F. L.; Palacios, M. A.; Andrizhiyevskaya, E. G.; Dekker, J. P.; van Grondelle, R. Identifying the Lowest Electronic States of the Chlorophylls in the CP47 Core Antenna Protein of Photosystem II. *Biochemistry* **2002**, *41*, 15224–15233.

(20) Krausz, E.; Hughes, J. L.; Smith, P. J.; Pace, R. J.; Peterson Arsköld, S. Assignment of the Low-Temperature Fluorescence in Oxygen-Evolving Photosystem II. *Photosynth. Res.* **2005**, *84*, 193–199.

(21) Renger, T.; Madjet, M. E.; Müh, F. How the Molecular Structure Determines the Flow of Excitation Energy in Plant Light-Harvesting Complex II. *J. Plant Physiol.* **2011**, *168*, 1497-1509.

(22) Hall, J.; Renger, T.; Picorel, R.; Krausz, E. Circularly Polarized Luminescence Spectroscopy Reveals Low-Energy Excited States and Dynamic Localization of Vibronic Transitions in CP43. *Biochim. Biophys. Acta* **2016**, *1857*, 115–128.

(23) Adolphs, J.; Müh, F.; Madjet, M. E.-A.; Schmidt am Busch, M.; Renger, T. Structure-Based Calculations of Optical Spectra of Photosystem I Suggest an Asymmetric Light-Harvesting Process. *J. Am. Chem. Soc.* **2010**, *132*, 3331-3343.

(24) Renger, T.; Marcus, R. A. On the Relation of Protein Dynamics and Exciton Relaxation in Pigment-Protein Complexes: An Estimation of the Spectral Density and a Theory for the Calculation of Optical Spectra. *J. Chem. Phys.* **2002**, *116*, 9997–10019.

(25) Nelder, J. A.; Mead, R. A Simplex Method for Function Minimization. *Comput. J.* **1965**, *7*, 308–313.

(26) Kell, A.; Feng, X.; Reppert, M.; Jankowiak, R. On the Shape of the Phonon Spectral Density in Photosynthetic Complexes. *J. Phys. Chem. B* **2013**, *117*, 7317−7323.

(27) Renger, T.; Marcus, R. A. Photophysical Properties of PS-2 Reaction Centers and a Discrepancy in Exciton Relaxation Times. *J. Phys. Chem. B* **2002**, *106*, 1809–1819.

(28) Chen, J.; Kell, A.; Acharya, K.; Kupitz, C.; Fromme, P.; Jankowiak, R. Critical Assessment of the Emission Spectra of Various Photosystem II Core Complexes. *Photosynth. Res.* **2015**, *124*, 253-265.

(29) Hofmann, C.; Aartsma, T. J.; Michel, H.; Köhler, J. Direct Observation of Tiers in the Energy Landscape of a Chromoprotein: A Single-Molecule Study. *Proc. Natl. Acad. Sci. U.S.A.* **2003**, *100*, 15534-15538.

(30) Chang, H. C.; Jankowiak, R.; Yocum, C. F.; Picorel, R.; Alfonso, M.; Seibert, M.; Small, G. J. Exciton Level Structure and Dynamics in the CP47 Antenna Complex of Photosystem II. *J. Phys. Chem.* **1994**, *98*, 7717–7724.

(31) de Paula, J. C.; Liefshitz, A.; Hinsley, S.; Lin, W.; Chopra, V.; Long, K.; Williams, S. A.; Betts, S.; Yocum, C. F. Structure-Function Relationships in the 47-kDa Antenna Protein and its Complex with the Photosystem II Reaction Center Core: Insights from Picosecond Fluorescence Decay Kinetics and Resonance Raman Spectroscopy. *Biochemistry* **1994**, *33*, 1455–1466.

(32) Riehl, J. P.; Richardson, F. S. Circularly Polarized Luminescence Spectroscopy. *Chem. Rev.* ***1986***, *86*, 1–16.

(33) Polívka, T.; Kroh, P.; Pšenčík, J.; Engst, D.; Komenda, J.; Hála, J. Hole-Burning Study of Excited Energy Transfer in the Antenna Protein CP47 of *Synechocystis* sp. PCC 6803 Mutant H114Q. *J. Lumin.* **1997**, *72-74*, 600–602.

(34) den Hartog, F. T. H.; Dekker, J. P.; van Grondelle, R.; Völker, S. Spectral Distributions of "Trap" Pigments in the RC, CP47, and CP47-RC Complexes of Photosystem II at Low Temperature: A Fluorescence Line-Narrowing and Hole-Burning Study. *J. Phys. Chem. B* **1998**, *102*, 11007–11016.

(35) Reimers, J. R.; Biczysko, M.; Bruce, D.; Coker, D. F.; Frankcombe, T. J.; Hashimoto, H.; Hauer, J.; Jankowiak, R.; Kramer, T.; Linnanto, J.; et al. Challenges Facing an Understanding of the Nature of Low-Energy Excited States in Photosynthesis. *Biochim. Biophys. Acta* **2016**, *1857*, 1627–1640.

(36) van Dorssen, R. J.; Breton, J.; Plijter, J. J.; Satoh, K.; van Gorkom, H. J.; Amesz, J. Spectroscopic Properties of the Reaction Center and of the 47 kDa Chlorophyll Protein of Photosystem II. *Biochim. Biophys. Acta* **1987**, *893*, 267-274.

(37) Guskov, A.; Kern, J.; Gabdulkhakov, A.; Broser, M.; Zouni, A.; Saenger, W. Cyanobacterial Photosystem II at 2.9-Å Resolution and the Role of Quinones, Lipids, Channels and Chloride. *Nat. Struct. Mol. Biol.* **2009**, *16*, 334–342.

(38) Krausz, E.; Hughes, J. L.; Smith, P. J.; Pace, R. J.; Peterson Årsköld, S. Oxygen-Evolving Photosystem II Core Complexes: A New Paradigm Based on the Spectral Identification of the Charge-Separating State, the Primary Acceptor and Assignment of Low-Temperature Fluorescence. *Photochem. Photobiol. Sci.* **2005**, *4*, 744–753.

(39) Shen, G.; Vermaas, W. F. J. Mutation of Chlorophyll Ligands in the Chlorophyll-Binding CP47 Protein as Studied in a *Synechocystis* sp. PCC 6803 Photosystem I-Less Background. *Biochemistry* **1994**, *33*, 7379-7388.

(40) Renge, I.; Mauring, K. Spectral Shift Mechanisms of Chlorophylls in Liquids and Proteins. *Spectrochim. Acta A* **2013**, *102*, 301–313.

(41) Kwa, S. L. S.; Völker, S.; Tilly, N. T.; van Grondelle, R.; Dekker, J. P. Polarized Site-Selection Spectroscopy of Chlorophyll a in Detergent. *Photochem. Photobiol.* **1994**, *59*, 219-228.

Chapter 3

Structure-based Exciton Hamiltonian and Dynamics for the Reconstituted Wild Type CP29 Protein Antenna Complex of the Photosystem II

Mahboobe Jassas[1], Jinhai Chen[1], Anton Khmelnitskiy[1], Anna Paola Casazza[3], Stefano Santabarbara[4], and Ryszard Jankowiak[1,2,*]

[1]Department of Chemistry and [2]Department of Physics, Kansas State University, Manhattan, KS 66506, U.S.A.; [3]Instituto di Biologia e Biotecnologia Agraria, del C.N.R., and [4] Photosynthesis Research Unit, Centro Studi sulla Biologia Cellulare e Molecolare delle Piante, C.N.R., 20133 Milano, Italy

Reproduced from *Journal of Physical Chemistry B* **2018**, 122, 4611−4624

Abstract

We provide an analysis of the pigment composition of reconstituted wild type CP29 complexes. The *obtained* stoichiometry of 9 ± 0.6 Chls *a* and 3 ± 0.6 Chls *b* per complex, with some possible heterogeneity in the carotenoid binding, is in agreement with 9 Chls *a* and 3.5 Chls *b* revealed by the modeling of low-temperature optical spectra. We find that ~50% of Chl *b*614 is lost during the reconstitution/purification procedure, while Chls *a* are almost fully retained. The excitonic structure and the nature of the low-energy (low-E) state(s) are addressed via simulations (using Redfield theory) of 5 K absorption and fluorescence/nonresonant hole-burned (NRHB) spectra obtained at different excitation/burning conditions. We show that, depending on laser excitation frequency, reconstituted complexes display two (independent) low-E states (i.e., the ***A*** and ***B*** traps) with different NRHB and emission spectra. The red-shifted state ***A*** near 682.4 nm is assigned to a minor (~10%) subpopulation (Sub. II) that most likely originates from an imperfect local folding occurring during protein reconstitution. Its lowest energy state ***A*** (localized on Chl *a*604) is easily burned with λ_B = 488.0 nm and has a red-shifted florescence origin band near 683.7 nm that is not observed in native (isolated) complexes. Prolonged burning by 488.0 nm light reveals a second low-E trap at 680.2 nm (state ***B***) with a fluorescence origin-band ~681 nm which is also observed when using a direct low-fluence excitation near 650 nm. The latter state is mostly delocalized over the *a*611, *a*612, *a*615 Chl trimer, and corresponds to the lowest energy state of the major (~90%) subpopulation (Sub. I) which exhibits a lower hole-burning quantum yield. Thus, we suggest that major Sub. I correspond to the native folding of CP29, whereas the red-shift of the Chl *a*604 site energy observed in the minor Sub. II occurs only in reconstituted complexes.

3.1 Introduction

In higher plants and green algae, the light harvesting complement associated with Photosystem II (PSII), i.e., the photocatalytic center responsible for oxygen evolution as a result of water splitting, consists of several chlorophyll (Chl) *a*/*b* and carotenoid (Car) binding proteins. The most abundant PSII antenna is organized as a functional trimer composed of various combinations of the *Lhcb1-2-3* gene products[1] and is often referred to as LHCII. The core complex of PSII, which harbors the reaction center (RC), binds three to four LHCII trimers. However, the largest core-antenna system (the so-called $C_2S_2M_2$ supercomplex[2]) retains only two LHCII trimers per RC when purified biochemically.[3] Detailed structural models are available for the LHCII trimer, indicating the presence of eight Chl *a*, six Chl *b* and four oxygenated carotenoids (xanthophyll) molecules, i.e., one neoxanthin (Neo), one violaxanthin (Vio) and two lutein (Lut) molecules[4,5] in each monomeric unit. This binding stoichiometry is in close agreement with other biochemical characterizations.[6-8]

The PSII antenna system of higher plants also contains core antenna subunits (CP43 and CP47) as well as three minor complexes (CP24, CP26 and CP29).[9] These minor antenna are the *Lhcb6*, *Lhcb5* and *Lhcb4* gene products, respectively.[10] All of these complexes are isolated as monomers and are bound as a single copy per RC, linking the core antenna subunits (CP43 and CP47) to the more external LHCII trimers. While CP29 and CP24 are adjacent to CP47 (and tightly bound to the core complex), CP26 is located near CP43.[11,12] Although the spectroscopic properties of all external antenna complexes have been extensively studied,[13-17] a crystallographic model of isolated complexes is available only for CP29.[18] This model revealed the presence of 8-9 Chl *a*, 4-5 Chl *b* and 3 xanthophylls (i.e., Neo, Vio and Lut), per complex.[18] It was suggested that the ranges of both Chl *a* and Chl *b* stoichiometries are due to possible mixed occupancy in one or two sites.[18]

The crystallographic CP29 model from ref 18 showed a remarkable similarity to that of LHCII,[4,5] at least in terms of the protein scaffold and location/orientation of Chls. In both LHCII and CP29 structures, the Chl molecules are grouped in two layers (Figure 3.1), one facing the (putative) stromal side, the other the lumenal side of the thylakoid membrane. The stromal layer in CP29 appears to contain eight Chls (i.e., *a*602, *a*603, *b*608, *a*609, *a*610, *a*611, *a*612 and *a*615 according to the nomenclature of Pan *et al*.[18] The lumenal layer includes five Chls (i.e., *a*604, *b*606, *b*607, *a*613 and *b*614). Thus, the X-ray structure (PDB ID: 3PL9) of the CP29 protein revealed the presence of 13 Chl molecules in total.[18] The arrangement of Chls in the isolated CP29 complex, based on X-ray crystallographic data, is shown in Figure 3.1 together with the proposed organization in excitonic domains (D1-D4).

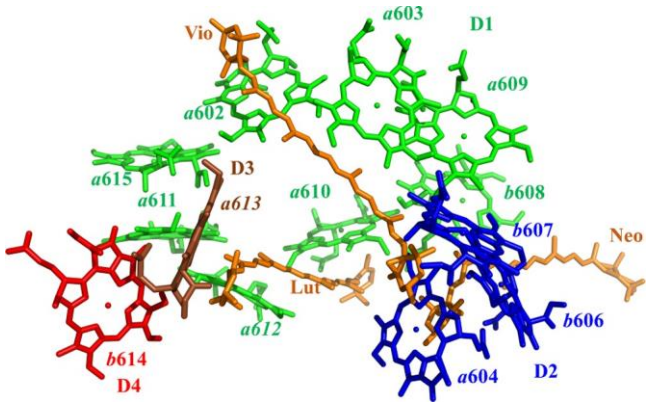

Figure 3.1 Arrangement of Chls in the isolated CP29. Chls are divided into four domains as in ref 19; Chls in domain 1 (D1) and domain 2 (D2) are shown in green and blue, respectively. Weakly coupled pigments, i.e., Chl *a*613 (brown) and Chl *b*614 (red) are assigned to domains D3 and D4, respectively. Cars: Lutein (Lut), Violaxanthin (Vio) and Neoxanthin (Neo) are in orange.

The largest domain 1 (D1; green) contains Chls *a*602, *a*603, *b*608, *a*609, *a*610, *a*611, *a*612, and *a*615. Two of the Chls which compose the lumenal layer of CP29 (*a*613, *b*614) appear to be relatively isolated excitonically and are assigned to domains D3 and D4, whereas the remaining three Chls (*a*604, *b*606 and *b*607) form another relatively strongly coupled excitonic domain D2.[19]

Interestingly, the number of Chls and Cars resolved in the CP29 X-ray structure exceeded the number of pigments revealed by various biochemical investigations.[7,20-22] Until recently, it was believed that the CP29 protein from higher plant PSII contained eight Chls per complex[21-24] in contrast to the 13 Chls revealed by the recent X-ray structure.[18] The binding stoichiometry (i.e., eight Chls per complex) was obtained for both the isolated CP29 purified from plant material (also called the "native" form[21-24]) and for the *in vitro* reconstituted CP29.[21] Other binding stoichiometries were also observed,[25-27] clearly suggesting that pigment analysis of CP29 proteins is not straightforward and could carry some uncertainty. This disagreement presents a constraint on the interpretation of the CP29 underlying electronic structure.

Very recently structural data resulting from cryo-electron microscopy on the $C_2S_2M_2$-type PSII-LHCII supercomplex[28] confirmed the presence of at least 13 Chl molecules as well as 3 xanthophylls per CP29 complex. (Various available structures are compared in Figure B.7 of the Appendix B). The structure of Wei *et al.*[29] revealed the presence of an additional Chl, labeled *a*616. This result was later confirmed by structures obtained at 2.7 and 3.2 Å resolutions using supercomplexes isolated from both stacked and unstacked thylakoid membranes, indicating the presence of ten Chls *a* and four Chls *b* in CP29.[28] Moreover, it appears that Chl *a*601 observed in the $C_2S_2M_2$ supercomplex[29] likely corresponds to the Chl *a*615 observed previously in the 3PL9 structure.[18] However, the purified CP29 will most likely lose the *a*616 pigment observed by Wei *et al.*[29] as it is located externally at the N-terminal region. Thus, it is possible that Chl *a*616 is generally lost during the isolation procedure of CP29, and that the high resolution (2.8 Å) structure displaying 13 Chls is appropriate to describe the isolated complex. Although several papers suggested that some Chls could have been lost during the preparation/purification procedure,[19,30]

it is unlikely that the CP29 protein contains only eight Chls as suggested by the LHCII sequence homology-based model.[23,31]

Even in place of a large body of both spectroscopic and computational investigations, the understanding of excitation energy transfer (EET) dynamics, as well as the energetic landscape of CP29, is still incomplete and controversial. For example, in ref 30 we showed that the lowest energy state in the native form of spinach CP29, assigned to the exit trap in energy transfer pathways, is mostly contributed to by *a*611, *a*612, *a*615, and *a*610 Chls. A similar conclusion was reached in ref 19 where it was also suggested that strongly coupled *a*611, *a*612, and *a*615 Chls mostly contribute to the lowest energy exciton state. This is reminiscent of what was proposed for LHCII where the *a*610, *a*611, *a*612 trimer was also suggested to be the most strongly coupled Chl cluster contributing to the lowest excitonic state.[16,32] However, computational studies, including molecular dynamics minimization of the crystallographic coordinates, suggested that the exciton state dominated by the contribution of Chls *a*602, *a*603 and *a*609 could also represent a low-E state, possibly the lowest one, albeit being almost isoenergetic to that arising from the *a*611, *a*612, *a*615 cluster.[33] Moreover, very recently Müh et al.[19] predicted theoretically that Chl *a*604 (located near Neo) could be the lowest energy pigment in native CP29 complexes. This was illustrated via the simulation of room temperature wild-type-minus-mutant difference spectra of reconstituted CP29, where a tyrosine residue next to Chl *a*604 was modified in the Y135F mutant.[19] Therefore, the optical properties of this important antenna are here re-investigated to confirm or reject the notion that Chl *a*604 could be the lowest energy pigment in the native CP29 complexes.

In this work we present a new pigment stoichiometry analysis, as well as high-resolution (low-temperature) hole-burning (HB) and fluorescence data that provide more insight on low-E trap(s) and heterogeneity in reconstituted CP29 complexes. Optical spectra are modeled using a

non-Markovian reduced density matrix approach.[34] Experimental constraints (i.e., electron-phonon coupling parameters and shapes of the phonon and vibrational spectral densities) are used in the simultaneous modeling of various types of optical spectra, providing somewhat different set of pigment site energies than previously reported,[19] a revised excitonic structure, and more details on EET dynamics. We suggest that reconstituted proteins might be heterogeneous in Car binding, which could lead to a different conformation of Neo and/or its absence in a fraction of complexes. It is also shown that our reconstituted CP29 complexes have two low-E states having different HB characteristics as well as shifted emission spectra, which we assign to two different subpopulations of CP29 complexes. Finally, the new excitonic structure and composition of low-E traps in both subpopulations are discussed in the context of spectral hole-growth kinetics measurements obtained for native CP29[35] and the previously reported EET dynamics.[19,30] Implications of these new assignments are briefly discussed.

3.2 Materials and Methods

3.2.1 Recombinant CP29 Complexes and Reconstitution Procedure

The *Lhcb4.1* coding sequence corresponding to the mature form of CP29 from *A. thaliana* was cloned into the pET32b expression vector as described in ref 22. The N-terminal His-tagged CP29 apoprotein was expressed in the BL21 *Escherichia coli* strain (Invitrogen) in the form of inclusion bodies, which were purified following the literature[36] and stored at -80 °C until use. Reconstitution of CP29-pigment complexes was performed exactly as described by Giuffra et al.[21] incubating inclusion bodies with pigments using a chlorophyll *a/b* ratio of 8. Total pigments were extracted from spinach and barley (*chlorina f2* mutant) thylakoids with 80% acetone.[37] Xanthophyll was purchased from Sigma. Pigment concentration was calculated from absorption measurements according to refs 38 and 39. To remove excess pigments from the reconstituted

complexes, the band from the sucrose gradient was loaded onto a Ni^{2+}-NTA column (Qiagen). For long term storage, fully purified reconstituted wild type (WT) CP29 complexes were diluted to 0.6 OD/cm at the Q_y absorption maximum in a buffer containing 10 mM Hepes pH 7.6, 0.03% β-dodecyl maltoside (DM), 60% glycerol (v/v), frozen in liquid nitrogen and kept at -80 °C. Pigments analysis was performed in a Jasco HPLC system coupled to a diode array detector (PU1580/LG-1580-2) using a C18 HPLC column (Spherisorb ODS1 5 µm, 25 x 0.46 cm; Phenomenex) using the protocol descried in ref 40. Further details are provided in the Appendix B.

3.2.2 Experimental Spectroscopic Methods

For low temperature experiments, samples were diluted with 1:2 (v/v) buffer:glass solution. The glass forming solution was 55:45 (v/v) glycerol:ethylene glycol. Details about the measurement setup were described elsewhere.[41] Here, only a brief description is given. A Bruker HR125 Fourier transform spectrometer was used to measure the absorption and HB spectra with resolutions of 4 and 2 cm^{-1}, respectively. The low temperature fluorescence spectra were collected by a Princeton Instruments Acton SP-3200 spectrograph equipped with a back-illuminated CCD camera (PI Action Spec10, 1,340×400) with a resolution of 0.1 nm. The laser sources for both NRHB and fluorescence was 488.0 nm produced from a Coherent Innova 200 argon ion laser, and tunable wavelengths came from a Coherent CR899 Ti:Sapphire laser (line width 0.07 cm^{-1}) pumped by a Spectra-Physics Millennia Xs diode laser (532 nm). Laser power in the experiments was precisely set by a continuously adjustable neutral density filter. All low temperature (5-77 K) experiments were performed using an Oxford Instruments Optistat CF2 cryostat with sample temperature read and controlled by a Mercury iTC temperature controller.

3.2.3 Modeling studies of various optical spectra

In the present work, optical spectra are modeled using the density matrix description of Renger and Marcus,[34] in order to more accurately reflect the influence of electron-phonon (el-ph) coupling and lifetime broadening on the calculated optical spectra. A detailed description of this theory has already been presented in refs 34 and 42. We use a non-Markovian reduced density matrix theory[34] with a Nelder-Mead Simplex algorithm for parameter optimization,[43] i.e. we use a search method for multidimensional unconstrained minimization. The algorithm searches the solution space and minimizes the root-mean square deviation while simultaneously fitting multiple spectra. Moreover, we assume that the phonon spectral density (weighted phonon profile) can be described by a continuous function, which is chosen to be a lognormal distribution[44] (see section 3.4.1). In all simulations vibrational modes are dynamically localized as in ref 45. In modeling studies, we consider CP29 complexes with a different number of pigments. Below, however, only relevant results are shown and discussed. Domains (1-4) of Q_y-transitions are defined in the same way as in previous modeling studies of the same complex.[19] A partially coherent energy relaxation is expected within the strongly coupled domains (1 and 2), while incoherent Förster type EET occurs between the low-E states of each domain. That is, one can assume that if the couplings V_{nm} within a certain group of pigments are large, and the couplings to other pigments in the complex are small (smaller than the differences in site energies and smaller than the reorganization energy), such a group can be treated as an independent domain, and the optical spectra of the complex can be calculated as a sum of the excitonic spectra of such groups (domains).[46] Absorption, emission, and nonresonant HB (NRHB) spectra are calculated using Redfield theory.[47] The latter spectra are calculated in a following way: after diagonalization of the Frenkel Hamiltonian, a pre-burn absorption spectrum is calculated from Redfield theory. The occupation numbers (squared

eigenvector coefficients) of the lowest energy exciton state are used to determine the pigments to be burned. This corresponds to the low-fluence approximation, where only pigments contributing to the lowest energy state are burned. To fit NRHB spectra the post-burn site-energy distribution of the burned pigment is found from the pre-burn site-energy distribution function (SDF), or if the energy landscape is modified the distribution is shifted to higher energies (*vide infra*), while all other diagonal elements of the Hamiltonian are unchanged. The Hamiltonian is again diagonalized and a post-burn absorption spectrum is calculated. The resulting NRHB spectrum is calculated as the pre-burn absorption subtracted from the post-burn absorption spectrum. The CD spectrum was not included in the simultaneous fit as Redfield theory used in this work cannot describe non-conservative nature of CD spectra measured for CP29 as higher energy excited states of the Chls and the $S_0 \rightarrow S_2$ transition of carotenoids, as well as the intrinsic CD of the Chls, would have to be taken into account.[48]

3.3 Experimental Results

3.3.1 Pigment Composition in Reconstituted Complexes

From the pigment composition analysis, the stoichiometry of chromophore binding is: 9 ± 0.6 Chl *a*, 3 ± 0.6 Chl *b*, 1 ± 0.09 Neo, 1.16 ± 0.18 Lut, and 0.88 ± 0.09 Vio molecules per complex. The average Chl *a*/*b* ratio was 3.0 ± 0.1 and $Chl_{(a+b)}$/Car was 3.9 ± 0.4. Considering integer Chl pigment site occupancies, the stoichiometry revealed by pigment analysis is 9 Chl *a* and 3 Chl *b* per complex, with some heterogeneity in the Car binding stoichiometry. We therefore conclude that the number of Chls bound to the reconstituted CP29 is equivalent to 12 ± 0.6 per complex, which is in good agreement with the number of pigments obtained from our modeling studies (*vide infra*) to get the best simultaneous fits of multiple optical spectra. Thus, the reconstituted CP29 mainly misses a fraction of Chl *b*, whereas Chl *a* is almost fully retained (for more details see the

Appendix B). We argue below that upon *in vitro* reconstitution, CP29 binds on average 12.5 Chls per complex, i.e., somewhat less than what was observed in the (native) structural models[18] but more than what reported previously for analogous reconstituted complexes.[21,22]

3.3.2 Experimental absorption, emission and nonresonant HB (NRHB) spectra

Figure 3.2 shows normalized 5 K absorption (curve a), emission (curve b) and NRHB (λ_B = 488.0 nm, curve c) spectra of the reconstituted CP29 complex. The absorption spectrum is similar to the spectra reported in the literature for native CP29 complexes[14,26,49] at similar low temperatures, showing a prominent Q_y-band centered at 674.6 nm in the Chl *a* region (curve a). The 665-670 nm shoulder sometimes observed in the native complex and which gives rise to an asymmetry in the Q_y absorption band, is less evident in the reconstituted complex. However, the two bands near 638.6 and 650.8 nm, due to the several Chl *b* molecules present in CP29, are clearly visible. Yet, in contrast to the literature data,[14,26,49] our emission spectrum (see Figure 3.2, curve b), obtained with an excitation wavelength (λ_{ex}) of 488.0 nm and low laser intensity of 300 $\mu W/cm^2$ (to minimize hole burning), shows a red-shifted fluorescence peak position near 683.7 nm. The full-width-at-half-maximum (*fwhm*) is about 175 cm^{-1}, while its half-band width on the high energy site is about 69 cm^{-1}. Thus, the (0,0)-band emission is significantly red-shifted in comparison to the often reported spectra for CP29 with typical maxima near 680-681 nm.[14,26,49] Regarding the red-shifted emission band mentioned above, we think that a contribution from aggregated CP29 complexes to spectrum b in Figure 3.2 is negligible (if any), as the emission spectrum of aggregated complexes has a maximum near 690 nm and is significantly broader (*fwhm* = 444 cm^{-1}).[30] We hasten to add that the emission origin band near 680-681 nm is also observed in our samples for λ_{ex} = 650.0 nm, as illustrated by curve c in Figure 3.3 (see section 3.3.3 for

details). The latter clearly indicates a heterogeneous nature of the reconstituted CP29 proteins studied in this work.

Figure 3.2 also shows the low-fluence ($f = I \times t = 6$ J/cm^2, where I and t are the laser intensity and burn time, respectively) NRHB spectrum, having a hole minimum at 682.4 nm accompanied by a broad anti-hole peaking near 674.6 nm (curve c). The bleach also reveals weak satellite holes near 638.8 and 649.2 nm in the Chl *b* region. The position of the main nonresonant hole ($\lambda_B = 488.0$ nm) is about 4 nm red-shifted with respect to those previously reported near 678-679 nm for the native CP29 complexes[30] upon similar NRHB conditions ($\lambda_B = 496.5$ nm). Note, as illustrated in the inset of Figure 3.2, that the bleach in the NRHB spectra shifts blue with increasing fluence. The most blue-shifted hole (green curve in the inset) has the main bleach at 681.1 nm. We suggest that the 682.4 nm hole belongs to the low-E trap in a subpopulation of complexes referred to hereafter as "state ***A***".

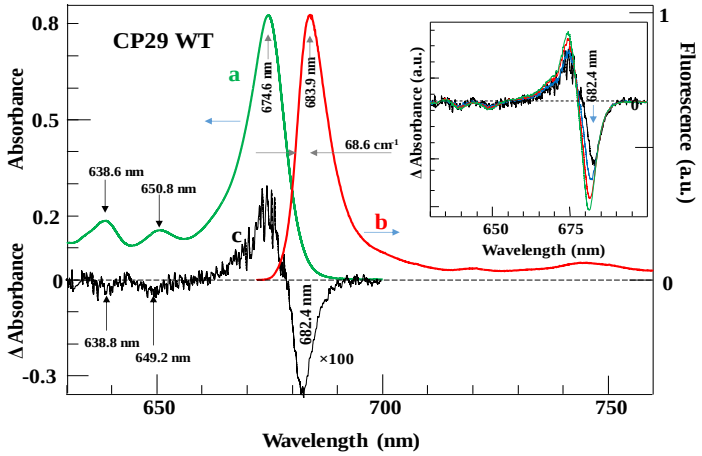

Figure 3.2 Curves a and b correspond to 5 K absorption and fluorescence spectra of the reconstituted CP29 complex (normalized to peak intensities). For fluorescence measurements the OD of the sample was reduced to ~0.1 to minimize reabsorption. Curve c is the low-fluence NRHB spectrum obtained with $\lambda_B = 488.0$ nm. Inset: Scaled NRHB spectra (aligned at the low-E wing) obtained for different f values (from top to bottom $f = 6$, 186, 906 and 1986 J/cm^2). The top NRHB spectrum is identical to curve c in the main frame.

3.3.3 Excitation Dependent Emission and NRHB-induced Shift of Fluorescence Spectra

As mentioned above, the fluorescence maximum depends on the excitation wavelength. This is further illustrated in Figure 3.3 where the 5 K emission spectra recorded with low-laser intensity (I = 300 μW/cm^2) at 488.0 nm (curve a) and 650.0 nm (curve c) are directly compared after normalization at their peak intensities. The emission maximum in curve c is blue-shifted by ~3 nm upon 650.0 nm excitation, which is similar to spectrum b (obtained at identical experimental conditions) which was recorded after the lowest energy trap (i.e., state ***A***) was largely bleached by high-fluence (f = 16627 J/cm^2) 488.0 nm excitation. That is, the nonresonant bleach of the lowest energy state ***A*** at 682.4 nm (most likely present only in a fraction of complexes) reveals the typically observed blue-shifted emission peaking near 680-681 nm. The latter spectrum, as expected, is not only very similar to that obtained by 650.0 nm excitation (curve c) but also to the ones typically observed in isolated CP29 complexes. We suggest that the 680-681 nm emission is characteristic for the majority of complexes in the reconstituted samples. Interestingly, rescaled spectra b and c (not shown) fit well the high energy wing of spectrum a, suggesting that spectrum a could also be weakly contributed to by the 680-681 nm emission. This observation also supports the presence of two subpopulations of complexes distinguishable on the basis of their 5 K emission spectra.

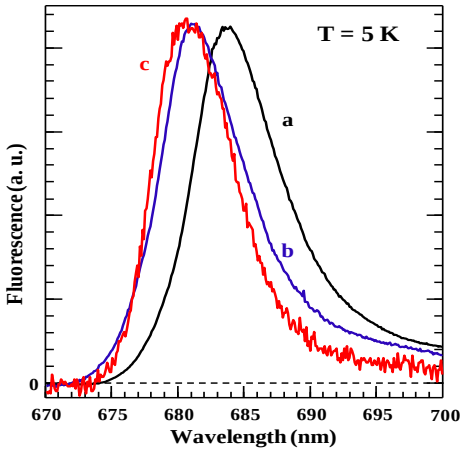

Figure 3.3 Spectra a and b (with the same *fwhm* of 7.9 nm/170 cm^{-1}) are the 5 K fluorescence spectra obtained with λ_{ex} = 488.0 nm (I = 300 μW/cm^2) before and after the bleach of state *A*. Curve c was obtained with the same low-laser intensity I (negligible NRHB) at λ_{ex} = 650.0 nm; see text for details.

Additional support regarding the presence of a heterogeneous population of reconstituted CP29 complexes comes from the analysis of NRHB spectra, which shows a composite nature of the fluence-dependent bleach. This is illustrated in the inset of Figure 3.4. The three lowest fluence HB spectra from the inset in Figure 3.2 are replotted in Figure 3.4 as curves a-c. In this case, we do not normalize the spectra in the long wavelength region as in the inset of Figure 3.2, i.e., spectra a-c in Figure 3.4 show measured hole depths. The absorption spectrum (gray curve) in Figure 3.4 is shown for easy comparison. The spectrum obtained for the lowest fluence of 6 J/cm^2 (curve a; red) appears to contain the contribution uniquely from the lowest energy state ***A***, i.e., this state is preferentially bleached. However, HB spectra obtained for 186 (curve b) and 906 (curve c) J/cm^2 appear to result from a superimposition of two components, whose relative contribution depends on the burning time. This is illustrated by curves b_1/a_1 (blue) and b_2/a_2 (green) in the inset of Figure 3.4, which correspond to the decomposition of curve b and c in the main frame, respectively.

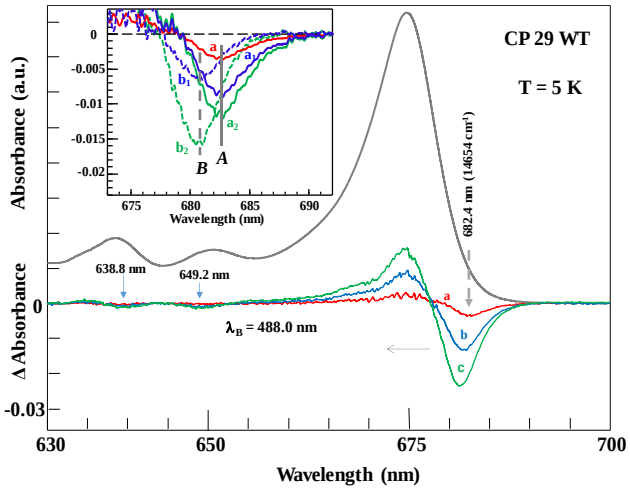

Figure 3.4 Curves a-c show fluence-dependent NRHB spectra (λ_B = 488.0 nm at T = 5 K) obtained with *f* of 6, 186, and 906 J/cm^2, respectively. The gray spectrum is the 5 K absorption. Spectrum a in the inset is the same as curve a in the main frame; curves b_1/a_1 (blue) and b_2/a_2 (green) in the inset are the deconvolution into two low energy traps, *A* and *B*, of the experimental holes b-c shown in the main frame.

It appears therefore that under these conditions a different low-E exciton trap (state ***B***), most likely belonging to a different subpopulation of complexes, contributes to the HB bleach together with state ***A***. Only at *f*-values larger than 1000 J/cm^2 the nonresonant hole shifts further blue and cannot be deconvolved into ***A*** and ***B*** traps (not shown). The additional blue-shift is caused by contribution from higher energy exciton state(s). See section 3.5.2 for further discussion.

Thus, the excitation-dependent emission spectra (Figure 3.3) and composite nature of *f*-dependent NRHB spectra (Figure 3.4) support the presence of two sub-populations. Subpopulation II (Sub. II) is characterized by a relatively large HB quantum efficiency and red-shifted emission (originating from state ***A***) peaking near 683.7 nm. The other subpopulation I (Sub. I) is characterized by the emission (0,0)-band near 680-681 nm, which occurs from a less red-shifted state ***B***, having a lower HB quantum yield. Besides, if there were only one low-E trap, the emission spectrum (obtained for low excitation intensity, i.e., no HB) should not depend on excitation wavelength as observed in Figure 3.3. Moreover, these states must be associated with different

CP29 subpopulations, because at 5 K the EET would otherwise inevitably localize on the lowest energy transition (state ***A*** in this case). Therefore, the observed bleaches are most likely associated with the presence of two independent low-E states (assigned above to states ***A*** and ***B***) with significantly different HB characteristics (e.g., different HB quantum yields), as well as different emission quantum yields.

3.3.4 Resonant HB Spectra

Further details on the composite nature of the low-E band(s) can be gained from the resonant HB spectra, which are shown in Figure 3.5. Spectrum c (red; ×5.8) shows the low-fluence spectrum burned at ν_{B2} = 15646 cm^{-1} (λ_{B2} = 639.1 nm), corresponding to a preferential excitation of the so-called 640-Chl *b* molecules. Curve c also shows a narrow zero phonon hole (ZPH) at the burning frequency, accompanied by a 3.5% nonresonant bleach centered at 14726 cm^{-1} (679.0 nm), which is blue-shifted with respect to the NRHB spectrum burnt with λ_{B1} = 488.0 nm (see curve b). Spectrum b was scaled to the same depth as hole c (i.e., the black spectrum is multiplied by a factor of 20). The energy of the main bleach in curve c (obtained for ν_{B2}) corresponds to that expected for state ***B*** giving rise to an emission near 681 nm. Note that burning at ν_{B2} (see curve c) also resolves several excited-state vibrational frequencies of Chls at 853, 871, 983 cm^{-1}. These values are in very good agreement with those reported for Chl *a*.[50]

Moreover, curves d and e show ZPHs obtained for ν_{B3} = 15355 cm^{-1} (λ_{B3} = 651.2 nm; preferentially exciting the so-called 650-Chls *b*) and ν_{B4} = 14941 cm^{-1} (λ_{B4} = 669.3 nm; exciting Q_y-transitions of Chls *a*), respectively. These ZPHs were superimposed on the same broad bleach as that revealed by spectrum c (not shown), which has been subtracted to reveal only the shape of the ZPHs. The *fwhm* of the ZPHs obtained at ν_{B2}, ν_{B3}, and ν_{B4} are 8.0, 4.8, and 4.5 cm^{-1}, respectively, that correspond to 7.5, 3.9, 3.6 cm^{-1} after correction for the 2 cm^{-1} detection spectral

resolution. Corresponding EET times from the 640-Chl *b* (ν_{B2}) and 650-Chl *b* (ν_{B3}), as well as EET from Chl *a* absorbing near 670 nm (ν_{B4}), to the lowest energy trap(s) are discussed in section 3.5.4. The Lorentzian fit of the ZPH at ν_{B2} is shown in the inset; the fits of the other two ZPH (holes d and e) are shown in Figure B.3 of the Appendix B.

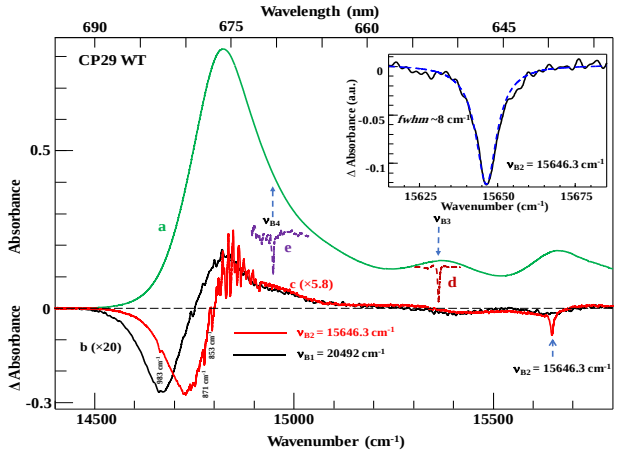

Figure 3.5 Spectra b and c show NRHB spectra burnt at ν_{B1} = 20492 cm^{-1} (λ_{B1} = 488.0 nm) and ν_{B2} = 15646 cm^{-1} (λ_{B2} = 639.1 nm), respectively. Spectra d (ν_{B3} = 15355 cm^{-1}; λ_{B3} = 651.2 nm) and e (ν_{B4} = 14941 cm^{-1}; λ_{B4} = 669.3 nm) show extracted ZPHs (see text for details). Curve a is 5 K absorption spectrum and is shown here for ease of comparison with the HB spectra. The inset shows the Lorentzian fit of the ZPH obtained at ν_{B2}. The hole depths in spectra b (at 682.4 nm) and c (at ~679.0 nm) are 7.1% and 3.5%, respectively.

3.4 Modeling of Optical Spectra

3.4.1 Calculated Absorption, Emission, and NRHB Spectra

The simultaneous fit of various optical spectra provides constraints on the pigment site energies (i.e., transition frequencies in the absence of inter-pigment coupling) that are critical to describe the excitonic structure and dynamics. Simulated absorption, emission, and NRHB spectra reported below are additionally constrained by the following inputs: 1) the vibrational frequencies and 2) the experimental shape of the phonon spectral density, $J(\omega)$, both obtained for CP29 complexes.[14] In simulations presented below the vibrational modes are dynamically localized,

although delocalization of vibrational modes leads only to small shifts of vibrational bands (data not shown). We also assume that the phonon spectral density (weighted phonon profile) can be described by a continuous function, which is chosen to be a lognormal distribution[44]

$$J_{ph}(\omega) = \frac{S_{ph}}{\omega\sigma\sqrt{2\pi}} e^{-\frac{\left[\ln\left(\frac{\omega}{\omega_c}\right)\right]^2}{2\sigma^2}} \tag{3.1}$$

where ω_c is the cutoff frequency, S_{ph} is the Huang-Rhys factor for phonons, σ is the standard deviation, and $J_{ph}(\omega \le 0) = 0$. For CP29 σ = 0.88 and ω_c = 65 cm^{-1}, while the Huang-Rhys factors (S_{ph}) were adjusted by simulations. The best fits were obtained with S_{ph} = 0.56 for all CP29 Chls, except Chl *a*604 for which a slightly smaller value of S_{ph} = 0.512 had to be used. To calculate the coupling matrix elements (V_{nm}) we use the 3PL9 structure of isolated CP29 with 13 Chls (nine Chls *a* and four Chls *b*).[18] V_{nm} parameters were calculated using the transition charge from electrostatic potential (TrEsp) or TrEsp-Poisson methodologies;[19] see Tables B.4 and B.5 in the Appendix B. Chls were placed in four domains defined in Figure 3.1.

As shown above the fluorescence origin bands and the main bleaches in the NRHB spectra showed an excitation wavelength dependence. These data clearly indicate the presence of a heterogeneous population of CP29 in our samples, which is also considered in the modeling studies described below. The calculations were performed for complexes containing either all 13 Chls or assuming that one or two pigments could be absent in reconstituted samples. Many different combinations were tested; however, the best simultaneous fits of absorption, emission, and HB spectra (*vide infra*) were obtained for 12.5 Chls, assuming that 50% of *b*614 (contributing to the 640 nm band) was lost in our preparations. Note that Chl *b*614 is located in the outmost region of CP29 and could be partly lost during reconstitution and purification procedures. That is, the simulated absorption spectra (dashed blue lines) shown in Figures 3.6 and 3.7 correspond to 9 Chl

a and 3.5 Chl *b* per complex. The black lines (spectra a-c) in Figures 3.6A and 3.7A are the experimental spectra.

Figure 3.6A shows the best simultaneous fits of absorption (a′), emission (b′), and NRHB (c′) spectra using the mixture model due to contributions from Sub. I and Sub. II defined above. In this case we fit simultaneously the 650.0 nm excited emission spectrum and HB spectrum obtained with λ_B = 651.2 nm. Frame 3.6B shows that Sub. I (a_1′ contribution) accounts for ~90% of the total absorption, while Sub. II (a_2′ contribution) accounts only for 10%. The experimental emission maximum obtained with 650.0 excitation (curve b in Figure 3.6A) is at 680.3 nm. Modeling studies also suggest (see Figure 3.6B) that this curve is contributed by two subpopulations, i.e., Sub. I (b_1′ ~63%) and Sub. II (b_2′~37%). Note that the percentages for emission and NRHB spectra can be different when compared to the absorption spectrum, as different subpopulations may have somewhat different fluorescence quantum yields and HB efficiencies, respectively. In fact, such behavior was observed experimentally for the FMO antenna in ref 51. Under these experimental conditions the NRHB spectrum obtained at λ_B = 651.2 nm, i.e., reflecting the EET from 650-Chls *b* to Chls *a* displays a main bleach near 680 nm assigned to the lowest energy state ***B***. Interestingly, λ_B = 651.2 NRHB spectrum is well described when considering exclusively a contribution from the dominant Sub. I, though a small contribution from Sub. II cannot be entirely excluded. On the other hand, contributions from both subpopulations are required to describe the absorption and emission spectra, suggesting that either ν_B = 15355 cm^{-1} excitation (λ_B = 651.2 nm) does not efficiently bleach the lowest exciton of the minor Sub. II and/or Sub. II has relatively larger fluorescence quantum yield and is clearly observed as b_2′contribution in frame B.

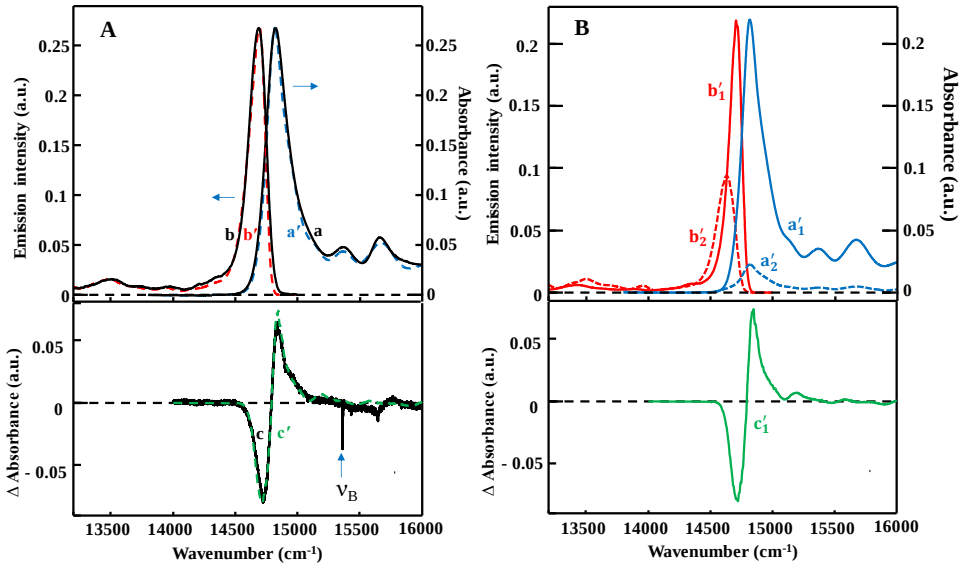

Figure 3.6 Black spectra a-c are the 5 K experimental absorption, emission (λ_{ex} = 650.0 nm), and NRHB (ν_B = 15355 cm^{-1}; λ_B = 651.2 nm) spectra, respectively, obtained for the reconstituted CP29. Blue (a′), red (b′), and green (c′) curves in frame (A) correspond to the calculated absorption, emission, and NRHB spectra, respectively, assuming 12.5 Chls per complex. NRHB spectrum (c) was obtained with low fluence. The calculated spectra in frame (A) represent the sum of contributions from Sub. I and Sub. II; the individual contributions to absorption (spectra a_1' and a_2'), emission (b_1' and b_2'), and NRHB (c_1') spectra are shown in frame (B). Note that NRHB spectrum obtained at these experimental conditions, in contrast to data shown in Figure 3.7B, is only contributed by c_1' of Sub. I. The best fit was obtained with S_{ph} = 0.56 for all Chls except of Chl *a*604 (S_{a604}= 0.512), $S_{vib\text{-}em}$ = 0.34, $S_{vib\text{-}abs}$ = 0.34.

The fit and the relative contribution to the absorption spectrum in Figure 3.7A is the same as that in Figure 3.6A. Figure 3.7A also shows the comparison of the simulated and experimental emission and NRHB spectra obtained for λ_B = 488.0, which were significantly red-shifted (see Figures 3.2 and 3.5) with respect to data obtained with λ_{ex} = 650.0 nm and λ_B = 651.2 nm shown in Figure 3.6A. Here, the emission peaks at 683.7 nm and the minima of the NRHB spectra obtained for f = 6 and 186 J/cm^2 are at 682.4 nm and 681.7 nm, respectively. Thus, at these experimental conditions different contributions from Sub. I and Sub. II are necessary to fit these spectra (Figure 3.7B). In this case, the red-shifted emission originates mostly from Sub. II (b'_2 ~90%), while Sub. I (b'_1) contributes only ~10% in agreement with experimental observations.

However, in contrast to λ_B = 651.2 nm burning, the λ_B = 488.0 nm excited NRHB spectrum obtained for f = 186 J/cm^2 is contributed to by both Sub. I (c'_1 ~ 40%) and Sub. II (c'_2 ~ 60%). Moreover, as shown in the inset of Figure 3.7B the NRHB obtained at f = 6 J/cm^2 (curve d), is only contributed by Sub. II (i.e., c'_2 ~100%). These data are in very good agreement with our simple deconvolution of NRHB spectra shown in the inset of Figure 3.4. Note that the major Sub. I (a'_1 contribution to the absorption spectrum) has much weaker contribution to the emission (b'_1) when excited at 488.0 nm, and a relatively smaller HB bleach, as illustrated by curve c'_1. Apparently, these two subpopulations have different compositions of the corresponding lowest energy states, different HB yields, and excitation-dependent energy transfer dynamics.

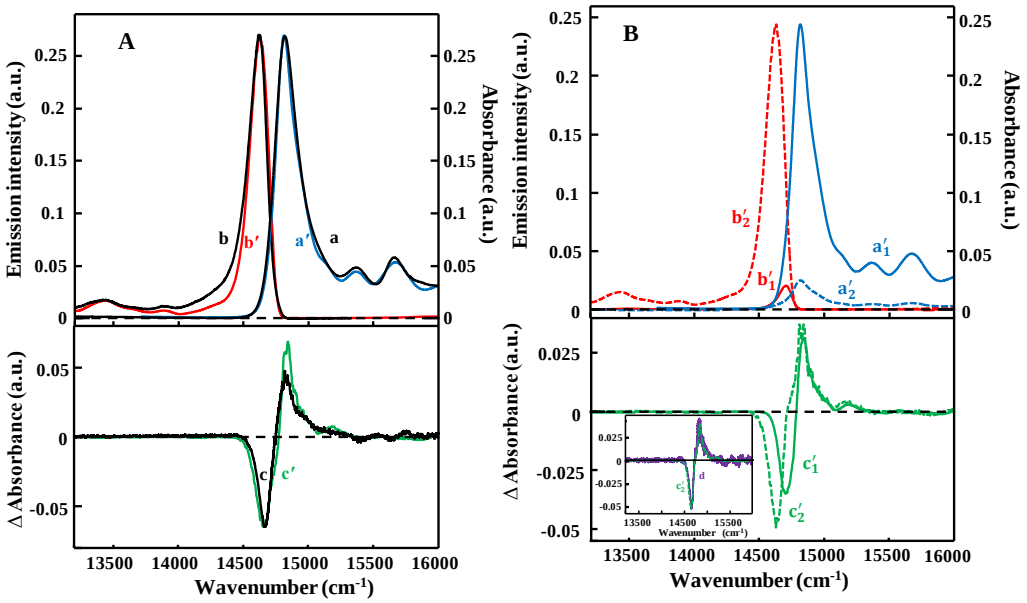

Figure 3.7 Spectra a, b, and c/d are the 5 K experimental absorption, emission (ν_{ex} = 20492 cm^{-1}; λ_{ex} = 488.0 nm), and NRHB (ν_B = 20492 cm^{-1}; λ_B = 488.0 nm) spectra, respectively. NRHB spectra c and d were obtained with f of 186 J/cm^2 and 6 J/cm^2, respectively. Blue, red, and green curves in panel (A) represent the calculated absorption (a′), emission (b′), and NRHB (c′) spectra, respectively. Panel (B) shows the relative contributions to the total absorption/emission/HB spectra from Sub. I (i.e., $a_1'/b_1'/c_1'$) and Sub. II (i.e., $a_2'/b_2'/c_2'$). The inset in frame (B) shows experimental NRHB for f = 6 J/cm^2 and its c_2' fit corresponding to Sub. II.

Thus, the spectral simulations point toward the presence of a major Sub. I associated with a low-E trap identified with state ***B***, and a minor Sub. II with a trap at lower energy assigned to state ***A***. These energy traps are characterized by different NRHB quantum yields and shifted (0,0)-bands of the corresponding fluorescence spectra. Moreover, the difference between the calculated emission spectra shown in Figures 3.6A and 3.7A in the spectral region of 14000-14500 cm^{-1} suggests that Chls contributing to the lowest energy states ***A*** and ***B*** may have different Huang-Rhys factors of the low-frequency vibrations.

3.4.2 Pigment Site Energies

Table 3.1 summarizes the parameters used to simulate the spectra shown in Figures 3.6 and 3.7. Pigment site energies (E_0^n) and inhomogeneous broadenings (Γ_{inh}) are given in cm^{-1}. The E_0^n values are compared to those obtained by Müh et al.[19] who used a value of Γ_{inh} = 130 cm^{-1} for all Chls. The differences in site-energies and Γ_{inh} originate in part from different shapes of experimental absorption and emission spectra obtained for the reconstituted CP29 at T = 5 K which require considering a mixture model as discussed in the previous paragraphs. In addition, in the present calculations the experimental $J_{ph}(\omega)$ previously obtained for CP29 complex[14] was utilized. On the other hand, Müh et al. when fitting native (isolated) CP29, employed the often used $J_{ph}(\omega)$ extracted from the 1.6 K FLN spectra of B777 complexes[34] (see figure B.2; left frame in the Appendix B). It is worth noticing, however, that the simulations shown in Figures 3.6 and 3.7 are in much closer agreement with the experimental data than those reported previously in ref 19. We hasten to add that only the parameters obtained for the major Sub. I should be directly compared with those of native (isolated) CP29 reported in refs 19 and 30, as Sub. II most likely originates from imperfect *in vitro* reconstitution of CP29 (*vide infra*).

Table 3.1 Parameters used to simulate the absorption, emission, and NRHB spectra for the reconstituted CP29 using a mixture model.[a]

	This Work (reconstituted CP29)		From ref 19[b] (native) isolated CP29
Chl#	E_0^n	Γ_{inh}	E_0^n
***a*602**	14920	207	14980
***a*603**	15055	207	14900
***a*604**	14817/14690	157	14810
***b*606**	15685	203	15684
***b*607**	15398	207	15439
***b*608**	15387	207	15439
***a*609**	14951	176	14980
***a*610**	14945	202	14920
***a*611**	14953	207	14850
***a*612**	14955	207	14900
***a*613**	14945	207	14880
***b*614**	15676	207	15674
***a*615[c]**	14965	207	14940

[a]The first column labels the nine Chl *a* (in black) and four Chl *b* (in blue), in accordance to the 3PL9 pdb file. The E_0^n values of the lowest energy pigment are in red. The only difference between Sub. I and Sub. II is the site energy of Chl *a*604, *i.e.* 14817 and 14690 cm^{-1}, respectively. The values of E_0^n and Γ_{inh} are given in cm^{-1}. We used TrEsp coupling constants (V_{nm}) reported in Table B.5 of the Appendix B. [b]In ref 19 Γ_{inh} = 130 cm^{-1} was used for all Chls. [C] In the $C_2S_2M_2$ supercomplex structure *a*615 most likely corresponds to Chl *a*601 reported in ref 28. In this work, effective dipole strengths of 21 D^2 and 13 D^2 are used for Chl *a* and Chl *b* molecules, respectively.

3.4.3 On the Occupation of Chl *b*614 Site

Because literature reports regarding the number of Chls in the reconstituted CP29 are controversial, it is important to discuss the number of Chl pigments in our samples. As mentioned above, the simulations were performed considering 11-13 Chls per complex. Spectra were calculated for various combinations of lost pigments. The best fits were obtained assuming 12.5 Chls per complex, i.e. when 50% of Chl *b*614 was removed from the structure or was assigned zero oscillator strength; both cases are equivalent to depletion of this pigment. The spectra for 12.5

Chls were calculated taking the average of spectra calculated for 13 and 12 Chls. This is illustrated in Figure 3.8, which shows the Chl *b* Q_y absorption region of calculated spectra considering either 13 (curve a, blue) or 12 (with deleted *b*614; curve b, red) Chls, respectively. It is worth noting both the large difference in absorption in the 640 nm region between spectra a and b, highlighting the contribution of Chl *b*614 in this spectral window, and the fact that neither of these two spectra matches the experimental curve (dashed green, d). However, the mixture model (curve c, purple) that considers equally weighted 13 and 12 Chls samples describes the experimental data very well. Thus, the best fit is obtained assuming Chl *b*614, whose fitted site energy is 15676 cm^{-1} (638 nm), has only 50% occupation (compare spectra c and d). Indeed, spectrum e = c – b (pink line) corresponds to ~50% of oscillator strength assigned to Chl *b*614 supporting our analysis. Therefore, it can be concluded that the reconstituted complexes used in this study have on average 12.5 Chls per complex, corresponding to full occupancy of Chls *a* and of most of the Chl *b* sites. This is consistent with ref 19 for native CP29 complexes, where the authors suggested that up to one Chl *b* (*b*614) could be lost in the isolated (native) CP29 complex.[26] Interestingly, curve b is very similar to the experimental absorption spectrum of mutant B3 (thick dashed gray line) that lacks Chl *b*614, supporting our analysis.[22,23] Detailed analysis of CP29 mutants is in progress and beyond the scope of this article.

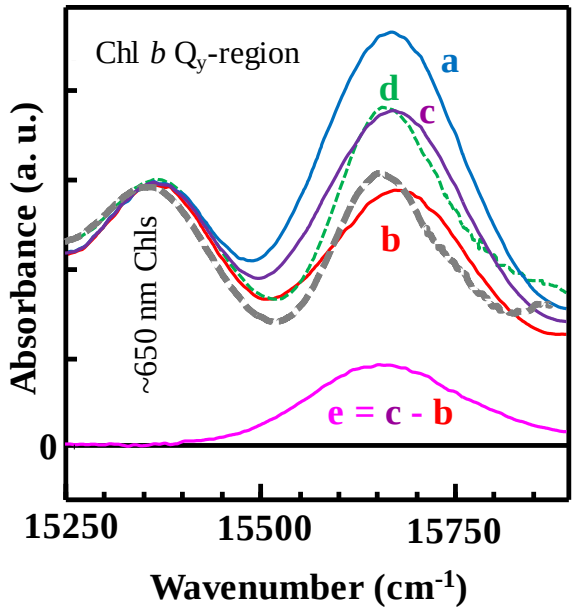

Figure 3.8 Curves a (blue) and b (red) are the calculated absorption spectra for a mixture model in the Chl *b* Q_y-region for 13 and 12 Chls (no *b*614), respectively. Curve c (purple) is the calculated absorption for 12.5 Chls, i.e., assuming 50% of Chl *b*614 is lost. Curve d (dashed green) is the experimental absorption spectrum in the Chl *b* region from Figure 3.2 (curve a). The pink curve (e) shows the difference between spectra c and b. The thick (dashed) gray spectrum is the absorption of the B3 mutant, which does not contain Chl *b*614. The curves (a-d) are normalized to the contribution of the so-called 650 nm Chls *b*.

3.4.4. On the Site Energy of *a*604 Chl

The calculated site energies of Chl *a*604 in ref 19 using CDC/PBQC are 14816/14827 cm^{-1}. Subsequently, the optimized site energy of the same Chl (by fitting experimental spectra obtained for native CP29 in ref 26) was reported as 14810 cm^{-1} (675.2 nm). These energies are in very good agreement with the site energy of *a*604, 14817 cm^{-1} (674.9 nm), assigned in this work to the major (90%) Sub. I (see Table 3.1). Interestingly, Müh et al.[19] suggested that the site energy of Chl *a*604, which is spatially close to Neo, can be influenced by the positioning of the hydroxyl groups of both the nearby residue tyrosine 135 (Y135) and the Neo molecule itself. Simulations of the Y135F mutant constructed *in silico* (where Y135 is replaced with phenylalanine) indicated that the site energy of Chl *a*604 was red-shifted by 76 cm^{-1} with respect to the native WT CP29

when the interactions with this residue were altered. The Y135F mutation has been engineered and experimentally investigated in reconstituted CP29 by Caffarri and coworkers.[27] Müh et al. showed that the 76 cm^{-1} shift predicted from the *in silico* computation was in very good agreement with the experimental data of the reconstituted Y135F mutant. Likewise, when using the site energies necessary to describe the major Sub. I (see Table 3.1) in the present study, and by considering a similar red-shift of 83 cm^{-1} for Chl *a*604 (as an effect of the Y to F substitution), we can also simulate the 300 K absorbance difference (ΔOD) spectra of reconstituted (recombinant) WT CP29 and Y135F mutant reported by Caffarri *et al.*[27] This is illustrated in Figure 3.9 where the dashed (green) and solid (red) lines correspond to the experimental[27] and simulated (this work) ΔOD spectra.

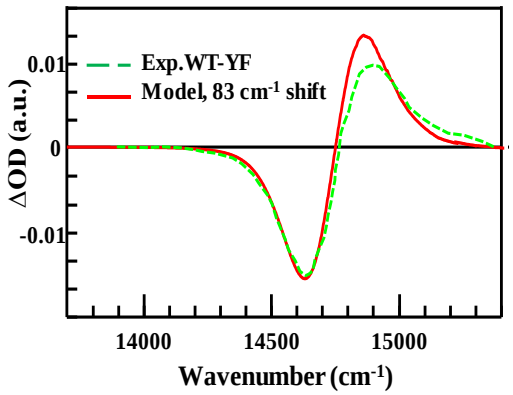

Figure 3.9 Absorbance difference (ΔOD) between the reconstituted WT CP29 and its Y135F mutant. Dashed and solid lines correspond to the experimental[27] and our simulated (using TrEsp coupling constants) ΔOD spectra, respectively.

The solid (red) line in Figure 3.9 was obtained considering the site energies of Sub. I (see Table 3.1). The agreement with experiment is very good, proving that site energy of *a*604 in the majority of CP29 complexes (in both native WT and reconstituted WT CP29 complexes) must be near 14817 cm^{-1} (674.9 nm). However, we believe that the red-shifted Chl *a*604 (observed in Sub. II at 14690 cm^{-1}) *should not* be observed in the native CP29. Therefore, our experimental and

modeling results suggest that Chl *a*604 is the energy sink only in Sub. II (see Figure 3.11 for details) which is clearly observed in a fraction (~10%) of complexes, most likely resulting from imperfect refolding during protein reconstitution, leading to a situation mimicking that encountered in the Y135F mutant.

3.5 Discussion

As shown above by our simulated optical spectra, reconstituted WT CP29 complexes most likely contain about 12.5 Chls, in close agreement with the X-ray structure assignment[18] and the pigment analysis discussed in the Appendix B. These findings are also consistent with previous modeling studies of native (isolated) CP29, which also reported about 12 Chls per complex,[19,30] although significant differences in Chl site energies were obtained from spectral modeling. To model the shape of the absorption spectrum, excitation-dependent emission and NRHB spectra, we had to assume that our sample possesses two spectroscopically distinguishable subpopulations with different site energies of Chl *a*604 and two different low-E exciton states ***B*** (Sub. I) and ***A*** (Sub. II), leading to a composite emission spectrum. Below, we discuss the origin of both subpopulations, as well as the corresponding exciton states and their pigment contributions. Dynamics is examined via resonant HB spectra in the context of EET pathways. The binding configuration of Neo and its influence on the local protein environment as well as its possible impact on the excitonic structure is also briefly addressed.

3.5.1 Structural Differences of CP29 X-ray Structures

Here, we briefly discuss small differences between available CP29 structural models. One could argue that we should also consider the 3.2 Å CP29 structure observed within the PSII-LHCII supercomplex (PDB ID: 3JUC[29]) with 10 Chls *a* and 3 Chls *b* (where Chl *b*614 was believed to be lost during purification), and/or the very recent 2.7-3.2 Å CP29 structure observed within the

$C_2S_2M_2$ supercomplex (PDB IDs: 5XNM/5XNL).[28] The latter appears to contain 14 Chls (10 Chls *a* and 4 Chls *b*) with a full occupation of the *b*614 site and one additional Chl *a* (see Figure B.7 in the Appendix B) That is, the most recent CP29 structure revealed[28] an additional Chl *a* (*a*616) located externally at the N-terminal region in the $C_2S_2M_2$ supercomplex. However, it is unlikely that the reconstituted WT CP29 will contain this pigment, since *a*616 is located at the interfacial region between CP29 and CP47 and is coordinated by the main chain oxygen of the F80 residue at the N-terminal loop of CP29; see Figure B.8 in Appendix B. Therefore, if CP29 is purified without CP47 for stabilization, the long N-terminal loop of CP29 might be flexible and *a*616 will most likely be lost. It is moreover worth noting that the *a*601 pigment observed in the $C_2S_2M_2$ supercomplex[28] is most likely the Chl *a*615 already observed in 3PL9 structure. Although CP29 seems then to be binding 14 Chls, 10 Chls *a* and 4 Chls *b* (see Table B.8 in the Appendix B) in an intact environment, its unperturbed excitonic structure could only be modeled within the entire supercomplex, which is, in any case, a very difficult proposition. Therefore, we opted to model the optical spectra of the reconstituted complex using the high resolution (2.8 Å) structure of isolated CP29 (PDB ID: 3PL9).

3.5.2 On the Origin of Two Subpopulations and the Nature of the Lowest Energy Emitting States

The spectra of reconstituted CP29 complexes are contributed to by two subpopulations (each with 12.5 Chls), i.e., Sub. I (90%) and Sub. II (10%), each with different spectral characteristics. The difference between Sub. I and Sub. II is the site energy of Chl *a*604, i.e., 14817 and 14690 cm^{-1}, respectively (Table 3.1). The presence of two subpopulations having two different site energies of Chl *a*604 is likely caused by a different orientation of the Neo molecule in a small fraction of the reconstituted sample, and/or a small fraction of reconstituted complexes without

Neo. In both cases, the H-bond between Neo and Y135 could be broken, thereby impacting the site energy of *a*604. Namely, according to calculations reported in ref 19, although Neo does not significantly affect the site energy of Chl *a*604, its hydroxyl group forms a H-bond with the hydroxyl group of the adjacent Y135 residue. Thus, the H-bond network of two hydroxyl groups can assume two different orientations relative to the tetrapyrrole macrocycle of Chl *a*604. The latter, as shown in refs 16 and 19 leads to two energetic conformations, giving rise to either a blue- or a red-shifted energy transition, as illustrated schematically in Figure 3.10, top. In the blue-conformation, the 3´-hydroxyl group of Neo points towards the tetrapyrrole macrocycle of Chl *a*604 and accepts the H-bond from Y135. This, in turn, based on calculations for the Y135F mutant[19] shifts the site energy of Chl *a*604 to the blue by 76 cm^{-1}. The less stable conformation (see top left structure in Figure 3.10) in which the 3´-hydroxyl group of Neo points away from the Chl macrocycle (and donates a H-bond to Y135) is characterized by an additional red-shift of 136 cm^{-1} of the site energy of Chl *a*604 when compared to the Y135F mutant.[16,19]

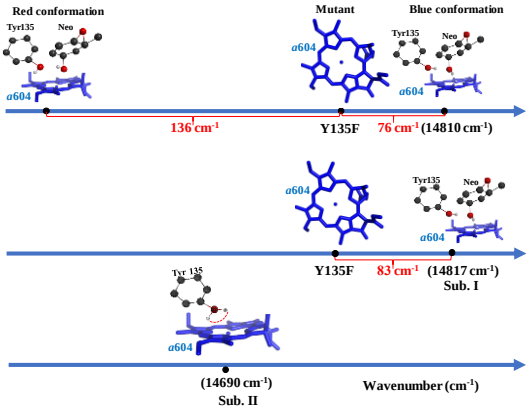

Figure 3.10 Schematic representation of site energy shifts of Chl *a*604 for the red-shifted conformation, mutant Y135F, and blue-conformation (see top panel) based on refs 16 and 19. The lower two panels illustrate site energy shifts observed for Sub. II, mutant Y135F, and Sub. I based on data reported in this manuscript. It is indicated that there are two subpopulations regarding the different orientation of Neo molecule (or losing Neo molecule during purification procedures) in the small fraction of the sample.

We propose that in the majority (90%) of reconstituted complexes *a*604 is in the more stable blue-conformation (Sub. I) in which Neo accepts the H-bond from Y135, leading to the 83 cm^{-1} blue-shift of its site energy with respect to the Y135F mutant (Figure 3.10, middle panel). In turn, the remaining fraction of complexes (10%) does not have such H-bond since the hydroxyl group of Y135 in this subpopulation may assume various orientations relative to the tetrapyrrole macrocycle of Chl *a*604 leading to an additional red-shift of *a*604 (in Sub. II) in agreement with the experiments. That is, in Sub. II (near Chl *a*604) there is no H-bond between Tyr135 and Neo, and, as a result, it is reasonable to assume that Y135 may adopt varying orientations of its OH-group (Figure 3.10, bottom panel). Based on our data, this should lead to a 127 cm^{-1} red-shift of the *a*604 site energy (now at 14690 cm^{-1}) compared to that in Sub. I. As mentioned above, this conformational state is probably the result of some imperfect refolding of CP29 *in vitro*, and it is, therefore, unlikely to occur in native CP29 complexes. It nonetheless highlights how small reconfigurations within even a single chromophore binding site can serve in tuning the overall energy landscape of the complex.

The excitonic structure and composition of the lowest energy exciton states is shown in Figure B.6 in the Appendix B. The exciton energy level diagram is presented in Figure 3.11, where the differences in the exciton state energies (ε_M) of the Chls which are part of the stromal- and luminal-layer are shown separately. Further detail on the exciton energies (in cm^{-1}/nm) obtained here from the modeling of reconstituted CP29 optical spectra are summarized in Table B.3 (Appendix B) where they are compared to those obtained for native (isolated) WT CP29 by Müh et al.[19] The thick black and red bars in Figure 3.11 indicate the lowest exciton states of Sub. I ($\varepsilon_{1,\text{Sub. I}}$) and Sub. II ($\varepsilon_{1,\text{Sub.II}}$) are at 677.7 and 681.5 nm, respectively (for more details see Tables B.2 and B.3 in Appendix B). Brackets connect exciton states that are significantly delocalized over

several pigments. Recall that the $\varepsilon_{1,\text{Sub.I}}$ state (assigned above to state ***B***) is mostly contributed to by Chls *a*611(28%), *a*615 (19%), *a*612 (16%), and *a*602 (16%) whereas state $\varepsilon_{1,\text{Sub.II}}$ (assigned to state ***A***) is mostly contributed by *a*604 (~98%). The 2nd lowest energy state of the major Sub. I (also mostly contributed by *a*604 (98%)) shifts in Sub. II from 14808 cm^{-1} (675.3) to 14673 cm^{-1} (681.5 nm) due to a red-shift (127 cm^{-1}) of the site energy of Chl *a*604, as already discussed above. Thus, whereas the first exciton in Sub. I is delocalized over several Chls (delocalization length ~3), the second exciton in this subpopulation is localized on *a*604. In contrast, the first exciton in Sub. II is localized on *a*604, while the second exciton state is delocalized over three Chls (see Table B.4 in the Appendix B).

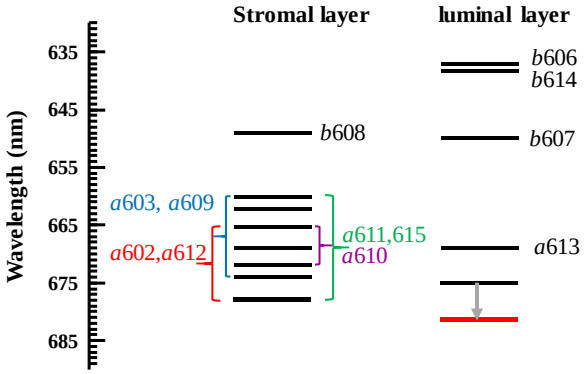

Figure 3.11 Exciton energy level diagram for the reconstituted CP29 complex at 5 K. The thick black and red bars indicate the lowest exciton states (eigenvalues) of Sub. I ($\varepsilon_{1,\text{Sub. I}}$) and Sub. II ($\varepsilon_{1,\text{Sub.II}}$) at 677.7 and 681.5 nm, respectively. The 2nd lowest energy state of the major Sub. I at 14808 cm^{-1} (675.3) nm (mostly contributed by *a*604; ~98%) shifts in Sub. II to 14673 cm^{-1} (681.5 nm) due to a red-shift (127 cm^{-1}) of the site energy of Chl *a*604.

Moreover, *a*613, *a*604 and all Chls *b* mostly contribute to individual exciton states, as indicated by the corresponding Chl numbers.

Finally, we note that based on *ab initio* calculations and the description of the optical spectra of the CP29 antenna complex it was suggested that the lowest energy state might be delocalized over pigments *a*609, *a*603, and *a*602 (stromal side of the membrane).[33] According to

this model, the main contribution to the lowest excitonic state arose from *a*609, whereas the next exciton state was suggested to be dominated by the *a*611-*a*612 dimer.[33] This scenario, however, is inconsistent with our modeling data (not shown) and the steady-state absorption spectra obtained for the A5 (*a*603) and B5 (*a*609) mutants; that is, the differences in the Q_y-region absorptions due to the lack of *a*603 and *a*609 pigments are not in the reddest part of the corresponding absorption spectra (see the Supporting Information in ref 52). These authors also suggested that *a*603 and *a*609 pigments did not significantly contribute to the lowest energy exciton. Nevertheless, more work is needed for various CP29 mutants to further refine possible pigment site energies. Data presented in this work obtained for the reconstituted WT CP29 complexes are crucial for proper analysis of various mutants; the latter, however, is beyond the scope of this work.

3.5.3 On the Nonresonant Bleach in the Q_y-Region of Chls *b* and Their Site Energies

Chls *b* are mostly localized and contribute to the ~650 and ~640 nm bands (Figures B.6 and 3.11). These assignments of Chls *b* exciton states are in close agreement with those of ref 19, although the site energies of *b*607 and *b*608 are red-shifted by ~40 and ~50 cm^{-1}, respectively. Site energies of Chls *b*606 and *b*614 are instead the same as in ref 19; see Table 3.1 for details. However, the above two assignments are different from those suggested by two-dimensional electronic spectroscopy,[53] where the authors used the angles between the transition dipole moments to determine the site energies. Their approach suggested that Chls *b*606 and *b*607 contribute to the 640 nm band. This assignment is, however, not consistent with the absorption spectra of the B3 mutant that lacks Chl *b*614, which clearly indicates that this pigment must contribute to the so-called 640 nm band (see Figure 3.8). Finally, recall that the NRHB spectrum in Figure 3.2 shows weak bleaches near Chls *b* absorption regions, i.e., at 638.8 nm and 649.2 nm. These can be interpreted in terms of excitonic responses due to the bleach of the lowest energy

state(s), as suggested in ref 49. However, it is more likely that such small changes could be induced by protein conformational rearrangements associated with the chromophore burning process. This is in line with our modeling results that did not reveal any excitonic response near Chl *b* absorption bands (see Figures 3.6 and 3.7), as the coupling between Chls *a* and Chls *b* is very small (see Table B.5). Besides, we have shown that in native spinach CP29[30] the depths of the ~640 and ~650 nm holes and their ratio to the lowest energy bleach near 680 nm, as a function of *f*, was not correlated, excluding the above mentioned excitonic response.

3.5.4 Excitation Energy Transfer Times

Resonant holes, as indicated by the main bleach of state ***B***, clearly suggest that the observed EET times characterize the major subpopulation of complexes (Sub. I) that might be compared to the native CP29 protein. The *fwhm* of the ZPHs obtained at ν_{B2}, ν_{B3}, and ν_{B4} are 8.0, 4.8 and 4.5 cm^{-1}, respectively. The inset in Figure 3.4 shows that the Lorentzian fit of the ZPH burned at ν_{B2} correspond to a *fwhm* of 8.0 cm^{-1}, which after spectral correction reduces to 7.5 cm^{-1}. Using Γ_{hom} (cm^{-1}) $\approx 1/2\pi c\tau_{EET}$, where *c* is the speed of light and Γ_{hom} is the homogeneous linewidth (where $\Gamma_{hom} = ½\ \Gamma_{ZPH}$), it can be estimated that the *average* EET time (τ_{EET}) from Chl *b* molecules (absorbing near 640 nm) to the lowest energy traps located near 679 nm is 1.4 ± 0.1 ps. The τ_{EET} from Chls *a* (absorbing near 670 nm, ν_{B4}) and Chls *b* (absorbing near 650 nm, ν_{B3}) to the lowest energy trap mentioned above, corrected for spectral resolution of 2 cm^{-1} and based on the Lorentzian fits (see Figure B.3 in the Appendix B), are 3 ± 0.5 and 2.7 ± 0.5 ps, respectively. EET from Chls *b* bands to the Chls *a* band was also measured in CP29 by 2DES.[53] Both of these transfer processes at room temperature occurred within 3.6 ps, in reasonable agreement with our HB data. The depopulation of the excited state of the two Chls *b* absorbing near 650 nm was previously reported to be 4.0 ± 0.7 ps[30] in spinach CP29. Comparable value of 4.2 ± 0.3 ps was also observed

at 5 K in ref 49. These figures are consistent with EET obtained here for the reconstituted CP29 complex. However, a somewhat smaller lifetime of 2.2 ± 0.5 ps was observed in CP29 for the "red" Chls *b* (absorption around 650 nm) at 77 K in ref 54 that is even closer in agreement with the present results.

3.6 Concluding Remarks

Pigment analysis of reconstituted complexes, in agreement with theoretical modeling of various low-temperature optical spectra, suggests that, on average, reconstituted CP29 complexes contain 9 Chls *a* and 3.5 Chls *b*. It is shown that most likely ~50% of Chl *b*614 is lost during the reconstitution and purification procedures. Thus, although remarkably similar to the native form, reconstituted CP29 shows some subtle differences and purification protocols might have to be optimized to eliminate Chl(s) losses and to closely match the native form of the complex. Irrespective of this, the previously discussed models based on the presence of only 8 Chls in reconstituted CP29 are incapable of describing the experimental results and should be therefore discarded. The simultaneous fit of absorption, fluorescence and NRHB spectra at 5 K, employing models based on the available X-ray structure and a density matrix approach, provide new insight into the excitonic structure of the reconstituted CP29 complex that revealed its heterogeneous nature. The spectra are best modeled assuming two subpopulations characterized by different site energies of the *a*604 Chl *a* and, as a result, by two different low-E traps. Depending on the laser excitation frequency, reconstituted complexes exhibit two low-E traps (states ***A*** and ***B***) with different hole-burning characteristics and excitation dependent emission spectra. State ***A*** near 682.4 nm is assigned to the minor Sub. II that most likely originates from imperfectly reconstituted proteins. This state is easily burned (with λ_B = 488.0 nm via $S_0 \rightarrow S_2$ transition of the carotenoids at T = 5 K) and appears to be localized on Chl *a*604 which is responsible for the observed red-

shifted emission near 683.7 nm. Prolonged bleaching by 488.0 nm or excitation at 650.2 nm reveals a second low energy trap (state ***B***) near 680.2 nm having a fluorescence origin-band near 681 nm. The latter state has a lower HB quantum yield and corresponds to the lowest energy trap ***B*** of the major Sub. I. This state is mainly delocalized over the *a*611, *a*612, *a*615 trimer in agreement with the literature data obtained for native (spinach) CP29[19,30] although with some differences in the pigment site energies. However, the presence of the minor Sub. II is probably the result of some imperfect refolding of CP29 *in vitro*, and it is, therefore, unlikely to occur in native complexes, as suggested in ref 19. We anticipate then, that the site energies obtained in this study (Table 3.1) should be further tested to describe time-domain and temperature-dependent data of reconstituted CP29 complexes, to further narrow the possible choices of parameters.

ACKNOWLEDGEMENTS

This work was supported by the Chemical Sciences, Geosciences and Biosciences Division, Office of Basic Energy Sciences, Office of Science, U.S. Department of Energy (Grants No. DE-SC0006678 to R.J.). We acknowledge Drs Adam Kell and Tonu Reinot for their contributions at the early stage of this work and useful discussions. A.P.C. and S.S. acknowledge the assistance of Dr. William Remelli during the HPLC analysis.

References

(1) Jansson, S. A Guide to the *Lhc* Genes and Their Relatives in *Arabidopsis. Trends Plant Sci*. 1999, *4*, 236−240.

(2) Kouřil, R.; Dekker, J. P.; Boekema, E. J. Supramolecular Organization of Photosystem II in Green Plants. *Biochim. Biophys. Acta.* **2012**, *1817*, 2-12.

(3) Caffarri, S.; Kouřil, R.; Kereïche, S.; Boekema, E. J.; Croce, R. Functional Architecture of Higher Plant Photosystem II Supercomplexes. *The EMBO Journal* **2009**, *28*, 3052–3063.

(4) Liu, Z.; Yan, H.; Wang, K.; Kuang, T.; Zhang, J.; Gui, L.; An, X.; Chang, W. Crystal Structure of Spinach Major Light-Harvesting Complex at 2.72 Å Resolution. *Nature* **2004**, *428*, 287−292.

(5) Standfuss, R.; Terwisscha van Scheltinga, A. C.; Lamborghini, M.; Kühlbrandt, W. Mechanisms of Photoprotection and Nonphotochemical Quenching in Pea Light-Harvesting Complex at 2.5 Å Resolution. *The EMBO Journal* **2005**, *24*, 919−928.

(6) Dainese, P.; Bassi, R. Subunit Stoichiometry of the Chloroplast Photosystem-II Antenna System and Aggregation State of the Component Chlorophyll-a/b Binding Proteins. *J. Biol. Chem.* **1991**, *266*, 8136–8142.

(7) Peter, G. F.; Thornber, J. P. Biochemical Composition and Organization of Higher Plant Photosystem-II Light Harvesting Pigment-Proteins. *J. Biol. Chem.* **1991**, *266*, 16745–16754.

(8) Green, B. R.; Durnford, D. G. The Chlorophyll-Carotenoid Proteins of Oxygenic Photosynthesis. *Annu. Rev. Plant Physiol. Plant Mol. Biol.* **1996**, *47*, 685–714.

(9) Bassi, R.; Rigoni, F.; Giacommeti, G. M. Chlorophyll-Binding Proteins with Antenna Function in Higher Plants and Green Algae. *Photochem. Photobiol.* **1990**, *52*, 1187–1206.

(10) Jansson, S.; Pichersky, E.; Bassi, R.; Green, B. R.; Ikeuchi, M.; Melis, A.; Simpson, D. J.; Spangfort, M.; Staehelin, L. A.; Thornber, J. P. A Nomenclature for the Genes Encoding the Chlorophyll a/b-Binding Proteins of Higher Plants. *Plant Mol. Biol. Rep*. **1992**, *10*, 242-253.

(11) Rigoni, F.; Barbato, R.; Friso, G.; Giacometti, G. M. Evidence for Direct Interaction Between Chlorophyll Proteins CP29 and CP47 in Photosystem II, *Biochem. Biophys. Res. Comm.* **1992**, *184*,1094-1100.

(12) Yakushevska, A. E.; Keegstra, W.; Boekema, E. J.; Dekker, J. P.; Andersson, J.; Jansson, S.; Ruban, A. V.; Horton, P. The Structure of Photosystem II in *Arabidopsis*: Localization of the CP26 and CP29 Antenna Complexes. *Biochemistry* **2003**, *42*, 608-613.

(13) Marin, A.; Passarini, F.; Croce, R.; van Grondelle, R. Energy Transfer Pathways in the CP24 and CP26 Antenna Complexes of Higher Plant Photosystem II: A Comparative Study. *Biophysical Journal* **2010**, *99*, 4056–4065.

(14) Rätsep, M.; Pieper, J.; Irrgang, K. D.; Freiberg, A. Excitation Wavelength-Dependent Electron-Phonon and Electron-Vibrational Coupling in the CP29 Antenna Complex of Green Plants. *J. Phys. Chem. B* **2008,** *112*, 110-118.

(15) Reppert, M.; Zazubovich, V.; Dang, N. C.; Seibert, M.; Jankowiak, R. Low-Energy Chlorophyll States in the CP43 Antenna Protein Complex: Simulation of Various Optical Spectra. II. *J. Phys. Chem. B* **2008,** *112*, 9934–9947.

(16) Müh, F.; Madjet, M. E.-A.; Renger, T. Structure-Based Identification of Energy Sinks in Plant Light-Harvesting Complex II. *J. Phys. Chem B* **2010**, *114*, 13517-13535.

(17) Jassas, M.; Reinot, T.; Kell, A.; Jankowiak, R. Toward an Understanding of the Excitonic Structure of the CP47 Antenna Protein Complex of Photosystem II Revealed via Circularly Polarized Luminescence. *J. Phys. Chem. B* **2017**, *121*, 4364−4378.

(18) Pan, X.; Li, M.; Wan, T.; Wang, L.; Jia, C.; Hou, Z.; Zhao, X.; Zhang, J.; Chang, W. Structural Insights into Energy Regulation of Light-harvesting Complex CP29 from Spinach. *Nat. Struct. Mol. Biol.* **2011**, *18*, 309-315.

(19) Müh, F.; Lindorfer, D.; Schmidt am Busch, M.; Renger, T. Towards a Structure-Based Exciton Hamiltonian for the CP29 Antenna of Photosystem II. *Phys. Chem. Chem. Phys*. **2014**, *16*, 11848-11863.

(20) Jennings, R.C.; Bassi, R.; Zucchelli, G. Antenna Structure and Energy Transfer in Higher Plant Photosystems. *Top. Curr. Chem*. **1996**, *177*, 147-181.

(21) Giuffra, E.; Cugini, D.; Croce, R.; Bassi, R. Reconstitution and Pigment-Binding Properties of Recombinant CP29, *European Journal of Biochemistry* **1996**, *238*, 112-120.

(22) Belgio, E.; Casazza, A.P.; Zucchelli, G.; Garlaschi, F.M.; Jennings, R.C. Band Shape Heterogeneity of the Low Energy Chlorophylls of CP29: Absence of Mixed Binding Sites and Excitonic Interactions, *Biochemistry* **2010,** *49*, 882-892.

(23) Bassi, R.; Croce, R.; Cugini, D.; and Sandona, D. Mutational Analysis of a Higher Plant Antenna Protein Provides Identification of Chromophores bound into multiple sites. *Proc. Natl. Acad. Sci. U.S.A.* **1999,** *96*, 10056–10061.

(24) Giuffra, E.; Zucchelli, G.; Sandonà, D.; Croce, R.; Cugini, D.; Garlaschi, F. M.; Bassi, R.; Jennings, R. C. Analysis of Some Optical Properties of a Native and Reconstituted Photosystem II Antenna Complex, CP29: Pigment Binding Sites Can be Occupied by Chlorophyll a or Chlorophyll b and Determine Spectral Forms. *Biochemistry* **1997**, *36*, 12984-12993.

(25) Henrysson, T.; Schröder, W. P.; Spangfort, M.; Kerlund, H.-E. Isolation and Characterisation of the Chlorophyll a/b Protein Complex CP29 From Spinach. *BBA- Bioenergetics* **1989**, *977*, 301-308.

(26) Pascal, A.; Gradinaru, C.; Wacker, U.; Peterman, E.; Calkoen, F.; Irrgang, K.-D.; Horton, P.; Renger, G.; van Grondelle, R.; Robert, B; et al. Spectroscopic Characterization of the Spinach Lhcb4 Protein (CP29), a Minor Light-Harvesting Complex of Photosystem II. *Eur. J. Biochem.* **1999**, *262*, 817-823.

(27) Caffarri, S.; Passarini, F.; Bassi, R.; Croce, R. A Specific Binding Site for Neoxanthin in the Monomeric Antenna Proteins CP26 and CP29 of Photosystem II. *FEBS Lett.* **2007**, *581*, 4704-4710.

(28) Su, X.; Ma, J.; Wei, X.; Cao, P.; Zhu, D.; Chang, W.; Liu, Z.; Zhang, X.; Li, M. Structure and Assembly Mechanism of Plant C2S2M2-Type PSII-LHCII Supercomplex. *Science* **2017**, *357*, 815–820.

(29)Wei, X.; Su, X.; Cao, P.; Liu, X.; Chang, W.; Li, M.; Zhang, X.; Liu, Z. Structure of Spinach Photosystem II−LHCII Supercomplex at 3.2 Å Resolution. *Nature* **2016**, *534*, 69−74.

(30) Feng, X.; Pan, X.; Li, M.; Pieper, J.; Chang, W.; Jankowiak, R. Spectroscopic Study of the Light-Harvesting CP29 Antenna Complex of Photosystem II-Part I. *J. Phys. Chem. B* **2013**, *117*, 6585−6592.

(31) Cinque, G.; Croce, R.; Holzwarth, A.; Bassi, R. Energy Transfer Among CP29 Chlorophylls: Calculated Förster Rates and Experimental Transient Absorption at Room Temperature. *Biophys J.* **2000**. *79*, 1706-1717.

(32) Novoderezhkin, V. I.; Palacios, M. A.; van Amerongen, H.; van Grondelle R. Excitation Dynamics in the LHCII Complex of Higher Plants: Modeling Based on the 2.72 Å Crystal Structure. *J. Phys. Chem. B* **2005**, *109*, 10493-10504.

(33) Jurinovich, S.; Viani, L.; Prandi, I. G.; Renger, T.; Mennucci, B. Towards an ab Initio Description of the Optical Spectra of Light-Harvesting Antenna: Application to the CP29 Complex of Photosystem II. *Phys. Chem. Chem. Phys.* **2015**, *17*,14405-14416.

(34) Renger, T.; Marcus, R. A. On the Relation of Protein Dynamics and Exciton Relaxation in Pigment-Protein Complexes: An Estimation of the Spectral Density and a Theory for the Calculation of Optical Spectra. *J. Chem. Phys.* **2002**, *116*, 9997–10019.

(35) Herascu, N.; Najafi, M.; Amunts, A.; Pieper, J.; Irrgang, K.-D.; Picorel, R.; Seibert, M.; Zazubovich, V. Parameters of the Protein Energy Landscapes of Several Light-Harvesting Complexes Probed via Spectral Hole Growth Kinetics Measurements. *J. Phys. Chem. B* **2011**, *115*, 2737–2747.

(36) Paulsen, H.; Rumler, U.; Rudiger, W. Reconstitution of Pigment-Containing Complexes from Light Harvesting Chlorophyll *a/b* Binding Protein Overexpressed in Escherichia coli. *Planta.***1990**, *181*, 204-211.

(37) Davies, B. H. Carotenoids, in: T.W. Goodwin (Ed.), Chemistry and biochemistry of plant pigments, Academic Press, New York, **1976**. 38-165.

(38) Porra, R. J.; Thompson, W. A.; Kriedermann, P. E. Determination of Accurate Extinction Coefficients and Simultaneous Equations for Assaying Chlorophylls *a* and *b* Extracted with Four Different Solvents: Verification of the Concentration of Chlorophyll Standards by Atomic Absorption Spectroscopy. *Biochim Biophys Acta.***1989**, *975*, 384-394.

(39) Lichtenthaler, H.K. Chlorophylls and Carotenoids: Pigments of Photosynthetic Biomembranes. *Methods in Enzymology* **1987**, *148*, 351-382.

(40) Britton, G.; Young, A.J. Methods for the Isolation and Analysis of Carotenoids. In: Young A.J., Britton G. (eds) Carotenoids in Photosynthesis. Springer, **1993**. Dordrecht.

(41) Feng, X.; Neupane, B.; Acharya, K.; Zazubovich, V.; Picorel, R.; Seibert, M.; Jankowiak, R. Spectroscopic Study of the CP43 Complex and the PSI-CP43′ Supercomplex of the Cyanobacterium *Synechocystis* PCC 6803. *J. Phys. Chem. B* **2011**, *115*, 13339–13349.

(42) Reppert, M. Modeling of Resonant Hole-Burning Spectra in Excitonically Coupled Systems: The Effects of Energy-Transfer Broadening. *J. Phys. Chem. Letters* **2011**, *2*, 2716−2721.

(43) Nelder, J. A.; Mead, R. A Simplex Method for Function Minimization. *Comput. J.* **1965**, *7*, 308–313.

(44) Kell, A.; Feng, X.; Reppert, M.; Jankowiak, R. On the Shape of the Phonon Spectral Density in Photosynthetic Complexes. *J. Phys. Chem. B* **2013**, *117*, 7317−7323.

(45) Hall, J.; Renger, T.; Picorel, R.; Krausz, E. Circularly polarized luminescence spectroscopy reveals low-energy excited states and dynamic localization of vibronic transitions in CP43. *Biochim. Biophys.Acta.* **2016**, *1857*, 115–128.

(46) Raszewski, G.; Renger, T. Light Harvesting in Photosystem II Core Complexes Is Limited by the Transfer to the Trap: Can the Core Complex Turn into a Photoprotective Mode? *J. Am. Chem. Soc.* **2008**, *130*, 4431– 4446.

(47) Redfield A.G. On the Theory of Relaxation Processes, *IBM J. Res. Dev.* **1957**, *1*,19–31.

(48) Lindofer, D.; Müh, F.; Renger, T. Origin of Non-Conservative Circular Dichroism of the CP29 Antenna Complex of Photosystem II. *Phys. Chem. Chem. Phys.* **2017**, *19*, 7524-7536.

(49) Pieper, J.; Irrgang, K.-D.; Rätsep, M.; Voigt, J.; Renger, G.; Small, G. J. Assignment of the Lowest Q_Y-state and Spectral Dynamics of the CP29 Chlorophyll a/b Antenna Complex of Green Plants: A Hole-burning Study. *Photochem. Photobiol.* **2000**, *71*, 574−581.

(50) Pieper, J.; Voigt, J.; Small, G. J. Chlorophyll a Franck−Condon Factors and Excitation Energy Transfer. *J. Phys. Chem. B* **1999**, *103*, 2319–2322.

(51) Kell, A.; Acharya, K.; Blankenship, R. E.; Jankowiak, R. On Destabilization of the Fenna–Matthews–Olson Complex of *Chlorobaculum tepidum*. *Photosynth. Res.* **2014**, *120*, 323-329.

(52) Ahn, K. T.; Avenson, J. T.; Ballottari, M.; Cheng, Y. C.; Niyogi, K. K.; Bassi, R.; Fleming, G.R. Architecture of a Charge-Transfer State Regulating Light Harvesting in a Plant Antenna Protein. *Science,* **2008,** *320*, 794-797.

(53) Schlau-Cohen, G. S.; Ishizaki, A.; Fleming, G. Two-Dimensional Electronic Spectroscopy and Photosynthesis: Fundamentals and Applications to Photosynthetic Light-Harvesting. *Chem. Phys*. **2011**, *386*,1-22.

(54) Gradinaru, C. C.; Pascal, A. A.; van Mourik, F.; Robert, B.; Horton, P.; van Grondelle, R.; van Amerongen, H. Ultrafast Evolution of the Excited States in the Chlorophyll *a*/*b* Complex CP29 from Green Plants Studied by Energy-Selective Pump-Probe Spectroscopy. *Biochem.* **1998**, *37*, 1143-1149.

Chapter 4

Alternative Excitonic Structure in the Baseplate (BChl *a*- CsmA Complex) of the Chlorosome from *Chlorobbaculum tepidum*

Adam Kell,[1] Jinhai Chen,[1] Mahboobe Jassas,[1] Joseph Kuo-Hsiang Tang,[2] and Ryszard Jankowiak[1,3,*]

[1]Department of Chemistry and [3]Department of Physics, Kansas State University, Manhattan, KS 66506, U.S.A.

[2]Department of Chemistry and Biochemistry, Clark University, Worcester, MA 01610, U.S.A.

Reproduced from *Journal of Physical Chemistry Letter* **2015**, 6, 2702−2707

Abstract

In the photosynthetic green sulfur bacterium *Chlorobaculum tepidum*, the baseplate mediates excitation energy transfer from the light harvesting chlorosome to the Fenna-Matthews-Olson (FMO) complex and subsequently towards the reaction center (RC). Literature data suggest that the baseplate is a 2D lattice of BChl *a*–CsmA dimers. However, recently it has been proposed, using 2D electronic spectroscopy (2DES) at 77 K, that at least four excitonically coupled BChl *a* are in close contact within the baseplate structure [J. Dostál et al., *J. Phys. Chem. Lett.* **2014**, *5*, 1743]. This finding is tested via hole burning (HB) spectroscopy (5 K). Our results indicate that the four excitonic states identified by 2DES likely correspond to contamination of the baseplate with the FMO antenna and possibly the RC. In contrast, HB reveals a different excitonic structure of the baseplate chromophores; where excitation is transferred to a localized trap state near 818 nm via exciton hopping, which leads to emission near 826 nm.

4.1 Introduction

4.1.1 Green Sulfur Bacteria

Green sulfur bacteria (GSB), which possess complete photosynthetic machinery, are anoxygenic phototrophs that thrive in an oxygen-free, sulfur-rich environment, and can live in extremely low-light ecosystems; for example, at depths of 100 m in the Black Sea[1] or in volcanic vents in the absence of solar radiation.[2] GSB contain unique antennas known as chlorosomes,[3,4] which differ from other antenna complexes by their large size (ellipsoidal bodies with a length varying from 100 to 200 nm, width of 50 to 100 nm and height of 15 to 30 nm[5]). Additionally, the bacteriochlorophylls (BChls) (up to 250,000) are reversibly self-assembled[6] with no supporting protein matrix, constituting a unique system among all classes of natural photosynthetic complexes. These properties make GSB very attractive as a model for biomimetic solar energy collection devices[7-12] and excitation energy transfer (EET) studies.

In addition, GSB contain a BChl *a* protein called the Fenna-Matthew-Olson (FMO) complex.[13,14] Between the chlorosomes and FMO complexes is the baseplate, i.e., oligomeric BChl *a*–CsmA (see Figure 4.1). FMO connects the chlorosome–baseplate system to the reaction center (RC) and functionally forms a bridge to transfer the excitation energy to the RC for charge separation.[15] Each chlorosome is suggested to interact with approximately 150-300 FMO trimers and 25-40 RCs.[16] The organization of CsmA proteins as a 2D crystalline lattice was directly observed via electron cryomicroscopy[3] and the structure of the CsmA protein has been determined by liquid state NMR.[17] However, the exact arrangement of the CsmA units in the baseplate, including relative orientation and distances between *individual* BChl *a* molecules, and strength of interaction with BChl *c* are not known.[9,18,19] Interactions between chlorosome pigments (BChl *c*) and BChl *a* of the baseplate were recently studied theoretically and are believed to be weak, with

only minor effect on baseplate transition energies.[20] The BChl *a* of the baseplate absorbs at about 796 nm and are not aggregated like the BChl *c* molecules. Stoichiometric measurements strongly indicate that in *Chlorobaculum* (*Cb.*) *tepidum* one CsmA protein binds a single BChl *a* molecule[9,21] and the presence of a single histidine residue (His25) supports this conclusion.[17,22] A detailed structure of the baseplate is not known, although several models of the BChl *a*–CsmA dimer have been proposed.[22-24] Interestingly, while the BChl dipole-dipole angles (30-125°) and center-to-center distances (7-18 Å) vary significantly in these models, the calculated dipole couplings (assuming $|\mu|$ = 6.1 D) are in the range of 30-35 cm^{-1}. Further studies of photosystems of various complexities (i.e., chlorosome–baseplate, chlorosome–baseplate–FMO and chlorosome–baseplate–FMO–RC) are of great interest and should shed more light on chlorosome–baseplate interactions as well as electronic structure and EET dynamics of the BChl *a*–CsmA system.

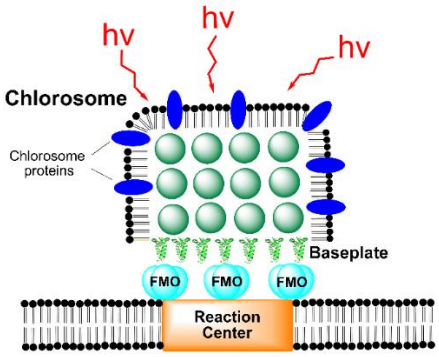

Figure 4.1 Schematic structural model for GSB.[11]

The chlorosome–baseplate photosynthetic system is of great interest since it is likely that it represents one of the earliest antenna systems. Despite the dynamical disorder effects on the electronic transitions of the BChl *c*, previous simulations showed that the exciton delocalizes over the entire aggregate (a single BChl *c* "roll") in 100-200 fs[24,25] and intra-chlorosomal EET in the tubular antenna elements towards the baseplate is extremely fast, i.e., less than 500 fs.[20] Experimentally, femtosecond pump-probe has also revealed energy equilibration on a 50-100 fs

timescale for both *Cb. tepidum* and *Chloroflexus* (*Cf.*) *aurantiacus*.[26,27] A two-color, femtosecond transient absorption study also suggested very fast intra-chlorosomal EET on the time range of 117-270 fs.[28] In the same study,[28] it was shown that excitation of the blue side of the BChl *c* Q_y absorption band (685 nm) while probing at 807 nm (where both the antenna elements and the baseplate absorb) leads to a fast transient absorption anisotropy decay component of about 1 ps for the chlorosomes of *Cb. tepidum*, *Prosthecochloris* (*P.*) *aestuarii* and *Cf. aurantiacus*. The time constant of ~1 ps was proposed to reflect both intra-chlorosomal EET from the initially excited state to lower-lying local states and EET between BChl *a* molecules of the baseplate. The longer anisotropy components of 6.6 ps (*Cf. aurantiacus*), 8.8 ps (*P. aestuarii*) and 12.1 ps (*Cb. tepidum*) were assigned to chlorosome to baseplate energy transfer.[28] In summary, the reported times of EET from the chlorosome to the baseplate are on a ps time scale, for example, 6-12 ps,[28] although longer time constants of 5-20 ps,[20] 12-40 ps,[29] 30-40 ps[30] and 280 ps[31] were also proposed to correspond to EET from the chlorosome to the baseplate pigments.

4.1.2 Excitonic Structure of Baseplate BChl *a*

Very recently it has been suggested that the organization of baseplate BChl *a* is more complex than previously indicated;[32] being comprised of a BChl *a* multimer. That is, it was proposed that 2D electronic spectroscopy (2DES) at 77 K revealed spectroscopic features typical of an excitonic system of at least four coupled BChl *a*. In this work, we examine that electronic/excitonic structure of baseplate chromophores focusing on sample purity, as a small contamination by FMO and RC complexes could lead to a more complex excitonic structure. We also address the EET dynamics between BChl *c* → BChl *a* and BChl *a* → BChl *a* via highly selective spectroscopic techniques, i.e., resonant and nonresonant hole burning (HB) spectroscopy, to provide more insight into the relationship between excitonic structure, function and dynamics

of the chlorosome–baseplate system. It is anticipated that a better understanding of excitonic structure and EET pathway(s) between BChl *a* in the 2D paracrystalline lattice of CsmA proteins could inspire future designs of more efficient light harvesting devices.[22]

4.2 Experimental Results

4.2.1 Low-Temperature Absorption and Emission Spectra

Figure 4.2A shows two 5 K absorption spectra (normalized at 756 nm) obtained for two chlorosome–baseplate samples of different purities (see curves a and b). Although absorption spectra in Figure 4.2A are similar to those reported in the literature,[32] low-temperature spectra a and b differ in the 790-830 nm baseplate transition region, suggesting that curve b is slightly contaminated by FMO (and possibly RC) complexes (*vide infra*). Frame B shows emission spectra from chlorosome–baseplate and chlorosome–baseplate–FMO–RC samples, with main bands at 781.6 nm (BChl *c*) and 825.7 nm (BChl *a*).

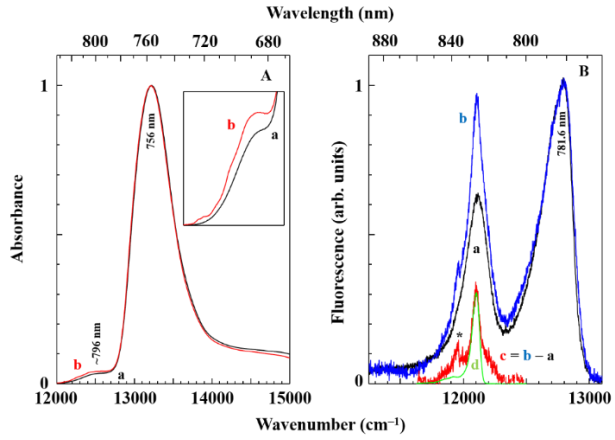

Figure 4.2 (A) Normalized low-temperature (5 K) absorption spectra obtained for two chlorosome–baseplate samples. Curve a represents the absorption of chlorosome–baseplate, while curve b shows that the corresponding sample had slight contamination of FMO/RC antenna. The inset shows the 11800-12800 cm^{-1} region. (B) Emission spectra obtained for chlorosome–baseplate (curve a) and chlorosome–baseplate–FMO–RC (curve b) samples with main bands at 781.6 and 825.7 nm corresponding to the chlorosome and baseplate emission, respectively. Spectrum c = b – a. Spectrum d (green curve) is the 5 K emission from intact, isolated FMO complexes.[33]

4.2.2 Hole-Burned Spectra

The low-energy part of the 5 K absorption spectrum of chlorosome–baseplate is shown by curve a in Figure 4.3A. Spectrum b is the nonresonant (persistent) nonphotochemical HB spectrum (λ_B = 488.0 nm). The HB spectrum was obtained with a fluence (f) of approximately 2,100 J/cm^2, where $f = I \cdot t_B$ with I and t_B corresponding to laser intensity and burn time, respectively. The hole shape is fit by a Gaussian (black curve) with position at 12,200 cm^{-1} (818.3 nm) and fwhm of 240 cm^{-1}. Spectrum b from frame A is replotted in frame B for comparison with HB spectra obtained for two other excitation wavelengths, that is, λ_B = 781.0 nm (curve c) and λ_B = 804.0 nm (curve d). All spectra reveal just one broad low-energy trap state at 818.3 nm. Spectra c and d also show the zero-phonon holes (ZPHs) at λ_B with fwhm (corrected for spectral resolution) of 3.6 and 5.3 cm^{-1}, respectively. Recall that the width of the ZPH in resonant HB spectra depends on the lifetime of the excited state and "pure" dephasing and/or EET time (τ_{EET}).[34] Note that λ_B = 781.0 nm lies with the low-energy exciton state of the BChl *c* aggregate,[30] that is, at this wavelength chlorosome BChl *c* molecules are excited resonantly. Such a low-energy state for chlorosomes was clearly observed in the zero-phonon action (ZPA) spectrum[30] and 2DES data (real part) for chlorosomes from *Cb. tepidum*.[32] The ZPA spectrum (obtained for constant f) for the low-energy state of the baseplate is shown in the inset of frame B. The widths of the three ZPHs are resolution limited. Interestingly, the envelope of the ZPA spectrum is similar to the Gaussian fit of the lowest energy trap near 818.3 nm.

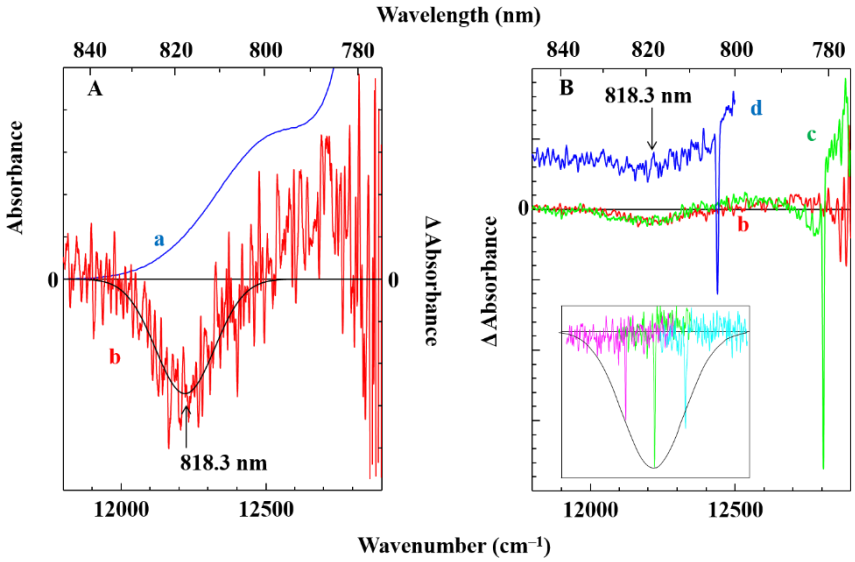

Figure 4.3 (A) Spectra a and b are the 5 K absorption and HB spectra (λ_B = 488.0 nm; $f \approx$ 2,100 J/cm^2) obtained for chlorosome–baseplate. (B) Spectrum b from frame A is replotted and compared to HB spectra obtained for λ_B = 781.0 nm (green curve c) and λ_B = 804.0 nm (blue curve d, offset for clarity). All spectra reveal the lowest energy trap state at 818.3 nm. The inset in frame B shows the ZPA spectrum burned in the lowest energy state of the baseplate.

Curves a in Figure 4.4 are 5.5 K absorption spectra while curves b-e correspond to *f*-dependent, nonresonant HB spectra obtained with λ_B = 488.0 nm. Frames A and B show spectra for chlorosome–baseplate samples with increasing amounts of FMO and RC antenna, respectively. Based on previous study of isolated FMO complexes,[33] holes labeled 1-3 (located near 827, 818 and 806 nm) were also observed in FMO complexes. The weak feature near 797 nm may result from bleach of RC antenna pigment, as both frames of Figure 4.4 show RC contamination. The asterisks label the four very similar electronic transitions resolved in 77 K time-evolution spectra, which were previously assigned to the baseplate[32] (*vide infra*).

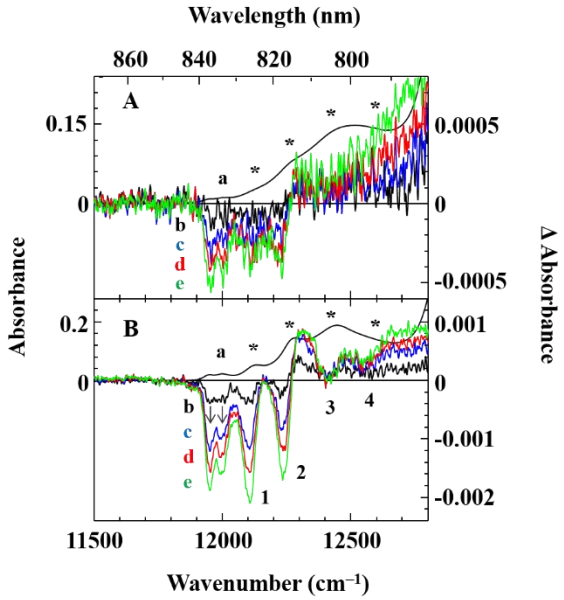

Figure 4.4 (A): Chlorosome–baseplate sample with a small amount of FMO–RC. (B): Chlorosome–baseplate sample with a large amount of FMO–RC. Curves a are 5 K absorption spectra, while curves b-e correspond to *f*-dependent, nonresonant HB spectra (λ_B = 488.0 nm). $f \approx$ 20, 230, 860 and 2,100 J/cm^2 for holes b-e, respectively. Asterisks mark the energetic positions of states determined from 77 K 2DES data,[32] with holes labeled 1-4 indicating similar states in 5 K HB spectra. The two grey arrows mark bleaches of the lowest energy state of the RC antenna.

4.3 Discussion

4.3.1 On Pure Chlorosome–Baseplate Systems

Extensive studies of multiple samples revealed that only spectra in Figure 4.2 (curves a) correspond to pure absorption and emission of the chlorosome–baseplate system that is free of detectable FMO/RC contamination (*vide infra*). The fluorescence difference spectrum in Figure 4.2B (i.e., curve c = b – a) clearly shows a narrow emission band at 826.4 nm that is identical to the fluorescence spectrum measured for isolated (intact) FMO complexes[33] (see green curve d); indicating that spectrum b is contaminated with FMO. The weak narrow emission band in curve c, labeled by an asterisk, corresponds to the previously mentioned minor contamination from the RC. Comparison of emission spectra obtained for various chlorosome–baseplate samples revealed

that samples are often contaminated by FMO or FMO/RC complexes; while the emission spectrum of chlorosome–baseplate–FMO–RC is always similar to spectra measured for whole cells.[30,35]

We note that we could not burn any resonant holes in the vicinity of the chlorosome (BChl *c*) absorption band maximum (756 nm). This is consistent with various time-domain spectroscopic data, which showed that exciton relaxation in chlorosomes occurs on a very fast timescale, i.e., 100-200 fs.[26-28] That is, femtosecond relaxation competes with the HB process, leading to an extremely small HB quantum yield at these frequencies. The ZPH at 781.0 nm in Figure 4.3B (curve c) is fitted with a Lorentzian profile and corrected for spectral resolution, where the fwhm (Γ_{hole} = 3.6 cm^{-1}) corresponds to a homogeneous linewidth (Γ_{hom}) of 1.8 cm^{-1}. (Note that $\Gamma_{hole} = 2\Gamma_{hom}$).[34,36] This shows that τ_{EET} from BChl *c* → BChl *a* is ~3 ps, in agreement with literature data.[30] This value was obtained from Equation 5.1

$$\Gamma_{hom}(cm^{-1}) = \frac{1}{2\pi c T_1} + \frac{1}{\pi c T_2^*} + \frac{1}{2\pi c \tau_{EET}} \approx \frac{1}{2\pi c \tau_{EET}}, \quad (5.1)$$

where T_1 is the fluorescence lifetime, T_2^* is the "pure" dephasing time (which at 5 K is very large in comparison to T_1), and *c* is the speed of light in cm/s.[34] Interestingly, selective excitation at λ_B = 804.0 nm (curve d) also shows a ZPH that, after correction for spectral resolution, gives Γ_{hom} = 2.7 cm^{-1}. This suggests that there is likely uncorrelated EET from the baseplate BChl *a* absorbing at energies > ~12400 cm^{-1} to low-energy BChl *a*; that is, energy cascading down the energy ladder in agreement with the observed low-energy trap at 818.3 nm (12220 cm^{-1}, fwhm = 240 ± 30 cm^{-1}). Thus, we propose that baseplate emission originates from the tail states of the density of states (DOS) where exciton dwell time exceeds its intrinsic lifetime. The estimated τ_{EET} from high-energy BChl *a* to the low-energy BChl *a* within the baseplate absorption band is about 2 ps. HB spectra imply that excitation ends up in the baseplate states near 818.3 nm, meaning that energy is efficiently transferred to a localized state that leads to the observed emission near 826 nm (see

Figure 4.2B). Of course, in chlorosome–baseplate–FMO systems, energy would be further transferred into the lowest energy state(s) of FMO and subsequently to the RC. We show below that minor contamination(s), if present, while not resolved in absorption at 77 K and/or room temperature, may still drastically change interpretation of the excitonic structure and dynamics of BChl *a* molecules constituting the baseplate.

4.3.2 The Nature of Excitonic States Observed in Chlorosome–Baseplate Systems Contaminated with FMO and RC

To address the differences in electronic structure of baseplate chromophores observed in this work and ref 32, we present in Figure 4.4 low-temperature (5 K) absorption and *f*-dependent, nonresonant HB spectra obtained for two chlorosome–baseplate samples, which contain amounts of FMO and RC contributions (*vide supra*). The holes observed near 827, 818 and 806 nm most likely correspond to FMO excitonic states.[33] We hasten to add that the FMO bands are slightly shifted in comparison with isolated FMO since they are superimposed on the baseplate absorption band and weak RC absorption in the same spectral region, complicating any interpretation of their electronic/excitonic structure. While the weak feature near 797 nm may result from bleach of high-energy FMO pigments, it could also be ascribed to RC antenna pigments, as both frames of Figure 4.4 show RC contamination. The presence of the RC antenna pigments is consistent with the observation of the two holes near 834 and 837 nm (see arrows in Figure 4.4B), which are known to correspond to the low-energy states of the RC antenna pigments.[37,38] The P840 band is not observed in these spectra due to partial photo-oxidation of the special pair, whose contribution has been revealed by redox chemistry (to be reported elsewhere). Since the data for the pure chlorosome–baseplate system (shown in Figure 4.3) show drastically different behavior, and spectra shown in Figure 4.4 are in very good agreement with 2DES data,[32] we suggest that the four

electronic transitions reported in ref 32 should not be assigned to baseplate pigments, but to the excitonic states of BChl *a* residing within the FMO/RC antenna. Thus, the assignment (indicated via asterisks) of the 77 K energy states located near 12590 cm^{-1} (794 nm), 12420 cm^{-1} (805 nm), 12260 cm^{-1} (815 nm) and 12120 cm^{-1} (825 nm)[32] to the BChl *a* baseplate, in light of the data shown above, is most likely incorrect. Note that the bands labeled 1-4 are slightly red-shifted compared to 2DES data, due to lower temperature (5 K versus 77 K) and different spectral resolutions used (4 cm^{-1} versus 50 cm^{-1}).

4.3.3 Baseplate Structure

The baseplate structure seems to be less complex than proposed in ref 32. Our data support an arrangement of weakly-coupled dimers as reported in refs 22, 23 and 24, and exciton hopping along the 2D network of CsmA dimers to the low-energy trap at 818.3 nm, which emits at 825.7 nm. Thus, our data are consistent with the model reported in ref 22 that baseplate CsmA proteins arranged as a 2D paracrystalline lattice[3] bind one BChl *a* per CsmA protein, while EET can be understood in terms of a random walk on an energetically disordered network where the excitation can move coherently within the DOS distribution of site energies.[39,40] Thus, an electronic excitation could visit many sites via hopping (i.e., downhill jumps) and "freeze" at the energetically broad low-energy trap that is most likely located at the interface between the baseplate and FMO proteins. A qualitative description of energy relaxation in systems with large energetic disorder and a random walk on the 2D surface of the baseplate BChl *a* molecules is beyond the scope of this paper and it remains to be established whether the Anderson-Mott transition could be invoked to explain the origin of the low-energy trap. This could have important implications regarding efficiency of EET from the baseplate pigments to the FMO complexes.

From the data reported in this work, there is excellent spectral overlap between emission of baseplate pigments and low-energy exciton states of FMO expected for an efficient Förster-type EET from the baseplate to the FMO complex, which in turn (in intact GSB), further transfers energy to the RC for charge separation.[15] While detailed structural information is not available, a distance of 15 Å between the baseplate and FMO was estimated in recent theoretical calculations.[24] Nevertheless, if FMO complexes are present in the chlorosome–baseplate system, excitation energy is efficiently transferred to FMO; decreasing the bleach of baseplate pigments in agreement with the shapes of HB spectra (see Figure 4.4). Finally, we note that data obtained for intact, isolated FMO samples[33] are in perfect agreement with data presented in this work. For example, the maximum of the FMO fluorescence band (826.4 nm)[33] fits well the fluorescence difference curve shown in Figure 4.2B; confirming one of our conclusions in ref 33, that absorption and fluorescence spectra reported in the literature (often measured for different FMO samples) were slightly blue-shifted due to purification/isolation procedures and/or destabilization effects.

4.4 Concluding Remarks

It has been shown that the low-energy trap of baseplate pigments spans the same energy range as FMO pigments (from about 12000 to 12400 cm^{-1}), i.e., the baseplate pigments are well coupled to the two lowest energy states of FMO. This in turn suggests that energy harvested by baseplate pigments can be efficiently transferred to FMO within the 2D lattice. The low-energy trap in the baseplate at 818.3 nm is most likely formed via exciton hopping and HB data is consistent with dimers of CsmA proteins containing two BChl *a* molecules sandwiched between the hydrophobic regions and bound near the histidine.[22,23] In summary, our results indicate the following: *i*) nonresonant and resonant HB spectra obtained at 5 K for the pure chlorosome–baseplate system question the recent suggestion that at least four BChl *a* are in close contact within

the baseplate protein;[32] *ii*) there is a large static diagonal disorder of baseplate BChl *a* (absorption bandwidth ~ 625 cm^{-1}) with a localized trap state at 818.3 nm (fwhm ~ 240 cm^{-1}) that leads to emission at 825.7 nm; and *iii*) the four excitonic states identified at 77 K via 2DES[32] most likely correspond to contamination of the baseplate with the FMO antenna and possible the RC. Finally, HB spectra show that EET from the chlorosome BChl *c* → BChl *a* of the baseplate and BChl *a* → BChl *a* (within the baseplate) occur in 2.9 ± 0.1 and 2.0 ± 0.1 ps, respectively, indicating that the baseplate receives the exciton quickly, rapidly directing it to the lowest energy baseplate trap (with a maximum at 818.3 nm), which releases the exciton to the FMO complexes.

4.5 Experimental Methods

The *Cb. tepidum* cultures grown at 45 °C were harvested at the steady-state growth. The membrane fraction was obtained through ultracentrifugation at 48,000 rpm for 2 hr. The chlorosome was extracted from membrane fractions using 2 NaI in 20 mM Tris-HCl followed by sucrose gradient separation via ultracentrifugation at 28,000 rpm for 16 hr, which gave a concentrated top layer and less concentrated middle layer. The top layer contains more concentrated and pure chlorosomes (i.e., the chlorosome–baseplate complex) and the middle layer contains chlorosome with contamination of other antenna complexes. For HB experiments, samples were diluted with 50:50 (v/v) buffer:glass solution. The glass forming solution was 55:45 (v/v) glycerol:ethylene glycol.

Details about the measurement setup were described elsewhere.[41] Here only a brief description is given. A Bruker HR125 Fourier transform spectrometer was used to measure the absorption and HB spectra with resolutions of 4 and 2-4 cm^{-1}, respectively. The fluorescence spectra were collected by a Princeton Instruments (PI) Acton SP-3200 spectrograph equipped with a back-illuminated CCD camera (PI Action Spec10, 1,340×400) with a resolution of 0.1 nm. The laser

source for both nonresonant HB and fluorescence was 488.0 nm produced from a Coherent Innova 200 argon ion laser, and tunable wavelengths came from a Coherent CR899 Ti:Sapphire laser (line width 0.07 cm^{-1}) pumped by a Spectra-Physics Millenia Xs diode laser (532 nm). Laser power in the experiments was precisely set by a continuously adjustable neutral density filter. All experiments were performed at 5 and 77 K inside an Oxford Instruments Optistat CF2 cryostat with sample temperature read and controlled by a Mercury iTC temperature controller.

ACKNOWLEDGMENT

The authors acknowledge the Division of Chemical Sciences, Geosciences, and Biosciences, Office of Basic Energy Sciences of the U.S. Department of Energy through Grant DE-SC0006678 (to RJ). JKT was supported by start-up funds from Clark University and thanks group members for assisting in sample preparation.

References

(1) Manske, A. K.; Glaeser, J.; Kuypers, M. M. M.; Overmann, J. Physiology and Phylogeny of Green Sulfur Bacteria Forming a Monospecific Phototrophic Assemblage at a Depth of 100 Meters in the Black Sea. *Appl. Environ. Microbiol.* **2005**, *71*, 8049–8060.

(2) Beatty, J. T.; Overmann, J.; Lince, M. T.; Manske, A. K.; Lang, A. S.; Blankenship, R. E.; van Dover, C. L.; Martinson, T. A.; Plumley, F. G. An Obligately Photosynthetic Bacterial Anaerobe from a Deep-Sea Hydrothermal Vent. *Proc. Natl. Acad. Sci. U.S.A.* **2005**, *102*, 9306–9310.

(3) Oostergetel, G. T.; van Amerongen, H.; Boekema, E. J. The Chlorosome: A Prototype for Efficient Light Harvesting in Photosynthesis. *Photosynth. Res.* **2010**, *104*, 245–255.

(4) Orf, G. S.; Blankenship, R. E. Chlorosome Antenna Complexes from Photosynthetic Bacteria. *Photosynth. Res.* **2013**, *116*, 315–331.

(5) Martinez-Planells, A.; Arellano, J. B.; Borrego, C. M.; López-Iglesias, C.; Gich, F.; Garcia-Gil, J. Determination of the Topography and Biometry of Chlorosomes by Atomic Force Microscopy. *Photosynth. Res.* **2002**, *71*, 83–90.

(6) Balaban, T. S.; Tamiaki, H.; Holzwarth, A. R. Chlorins Programmed for Self-Assembly. *Top. Curr. Chem.* **2005**, *258*, 1–38.

(7) Balaban, T. S.; Holzwarth, A. R.; Schaffner, K.; Boender, G.-J.; de Groot, H. J. M. CP-MAS ^{13}C-NMR Dipolar Correlation Spectroscopy of ^{13}C-Enriched Chlorosomes and Isolated Bacteriochlorophyll *c* Aggregates of *Chlorobium tepidum*: The Self-Organization of Pigments Is the Main Structural Feature of Chlorosomes. *Biochemistry* **1995**, *34*, 15259–15266.

(8) Miyatake, T.; Tamiaki, H.; Holzwarth, A. R.; Schaffner, K. Self-Assembly of Synthetic Zinc Chlorins in Aqueous Microheterogeneous Media to an Artificial Supramolecular Light-Harvesting Device. *Helv. Chim. Acta* **1999**, *82*, 797–810.

(9) Sakuragi, Y.; Frigaard, N.-U.; Shimada, K.; Matsuura, K. Association of Bacteriochlorophyll *a* with the CsmA Protein in Chlorosomes of the Photosynthetic Green Filamentous Bacterium *Chloroflexus aurantiacus*. *Biochim. Biophys. Acta* **1999**, *1413*, 172–180.

(10) Prokhorenko, V. I.; Holzwarth, A. R.; Müller, M. G.; Schaffner, K.; Miyatake, T.; Tamiaki, H. Energy Transfer in Supramolecular Artificial Antennae Units of Synthetic Zinc Chlorins and Co-aggregated Energy Traps. A Time-Resolved Fluorescence Study. *J. Phys. Chem. B* **2002**, *106*, 5761–5768.

(11) Tang, K.-H.; Zhu, L.; Urban, V. S.; Collins, A. M.; Biswas, P.; Blankenship, R. E. Temperature and Ionic Strength Effects on the Chlorosome Light-Harvesting Antenna Complex. *Langmuir* **2011**, *27*, 4816–4828.

(12) Borisov, A. Y. On the Structure and Function of "Chlorosomes" of Green Bacteria. *Biophysics* **2012**, *57*, 562–564.

(13) Olson, J. M. The FMO Protein. *Photosynth. Res.* **2004**, *80*, 181–187.

(14) Milder, M. T. W.; Brüggemann, B.; van Grondelle, R.; Herek, J. L. Revisiting the Optical Properties of the FMO Protein. *Photosynth. Res.* **2010**, *104*, 257–274.

(15) Blankenship, R. E. *Molecular Mechanism of Photosynthesis*; Blackwell Science: Oxford, 2002.

(16) Frigaard, N.-U.; Li, H.; Martinsson, P.; Das, S. K.; Frank, H. A.; Aartsma, T. J.; Bryant, D. A. Isolation and Characterization of Carotenosomes from a Bacteriochlorophyll *c*-less Mutant of *Chlorobium tepidum*. *Photosynth. Res.* **2005**, *86*, 101–111.

(17) Pedersen, M. Ø.; Underhaug, J.; Dittmer, J.; Miller, M.; Nielsen, N. C. The Three-Dimensional Structure of CsmA: A Small Antenna Protein from the Green Sulfur Bacterium *Chlorobium tepidum*. *FEBS Lett.* **2008**, *582*, 2869–2874.

(18) Feick, R. G.; Fuller, R. C. Topography of the Photosynthetic Apparatus of *Chloroflexus aurantiacus*. *Biochemistry* **1984**, *23*, 3693–3700.

(19) Montaño, G. A.; Wu, H.-M.; Lin, S.; Brune, D. C.; Blankenship, R. E. Isolation and Characterization of the B798 Light-Harvesting Baseplate from the Chlorosomes of *Chloroflexus aurantiacus*. *Biochemistry* **2003**, *42*, 10246–10251.

(20) Linnanto, J. M.; Korppi-Tommola, J. E. I. Exciton Description of Chlorosome to Baseplate Excitation Energy Transfer in Filamentous Anoxygenic Phototrophs and Green Sulfur Bacteria. *J. Phys. Chem. B* **2013**, *117*, 11144–11161.

(21) Bryant, D. A.; Vassilieva, E. V.; Frigaard, N.-U.; Li, H. Selective Protein Extraction from *Chlorobium tepidum* Chlorosomes Using Detergents. Evidence That CsmA Forms Multimers and Binds Bacteriochlorophyll *a*. *Biochemistry* **2002**, *41*, 14403–14411.

(22) Pedersen, M. Ø.; Linnanto, J.; Frigaard, N.-U.; Nielsen, N. C.; Miller, M. A Model of the Protein–Pigment Baseplate Complex in Chlorosomes of Photosynthetic Green Bacteria. *Photosynth. Res.* **2010**, *104*, 233–243.

(23) Kovács, S. Á.; Bricker, W. P.; Niedzwiedzki, D. M.; Colletti, P. F.; Lo, C. S. Computational Determination of the Pigment Binding Motif in the Chlorosome Protein A of Green Sulfur Bacteria. *Photosynth. Res.* **2013**, *118*, 231–247.

(24) Huh, J.; Saikin, S. K.; Brookes, J. C.; Valleau, S.; Fujita, R.; Aspuru-Guzik, A. Atomistic Study of Energy Funneling in the Light-Harvesting Complex of Green Sulfur Bacteria. *J. Am. Chem. Soc.* **2014**, *136*, 2048–2057.

(25) Fujita, T.; Brookes, J. C.; Saikin, S. K.; Aspuru-Guzik, A. Memory-Assisted Exciton Diffusion in the Chlorosome Light-Harvesting Antenna of Green Sulfur Bacteria. *J. Phys. Chem. Lett.* **2012**, *3*, 2357–2361.

(26) Savikhin, S.; Zhu, Y.; Lin, S.; Blankenship, R. E.; Struve, W. S. Femtosecond Spectroscopy of Chlorosome Antennas from the Green Photosynthetic Bacterium *Chloroflexus aurantiacus*. *J. Phys. Chem.* **1994**, *98*, 10322–10334.

(27) Savikhin, S.; van Noort, P. I.; Zhu, Y.; Lin, S.; Blankenship, R. E.; Struve, W. S. Ultrafast Energy Transfer in Light-Harvesting Chlorosomes from the Green Sulfur Bacterium *Chlorobium tepidum*. *Chem. Phys.* **1995**, *194*, 245–258.

(28) Martiskainen, J.; Linnanto, J.; Aumanen, V.; Myllyperkïo, P.; Korppi-Tommola, J. Excitation Energy Transfer in Isolated Chlorosomes from *Chlorobaculum tepidum* and *Prosthecochloris aestuarii*. *Photochem. Photobiol.* **2012**, *88*, 675–683.

(29) Fetisova, Z.; Freiberg, A.; Mauring, K.; Novoderezhkin, V.; Taisova, A.; and Timpmann, K. Excitation Energy Transfer in Chlorosomes of Green Bacteria: Theoretical and Experimental Studies. *Biophys. J.* **1996**, *71*, 995–1010.

(30) Pšenčík, J.; Políka, T.; Němec, P.; Dian, J.; Kudrna, J.; Malý, P.; Hála, J. Fast Energy Transfer and Exciton Dynamics in Chlorosomes of the Green Sulfur Bacterium *Chlorobium tepidum*. *J. Phys. Chem. A* **1998**, *102*, 4392–4398.

(31) Prokhorenko, V. I.; Steensgaard, D. B.; Holzwarth, A. R. Exciton Dynamics in the Chlorosomal Antennae of the Green Bacteria *Chloroflexus aurantiacus* and *Chlorobium tepidum*. *Biophys. J.* **2000**, *79*, 2105–2120.

(32) Dostál, J.; Vácha, F.; Pšenčík, J.; Zigmantas, D. 2D Electronic Spectroscopy Reveals Excitonic Structure in the Baseplate of a Chlorosome. *J. Phys. Chem. Lett.* **2014**, *5*, 1743–1747.

(33) Kell, A.; Acharya, K..; Blankenship, R. E.; Jankowiak, R. On Destabilization of the Fenna-Matthews-Olson Complex of *Chlorobaculum tepidum*. *Photosynth. Res.* **2014**, *120*, 323–329.

(34) Jankowiak, R.; Reppert, M.; Zazubovich, V.; Pieper, J.; Reinot, T. Site Selective and Single Complex Laser-Based Spectroscopies: A Window on Excited State Electronic Structure, Excitation Energy Transfer, and Electron-Phonon Coupling of Selected Photosynthetic Complexes. *Chem. Rev.* **2011**, *111*, 4546–4598.

(35) Psencik, J.; Schaafsma, T. J.; Searle, G. F. W.; Hala, J. Fluorescence Detected Magnetic Resonance of Monomers and Aggregates of Bacteriochlorophylls of Green Sulfur Bacteria *Chlorobium* sp. *Photosynth. Res.* **1997**, *52*, 83–92.

(36) *Persistent Spectral Hole-Burning: Science and Applications*; Moerner, W. E., Ed.; Topics in Current Physics, Volume 44; Springer: Berlin, 1988.

(37) Miller, M.; Cox, R. P.; Olson, J. M. Low-Temperature Spectroscopy of Isolated FMO-Protein and a Membrane-Free Reaction Center Complex from the Green Sulfur Bacterium *Chlorobium tepidum*. *Photosynth. Res.* **1994**, *41*, 97–103.

(38) He, G.; Niedzwiedzki, D. M.; Orf, G. S.; Zhang, H.; Blankenship, R. E. Dynamics of Energy and Electron Transfer in the FMO-Reaction Center Core Complex from the Phototrophic Green Sulfur Bacterium *Chlorobaculum tepidum*. *J. Phys. Chem. B* **2015,** *119*, 8321-8329.

(39) Richert, R.; Bässler, H.; Energetic Relaxation of Triplet Excitation in Vitreous Benzophenone. *Chem. Phys. Lett.* **1985**, *118*, 235–239.

(40) Movaghar, B.; Grünewald, M.; Ries, B.; Bässler, H.; Würtz, D. Diffusion and Relaxation of Energy in Disordered Organic and Inorganic Materials. *Phys. Rev. B* **1986**, *33*, 5545–5554.

(41) Feng, X.; Neupane, B.; Acharya, K.; Zazubovich, V.; Picorel, R.; Seibert, M.; Jankowiak, R. Spectroscopic Study of the CP43 Complex and the PSI-CP43′ Supercomplex of the Cyanobacterium *Synechocystis* PCC 6803. *J. Phys. Chem. B* **2011**, *115*, 13339–13349.

Chapter 5

On Excitation Energy Transfer within the Baseplate BChl *a*-CsmA Complex of *Chloroflexus aurantiacus*

Mahboobe Jassas,[†] Carrie Goodson[‡], Robert E. Blankenship[‡], Ryszard Jankowiak[†,§], and Adam Kell[†,#,*]

[†]Department of Chemistry and [§]Department of Physics, Kansas State University, Manhattan, Kansas 66506, United States

[‡]Departments of Biology and Chemistry, Washington University in St. Louis, St. Louis, Missouri 63130, United States

Reproduced from *Journal of Physical Chemistry B* **2019**, 123, 9786-9791

Abstract

Recently, a hybrid approach combining solid-state NMR spectroscopy and cryo-electron microscopy showed that the baseplate in the green sulfur bacterium *Chlorobaculum tepidum* is a 2D lattice of BChl *a*–CsmA dimers [Nielsen, J. T.; et al., *Nat. Commun*. **2016**, *7*, 12454–12465]. While the existence of the BChl *a*–CsmA subunit was previously known, the proposed orientations of the BChl *a* pigments had only been elucidated from spectral data up to this point. Regarding the electronic structure of the baseplate, two models have been proposed. 2D electronic spectroscopy data was interpreted as revealing that at least four excitonically coupled BChl *a* might be in close contact Conversely, spectral hole burning data suggested the lowest energy state was localized, yet additional state are sometimes observed due to the presence of the Fenna–Matthews–Olson (FMO) antenna protein. To solve this conundrum, this work studies the chlorosome-baseplate complex from *Chloroflexus aurantiacus*, which does not contain the FMO protein. The results confirm that in both *C. tepidum and C. aurantiacus* excitation energy is transferred to a localized low-energy trap state near 818 nm with similar rates, most likely via exciton hopping.

5.1 Introduction

The green filamentous bacterium *Chloroflexus aurantiacus* employs chlorosomes as photosynthetic antennas. They are the major light-harvesting bodies and contain on the order of tens of thousands to hundreds of thousands of bacteriochlorophyll (BChl) *c* pigments, which self-aggregate without any assistance from the peptides in the hydrophobic environment, enveloped in an ellipsoidal lipid monolayer.[1-5] The structure of chlorosomes from this bacterium was investigated using a combination of cryo-electron microscopy and X-ray diffraction.[6-8] Chlorosomes are located on the cytoplasmic side of the plasma membrane and interface with the membrane via a so-called baseplate. The baseplate is composed of a regular array of the chlorosomal protein CsmA, forming a complex with BChl *a* and carotenoid molecules. Figure 5.1 shows the relative arrangement of the chlorosome and the membrane-bound reaction center (RC). The baseplate is present only on one side of the chlorosome, and the lattice dimensions suggest that the building block is a CsmA protein dimer.[9] The CsmA protein subunits have molecular masses of 5.7 and 6.2 kDa in *C. aurantiacus* and *Chlorobaculum tepidum*, respectively.[10] BChl *a* molecules within the baseplate act as mediators of excitation energy transfer (EET) from the chlorosomal body towards the FMO antenna and reaction center (RC) in *C. tepidum*, and to the B808-866 core antenna/RC system in *C. aurantiacus*.[11-13] The primary pigment in chlorosomes from both *C. aurantiacus* and the green sulfur bacterium *C. tepidum*, is BChl *c* (~99%),[14] but lipid, protein, quinone and small amount of BChl *a* are also present.[15] The size and the thickness of chlorosomes depend on growth conditions.[16,17] In low-light intensity growth conditions, the number of chlorosomes per cell increases leading to a thickening of chlorosomes, though the latter does not affect their length or width. The thickening of the chlorosomes leads to an increase of the BChl *c*/BChl *a* ratio (i.e., the ratio is inversely proportional to the light intensity during

growth).[18,19] It has been also shown that each chlorosome has the same sized baseplate.[18] The baseplate BChl *a* pigments absorb near 800 nm at low temperature and are not aggregated like the BChl *c* molecules of chlorosomes. Stoichiometric measurements strongly indicate that in *C. tepidum* one CsmA protein binds a single BChl *a* molecule[20,21] and the presence of a single histidine residue (His25) supports this conclusion.[22,23] Interactions between chlorosome pigments (BChl *c*) and BChl *a* of the baseplate have been studied theoretically and are believed to be weak, with only minor effect on baseplate transition energies.[24] A time constant of ~1 ps was proposed to reflect both intra-chlorosomal EET from the initially excited state to lower-lying local states and EET between BChl *a* molecules of the baseplate.[25] The reported EET times from the chlorosome to the baseplate are also on a ps time scale, for example, 6-12 ps[25] and 5-20 ps,[24] although longer time constants of 12-40 ps,[26] 30-40 ps[27] and 280 ps[14] were also proposed. Recently we have shown, using hole-burning (HB) spectroscopy, that low temperature EET from the chlorosome BChl *c* → BChl *a* of the baseplate and BChl *a* → BChl *a* (within the baseplate) in *C. tepidum* occur in 2.9 ± 0.1 and 2.0 ± 0.1 ps, respectively.[28] The large energetic disorder produces an Anderson-type exciton localization[28,29] which traps excitation energy in the lowest energy state near 818 nm. From HB data, the EET times are determined by the width of a resonantly burned zero-phonon hole (ZPH). That is, the spectral hole width represents homogeneous broadening related to the depopulation of the probed state. Since the fluorescence lifetime is on the order of nanoseconds and the pure dephasing time at liquid helium temperatures is even longer, the resulting width gives the EET time directly by $\Gamma_{ZPH} = \frac{1}{\pi c \tau_{EET}}$.[30] Due to finite spectral resolution, the ZPH is technically a Voigt profile (convolution of Lorentzian and Gaussian curves), however, the Lorentzian shape dominates for "fast" relaxation. Where necessary the reported Lorentzian full-width at half-maxima (*fwhm*) have been corrected to account for the spectral resolution.

Previously, the organization of CsmA proteins as a 2D crystalline lattice was directly observed via electron cryo-microscopy[8] and the structure of the CsmA protein has been determined by liquid state NMR.[31] Various models were proposed for the BChl *a*–CsmA dimer, but BChl dipole-dipole angles (30-125°) and center-to-center distances (7-18 Å) varied significantly.[23,32,33] Interestingly, the calculated coupling matrix elements (V_{mn}) have similar values of –(30-35) cm^{-1} (assuming $|\vec{\mu}|$ = 6.1 D). The high-resolution structure of the CsmA baseplate from *C. tepidum* (including relative orientation and distances between *individual* BChl *a* molecules) was recently obtained using a hybrid approach combining solid-state NMR spectroscopy, cryo-electron microscopy, isotropic and anisotropic circular dichroism and linear dichroism.[34] In that work, the authors showed that the baseplate is composed of rods of repeated dimers of the strongly amphipathic CsmA with BChl *a* pigments sandwiched within the dimer at the hydrophobic side of the helix. Using the new structure V_{mn} = 100 cm^{-1} between the BChls constituting baseplate dimers. Subsequently, the structure of the BChl *a* pigments was modified after discrepancies between experimental data and modeling were found, especially pertaining to the linear dichroism spectrum.[35] The modification consists of rotating the Q_y transition dipole of the BChl *a* dimer towards each other by 30° each, resulting in V_{mn} = 60 cm^{-1}. While the structure of the *C. aurantiacus* baseplate is not known, and there appear still lingering questions about the BChl orientation in *C. tepidum*, the recent structural data provides a critical starting point for interpreting low-temperature *C. aurantiacus* spectral features. *C. aurantiacus* is of key interest in this work since chlorosomes from species belonging to *Chloroflexi* are directly connected to the membrane, i.e., they do not possess the FMO protein, in contrast to *C. tepidum*.[1,36,37] However, in both cases, the excitation energy is ultimately delivered to the RCs within the membrane, where charge separation takes place, and is subsequently used to drive cellular processes.[1,37] In addition to its role in EET, it has been proposed that the baseplate

is essential for the long-range order of BChl *c* aggregates.[38] Studies of the chlorosome–baseplate from *C. aurantiacus* reported below should shed more light on baseplate pigments as well as their excitonic structure and EET dynamics. Below we show that both *C. tepidum* and *C. aurantiacus* have a large static diagonal disorder of baseplate pigments with similar EET rates to the localized trap state near 818 nm.

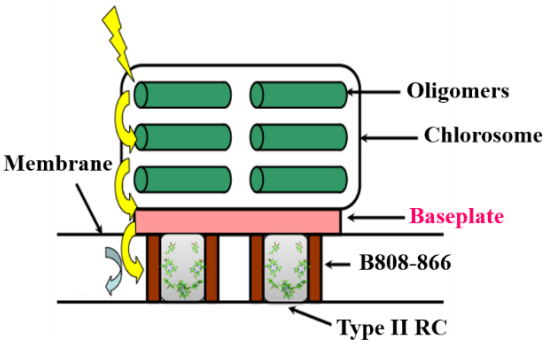

Figure 5.1 Schematic structural model for *C. aurantiacus*. The chlorosome is directly connected to the membrane (hosting the core antenna and type II RC) via the baseplate.

5.2 Materials and Methods

5.2.1 Chlorosome Isolation

Chlorosomes were isolated following the procedure of Gerola and Olson[39] as modified by van de Meene et al.[40] Briefly, pelleted cells of *C. aurantiacus* were suspended at 0.25 g/mL in chlorosome buffer (20mM TRIS, 2M NaSCN, pH 8.0) with ascorbic acid added to 0.01 M and incubated for 30 min at room temperature. The sample was homogenized with a glass plunger and sonicated on ice two times for 30 s at 45% power (30 s between sonications) and centrifuged at 3500g for 5 min to remove debris and unbroken cells. Concentration was achieved with Amicon 100 K MWCO filters (ThermoFisher) at 4000g for 20 min. The sample was loaded onto a discontinuous sucrose gradient (10%, 20%, 50%) in chlorosome buffer and centrifuged at 140

000g for 16 hr at 4 ºC in a SW 32 Ti ultracentrifuge rotor. Chlorosome bands were located in the upper fractions and 10%/20% interface and selected for those showing a room temperature peak at 741 nm wavelength but without peaks at 808 or 865 nm. For HB experiments, the samples were diluted to the desired OD by buffer and glass-forming solution at 40:60 (v/v) sample/glass solution. The glass-forming solution was 55:45 (v/v) glycerol/ethylene glycol.

5.2.2 Experimental Spectroscopic Methods

Details about the measurement setup are described elsewhere.[41] In short, a Bruker HR125 Fourier Transform Infrared spectrometer was used to measure the absorption and HB spectra with resolution of 2 cm^{-1}. The fluorescence spectra were collected by a Princeton Instruments (PI) Acton SP-3200 spectrograph equipped with a back-illuminated CCD camera (PI Acton Spec10, 1340 × 400) with a resolution of 0.1 nm. The laser source for both non-resonant HB and fluorescence was 488.0 nm, produced from a Coherent Innova 200 argon ion laser. Tunable wavelengths for resonant HB came from a Coherent CR899 Ti:sapphire laser (line width 0.07 cm^{-1}) pumped by a Spectra-Physics Millenia Xs diode laser (532 nm). Laser power in the experiments was precisely set by a continuously adjustable neutral density filter. All low-temperature (5-77 K) experiments were performed using an Oxford Instrument Optistat CF2 cryostat with sample temperature read and controlled by a Mercury iTC temperature controller.

5.3 RESULTS AND DISCUSSION

5.3.1 Low-Temperature Absorption and Emission Spectra

The low-temperature absorption and fluorescence spectra of isolated chlorosomes are shown in Figure 5.2. The absorption (red curve a) shows, in addition to the oligomeric BChl *c* (743.0 nm) and baseplate BChl *a* (799.2 nm) origin bands, a small peak at 670 nm (most likely due to degradation products of BChl c; perhaps bacteriopheophytin c[10,39,42] and a tiny peak at 870.9

nm (see the red star) due to a small contamination by the B808-866 complex (which also contains BChl *a*). The relatively strong fluorescence from the baseplate at ~ 820.8 nm (blue curve b), in contrast to the relatively low intensity of the 799.2 nm absorption band, indicates that there is significant energy transfer from the BChl c aggregates to the baseplate, in agreement with literature data.[42]

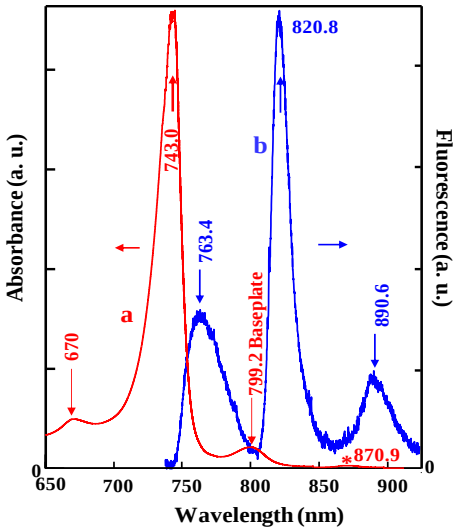

Figure 5.2 Curves a and b are absorption and emission for isolated chlorosomes of *C. aurantiacus* at 5 K, respectively.

5.3.*2 C. aurantiacus* Versus *C. tepidum*

C. aurantiacus and *C. tepidum* chlorosome/baseplate systems studied in this work were obtained at low-light growth conditions. It has been suggested that a larger rod diameter in *C. tepidum*, and possibly different orientations of the transition dipole moments of BChl *c* in the concentric walls, lead to a broader and red-shifted BChl *c* Q_y band[11,25,43] This is demonstrated in Figure 5.3, which compares 5 K absorption (frame A) and fluorescence (frame B) spectra obtained for *C. aurantiacus* (blue curves a and a′) and *C. tepidum* (black curves b and b′). Absorption maxima/*fwhm* of the BChl *c* bands are 743.0/19.5 nm and 756.0/33.7 nm for *C. aurantiacus* and

C. tepidum, respectively. The fact that the BChl *c* Q_y band of *C. aurantiacus* is about 50% narrower than that of *C. tepidum* suggests a more ordered pigment organization in the former than in the latter chlorosomes.[11] The weak 799.2 nm band in spectra a and b, as mentioned above, corresponds to baseplate BChl *a* absorption (see red arrow). This band is less resolved in *C. tepidum* (curve b), which is somewhat due to the higher relative proportion of BChl *a* in *C. aurantiacus* chlorosomes. (~5 to 8% of the total BChl *c*)[9,44] than in *C. tepidum* (~0.5 to 2%).[3,7,39] The corresponding emission spectra (curves a′ and b′) normalized at the baseplate emission maxima are shown in frame B. Fluorescence maxima of BChl *c*/BChl *a* are at 763.4/820.8 nm and 781.6/825.7 nm for *C. aurantiacus* and *C. tepidum*, respectively. While the *fwhm* of baseplate BChl *a* emission bands are similar (~14-15 nm), chlorosome BChl *c* emission from *C. aurantiacus* is broader by a factor of ~2.2 than that observed in *C. tepidum*. Also, the relative population ratios of BChl *c*/BChl *a* calculated from integrated emission intensities in spectra a′ and b′ are significantly different, i.e., about 0.6 and 1.4, respectively. Interestingly, emission maxima in curves a′ and b′ are shifted (820.8 vs 825.7 nm) although the corresponding absorption bands are very similar (*vide infra*). While there is a 0.7 nm shift between the lowest energy states (see below), tentatively, the additional difference in fluorescence maxima of the baseplate bands can be explained by differences in electron-phonon coupling. Details of the structure-based simulatons used to determine the electron-phonon coupling are given in the Appendix C. the simultaneous modeling of several optical spectra reveals information on the localization of the baseplate excitonic states (discussed more below in the entext of HB spectra).

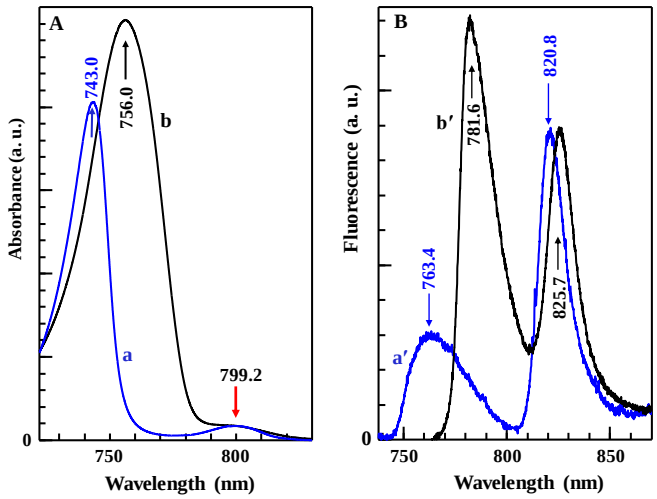

Figure 5.3 Frames A and B show 5 K absorption/fluorescence spectra of *C. aurantiacus* (curves a/a′) and *C. tepidum* (curves b/b′), respectively. All curves are normalized at the maxima of baseplate absorption and emission spectra.

5.3.3 Hole-burned Spectra and the Low-Temperautre Energy Trap

The baseplate 5 K absorption band of *C. aurantiacus*, with a maximum at 799.2 nm, is shown by curve a in Figure 5.4. Curves b, c and d are persistent HB spectra obtained at burn wavelengths (λ_B) of 798.0, 781.0, and 759.0 nm and for laser fluences (f) of 11.3, 60, and 19 J cm^{-2}, respectively. All three low-fluence holes have percent hole depths of ~1%. The spectra obtained for *C. aurantiacus* reveal a low-energy trap state at 817.6 nm (with *fwhm* of 190 cm^{-1}) that is very similar to that previously observed in *C. tepidum* chlorosomes (818.3 nm with *fwhm* of 240 cm^{-1}).[28] The experimental zero-phonon hole (ZPH) burned at 781.0 nm (red curve), and its Lorentzian fit (black curve) with *fwhm* of ~ 5.3 cm^{-1} are replotted in the inset. The *fwhm* of ZPHs burned at 781.0 and 798.0 nm show that the BChl *a* → BChl *a* EET time is about 2 ps, i.e., similar to that observed in baseplate of *C. tepidum*.[28] A similar EET time was obtained for λ_B of 802.0 nm (data not shown) suggesting similar EET times across the baseplate absorption band. The ZPH burned at 759.0 nm (curve d, green), resonant with the chlorosome BChl *c* absorpbance, with a *fwhm* of

4.2 cm^{-1} , shows that the BChl *c* → BChl *a* EET time is about 2.5 ps. Note that BChl *c* → BChl *a* EET occurs in ~2.9 ps for *C. tepidum*.[28]

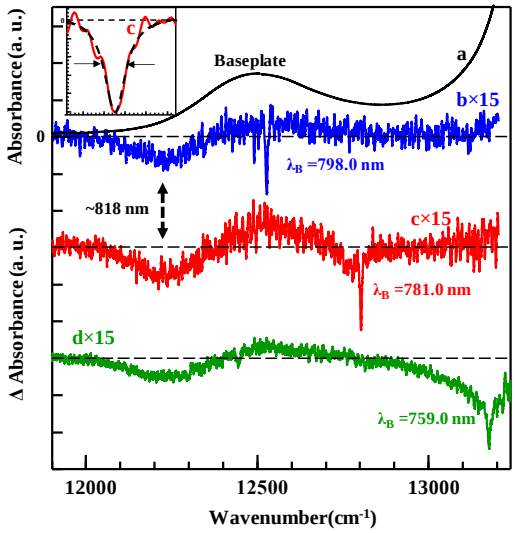

Figure 5.4 Curve a is 5 K absorption of the baseplate of the *C. aurantiacus*. Curves b, c and d are resonant (persistent) HB spectra and were obtained using burn wavelength of 798.0, 781.0 and 759.0 nm, respectively. Inset shows the ZPH burned at 781.0 nm (red) with a Lorentzian fit (dashed curve).

5.3.4 On the Purity of the Chlorosome-Baseplate Sample

The 5 K absorption bands of the baseplate and B808-866 membrane-bound light-harvesting complex are shown by curve a (black) in Figure 5.5. Curve b (green) is non-resonant excitation at λ_B = 532.0 nm (f = 600 J cm^{-2}) while curve d (blue) is a resonant HB spectrum obtained at 820.0 nm (f = 7 J cm^{-2}). After the persistent hole is burned (i.e., curve d) the sample is annealed to 70 K for 20 min and again cooled to 5 K. Curve c (red) is the difference between 5 K (preburn) absorption before and after annealing the sample (5 K sample warm up to 70 K and again cool down to 5 K). Curve f is a new hole burned spectrum measured after annealing. Curve e (pink) is the difference between spectra d and f (i.e., d minus f), that shows the bleaching of the membrane antenna. Thus, depending on the way the experiment is done, one can reveal a broad bleach (11 447

cm^{-1}; 873.6 nm; see pink arrows) assigned to the B808-866 complex which is still present in our samples, as suggested by data shown in Figure 5.2 (see the very weak band indicated by an asterisk). The increased bleach at 11 447 cm^{-1} (873.6 nm) in the nonresonant spectrum (curve c) is due to the excitation of Cars bound to the B808-866 complex, which absorb strongly at 532 nm. Conversely, there is insignificant B808 absorption at 820 nm (see Appendix C) and the response at 11 447 cm^{-1} (~873.6 nm) to the resonant excitation is much weaker. It is also possible that some B808-866 complexes are not bound to the chlorosomes. It is worth noting that $A_{chlorosomes}/A_{baseplate}$ and $A_{chlorosomes}/A_{B808-866}$ ratio is about 20 and 200, respectively. That is, in comparison with isolated chlorosomes used in the literature, the contamination by the B808-866 complex in our samples is negligibly small. Previously, a weak bleaching in the 808-866 nm region was observed by transient absorption data of the isolated chlorosomes, probably due to the direct excitation of some remaining B808-866 complex in the sample.[10] The hole widths measured at λ_B = 820.0 nm are 3.3 and 4 cm^{-1} for curves d and f, respectively. These values correspond to population lifetimes of about 5-6 ps, indicating BChl *a*-CsmA → B808-866 EET is on the order of several ps.

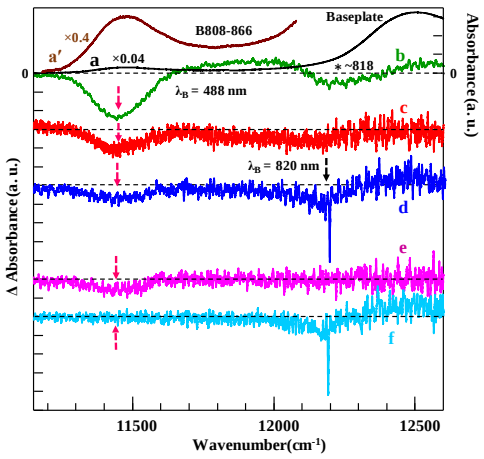

Figure 5.5 Absorption (5 K) of the BChl *a* baseplate and core antenna region (curve a) and expanded B808-866 band (curve a′). Curve b is the nonresonant HB spectrum, while curves d and f are resonant HB spectra obtained at different experimental conditions (see text for details). Curve c is the difference absorption spectrum of before and after temperature annealing. Curve e is the difference between curves d and f.

5.4 Conclusions

The BChl *a*–CsmA baseplate is an integral part of the chlorosome complex in both green sulfur bacteria and filamentous anoxygenic phototrophs. Its role along the energy transfer pathway is to accept excitation energy from the chlorosome BChl *c* and transfer the energy to BChl *a* bound to either the FMO (e.g., *C. tepidum*) or B808-866 (e.g., *C. aurantiacus*) protein complexes. Thus, the lowest energy trap state of the baseplate is of interest for understanding the overall EET process in photosystems of the aforementioned bacteria. The results presented in this work, for pure isolated chlorosomes, indicate both *C. tepidum* and *C. aurantiacus* baseplates have the same low-energy trap near 818 nm. HB data obtained for both bacteria suggest that excitation within the corresponding baseplate systems is transferred to a localized trap state via exciton hopping, which leads to red-shifted emission near 826 nm and 821 nm for *C. tepidum* and *C. aurantiacus*, respectively. The measured BChl *a* → BChl *a* EET time within the baseplate occurs in 2.0 ± 0.1 ps. This result contradicts an earlier interpretation of 2DES data that concluded the *C. tepidum* baseplate is composed of an excitonically coupled tetramer.[45] The consistency between the HB data of *C. tepidum* and *C. aurantiacus* suggests that, in both bacteria, the baseplate electronic structure is mainly determined by the disordered BChl *a*–CsmA lattice leading to localized states; and not excitonic interactions across multiple BChl *a*–CsmA dimers leading to delocalized excitons.

Acknowledgment

This research was conducted under the auspices of the Photosynthetic Antenna Research Center (PARC), an Energy Frontier Research Center funded by the DOE, Office of Science, Office of Basic Energy Sciences under Award Number DE-SC 0001035.

References

(1) Olson, J. M. Chlorophyll Organization and Function in Green Photosynthetic Bacteria. *Photochem. Photobiol.* **1998**, *67*, 61–75.

(2) Montaño, G. A.; Bowen, B. P.; LaBelle, J. T.; Woodbury, N. W.; Pizziconi, V. B.; Blankenship, R. E. Characterization of *Chlorobium tepidum* Chlorosomes: A Calculation of Bacteriochlorophyll *c* per Chlorosome and Oligomer Modeling. *Biophys. J.* **2003**, *85*, 2560–2565.

(3) Frigaard, N.-U.; Bryant, D. Chlorosomes: Antenna Organelles in Photosynthetic Green Bacteria. *Microbiol. Monogr.* **2006**, *2*, 79–114.

(4) Oostergetl, G. T.; van Amerongen, H.; Boekema, E. J. The Chlorosome: A Prototype for Efficient Light Harvesting in Photosynthesis. *Photosynth. Res.* **2010**, *104*, 245–255.

(5) Orf, G. S.; Blankenship, R. E. Chlorosome Antenna Complexes from Green Photosynthetic Bacteria. *Photosynth. Res.* **2013**, *116*, 315–331.

(6) Pšenčík, J.; Ikonen, T. P.; Laurinmäki, P.; Merckel, M. C.; Butcher, S. J.; Serimaa, R. E.; Tuma, R. Lamellar Organization of Pigments in Chlorosomes, the Light Harvesting Complexes of Green Photosynthetic Bacteria. *Biophys. J.* **2004**, *87*, 1165–1172.

(7) Pšenčík, J.; Arellano, J. B.; Ikonen, T. P.; Borrego, C. M.; Laurinmäki, P. A.; Butcher, S. J.; Serimaa, R. E.; Tuma, R. Internal Structure of Chlorosomes from Brown-Colored *Chlorobium* Species and the Role of Carotenoids in Their Assembly. *Biophys. J.* **2006**, *91*, 1433–1440.

(8) Oostergetel, G. T.; Reus, M.; Gomez Maqueo Chew, A.; Bryant, D. A.; Boekema, E. J.; Holzwarth, A. R. Long-Range Organization of Bacteriochlorophyll in Chlorosomes of *Chlorobium tepidum* Investigated by Cryo-Electron Microscopy. *FEBS Lett.* **2007**, *581*, 5435–5439.

(9) Pšenčík, J.; Collins, A. M.; Lilijeroos, L.; Torkkeli, M.; Laurinmäki, P.; Ansink, H. M.; Ikonen, T. P.; Serimaa, R. E.; Blankenship, R. E.; Tuma, R.; Butcher, S. J. Structure of Chlorosomes from the Green Filamentous Bacterium *Chloroflexus aurantiacus*. *J. Bacteriol.* **2009**, *191*, 6701–6708.

(10) Montaño, G. A.; Wu, H.-M.; Lin, S.; Brune, D. C.; Blankenship, R. E. Isolation and Characterization of the B798 Light-Harvesting Baseplate from the Chlorosomes of *Chloroflexus aurantiacus*. *Biochemistry* **2003**, *42*, 10246–10251.

(11) Martiskainen, J.; Linnanto, J.; Kananavičius, R.; Lehtovuori, V.; Korppi-Tommola, J. Excitation Energy Transfer in Isolated Chlorosomes from *Chloroflexus aurantiacus*. *Chem. Phys. Lett.* **2009**, *477*, 216−220.

(12) Savikhin, S.; Zhu, Y.; Blankenship, R. E.; Struve, W. S. Ultrafast Energy Transfer in Chlorosomes from the Green Photosynthetic Bacterium *Chloroflexus aurantiacus*. *J. Phys. Chem.* **1996**, *100*, 3320–3322.

(13) Causgrove, T. P.; Brune, D. C.; Wang, J.; Wittmershaus, B. P.; Blankenship, R. E. Energy Transfer Kinetics in Whole Cells and Isolated Chlorosomes of Green Photosynthetic Bacteria. *Photosynth res*. **1990**, *26*, 39-48.

(14) Prokhorenko, V. I.; Steensgaard, D. B.; Holzwarth, A. R. Exciton Dynamics in the Chlorosomal Antennae of the Green Bacteria *Chloroflexus aurantiacus* and *Chlorobium tepidum*. *Biophys. J.* **2000**, *79*, 2105–2120.

(15) Frigaard, N.-U.; Takaichi, S.; Hirota, M.; Shimada, K.; Matsuura, K. Quinones in chlorosomes of green sulfur bacteria and their role in the redox-dependent fluorescence studied in chlorosome-like bacteriochlorophyll c aggregates. *Arch Microbiol. Monogr*. **1997**, *167*, 343–349.

(16) Borrego, C. M.; Gerola, P. D.; Miller, M.; Cox, R. P. Light Intensity Effects on Pigment Composition and Organisation in the Green Sulfur Bacterium *Chlorobium tepidum*. *Photosynth. Res.* **1999**, *59*, 159–166.

(17) Yakovlev, A. G.; Taisova, A. S.; Fetisova, Z. G. Light Control Over the Size of an Antenna Unit Building Block as an Efficient Strategy for Light Harvesting in Photosynthesis. *FEBS Lett.* **2002**, *512*, 129–132.

(18) Sprague, S. G.; Staehelin, L. A.; DiBartolomeis, M. J.; Fuller, R. C. Isolation and Development of Chlorosomes in the Green Bacterium *Chloroflexus aurantiacus*. *J. Bacteriol.* **1981**, *147*, 1021–1031.

(19) Betti, J. A.; Blankenship, R. E.; Natarajan, L. V.; Dickinson, L. C.; Fuller, R. C. Antenna Organization and Evidence for the Function of a New Antenna Pigment Species in the Green Photosynthetic Bacterium *Chloroflexus aurantiacus*. *Biochim. Biophys. Acta* **1982**, *680*, 194–201.

(20) Sakuragi, Y.; Frigaard, N.-U.; Shimada, K.; Matsuura, K. Association of Bacteriochlorophyll *a* with the CsmA Protein in Chlorosomes of the Photosynthetic Green Filamentous Bacterium *Chloroflexus aurantiacus*. *Biochim. Biophys. Acta* **1999**, *1413*, 172–180.

(21) Bryant, D. A.; Vassilieva, E. V.; Frigaard, N.-U.; Li, H. Selective Protein Extraction from *Chlorobium tepidum* Chlorosomes Using Detergents. Evidence That CsmA Forms Multimers and Binds Bacteriochlorophyll *a*. *Biochemistry* **2002**, *41*, 14403–14411.

(22) Pedersen, M. Ø.; Pham, L.; Steensgaard, D. B.; Miller, M. A Reconstituted Light-Harvesting Complex from the Green Sulfur Bacterium *Chlorobium tepidum* Containing CsmA and Bacteriochlorophyll *a*. *Biochemistry* **2008**, *47*, 1435–1441.

(23) Pedersen, M. Ø.; Linnanto, J.; Frigaard, N.-U.; Nielsen, N. C.; Miller, M. A Model of the Protein–Pigment Baseplate Complex in Chlorosomes of Photosynthetic Green Bacteria. *Photosynth. Res.* **2010**, *104*, 233–243.

(24) Linnanto, J. M.; Korppi-Tommola, J. E. I. Exciton Description of Chlorosome to Baseplate Excitation Energy Transfer in Filamentous Anoxygenic Phototrophs and Green Sulfur Bacteria. *J. Phys. Chem. B* **2013**, *117*, 11144–11161.

(25) Martiskainen, J.; Linnanto, J.; Aumanen, V.; Myllyperkïo, P.; Korppi-Tommola, J. Excitation Energy Transfer in Isolated Chlorosomes from *Chlorobaculum tepidum* and *Prosthecochloris aestuarii*. *Photochem. Photobiol.* **2012**, *88*, 675−683.

(26) Fetisova, Z.; Freiberg, A.; Mauring, K.; Novoderezhkin, V.; Taisova, A.; and Timpmann, K. Excitation Energy Transfer in Chlorosomes of Green Bacteria: Theoretical and Experimental Studies. *Biophys. J.* **1996**, *71*, 995–1010.

(27) Pšenčík, J.; Políka, T.; Němec, P.; Dian, J.; Kudrna, J.; Malý, P.; Hála, J. Fast Energy Transfer and Exciton Dynamics in Chlorosomes of the Green Sulfur Bacterium *Chlorobium tepidum*. *J. Phys. Chem. A* **1998**, *102*, 4392–4398.

(28) Kell, A.; Chen, J.; Jassas, M.; Tang, J. K.-H.; Jankowiak, R. Alternative Excitonic Structure in the Baseplate (BChl *a* – CsmA Complex) of the Chlorosome from *Chlorobaculum tepidum*. *J. Phys. Chem. Lett.* **2015**, *6*, 2702–2707.

(29) Malý, P.; van Grondelle, R. Interplay of Disorder and Delocalization in Photosynthetic Light Harvesting. *Curr. Opin. Chem. Biol.* **2018**, *47*, 1–6.

(30) Jankowiak, R.; Reppert, M.; Zazubovich, V.; Pieper, J.; Reinot,T. Site Selective and Single Complex Laser-Based Spectroscopies: A Window on Excited State Electronic Structure, Excitation Energy Transfer, and Electron−Phonon Coupling of Selected Photosynthetic Complexes. Chem. Rev. 2011, 111, 4546−4598.

(31) Pedersen, M. Ø.; Underhaug, J.; Dittmer, J.; Miller, M.; Nielsen, N. C. The Three-Dimensional Structure of CsmA: A Small Antenna Protein from the Green Sulfur Bacterium *Chlorobium tepidum*. *FEBS Lett.* **2008**, *582*, 2869–2874.

(32) Kovács, S. Á.; Bricker, W. P.; Niedzwiedzki, D. M.; Colletti, P. F.; Lo, C. S. Computational Determination of the Pigment Binding Motif in the Chlorosome Protein A of Green Sulfur Bacteria. *Photosynth. Res.* **2013**, *118*, 231–247.

(33) Huh, J.; Saikin, S. K.; Brookes, J. C.; Valleau, S.; Fujita, R.; Aspuru-Guzik, A. Atomistic Study of Energy Funneling in the Light-Harvesting Complex of Green Sulfur Bacteria. *J. Am. Chem. Soc.* **2014**, *136*, 2048–2057.

(34) Nielsen, J. T.; Kulminskaya, N. V.; Bjerring, M.; Linnanto, J. M. Rätsep, M.; Pedersen, M. Ø.; Lambrev, P. H.; Dorogi, M.; Garab G.; Thomsen, K.; Jegerschöld, C.; Frigaard, N. U.; Lindahl,

M.; Nielsen, N. C. *In situ* High-Resolution Structure of the Baseplate Antenna Complex in *Chlorobaculum tepidum. Nat. Commun*. **2016**, *7*, 12454.

(35) Lindorfer, D.; Renger, T. Theory of Anisotropic Circular Dichroism of Excitonically Coupled Systems: Application to the Baseplate of Green Sulfur Bacteria. *J. Phys. Chem. B* **2018**, *122*, 2747–2756.

(36) Staehelin, L. A.; Golecki, J. R.; Fuller, R. C.; Drews, G. Visualization of the supramolecular architecture of chlorosomes (chlorobium type vesicles) in Freeze-Fractured Cells of *Chloroflexus aurantiacus*. *Arch Microbiol.* **1978**, *119*, 269–277.

(37) Tang, K.-H.; Zhu, L.; Urban, V. S.; Collins, A. M.; Biswas, P.; Blankenship, R. E. Temperature and Ionic Strength Effects on the Chlorosome Light-Harvesting Antenna Complex. *Langmuir* **2011**, *27*, 4816–4828.

(38) Arellano, J. B.; Torkkeli, M.; Tuma, R.; Laurinmäki, P.; Melø, T. B.; Ikonen, T. P.; Butcher, S. J.; Serimaa, R. E.; Pšenčík, J. Hexagonal-Induced Order–Disorder Transitions in Lamellar Self-Assembling Aggregates of Bacteriochlorophyll *c* in *Chlorobium tepidum* Chlorosomes. *Langmuir* **2008**, *24*, 2035–2041.

(39) Gerola, P. D.; Olson, J. M. A new bacteriochlorophyll a-protein complex associated with chlorosomes of green sulfur bacteria. *Biochimica et Biophysica Acta.* **1986**, *848*, 69-76.

(40) van de Meene, A. M. L.; Olson, T. L.; Collins, A. M.; Blankenship, R. E. Initial Characterization of the Photosynthetic Apparatus of "*Candidatus* Chlorothrix halophila," a Filamentous, Anoxygenic Photoautotroph. *J. Bacteriol.* **2007**, *189*, 4196–4203.

(41) Feng, X.; Neupane, B.; Zazubovich, V.; Picorel, R.; Seibert, M.; Jankowiak, R. Spectroscopic Study of the CP43′ Complex and the PSI–CP43′ Supercomplex of the Cyanobacterium *Synechocystis* PCC 6803. *J. Phys. Chem. B* **2011**, *115*, 13339–13349.

(42) van Dorssen, R. J.; Vasmel, H.; Amesz, J. Pigment Organization and Energy Transfer in the Green Photosynthetic Bacterium *Chloroflexus aurantiacus*. II. The Chlorosome. *Photosynth. Res.* **1986**, *9*, 33–45.

(43) Linnanto, J. M.; Korppi-Tommola, J. E. I. Investigation on Chlorosomal Antenna Geometries: Tube, Lamella and Spiral-Type Self-Aggregates. *Photosynth. Res.* **2008**, *96*, 227–245.

(44) Schmidt, K.; Maarzahl, M.; Mayer, F. Development and Pigmentation of Chlorosomes in *Chloroflexus aurantiacus* Strain Ok-70-fl. *Arch. Microbiol.* **1980**, *127*, 87–97.

(45) Dostál, J.; Vácha, F.; Pšenčík, J.; Zigmantas, D. 2D Electronic Spectroscopy Reveals Excitonic Structure in the Baseplate of a Chlorosome. *J. Phys. Chem. Lett.* **2014**, *5*, 1743–1747.

Chapter 6

Conclusions

This work presents the application of low-temperature high-resolution laser spectroscopy technique, hole burning, and computer modeling towards the several light-harvesting antenna, i.e., CP29 and CP47 from higher plants, and baseplate complex of two green bacteria families. In CP47 core antenna project, using simultaneous fit of various low-temperature optical spectra such as, absorption, emission, circular dichroism (CD), circularly polarized luminescence (CPL), and nonresonant hole-burned spectra, we demonstrate that the spectra reported and calculated in the literature represent heterogeneous samples. Therefore, the proposed new energy flow in the CP47 antenna protein complex, which favored Chl 11 as the lowest energy pigment, is highly questionable. We suggest that the lowest energy exciton band is mostly contributed to by either Chl 26 or Chl 29. In second project, pigment analysis of reconstituted CP29 complexes in agreement with theoretical modeling of various low-temperature optical spectra suggests that ~50% of Chl *b*614 is lost during the reconstitution and purification procedures; therefore, reconstituted CP29 complexes contain, on average, 9 Chls *a* and 3.5 Chls *b*. Also, the modeling study of excitation-dependent emission and shift of fluorescence spectra induced by NRHB in the reconstitute CP29 revealed two independent low-energy states, i.e., the A and B Traps. The state A is assigned to the minor subpopulation II (10%), which most likely originates from imperfect reconstitute of CP29 proteins in vitro and unlikely to occur in the native complex. The state B is attributed to the major subpopulation I (90%), is mostly delocalized over the *a*611, *a*612, *a*615 Chl trimer. In the last two projects, the chlorosome-baseplate complex from green bacteria *Cb. tepidum* and *C. aurantiacus* studied which the main difference of these two complexes is the later one does

not contain the FMO antenna. We demonstrate that the nonresonant and resonant HB spectra question the suggestion that at least four BChl *a* are in close contact within the baseplate protein, and the four excitonic states most likely correspond to the contamination of the baseplate with the FMO antenna. The experimental data of two families of green bacteria are consistent with the model that baseplate CsmA protein arranged as dimers containing two Bchl *a* molecules sandwiched between the hydrophobic protein regions. We confirm that in both chlorosome-baseplate complexes excitation is transferred to a localized low-energy trap state near 818 nm with similar EET rates, most likely via exciton hopping.

Currently, a complementary study of CP29 mutants, i.e., A2 and B3 that lack of ligands of Chl 612 and Chl 614, respectively, is in progress. From preliminary experimental results and modeling studies, A2 expected to play an essential role in the transfer of excitation energy transfer from the peripheral antenna to the core. However, more pigment analysis is needed to describe the optical spectra precisely.

Appendix A

Supporting information for" Towards an Understanding of the Excitonic Structure of the CP47 Antenna Protein Complex of Photosystem II Revealed via Circularly Polarized Luminescence"

A.1. Effect of Isolated Pigments on Circularly Polarized Luminescence.

Figure A.1 shows that the shape of the circularly polarized luminescence (CPL) spectrum (fitted in Figure 2.2 A; main manuscript) may be affected when chlorophyll (Chl) 29 (which does not contribute to the CPL signal) contributes to the lowest energy state. In this case Chl 29 has a variable site energy with Chl 11 having a constant site energy of 14 580 cm^{-1}. Although Chl 29 is in a separate domain, its low site energy and Γ_{inh} may still affect the shape of the CPL spectrum (i.e., the positive and negative lobes), as this Chl contributes to the lowest energy absorption. Curves a, b, and c are the CPL spectra for Chl 29 site energies of 14 500, 14 559, and 14 618 cm^{-1}, respectively. The Γ_{inh} values for Chls 11 and 29 are 290 cm^{-1} and 269 cm^{-1}, respectively. For all remaining pigments Γ_{inh} = 140 cm^{-1}.

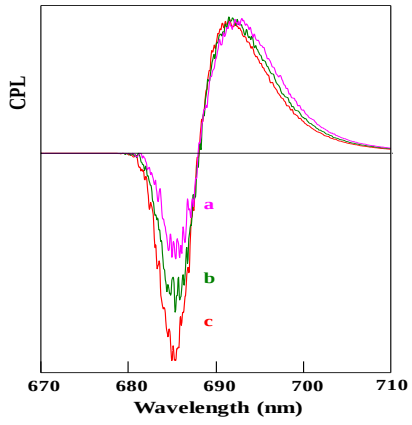

Figure A.1 CPL spectra calculated with different site energies of Chl 29 and fixed site energy of Chl 11.

A.2. Spectral Deconvolution of Destabilized CP47 Fluorescence.

Figure A.2 shows 2 K fluorescence spectra, adopted from ref [1], obtained for CP47 before (frame B; curve c) and after (frame A; curve a) 514 nm illumination. Spectra were measured with the same excitation intensity of ~0.1 mW/cm^2. Spectra b and d are fits using the typically observed F691 and F695 emissions observed in heterogeneous CP47 samples, and the adjusted difference between spectra a and c (F685 = a – c). The difference (a – c) is very similar to the F685 emission extracted previously with a maximum near 685 nm.[2] However, the fits clearly indicate that this sample already contained F685 emission (see frame B), indicating that a subpopulation of complexes was already permanently modified. The relative intensities of the F685, F691, and F695 are indicated by the vertical bars (see also Figure 2.3B in the main manuscript).

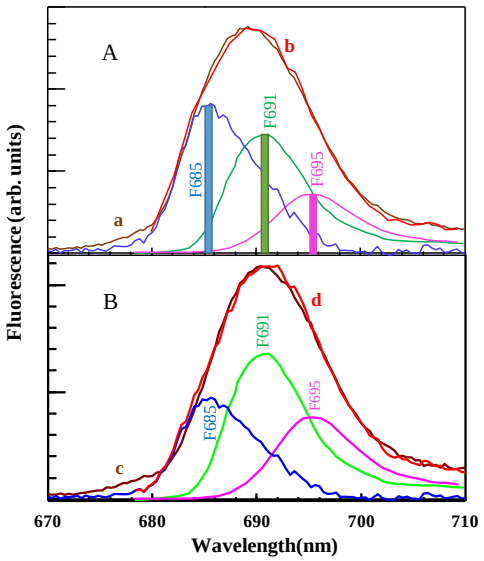

Figure A.2 2 K CP47 fluorescence spectra[1] obtained before (frame B; curve c) and after (frame A; curve a) 514 nm illumination. Spectra b and d are fits calculated as the sum of F685, F691, and F695 emissions. The relative intensity of the F685, F691, and F691 bands after illumination is indicated by the three bars.

Figure A.3 shows a modified Figure 8 from ref 2 with deconvolved fluorescence spectra using the F685, F691, and F695 bands. We argued before that the emission near 685 nm (F685), 691 nm

(F691), and 695 nm (F695) originate from fractions (subpopulations) of CP47 complexes in which the lowest energy traps lie at energies near ~684 nm, ~689 nm, and ~693 nm, respectively. The emission spectra are also consistent with HB data discussed in ref 2 and support our findings that many previously studied samples contained fractions of destabilized and/or photodamaged CP47 complexes. Our assignment of the F685 contribution is further supported by the shape of the grey (scaled) curve a in frame B of Figure A.3, which was obtained as a difference between the experimental fluorescence spectra shown in frames A and B. This spectrum is similar to the F685 band shown in Figure A.2, supporting our suggestion that many samples studied in various laboratories over the years had different *permanent* contribution from the F685 emission.

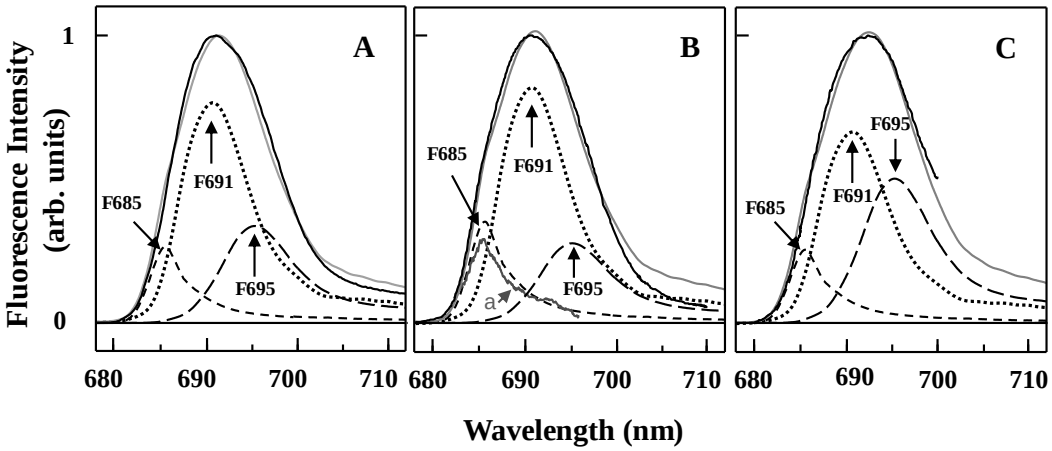

Figure A.3 Broad band fluorescence spectra (solid lines) of various CP47 samples adopted from ref 2. Frames A-C describe the composition of fluorescence spectra from refs 2-4 respectively. Deconvolution shows that these spectra can all be fitted with the same three major contributions: *i*) F685; *ii*) F691; and *iii*) F695 emission.

Figure A.4 (adopted from ref 2) compares nonresonant HB spectra obtained with λ_B = 496.5 nm for typical destabilized (frame A) and intact (frame B) samples. Note that the lowest energy burn states and the minima of the saturated holes in frames A and B are sample dependent, revealing that the composite nature of burned holes strongly depends on sample quality in agreement with different fluorescence spectra. Both samples, however, possess the lowest exciton state of intact

CP47 and F695 emission, which originates from the A1 state.[2] The shallow holes (shown in insets) clearly reveal the complex nature of destabilized samples. That is, the lowest exciton state of the intact sample near 693 nm (A1 band) is still observed in the destabilized sample, while the main bleach near 688-689 nm (AT1 band)[2] corresponds to the modified subpopulation characterized by the F691 emission.

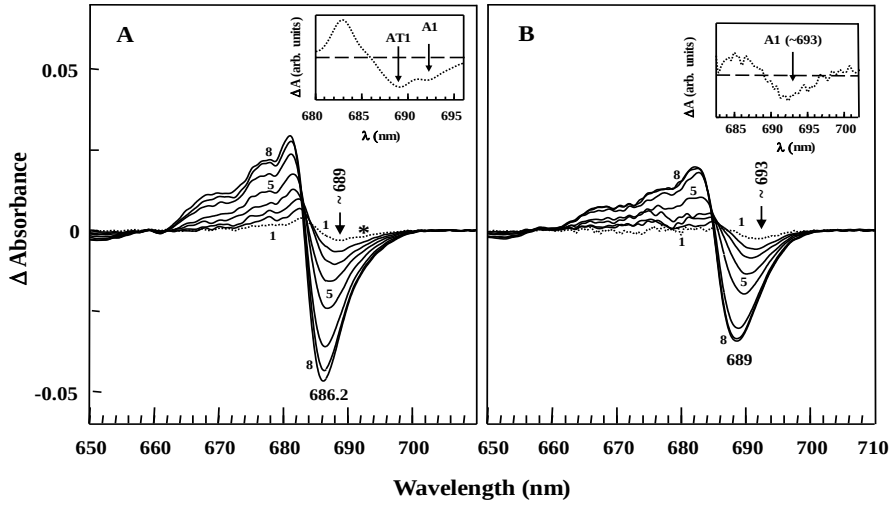

Figure A.4 Comparison of nonresonant HB spectra obtained with λ_B = 496.5 nm for destabilized (frame A) and intact (frame B) samples adopted from ref 2. Curves labeled 1-8 (in both frames) correspond to holes obtained for different burn fluences, while the insets correspond to expanded curves 1.

A.3. CP47 Electronic Coupling Constants.

Tables A.1 and A.2 show the coupling constants (off-diagonal matrix elements) calculated with the TrEsp method[5] for two X-ray structures of the Photosystem II core complex (PSII-cc). Structures 3ARC[6] (*Thermosynechococcus vulcanus*) and 3JCU[7] (spinach) have resolutions of 1.9 and 3.2 Å, respectively, and produce very similar coupling constants. Note that Tables A.1 and A.2 support the use of higher-resolution x-ray data from cyanobacteria even when simulating experimental spectra from spinach.

Table A.1 TrEsp Electronic Coupling Constants (cm^{-1}) for the 3ARC structure

Chl	11	12	13	14	15	16	17	21	22	23	24	25	26	27	28	29
11	0	57	19	-5	1	5	2	-4	7	3	2	-3	3	1	1	1
12		0	-89	20	6	-7	-6	5	-20	-14	-4	5	-9	-2	4	-2
13			0	5	-4	-66	-2	-7	28	15	1	-9	3	-2	-1	-4
14				0	-38	-15	65	5	-10	-4	-1	19	-34	7	-3	0
15					0	68	-19	-2	0	-5	-3	-6	-8	-4	12	10
16						0	7	-3	7	-5	6	-3	9	4	0	8
17							0	0	4	1	5	-1	17	4	-2	2
21								0	-19	-96	-15	20	-6	-3	4	-1
22									0	60	8	-15	10	3	-4	5
23										0	-13	50	0	-6	30	-7
24											0	0	54	34	-17	7
25												0	-60	96	22	3
26													0	-59	-2	1
27														0	-12	11
28															0	-7
29																0

Table A.2 TrEsp Electronic Coupling Constants (cm^{-1}) for the 3JCU Structure

Chl	11	12	13	14	15	16	17	21	22	23	24	25	26	27	28	29
11	0	51	20	-5	1	5	2	-5	8	4	2	-3	3	1	1	1
12		0	-94	21	5.6	-6	-6	5	-19	-14	-4	6	-10	-2	4	-2
13			0	6	-6	-65	-3	-8	30	17	1	-9	3	-2	-1	-5
14				0	-39	-14	68	5	-11	-5	-1	20	-40	7	-3	1
15					0	69	-21	-2	0	-5	-4	-6	-7	-4	13	9
16						0	7	-3	8	-4	5	-4	9	4	1	8
17							0	0	3	1	6	-1	17	4	-2	2
21								0	-16	-95	-16	21	-6	-3	3	-1
22									0	55	8	-14	10	4	-2	5
23										0	-13	50	-1	-6	32	-6
24											0	-11	63	35	-18	8
25												0	-74	100	24	5
26													0	-64	-3	1
27														0	-13	14
28															0	-16
29																0

A.4. Models I (Chl 26) and II (Chl 29), Case B.

Theoretical fits (solid lines) of the same spectra as those shown in Figure 2.4 of the main manuscript (filled curves) for Case B are shown in Figure A.5. Here all intradomain $V_{nm} < V_c$ (30 cm^{-1}) are also set to zero. The right panels in Figure A.5 show the respective first three excitonic states (top) and major pigment contributions (bottom) to the lowest energy ($\alpha = 1$) state. Compared to Case A, Case B shows marginally better fits with slightly different site energies, Γ_{inh} of individual pigments, and Huang-Rhys factors ($S_{ph} = 0.94$, $S_{vib\text{-}em} = 0.6$, $S_{vib\text{-}abs} = 0.46$). See Table A.3 for details (note that both cases have the same Chl ordering when comparing site energies). The same case for Model II, assuming Chl 29 is the lowest energy pigment, is shown in Figure A.6 with details presented in Table A.4.

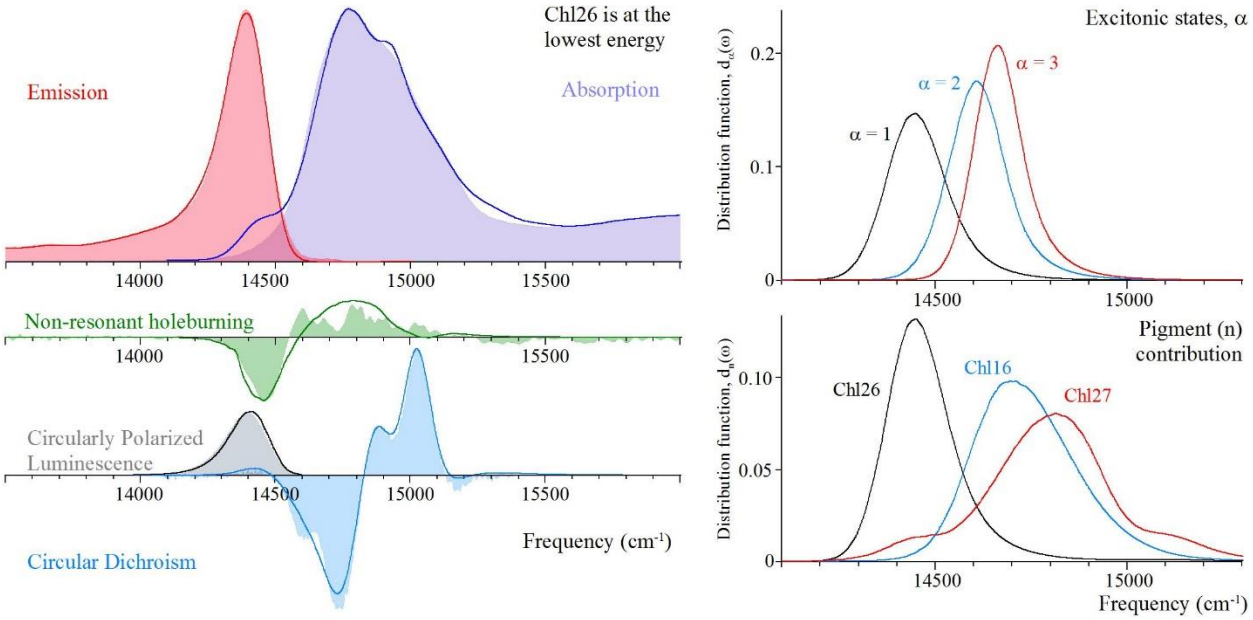

Figure A.5 *Left* (Case B): Chl 26 is the lowest energy pigment. The same experimental spectra as those in Figure 2.4 with new calculated curves (solid lines). *Right*: Chls contributing mostly to the lowest energy state ($\alpha = 1$) are Chl 26 (91.8%), Chl 27 (4.9%) and Chl 16 (0.83%). Fitting error = 2.49.

Table A.3 Summary of Model I Parameters Used to Simulate Spectra for Intact CP47[a]

	Case A		Case B	
Chl	E_0^n	Γ_{inh}	E_0^n	Γ_{inh}
11	14 910	277	14 893	288
12	14 888	231	14 879	210
13	14 863	206	14 831	279
14	14 939	287	14 885	352
15	14 805	278	14 830	295
16	14 798	262	14 795	265
17	15 122	242	14 995	301
21	14 811	226	14 800	231
22	14 990	138	15 017	109
23	14 986	206	14 985	208
24	15 180	281	15 169	353
25	15 105	127	15 079	143
26	14 479	155	14 481	159
27	14 771	310	14 810	396
28	14 746	196	14 742	219
29	14 775	197	14 785	271

[a]All values in units of cm^{-1}.

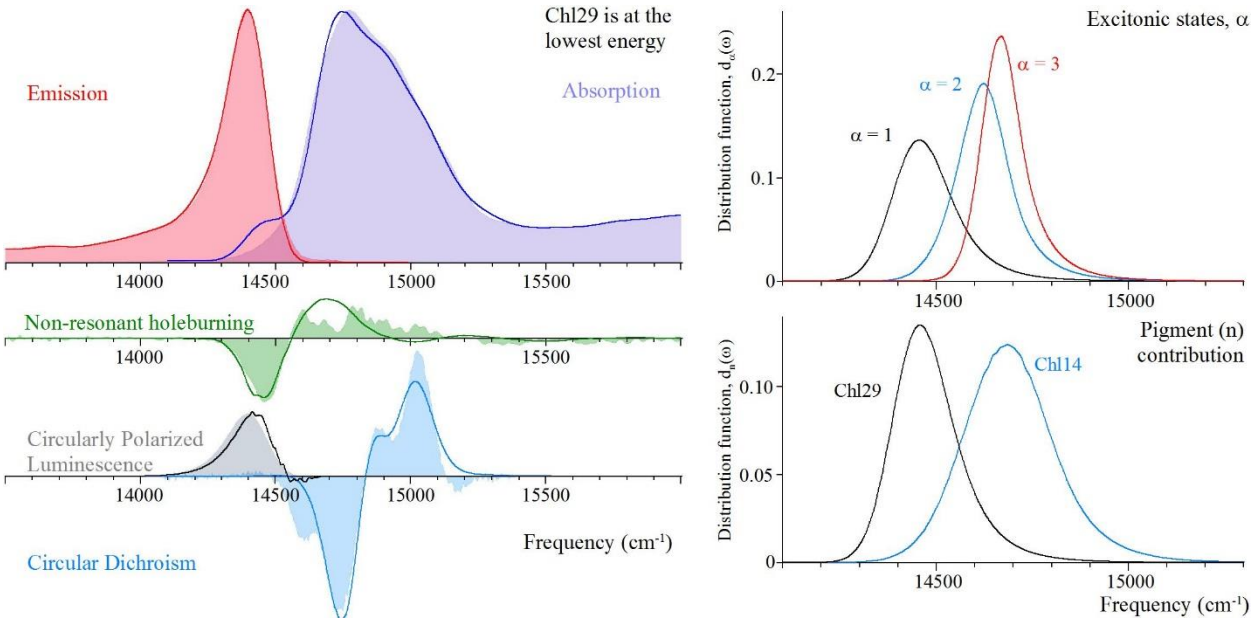

Figure A.6 *Left* (Case B): Chl 29 is the lowest energy pigment. The same experimental spectra as those in Figure 2.5 with new calculated curves (solid lines). *Right*: Chls contributing mostly to the lowest energy state (α = 1) are Chl 29 (94.7%) and Chl 14 (3.8%). Fitting error = 3.57.

Table A.4 Summary of Model II Parameters Used to Simulate Spectra for Intact CP47[a]

	Case A		Case B	
Chl	E_0^n	Γ_{inh}	E_0^n	Γ_{inh}
11	15 065	214	15 069	208
12	14 798	228	14 819	235
13	14 904	236	14 897	229
14	14 712	253	14 707	253
15	14 774	176	14 791	184
16	14 866	213	14 856	211
17	14 942	266	14 937	261
21	14 839	213	14 814	226
22	14 936	174	14 995	171
23	15 008	228	14 971	227
24	15 039	249	15 025	241
25	15 044	249	15 053	250
26	14 762	166	14 760	165
27	14 886	275	14 870	267
28	14 853	269	14 856	246
29	14 482	150	14 483	146

[a]All values in units of cm^{-1}.

Recall that all simultaneous fits shown in Figures 2.4/A.5 and 2.5/A.6 assume the same experimentally determined $J_{ph}(\omega)$ and included the newly extracted CPL curve for CPL_{695}, which further constrains the choice for low-energy Chls. Nevertheless, based on these fits alone one could suggest that Chl 26 is a better choice than Chl 29 for the lowest energy pigment. This is supported by a weak positive band in the calculated CD spectrum near 693 nm, also observed experimentally in the PSII-cc.[8] Comparison of fits shown in Figures 2.4/2.5 and A.5/A.6 reveals that the difference between Cases A and B is very small, as expected.

A.5. Model II (Chl 29), Case C.

As defined in the main manuscript, Case C considers V_{nm} parameters calculated with the TrEsp method and assumes that all intradomain $V_{nm} < V_c$ (30 cm^{-1}) are set to zero. Figure A.7 shows fits of experimental data for intact CP47 assuming Chl 29 is the lowest energy pigment. A omparison of parameters for both Models I (Figure 2.6 of main manuscript) and II (Figure A.7) is given in Table A.5.

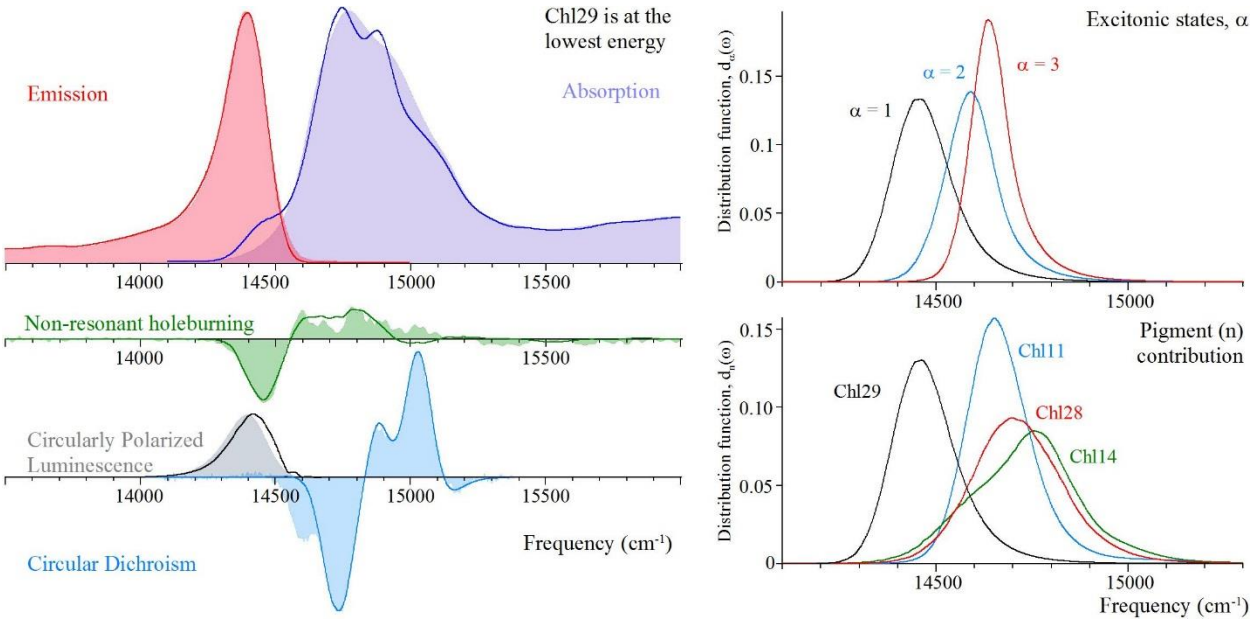

Figure A.7 *Left* (Case C): Chl 29 is the lowest energy pigment. The same experimental spectra as those in Figure 2.5 with new calculated curves (solid lines). *Right*: Chls contributing mostly to the lowest energy state (α = 1) are Chl 29 (91%), Chl 14 (4.6%), Chl 28 (2.1%), and Chl 11 (1.3%). Fitting error = 2.1.

Table A.5 Summary of Case C Parameters Used to Simulate Spectra for Intact CP47[a]

	Model I		Model II	
Chl	E_0^n	Γ_{inh}	E_0^n	Γ_{inh}
11	14 900	265	14 686	159
12	14 884	175	15 087	151
13	14 894	169	14 818	206
14	14 918	309	14 721	272
15	14 809	286	14 779	164
16	14 828	255	14 989	177
17	15 085	218	15 001	151
21	14 721	191	14 826	158
22	15 019	128	14 946	126
23	14 992	319	14 996	156
24	15 224	358	14 894	157
25	15 033	131	14 990	183
26	14 490	155	14 767	155
27	14 852	259	14 999	156
28	14 799	207	14 726	247
29	14 792	224	14 482	148

[a]All values in units of cm^{-1}.

A.6. Simultaneous Modeling of Various Optical Spectra Obtained for a Heterogeneous CP47 Sample.

Recent analysis of circular dichroism (CD) and CPL spectra suggested that the lowest energy pigment in the CP47 complex is Chl 11.[1] The authors concluded that previous assignments where Chl 24, Chl 26 or Chl 29 were proposed as the most likely candidates for the lowest energy pigment[9-11] are inconsistent with their *new analysis* of the CD and CPL spectra.[1] Structure-based quantum chemical/electrostatic calculations cannot resolve this issue, as several Chls, i.e., Chl 11,

Chl 23, Chl 26 and Chl 29, could have the lowest site energy, while the site energy of the Chl 12 is likely blue shifted.[1,11] Here (see also the main manuscript) we emphasize that literature assignments of pigment site energies in CP47 differ primarily due to differences in the experimental data simulated, different spectral densities, and often a different level of theory employed in calculations. For example, one cannot take parameters obtained via simple excitonic calculations[10] while fitting a set of experimental data which includes the 695 nm emission band (characteristic of intact CP47 complexes), and use them directly in Redfield-type calculations while fitting spectra obtained for a mixture of intact and destabilized complexes (characterized by much broader emissions with variable maxima between 689 and 692 nm). Such a comparison was employed in ref 11 in order to argue against the site energy assignments from simple excitonic calculations. Besides, all calculated Chl site energies should be taken with a grain of salt, as they rarely perfectly reproduce measured optical spectra. As demonstrated below and recently in ref [12], several different sets of parameters can describe the spectra very well.

As argued in the main manuscript, we do not think that the spectra simulated in ref 1 correspond to pure, intact CP47 complexes. Nevertheless, for completeness, we also model all spectra from Hall et al.[1] to demonstrate that the set of proposed parameters is not unique and other combinations of site energies provide much better simultaneous fits. We tested all pigments as possible lowest energy Chls. Several sets of parameters provide good fits, questioning the reliability of the recently proposed assignment.[1] An incorrect assignment of site energies will impact our understanding of excitation energy transfer in CP47 and the entire PSII-cc.

Below we show the outcomes obtained with our algorithm that reasonably well fit all data from ref 1, assigned by us to destabilized complexes. Recall, that in the main manuscript we argue that these spectra represent a mixture of three subpopulations of CP47 complexes, and should not be

fitted with one set of parameters. These fits are only for comparison with data presented in ref 1 and demonstrate that similar or better fits can be obtained with multiple sets of parameters. We emphasize that many parameters have not been determined experimentally as of yet, and, as a result, the fitting parameters need to be tested against different types of experimental data, including time-resolved spectroscopies. All models split the 16 Chls into five excitonic domains, as in refs 1 and 11, and use the same lognormal phonon spectral density[12] and vibrational modes,[10] although similar fits can be obtained for one domain (i.e., no V_{nm} values are set to zero). V_{nm} values are based on the 3ARC structure,[6] calculated with the Poisson-TrEsp (Figure A.9) and TrEsp (Figures A.8, A.10 and A.11) methods. Table A.6 summarizes fit parameters for Models I-IV.

A.6.1. Model I (Chl 26), Case C.

Figure A.8 clearly shows that Chl 11 does not have to be the lowest energy pigment in order to describe the positive low-energy band of the CPL spectrum. This contrasts the main conclusion given by Hall et al.[1] who also fitted the same absorption, emission, CPL and CD spectra, as those fitted below. Namely, we show that a different set of parameters with Chl 26 as the lowest energy pigment, provides even better fits of the experimental spectra of Hall et al.[1] Thus, the site energies reported in ref 1 are not unique, as fits of their spectra cannot exclude that Chl 26 is the lowest energy pigment. The contribution numbers for Chls 26, 27, and 15 are 64.5%, 13.6%, and 12.6%, respectively. S_{ph}, = 0.91, $S_{vib\text{-}em}$ = 0.54 and $S_{vib\text{-}abs}$ = 0.45.

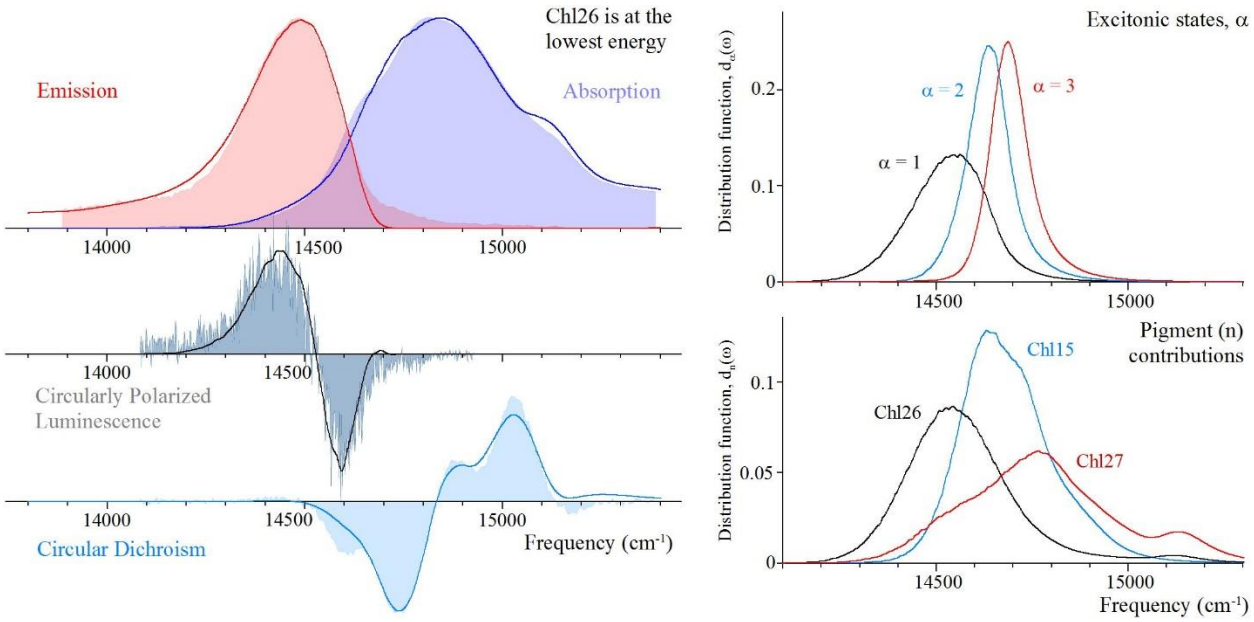

Figure A.8 *Left* (Case C): Best simultaneous fits (lines) of 5 K absorption (dark blue), emission (red), 2 K CPL (black) and CD (cyan) spectra compared to experiment (filled curves). *Right*: Contributions to 5 K absorption of the three lowest energy exciton states (top) and the three pigments (Chls 26, 27, and 15) which contribute most to the $\alpha = 1$ exciton state (bottom). Fitting error = 6.8.

A.6.2. Model II (Chl 29), Case B.

Figure A.9 shows the best fits with Chl 29 as the lowest energy Chl. To improve fits we used three values of Γ_{inh} (see Table A.6) and in our fitting algorithm the values of site energies, S and the three Γ_{inh} are treated as free parameters. The contribution numbers for Chls 29, 11, 27 and 24 are 46.7%, 40.7%, 6.5%, and 3.9%, respectively. S_{ph}, = 0.3, $S_{vib\text{-}em}$ = 0.65 and $S_{vib\text{-}abs}$ = 0.35.

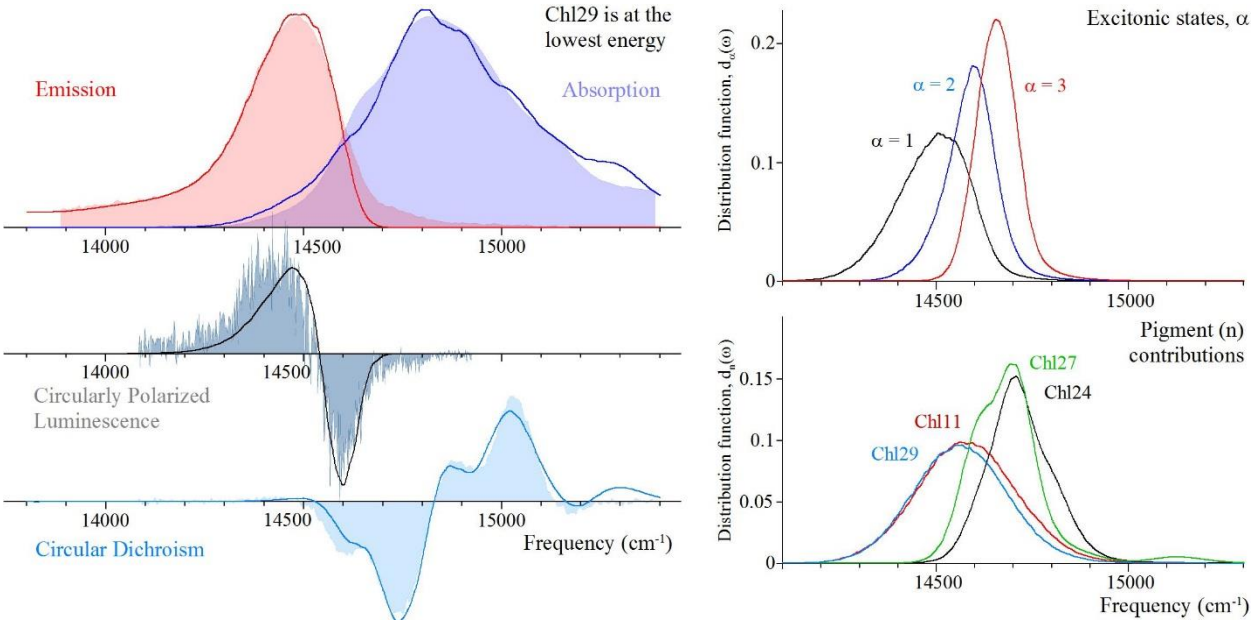

Figure A.9 *Left* (Case B): Best simultaneous fits (lines) of 5 K absorption (dark blue), emission (red), 2 K CPL (black) and CD (cyan) spectra compared to experiment (filled curves). *Right*: Contributions to 5 K absorption of the three lowest energy exciton states (top) and the four pigments (Chls 29, 11, 27, and 24) which contribute most to the α = 1 exciton state (bottom). Fitting error = 8.4.

A.6.3. Model III (Chl 11), Case C.

In Figure A.10 we show that it is also possible to obtain very good fits assuming Chl 11 as the lowest energy pigment. But the parameters extracted from our fits are very different than those reported in ref 1. Similarly to Model II, we use three different Γ_{inh} values for different groups of pigments (see Table A.6). The contribution numbers for Chls 11, 27, and 21 are 72.3%, 11%, and 3.7%, respectively. S_{ph}, = 0.3, $S_{vib\text{-}em}$ = 0.65 and $S_{vib\text{-}abs}$ = 0.35.

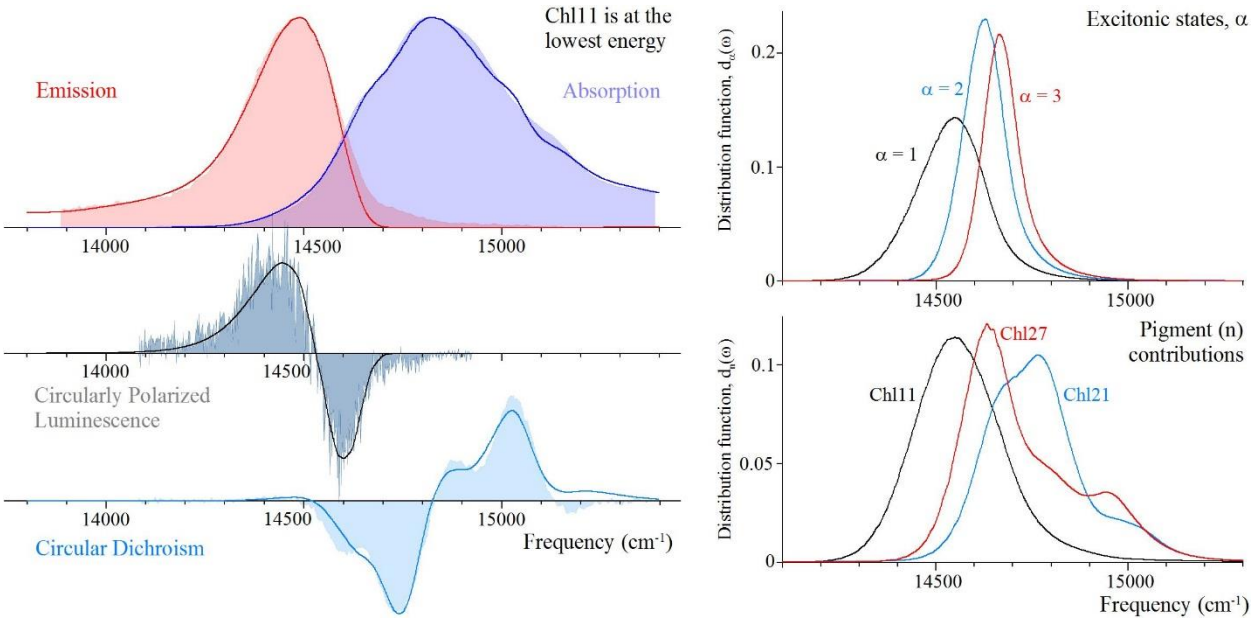

Figure A.10 *Left* (Case C): Best simultaneous fits (lines) of 5 K absorption (dark blue), emission (red), 2 K CPL (black) and CD (cyan) spectra compared to experiment (filled curves). *Right*: Contributions to 5 K absorption of the three lowest energy exciton states (top) and the four pigments (Chls 11, 27, and 21) which contribute most to the $\alpha = 1$ exciton state (bottom). Fitting error = 6.4.

A.6.4. Model IV (Chl 17), Case C.

Figure A.11 shows that good fits can be also obtained assuming Chl 17 as the most red-shifted pigment. All Γ_{inh} values are free parameters (see Table A.6 for details). The contribution numbers for Chls 17, 16 and 15 are 79.4%, 7.6%, and 3.1%, respectively. S_{ph}, = 0.8, $S_{vib\text{-}em}$ = 0.5 and $S_{vib\text{-}abs}$ = 0.5.

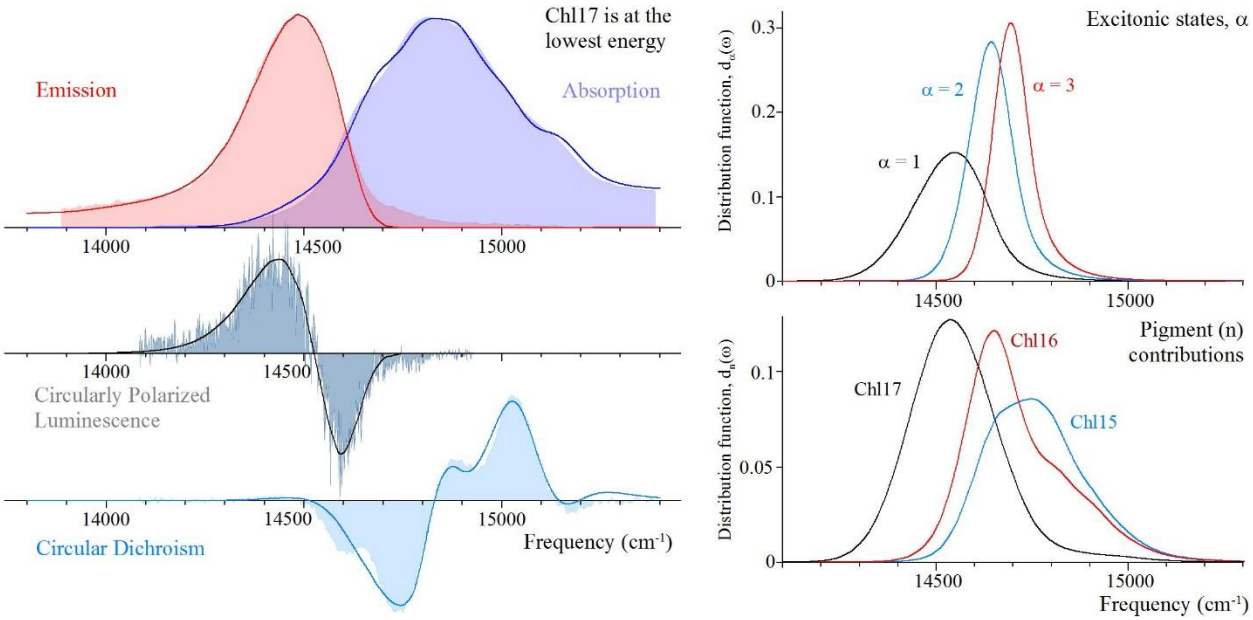

Figure A.11 *Left* (Case C): Best simultaneous fits (lines) of 5 K absorption (dark blue), emission (red), 2 K CPL (black) and CD (cyan) spectra compared to experiment (filled curves). *Right*: Contributions to 5 K absorption of the three lowest energy exciton states (top) and the three pigments (Chls 17, 16, and 15) which contribute most to the $\alpha = 1$ exciton state (bottom). Fitting error = 5.9.

The fits for Models I-IV are good, though not perfect. For example, improved fits of CD lead to worse fits of absorption and CPL spectra. This is most likely due to the fact that these spectra were obtained for very heterogeneous samples. Although, as mentioned above, we do not think that these spectra represent intact complexes, and, as a result, we suggest that the parameters listed in Table A.6 do not represent intact CP47 complexes, unless proven otherwise. In conclusion, more experimental data measured with different techniques for the same sample are needed to resolve this conundrum. See the main manuscript for more details.

Table A.6 Summary of parameters for Models I-IV used to simulate spectra for destabilized CP47[a]

	Model I		**Model II**		**Model III**		**Model IV**	
	Case C		**Case B**		**Case C**		**Case C**	
Chl	E_0^n	Γ_{inh}	E_0^n	Γ_{inh}	E_0^n	Γ_{inh}	E_0^n	Γ_{inh}
11	15 045	159	14 580	292	14 569	231	14 926	182
12	14 920	193	15 283	153	15 137	222	15 134	288
13	14 811	117	14 934	153	14 947	222	14 818	173
14	14 884	267	14 954	153	15 139	99	14 967	195
15	14 716	234	15 026	153	14 817	222	14 814	227
16	14 828	168	14 819	153	15 018	99	14 778	250
17	14 888	215	14 833	153	14 934	222	14 556	234
21	15 174	382	15 093	153	14 790	222	14 950	141
22	14 860	203	15 041	153	14 784	222	14 800	233
23	14 948	215	14 942	153	14 995	99	14 840	196
24	15 058	238	14 710	153	14 848	222	14 953	215
25	15 097	107	15 126	153	14 891	222	15 021	151
26	14 588	276	14 777	153	14 814	99	14 982	199
27	14 799	354	14 687	153	14 752	222	14 961	172
28	14 846	196	14 937	153	14 813	222	14 847	210
29	14 898	150	14 563	277	14 918	222	14 852	195

[a]All values in units of cm^{-1}.

References

(1) Hall, J.; Renger, T.; Müh, F.; Picorel, R.; Krausz, E. The Lowest-Energy Chlorophyll of Photosystem II is Adjacent to the Peripheral Antenna: Emitting States of CP47 Assigned via Circularly Polarized Luminescence. *Biochim. Biophys. Acta* **2016**, *1857*, 1580–1593.

(2) Neupane, B.; Dang, N. C.; Acharya, K.; Reppert, M.; Zazubovich, V. Picorel, R.; Seibert, M.; Jankowiak, R. Insight into the Electronic Structure of the CP47 Antenna Protein Complex of Photosystem II: Hole Burning and Fluorescence Study. *J. Am. Chem. Soc.* **2010**, *132*, 4214–4229.

(3) Polívka, T.; Kroh, P.; Pšenčík, J.; Engst, D.; Komenda, J.; Hála, J. Hole-Burning Study of Excited Energy Transfer in the Antenna Protein CP47 of *Synechocystis* sp. PCC 6803 Mutant H114Q. *J. Lumin.* **1997**, *72-74*, 600–602.

(4) den Hartog, F. T. H.; Dekker, J. P.; van Grondelle, R.; Völker, S. Spectral Distributions of "Trap" Pigments in the RC, CP47, and CP47-RC Complexes of Photosystem II at Low Temperature: A Fluorescence Line-Narrowing and Hole-Burning Study. *J. Phys. Chem. B* **1998**, *102*, 11007–11016.

(5) Madjet, M. E.; Abdurahman, A.; Renger, T. Intermolecular Coulomb Couplings from Ab Initio Electrostatic Potentials: Application to Optical Transitions of Strongly Coupled Pigments in Photosynthetic Antennae and Reaction Centers. *J. Phys. Chem. B* **2006**, *110*, 17268–17281.

(6) Umena, Y.; Kawakami, K.; Shen, J.-R.; Kamiya, N. Crystal Structure of Oxygen-Evolving Photosystem II at a Resolution of 1.9 Å. *Nature* **2011**, *473*, 55–60.

(7) Wei, X.; Su, X.; Cao, P.; Liu, X.; Chang, W.; Li, M.; Liu, Z. Structure of Spinach Photosystem II–LHCII Supercomplex at 3.2 Å Resolution. *Nature* **2016**, *534*, 69–74.

(8) Krausz, E.; Hughes, J. L.; Smith, P. J.; Pace, R. J.; Peterson Årsköld, S. Oxygen-Evolving Photosystem II Core Complexes: A New Paradigm Based on the Spectral Identification of the Charge-Separating State, the Primary Acceptor and Assignment of Low-Temperature Fluorescence. *Photochem. Photobiol. Sci.* **2005**, *4*, 744–753.

(9) Raszewski, G.; Renger, T. Light Harvesting in Photosystem II Core Complexes is Limited by the Transfer to the Trap: Can the Core Complex Turn into a Photoprotective Mode? *J. Am. Chem. Soc.* **2008**, *130*, 4431–4446.

(10) Reppert, M.; Acharya, K.; Neupane, B.; Jankowiak, R. Lowest Electronic States of the CP47 Antenna Protein Complex of Photosystem II: Simulation of Optical Spectra and Revised Structural Assignments. *J. Phys. Chem. B* **2010**, *114*, 11884–11898.

(11) Shibata, Y.; Nishi, S.; Kawakami, K.; Shen, J.-R.; Renger, T. Photosystem II Does Not Possess a Simple Excitation Energy Funnel: Time-Resolved Fluorescence Spectroscopy Meets Theory. *J. Am. Chem. Soc.* **2013**, *135*, 6903–6914.

(12) Reinot, T.; Chen, J.; Kell, A.; Jassas, M.; Robben, K. C.; Zazubovich, V.; Jankowiak, R. On the Conflicting Estimations of Pigment Site Energies in Photosynthetic Complexes: A Case Study of the CP47 Complex. *Anal. Chem. Insights* **2016**, *11*, 35-48.

Appendix B

Supporting Information for "Structure-based Exciton Hamiltonian and Dynamics for the Reconstituted Wild Type CP29 Protein Antenna Complex of the Photosystem II "

B.1. HPLC pigment analysis of reconstituted complexes.

Pigments were extracted from the complexes using a 1:3 chloroform:methanol mixture. The extract was cleared by centrifugation (13200 rpm for 5 minutes). Pigments analysis was performed in a Jasco HPLC system (PU1580/LG-1580-2) using a C18 HPLC column (Spherisorb ODS1 5 µm, 25 × 0.46 cm; Phenomenex) and monitored with a PDA detector (MD1515) in the 350–800 nm range. The column was first equilibrated with an acetonitrile (ACN):H_2O 9:1 mixture. The pigment separation was performed by a linear two component gradient, consisting of an ACN:H_2O 9:1 mixture and ethyl acetate (AcOEt). The ACN:H_2O proportion was held constant, whereas the ACN:H_2O/AcOEt ratio changed from 0 and 60%. The gradient was followed by an isocratic step of 100% AcOEt for 15 minutes. The flow rate was kept constant at 0.75 mL/min. Peaks were assigned on the basis of both their retention time and corresponding spectra.[1] For relative pigments quantification, wavelength pixels were binned to increase the signal to noise ratio. The chromatograms were recorded at 447, 645 and 660 nm and analyzed via Gaussian deconvolution to quantify the content of the different Car(s), Chls *b* and Chls *a*. The stoichiometry of pigment binding to the reconstituted CP29 was determined by using a double standardization procedure: i) relying on the "internal" Chl *a*/Chl *b* and the $Chl_{(a+b)}$/Car ratios, as well as ii) using the chromatograms and the well-established stoichiometries of LHCII pigment coordination.

Structural studies indicate that only one molecule of Neo is bound to either CP29 or each monomer of LHCII.[2] Therefore, the Neo was used as a reference for both samples.

B.2. Analysis of the pigment stoichiometry in CP29.

The black lines in Figure B.1 are the representative experimental chromatograms obtained for isolated (native) LHCII (top) and reconstituted CP29 (bottom), respectively.

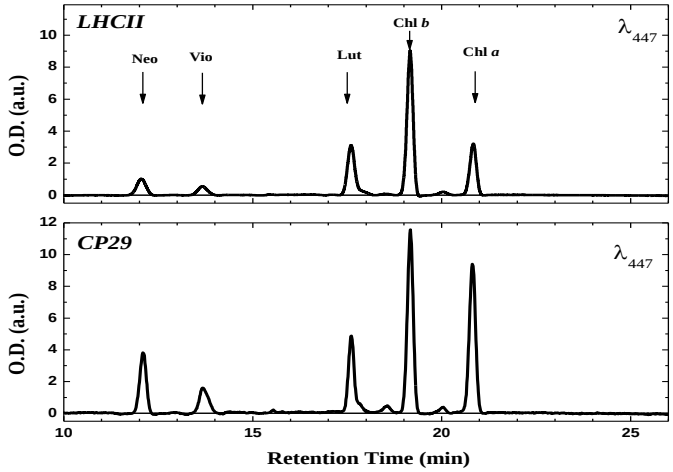

Figure B.1 Top and bottom frames compare representative chromatograms obtained for isolated (native) LHCII and reconstituted CP29, respectively. The CP29 complex was used in our spectroscopic and modeling studies. Both chromatograms were detected at a wavelength of 447 nm. (To increase the signal-to-noise ratio the channels on the diode array detector were binned around the center wavelength resulting in a *fwhm* equivalent to 6 nm).

The peaks are assigned based on both their retention time and their spectra, detected by the on-line diode array system. The chromatograms clearly indicate the complexes contain the same types of pigments, as expected from literature data. Neoxanthin (Neo) is identified as the first eluted peak. Irrespective of analysis details, it is clear that when using Neo as an internal reference, CP29 binds less lutein and has a higher Chl *a*/Chl *b* ratio than LHCII. However, the ratio of Chl *a* to Neo is qualitatively similar in the LHCII and CP29 complexes. Even within the experimental variability (Table B.1 reports the standard deviations), the trend was conserved amongst several runs. The stoichiometry of Chl *b* and Chl *a* detected at 447 nm is also consistent with chromatograms

obtained monitoring at either 645 or 660 nm, which are preferential detection wavelengths for these two pigments.

B.3. Determination of pigment-binding stoichiometry.

In this study the determination of pigment-binding stoichiometry is based on: i) the use of Neo as an internal standard, because the structural studies indicate the presence of one molecule of this pigment per monomeric unit both in CP29 and in LHCII, and ii) the well-established pigment stoichiometry of isolated LHCII as a reference standard.

Table B.1 Summary of the pigment analysis performed on four different pigment extractions from isolated LHCII and reconstituted CP29.

	CP29 A/Neo[*]	**LHCII** A/Neo[*]	**CP29/LHCII** Ratios[§]	**LHCII** Stoichiometry[$]	**CP29** Stoichiometry[#]
Neo	1.0 ± 0.1	1.0 ± 0.1	1.0 ± 0.1	1.00	1.0 ± 0.1
Vio	0.5 ± 0.1	0.5 ± 0.1	0.9 ± 0.1	1.00	0.9 ± 0.1
Lut	1.3 ± 0.1	2.3 ± 0.1	0.6 ± 0.1	2.00	1.2 ± 0.2
Chl *b*	2.7 ± 0.2	5.5 ± 0.2	0.5 ± 0.1	6.00	2.9 ± 0.6
Chl *a*	2.4 ± 0.2	2.2 ± 0.1	1.1 ± 0.1	8.00	9.0 ± 0.6
$Chl_{(a+b)}$				14	11.9 ± 0.8
Chl a/b				1.33	3.0 ± 0.6

[*]A/Neo is the area of each peak in the chromatogram divided by the area assigned to Neoxanthin; the confidence levels are estimated considering the uncertainties of each peak integration and the propagation due to the internal normalization, convoluted with the inter-sample variability. [§]Ratios are [A/Neo(CP29)]/[A/Neo(LHCII)]; [#]errors are from propagation of the confidence levels. [$]LHCII stoichiometry is taken from the structure and assumed to be exact. Therefore, the uncertainties of CP29 stoichiometry shown in Table B.1 could be *underestimated*. It is worth noticing that, although the uncertainties on the chromatograms analysis are relatively contained, the propagation of errors leads to rather large confidence levels on the estimated absolute number of Chl per complex.

The Chl *a*/*b* ratios shown in Table B.1 agree with those estimated in parallel spectrophotometric measurements, that yielded values of 1.31 ± 0.1 and 3.0 ±0.1 for LHCII and CP29, respectively. Moreover, these values agree very nicely with most of the literature reports concerning isolated LHCII,[3,4] and are in close agreement with the values found for reconstituted CP29[5,6] From this

analysis the number of Chls bound to CP29 is equivalent to 11.9 ± 0.8 per complex. Since a fractional number of Chls are hard to visualize, the reconstituted CP29 complex has "lost" some Chls with respect to the pigment observed in the structural data[7] with the most likely stoichiometry being 12 Chl per complex on average. However, notice that the confidence interval allows for ±1 Chl per complex. The comparison with structural data suggests that reconstituted CP29 mainly loses Chl *b*, whereas Chl *a* is almost fully retained.

B.4. Phonon and vibrational spectral densities.

Left frame in Figure B.2 compares the CP29 phonon spectral density $J(\omega)$ (blue curve) used in our modeling studies with that used in by Müh et al.[8] (red curve). Our $J(\omega)$ is described by a continuous function, which is chosen to be a lognormal distribution.[9] The right frame shows the vibrational spectral density based on ref [10].

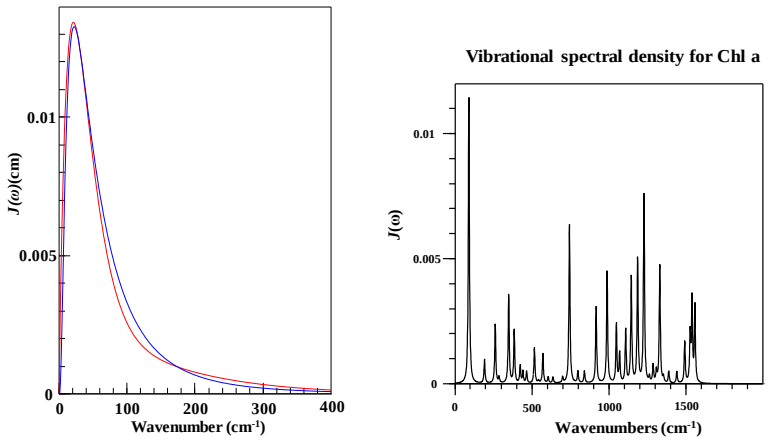

Figure B.2 Comparison of the CP29 phonon spectral density $J(\omega)$ (blue curve) used in our modeling studies with that used in by Müh et al.;[8] the latter $J(\omega)$ was obtained from the 1.6 K FLN spectra measured for B777 complexes from LH1 (red curve).[11] Integrated area normalized to unity for a direct comparison. Right frame shows the vibrational spectral density.[10]

This work uses the theory of Müh et al.[8] and Hall et al.[12] presented experimental evidence which was the motivation for taking dynamic localization of vibrational states into account. The

difference between this work and Müh et al. is that here a vibrational spectral density is used in the line shape (which results in overtone bands) instead of only fundamental bands. Equations 1 and 2 show the formulas for vibrational spectral density $J_{vib}(\tilde{\nu})$ and localized line shape $D_m(\tilde{\nu})$) functions, respectively.

$$J_{vib}(\tilde{\nu}) = \sum_i \frac{s_i}{2\pi} \frac{\Gamma}{(\tilde{\nu}-\tilde{\nu}_i)^2+\left(\frac{\Gamma}{2}\right)^2} \tag{B.1}$$

where Γ is *fwhm* and is taken to be the same for all modes (the value for Γ is given in the main text of this paper). The localized line shape function is given by Eq. 2

$$D_m(\tilde{\nu}) = \int_{-\infty}^{\infty} \mathrm{e}^{2\pi \mathrm{i}(\tilde{\nu}-\varepsilon_m+E_\lambda)\tau+G_{ph}(\tau)-G_{ph}(0)}\left(\mathrm{e}^{G_{vib}(\tau)}-1\right)d\tau \tag{B.2}$$

where ε_m is site energy and $G(\tau)$ are Fourier transforms of respective $J(\tilde{\nu})$ functions. $D_m(\tilde{\nu})$ represents localized vibrationally excited states, but does not include any contribution from 0-0 transitions. More detail can be found in the Supporting information of Müh et al. [8]

B.5. Zero-phonon holes.

Curves d and e (see Figure 3.5 in the main text) show zero-phonon holes (ZPHs) obtained for ν_{B3} = 15355 cm^{-1} and ν_{B4} = 14941 cm^{-1}, respectively. These holes are enlarged below (solid lines). The corresponding Lorentzian fits as shown as dashed curves. The EET times from Chls *b* (absorbing near 650 nm, ν_{B3}) and Chls *a* (absorbing near 670 nm, ν_{B4}) to the lowest energy trap(s), corrected for spectral resolution of 2 cm^{-1}, are 2.7 ± 0.5 and 3 ± 0.5 ps, respectively.

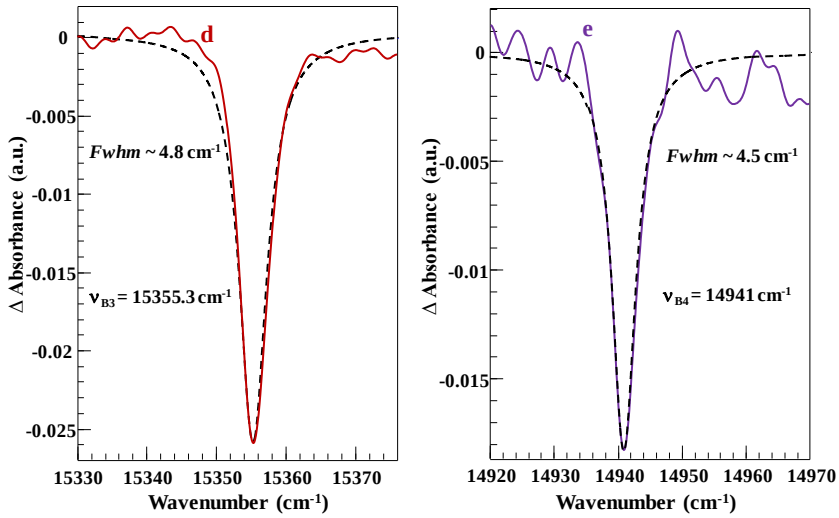

Figure B.3 Curves d and e show ZPHs obtained for ν_{B3} = 15355 cm^{-1} (λ_{B3} = 651.2 nm) and ν_{B4} = 14941 cm^{-1} (λ_{B4} = 669.3 nm), respectively. Dashed lines are the Lorentzian fits to the experimental ZPHs.

B.6. Exciton energies and electronic coupling constants.

The exciton energies ε_M (the eigenvalues; in cm^{-1}/nm) and pigment contributions obtained in this work from fitted site energies and excitonic coupling are shown in Tables B.2 and B.3. Table B.2 shows a direct comparison of values to those reported in ref 8. For Subpopulation (Sub.) I, the lowest exciton state is delocalized over several pigments (delocalization length is 3.03). The 2nd exciton is mostly localized on Chl *a*604 (delocalization length is 1.02). The lowest exciton state delocalization length is 2.3 and 2nd exciton is localized on *a*604 in the ref 8. For Sub. II, the lowest exciton state is localized on Chl *a*604. The 2nd exciton state is delocalized over *a*611, *a*615, *a*612, *a*602 Chls (delocalization length is 3.03).

Table B.2 Exciton energies ε_M (in cm^{-1}/nm) of reconstituted CP29 based on simultaneous fit of absorption, and excitation dependent emissions/nonresonant HB spectra obtained for Sub. I compared to ε_M values reported in ref 8. Major contributing pigments to various exciton states are indicated in the third and fifth columns.

M	**ε_M (cm^{-1}/nm)**	**Major contributing pigments (Sub I)**	**ε_M (cm^{-1}/nm)[8]**	**Major contributing pigments[8]**
1	14756 / 677.7	*a*611, *a*615, *a*612, *a602*	14770 / 677.0	*a*611, *a*615, *a*612
2	14808 / 675.3	*a*604	14800 / 675.7	*a*604
3	14836 / 674.0	*a*609, *a*602, *a*611, *a*603	14840 / 673.9	*a*603, *a*609
4	14883 / 671.9	*a*610, *a*615, *a*609, *a*602	14880 / 672.0	*a*613
5	14943 / 669.2	*a*613	14890 / 671.6	*a*602, *a*603, *a*610, *a*611, *a*612, *a*615
6	14954 / 668.7	*a*610, *a*602, *a*612, *a*615, *a*609	14930 / 669.8	*a*602, *a*603, *a*609, *a*610, *a*611, *a*612, *a*615
7	15028 / 665.4	*a*612, *a*610, *a*602, *a*615	14980 / 667.6	*a*602, *a*603, *a*609, *a*610, *a*611, *a*612
8	15105 / 662.0	*a*603, *a*611, *a*609, *a*615	15020 / 665.8	*a*602, *a*603, *a*609, *a*611, *a*612, *a*615
9	15157 / 659.8	*a*603, *a*611, *a*615, *a*609	15060 / 664.0	*a*602, *a*603, *a*609, *a*615
10	15393 / 649.6	*b*607	15430 / 648.1	*b*607
11	15401 / 649.3	*b*608	15440 / 647.7	*b*608
12	15674 / 638.0	*b*614	15670 / 638.2	*b*614
13	15699 / 637.7	*b*606	15690 / 637.3	*b*606

Table B.3 Exciton energies ε_M (in cm^{-1} and nm) of reconstituted CP29 based on simultaneous fit of absorption, and excitation dependent emissions/nonresonant HB spectra obtained for Sub. II (minor). Major contributing pigments to various exciton states are indicated in the fourth columns.

M	ε_M (cm^{-1})	ε_M (nm)	Major contributing pigments (sub II)
1	14673	681.5	*a*604
2	14756	675.7	*a*611, *a*615, *a*612, *a*602
3	14836	674.0	*a*609, *a*602, *a*611, *a*603
4	14883	671.9	*a*610, *a*615, *a*609, *a*602
5	14943	669.2	*a*613
6	14954	668.7	*a*610, *a*602, *a*612, *a*615, *a*609
7	15028	665.4	*a*612, *a*610, *a*602, *a*615
8	15105	662.0	*a*603, *a*611, *a*609, *a*615
9	15157	659.8	*a*603, *a*611, *a*615
10	15392	649.7	*b*607
11	15402	649.3	*b*608
12	15674	638.0	*b*614
13	15697	637.1	*b*606

Table B.4 shows the coupling constants (off-diagonal matrix elements) calculated with the TrEsp method for the 2.8 Å X-ray structure of CP29 (PDB ID: 3PL9[7]). If the Poisson-TrEsp V_{nm} values (Table B.5) are used, instead of TrEsp coupling constants, good fits of 5 K absorption, emission and nonresonant HB are obtained (Figure B.4) by just slightly modifying site energies and inhomogeneity of some Chls (Table B.6). For more comparison (see section 3.4.4 of the main text), the site energy of Chl *a*604 is red-shifted by 83 cm^{-1} (Figure B.5) to obtain the difference between WT and Y135F CP29. In this case data shown in Figure B.5 also support the experimental data from ref [13]. Therefore, the method of determining the coupling constants is not a critical factor.

Table B.4 TrEsp Coupling Constants (cm^{-1}) for CP29 Used in this Work.

Chl	*a*602	*a*603	*a*604	*b*606	*b*607	*b*608	*a*609	*a*610	*a*611	*a*612	*a*613	*b*614	*a*615
***a*602**	0	27	9	6	8	-10	-41	-9	0	13	-3	0	58
***a*603**		0	-1	-4	5	8	108	12	-1	1	3	-7	-4
***a*604**			0	101	35	-9	-6	-4	-5	2	3	-3	-5
***b*606**				0	29	-9	2	-2	-2	1	1	-2	-3
***b*607**					0	-5	-9	0	-3	2	4	-2	-3
***b*608**						0	40	67	8	-2	-4	2	8
***a*609**							0	-2	6	-1	-5	3	9
***a*610**								0	-47	26	9	-1	-13
***a*611**									0	98	-5	3	110
***a*612**										0	1	0	-2
***a*613**											0	-14	-6
***b*614**												0	2
***a*615**													0

Table B.5 Coupling constants V_{nm} (cm^{-1}) for CP29 Obtained by from the Poisson-TrEsp Method.[8]

Chl	*a*602	*a*603	*a*604	*b*606	*b*607	*b*608	*a*609	*a*610	*a*611	*a*612	*a*613	*b*614	*a*615
***a*602**	0	14	6	5	6	-7	-26	-4	0	7	-1	0	34
***a*603**		0	0	-3	5	4	81	6	-1	1	2	-4	-2
***a*604**			0	67	24	-4	-5	-1	-3	2	2	-2	-3
***b*606**				0	20	-4	2	-1	-2	2	1	-1	-2
***b*607**					0	-3	-6	1	-2	2	2	-1	-2
***b*608**						0	27	38	5	-1	-2	1	5
***a*609**							0	-1	4	-1	-3	1	6
***a*610**								0	-31	14	5	0	-9
***a*611**									0	73	-3	1	70
***a*612**										0	1	0	-1
***a*613**											0	-9	-4
***b*614**												0	0
***a*615**													0

B.7. CP29 mixture model for 12.5 pigments using Poisson-TrEsp coupling constants.

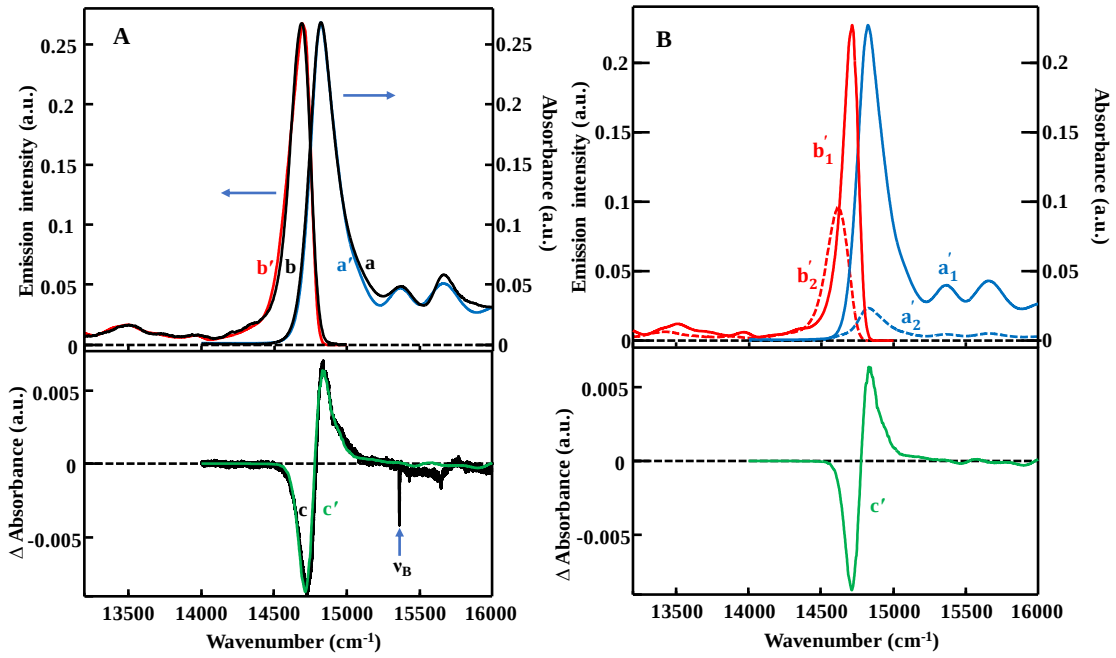

Figure B.4 CP29 mixture model for 12.5 pigments using V_{nm} from Table B.5 and E_0^n and $\Gamma_{inh}\Gamma_{\mathrm{inh}}$ from Table B.6. Spectra a, b, and c are the 5 K experimental absorption, emission, and nonresonant HB (ν_B = 15355 cm^{-1}; λ_B = 651.2 nm) spectra, respectively. Blue (a′), red (b′), and green (c′) curves in frame A represent the calculated absorption, emission, and HB spectra, respectively. Huang-Rhys factors are S_{ph} = 0.56 for all Chls except of Chl *a*604 (S_{a604}= 0.512) and S_{vib} = 0.34. HB spectrum was obtained with fluence *f* of 78 J/cm^2 (I = 65 mW; t = 600 s). Frame B shows the relative contributions to the total absorption (a_1'/a_2'), emission (b_1' at ~679.9 nm / b_2' at ~683.8 nm), and HB (c_1') spectra.

Table B.6 Site energies (E_0^n) and inhomogeneities (Γ_{inh}) in cm^{-1}, calculated for Poisson-TrEsp (second and third columns) and TrEsp (values in fourth and fifth columns) coupling constants. Site energies for the pigments in blue do not change and differences in inhomogeneities are about ±7 cm^{-1}.

Chl[#]	$E_0^{n(a)}$	$\Gamma_{inh}^{(a)}$	$E_0^{n(b)}$	$\Gamma_{inh}^{(b)}$
***a*602**	14895	200	14920	207
***a*603**	15061	200	15055	207
***a*604**	14801	159	14817	157
***b*606**	15685	200	15685	203
***b*607**	15398	198	15398	207
***b*608**	15387	200	15387	207
***a*609**	14909	175	14951	176
***a*610**	14925	204	14945	202
***a*611**	14926	200	14953	207
***a*612**	14955	219	14955	207
***a*613**	14918	205	14945	207
***b*614**	15677	200	15677	207
***a*615**	14921	200	14965	207

[#] Labeling of pigments based on ref 7.

[(a)] and [(b)] refer to calculations for Poisson-TrEsp and TrEsp coupling matrix elements (V_{nm}), respectively.

Compare Figure B.5 given below with Figure 3.9 in the main manuscript where the calculations were performed using TrESp coupling constants.

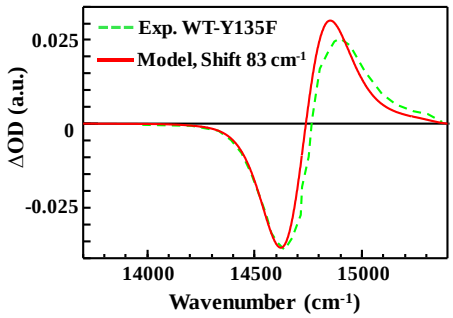

Figure B.5 Absorbance difference (ΔOD) spectra of reconstituted CP29 and the Y135F mutant. Dashed and solid lines correspond to the experimental[13] and simulated (using parameters from Tables B.5 and B.6) ΔOD spectra at room temperature, respectively.

B.8. Excitonic structure and composition of the lowest energy exciton states using TrEsp V_{nm}

Figure B.6 shows the exciton state contribution function ($d_m(\omega)$, converted to wavelength units) of each of the 13 Chls sites in reconstituted CP29, resulting from the simultaneous fit of absorption, emission, and NRHB spectra at 5 K. The solid lines describe the exciton states of the major Sub. I. The dashed line shows the contribution of *a*604 that dominates the lowest-energy state ***A*** of Sub. II. All remaining pigment contributions are the same in both subpopulations. Exciton delocalization is revealed by the occurrence of more than one peak in the distribution function of the *m*-th Chl.

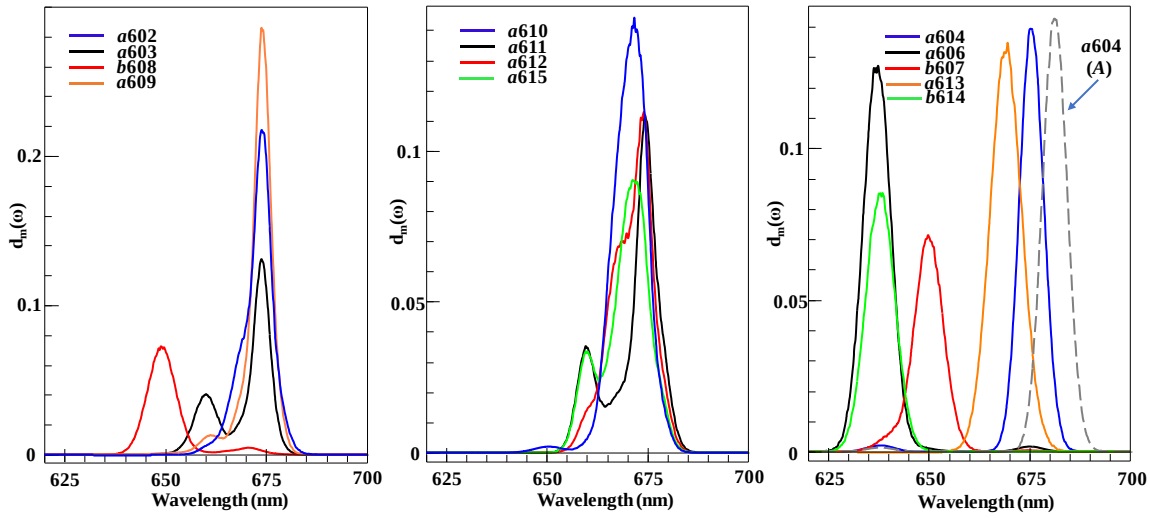

Figure B.6 Pigment contribution functions $d_m(\omega)$ of the 13 Chls sites in reconstituted CP29 based on simultaneous fits of absorption, emission, and NRHB spectra. The dashed gray line in the right frame show contribution from *a*604 of Sub. II.

B.9. The structures of the CP29 complex.

Three different structural models for CP29 have been presented corresponding to PDB IDs 3PL9[7] (resolution 2.8 Å), 3JCU[14] (resolution 3.2 Å) and 5XNM[15] (resolution 3.2 Å); see Figure B.7. The CP29 structure used for modeling in this work (3PL9), which is the only one available for the

native CP29 complex isolated from spinach, contains 9 Chls *a* and 4 Chls *b* (Figure B.7A). The CP29 structure observed within the PSII-LHCII supercomplex (3JCU[14]) resolved 10 Chls *a* and 3 Chls *b* as shown in Figure B.7B. Finally, Figure B.*7*C shows the CP29 structure observed within the $C_2S_2M_2$ supercomplex (5XNM[15]) displaying 10 Chls *a* and 4 Chls *b*. We note that the *a*601 pigment (light blue) observed in the supercomplexes[14] is most likely Chl *a*615 (pink) observed in the 3PL9[7] structure. Also, the purified CP29 will most likely lose the *a*616 pigment as it is located externally at the N-terminal region (for more details see Figure B.8). Thus, we do not think that *a*616 is present in our reconstituted sample and, as a result, in this manuscript we focus on the high-resolution (2.8 Å) CP29 structure with 13 Chls (3PL9).

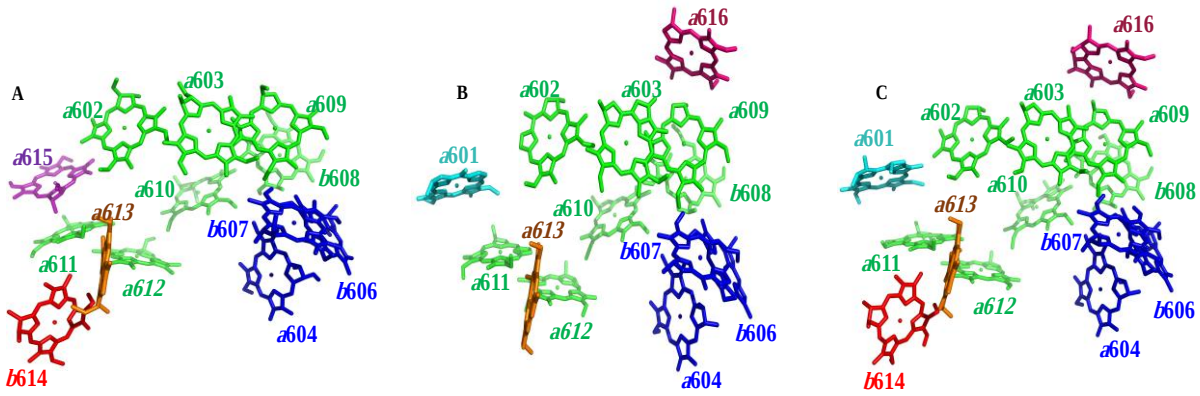

Figure B.7 Three different arrangements of pigments in the CP29 structure. Frame A: The 2011 CP29 structure based on X-ray crystallography data (3PL9[7]) with 9 Chls *a* and 4 Chls *b*. Frame B: The 2016 CP29 structure observed within the PSII-LHCII supercomplex (3JCU[14]) with 10 Chls *a* and 3 Chls *b* (where Chl *b*614 is believed to be lost during purification). Frame C: The 2017 CP29 structure observed within the $C_2S_2M_2$ supercomplex (5XNM[15]) with 10 Chls *a* and 4 Chls *b*.

Table B.7 Pigment comparison of three different structures of CP29, 3PL9,[7] 3JCU[14] and 5XNM.[15] Chl *a*601 in 3JCU and 5XNM are partially overlapped with Chl *a*615 in 3PL9.

3PL9 (2.9 Å)	**3JCU (3.2 Å)**	**5XNM (3.2 Å)**
-------	*a*601	*a*601
*a*602	*a*602	*a*602
*a*603	*a*603	*a*603
*a*604	*a*604	*a*604
*b*606	*b*606	*b*606
*b*607	*b*607	*b*607
*b*608	*b*608	*b*608
*a*609	*a*609	*a*609
*a*610	*a*610	*a*610
*a*611	*a*611	*a*611
*a*612	*a*612	*a*612
*a*613	*a*613	*a*613
*b*614	------	*b*614
*a*615	------	------
------	*a*616	*a*616

B.10. Figure showing the interfacial region between CP29 and CP47.

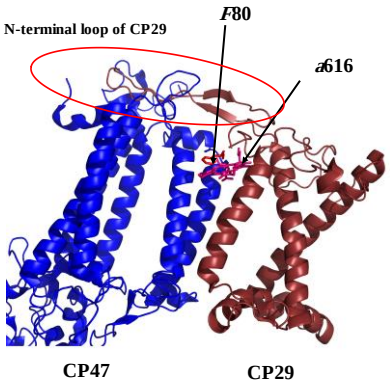

Figure B.8 The *a*616 pigment is located at the interfacial region between CP29 and CP47 and is coordinated by the main chain oxygen of F80 at the N-terminal loop of CP29. That is, if CP29 is purified without CP47 for stabilization, the long N-terminal loop of CP29 might be flexible and *a*616 will most likely be lost.

References

(1) Britton, G.; Young, A.J. Methods for the Isolation and Analysis of Carotenoids. In: Young A.J., Britton G. (eds) Carotenoids in Photosynthesis. Springer, **1993.** Dordrecht.

(2) Liu, Z.; Yan, H.; Wang, K.; Kuang, T.; Zhang, J.; Gui, L.; An, X.; Chang, W. Crystal Structure of Spinach Major Light-Harvesting Complex at 2.72 Å Resolution. *Nature* **2004**, *428*, 287−292.

(3) Peter, G. F.; Thornber, J. P. Biochemical Composition and Organization of Higher Plant Photosystem II Light Harvesting Pigment-Proteins. *J. Biol. Chem.* **1991**, *266*, 16745 - 16 754.

(4) Jennings, R.C.; Bassi, R.; Zucchelli, G. Antenna Structure and Energy Transfer in Higher Plant Photosystems. *Top. Curr. Chem*. **1996**, *177*, 147-181.

(5) Giuffra, E.; Cugini, D.; Croce, R.; Bassi, R. Reconstitution and Pigment-Binding Properties of Recombinant CP29. *European Journal of Biochemistry* **1996**, *238*, 112-120.

(6) Belgio, E.; Casazza, A.P.; Zucchelli, G.; Garlaschi, F.M.; Jennings, R.C. Band Shape Heterogeneity of the Low Energy Chlorophylls of CP29: Absence of Mixed Binding Sites and Excitonic Interactions, *Biochemistry* **2010,** *49*, 882-892.

(7) Pan, X.; Li, M.; Wan, T.; Wang, L.; Jia, C.; Hou, Z.; Zhao, X.; Zhang, J.; Chang, W. Structural Insights into Energy Regulation of Light-harvesting Complex CP29 from Spinach. *Nat. Struct. Mol. Biol.* **2011**, *18*, 309-315.

(8) Müh, F.; Lindorfer, D.; Schmidt am Busch, M.; Renger, T. Towards a Structure-Based Exciton Hamiltonian for the CP29 Antenna of Photosystem II. *Phys. Chem. Chem. Phys.* **2014**, *16*, 11848-11863.

(9) Kell, A.; Feng, X.; Reppert, M.; Jankowiak, R. On the Shape of the Phonon Spectral Density in Photosynthetic Complexes. *J. Phys. Chem. B* **2013**, *117*, 7317−7323.

(10) Rätsep, M.; Pieper, J.; Irrgang, K. D.; Freiberg, A. Excitation Wavelength-Dependent Electron-Phonon and Electron-Vibrational Coupling in the CP29 Antenna Complex of Green Plants. *J. Phys. Chem. B* **2008,** *112*, 110-118.

(11) Renger, T.; Marcus, R. A. On the Relation of Protein Dynamics and Exciton Relaxation in Pigment-Protein Complexes: An Estimation of the Spectral Density and a Theory for the Calculation of Optical Spectra. *J. Chem. Phys.* **2002**, *116*, 9997–10019.

12 Hall, J.; Renger, T.; Picorel, R.; Krausz, E. Circularly polarized luminescence spectroscopy reveals low-energy excited states and dynamic localization of vibronic transitions in CP43. *Biochim. Biophys.Acta.* **2016**, *1857*, 115–128.

(13) Caffarri, S.; Passarini, F.; Bassi, R.; Croce, R. A Specific Binding Site for Neoxanthin in the Monomeric Antenna Proteins CP26 and CP29 of Photosystem II. *FEBS Lett.* **2007**, *581*, 4704-4710.

(14) Wei, X.; Su, X.; Cao, P.; Liu, X.; Chang, W.; Li, M.; Zhang, X.; Liu, Z. Structure of Spinach Photosystem II−LHCII Supercomplex at 3.2 Å Resolution. *Nature* **2016**, *534*, 69−74.

(15) Su, X.; Ma, J.; Wei, X.; Cao, P.; Zhu, D.; Chang, W.; Liu, Z.; Zhang, X.; Li, M. Structure and Assembly Mechanism of Plant C2S2M2-Type PSII-LHCII Supercomplex. *Science* **2017**, *357*, 815–820.

Appendix C

Supporting Information for "On Excitation Energy Transfer within the Baseplate BChl *a*–CsmA Complex of *Chloroflexus aurantiacus*"

C.1. Modeling of various optical spectra.

The modeling approach is described in ref 1; in brief, the disorder is introduced into the diagonal matrix elements (i.e., E_0^n) by a Monte Carlo approach with normal distributions centered at E_0^n (n labeling various pigments) and with fwhm representing the inhomogeneous broadening (Γ_{inh}), which are site-dependent. Eigen decomposition of the interaction matrix provides eigen coefficients (c_n^M) and eigenvalues (ω_M). Phonon and vibrational Huang−Rhys (S) factors are used as free or fixed parameters and are optimized simultaneously against the experimental spectra. Moreover, it is assumed that the phonon spectral density (weighted phonon profile) can be described by a continus function, which is chosen to be a lognormal distribution,[2]

$$J_{ph}(\omega) = \frac{S_{ph}}{\omega\sigma\sqrt{2\pi}}\, e^{-[\ln\left(\frac{\omega}{\omega_c}\right)]^2/2\sigma^2} \qquad \text{(C.1)}$$

where ω_c is the cutoff frequency, S_{ph} is the Huang-Rhys factor for phonons, σ is the standard deviation, and $J_{ph}(\omega \leq 0) = 0$. The parameters for the $J_{ph}(\omega)$, ω_c = 45 cm^{-1} and σ = 0.85 were determined from excitation-dependent FLN calculations of the B777 complex.[3] The vibrational spectral density $J_{vib}(\omega)$ is used from ref 4 and in all simulations the intramolecular vibrational modes (J_{vib}) are dynamically localized.[5] Note that delocalization of vibrational modes leads only to small shifts of the vibrational bands. To calculate the coupling matrix elements (V_{nm}), we use the 5LCB structure of the *C. tepidum* baseplate[6] with rotated Q_y transition dipoles[7] and the TrEsp approach.[8]

The optical spectra are modeled using a non-Markovian reduced density matrix theory[9] with a Nelder-Mead Simplex algorithm for parameter optimization,[10] i.e., we use a search method for multidimensional unconstrained minimization. The algorithm searches the solution space and minimizes the root-mean square deviation while simultaneously fitting multiple spectra. The simultaneous fit of various optical spectra provides constraints on the pigment site energies (i.e., transition frequencies in the absence of interpigment coupling) that are critical to describe the excitonic structure and dynamics. Our in-house written software can simultaneously fit several experimental spectra at different temperatures, providing constraints on the pigment site energies of interest. NRHB spectra are modeled in the following way: after diagonalization of the Frenkel Hamiltonian, a preburn absorption spectrum is calculated from the Redfeild theory. The occupation numbers (squared eigenvector coefficients) of the lowest energy exciton state are used to determine the pigments to be burned. This corresponds to the low-fluence approximation, where only pigments contributiong to the lowest energy state are burned. To fit NRHB spectra, the postburn site-energy distribution of the burned pigment is found from the preburn site-energy distribution function or if the energy landscape is modified, the distribution is shifted to higher energies, whereas all other diagonal elements of the Hamiltonian are unchanged. The Hamiltonian is again diagonalized, and a postburn absorption spectrum is calculated. The resulting NRHB spectrum is calculated as the preburn absorption subtracted from the postburn absorption spectrum.

C.2. Investigation of CsmA-BChl a structure of *C. aurantiacus* and *C. tepidum*.

As *C. aurantiacus* and *C. tepidum* show the same low-energy trap at ~818 nm, it could be concluded that both have very similar baseplate structures, i.e., each CsmA binds one BChl *a* and the baseplate subunit is a BChl *a*-CsmA dimer. However, a key difference observed in optical spectra of the two bacterial baseplates is the single negative CD band observed in the baseplate Q_y

region of *C. aurantiacus*,[11-14] which was suggested as evidence for monomeric BChl *a* baseplate molecules.[7] In contrast, the baseplate of *C. tepidum* exhibits a clear, derivative-like CD signal indicative of an excitonic dimer. We suggest that the anomalous CD character of *C. aurantiacus* baseplate is not due to the intrinsic CD signal of the BChl *a* pigments as, in contrast to Chl *a*, the intrinsic rotational strength of BChl *a* is positive.[15] A possible alternative explanation is that the corresponding positive CD band of the *C. aurantiacus* BChl *a*-CsmA dimer reported before is most likely obscured by the chlorosome BChl *c* CD signal. The presence of overlapping CD bands is supported by previously reported data where the removal of BChl *c* led to the observation of the BChl *a* absorption band near 794 nm and characteristic excitonic dimer-like CD bands.[13] We note, however, that due to the large energetic disorder an exciton state is, on average, mainly contributed to by one BChl *a* of a dimer (80-90%). The effects of disorder on the excitonic structure are highlighted below. All parameters are summarized in Table C.1.

Table C.1 Parameters for BChl *a* monomer and dimer baseplate models

	Cb. tepidum		*C. aurantiacus*	
	Monomer	Dimer	Monomer	Dimer
Site Energy	12520	12520	12513	12500
Γ_{inh}	325	325	307	300
S_{ph}	2	2	1.2	1.2
$S_{vib,\ Abs/Emi}$	0.4/0.4	0.4/0.4	0.4/0.8	0.4/0.6

Figure C.1 shows baseplate 5 K absorption, fluorescence, and nonresonant HB spectra, as well as linear dichroism (LD) spectra from the literature (room temperature and 77 K for *Cb. tepidum*[6] and *C. aurantiacus*,[12] respectively), can be reasonably fit assuming no interactions between BChl *a* molecules ($V_{mn} = 0$). The pigment site energies are 12520 cm^{-1} (796.8 nm) and 12513 cm^{-1} (799.2 nm), and the *fwhm* of inhomogeneous broadening 325 and 307 cm^{-1} for *C. tepidum* and *C.*

aurantiacus, respectively. The fluorescence and HB signals only arise from the lowest energy states. To reproduce these spectra an effective baseplate lattice (consisting of more than one monomer) has to be taken into account, which implicitly adds EET to the model. The number of BChl *a* pigments necessary to fit the spectra are 12 and 16 for *C. tepidum* and *C. aurantiacus*, respectively. A previous theoretical study of *Cb. teidum* photosystems modeled the baseplate as 32 CsmA–BChl *a*.[16] Note that the number of CsmA–BChl *a* subunits used for the simulations below is not representative of the actual sizes of the baseplates, but rather is necessary to account for exciton migration across the baseplate lattice.

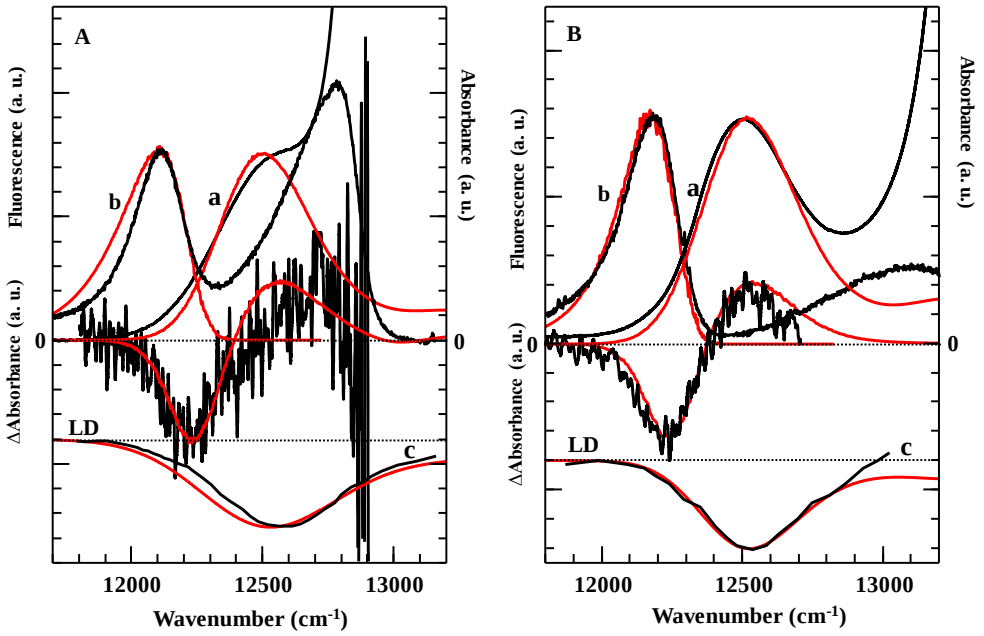

Figure C.1 BChl *a* monomer model. Simultaneous fit of 5 K absorption, fluoresence and NRHB spectra and room temperature LD spectrum of *C. tepidum* (left)[6] and 77 K LD spectrum of *C. aurantiacus* (right).[12] Effective baseplate sizes of 12 and 16 BChl *a*-CsmA complexes are needed to fit fluorescence and HB spectra of *C. tepidum* and *C. aurantiacus*, respectively.

However, it is well known that the *C. tepidum* baseplate contains BChl *a* dimers. The CD spectrum (not included in Figure C.1) cannot be explained by solely monomeric BChl *a*. Using the modifed cryo-electron structure[7] Figure C.2 shows fits of the low-temperature data assuming BChl *a* dimers with V = 50 cm^{-1}. Due to weak interdimer coupling the excitons are only

delocalized over a single dimer, and it is assumed that EET occurs by exciton hopping across the baseplate structure until the energy becomes trapped at a local energetic minimum. The resulting site energies and inhomogeneous widths are 12520 and 12500 cm^{-1}, and 325 and 300 cm^{-1}, for *Cb. tepdium* and *C. aurantiacus*, respectively. The main difference between optical spectra for *Cb. tepdium* and *C. aurantiacus* is the fluorescence spectra, which are shifted ~5 nm from each other. While the lowest energy states revealed by HB (indicative of the fluorescence origin band) are very similar, the larger Stokes shift for *C. tepidum* can be explained by a larger electron-phonon coupling strength. Indeed, the simulated spectra for the *C. tepidum* baseplate are fit with $S = 2$ while $S = 1.2$ for *C. aurantiacus*.

Even though the BChls interact in the dimer model, the coupling constant is an order of magnitude smaller than the inhomogeneous disorder and on the same order as the reorgantization energy (~80 cm^{-1}). These two contributions introduce Anderson-type and dynamic localizations. The former is taken into account implictly in our modeling in that random site energy assignments gurantee that some realizations of disorder will create dimers with two very different site energies, resulting in localization on a single BChl *a*. As the model only calculates the stationary exciton states, dynamic disorder is not included *a priori*; but such localization can be forced by setting coupling constants to be zero. This is effectively the reason for ignoring interdimer delocalization. Thus, the dimer model simulates an energy landscape where exciton "hopping" occurs along an energetic funnel towards a local minimum and each exciton may be quasi-localized on a single pigment depending on the intradimer site energy difference. Therefore, the addition of electronic coupling between the BChl *a* pigments of the dimer does little to perturb the simulated spectra, as the exciton states are still fairly localized on a single site. For the calculations presented in this work, the lowest energy state is 90% localized on a single BChl *a*. The exception of course is the CD spectrum,

where the signal is proprtional to the amount of exciton delocalization and only the dimer model can generate excitonic CD bands.

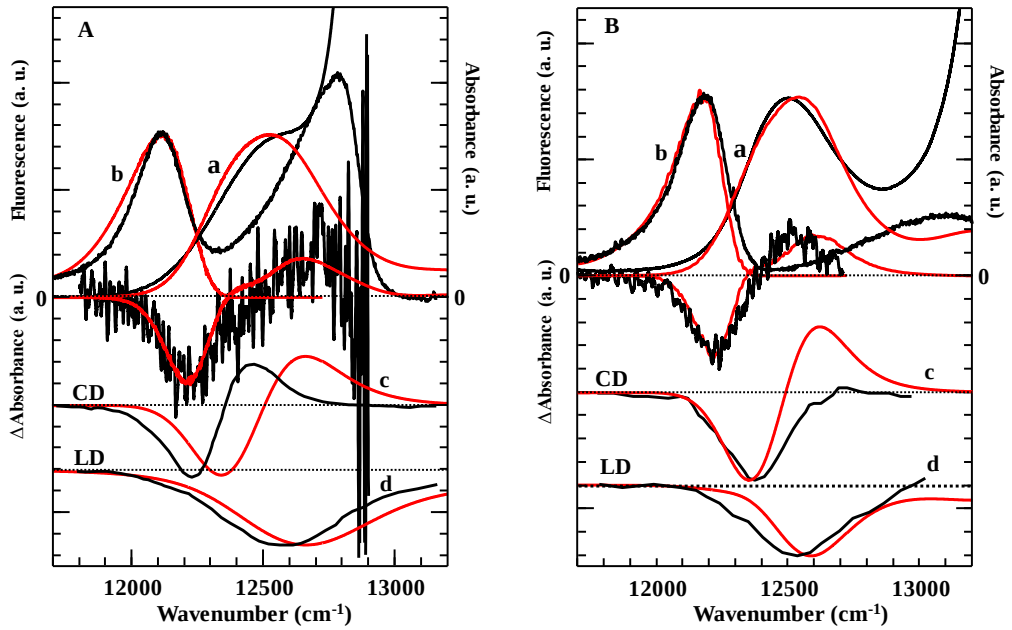

Figure C.2 BChl *a* dimer model. Simultaneous fit of 5 K absorption, fluoresence and NRHB spectra and 77 K CD spectra of *C. tepidum* (left)[6] and *C. aurantiacus* (right).[12] LD spectra are room temerature and 77 K for *C. tepidum* (left)[6] and *C. aurantiacus*,[12] respectively. Effective baseplate sizes of 6 and 8 BChl *a*-CsmA dimers for *C. tepidum* and *C. aurantiacus*, respectively, are needed to fit fluorescence and HB spectra.

Regarding our modeling studies we note that although the monomer model (without any interactions between BChls) fits the optical spectra reasonably well, we suggest that the baseplate of *C. aurantiacus* consists of dimers (in agreement with published structural data[6] but disorder keeps the exciton quasi-localized. That is, the dynamic disorder prevents interdimer delocalization and then Anderson localization keeps the exciton mainly localized on a single pigment (80-90%) as mentioned above. Therefore, the final fits obtained for the monomer and dimer models do not change the spectral shapes much, and the quality of spectral fits alone cannot be used to distinguish between the two models discussed in this work. However, the similarities between the HB spectra of both bacterial species indicate similar electronic structures. As the structure of *C. tepidum* is

known to consist of a two-dimensional lattice of BChl *a*–CsmA dimers, it follows that *C. aruantiacus* has a similar structure.

C.3. Comparison of isolated chlorosomes samples.

Figure C.3 shows comparisons between the absorption spectra of this work and from the literature. Curves a and b in frame A are isolated chlorosomes from ref 14 and our work, respectively. The $A_{chlorosomes}/ A_{baseplate}$ and $A_{chlorosomes}/A_{B808-866}$ ratios in the *C. aurantiacus* sample used in this work is about 20 and 200, respectively. Frame B compares the 1.8 K[17] absorption of isolated B808-866 (curve a) with the 5 K absorption of chlorosomes (this work) normalized at the B866 band. The B808 absorption is very weak compared to the baseplate BChl *a* such that contamination by the B808-866 complex is negligible.

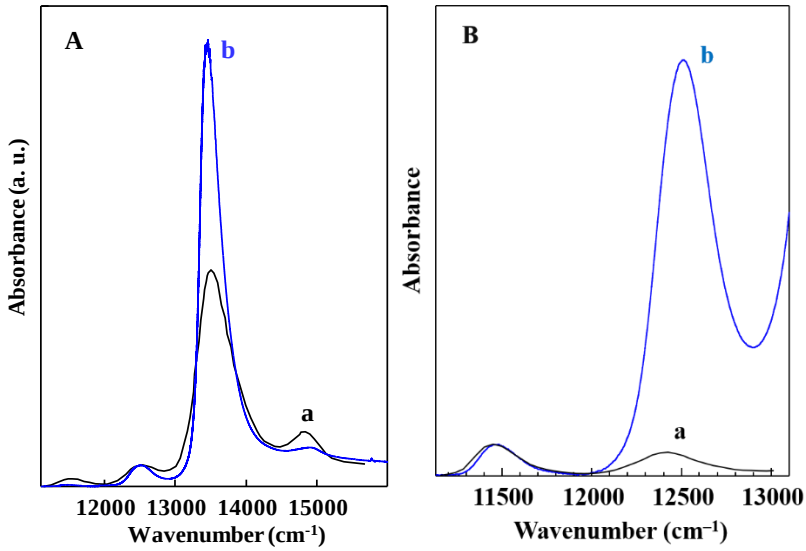

Figure C.3 Frame A: Comparison of isolated chlorosome absorption spectra from the literature (curve a)[14] and this work (curve b). Frame B: Comparison of isolated B808-866 (curve a)**Error! Bookmark not defined.** and chlorosome from this work (curve b).

References

(1) Kell, A.; Blankenship, R. E.; Jankowiak, R. Effect of Spectral Density Shapes on the Excitonic Structure and Dynamics of the Fenna–Matthews–Olson Trimer from *Chlorobaculum tepidum*. *J. Phys. Chem. A* **2016**, *120*, 6146–6154.

(2) Kell, A.; Feng, X.; Reppert, M.; Jankowiak, R. On the Shape of the Phonon Spectral Density in Photosynthetic Complexes. *J. Phys. Chem. B* **2013**, *117*, 7317–7323.

(3) Creemers, T. M. H.; de Caro, C. A.; Visschers, R. W.; van Grondelle, R.; Völker, S. Spectral Hole Burning and Fluorescence Line Narrowing in Subunits of the Light-Harvesting Complex LH1 of Purple Bacteria. *J. Phys. Chem. B* **1999**, *103*, 9770–9776.

(4) Rätsep, M.; Freiberg, A. Electron–Phonon and Vibronic Couplings in the FMO Bacteriochlorophyll *a* Antenna Complex Studied by Difference Fluorescence Line Narrowing. *J. Lumin.* **2007**, *127*, 251–259.

(5) Hall, J.; Renger, T.; Picorel, R. Krausz, E. Circularly Polarized Luminescence Spectroscopy Reveals Low-Energy Excited States and Dynamic Localization of Vibronic Transitions in CP43. *Biochim. Biophys. Acta* **2016**, *1857*, 115–128.

(6) Nielsen, J. T.; Kulminskaya, N. V.; Bjerring, M.; Linnanto, J. M. Rätsep, M.; Pedersen, M. Ø.; Lambrev, P. H.; Dorogi, M.; Garab G.; Thomsen, K.; Jegerschöld, C.; Frigaard, N. U.; Lindahl, M.; Nielsen, N. C. *In situ* High-Resolution Structure of the Baseplate Antenna Complex in *Chlorobaculum tepidum*. *Nat. Commun*. **2016**, *7*, 12454.

(7) Lindorfer, D.; Renger, T. Theory of Anisotropic Circular Dichroism of Excitonically Coupled Systems: Application to the Baseplate of Green Sulfur Bacteria. *J. Phys. Chem. B* **2018**, *122*, 2747–2756.

(8) Madjet, M. E.; Abdurahman, A.; Renger, T. Intermolecular Coulomb Couplings from Ab Initio Electrostatic Potentials: Application to Optical Transitions of Strongly Coupled Pigments in Photosynthetic Antennae and Reaction Centers. *J. Phys. Chem. B* **2006**, *110*, 17268–17281.

(9) Renger, T.; Marcus, R. A. On the Relation of Protein Dynamics and Exciton Relaxation in Pigment–Protein Complexes: An Estimation of the Spectral Density and a Theory for the Calculation of Optical Spectra. *J. Chem. Phys.* **2002**, *116*, 9997–10019.

(10) Nelder, J. A.; Mead, R. A. Simplex Method for Function Minimization. *Comput. J.* **1965**, *7*, 308–313.

(11) Brune, D. C.; Gerola, P. D.; Olson, J. M. Circular Dichroism of Green Bacterial Chlorosomes. *Photosynthesis Res.* **1990**, *24*, 253–263.

(12) van Dorssen, R. J.; Vasmel, H.; Amesz, J. Pigment Organization and Energy Transfer in the Green Photosynthetic Bacterium *Chloroflexus aurantiacus*. II. The Chlorosome. *Photosynth. Res.* **1986**, *9*, 33–45.

(13) Gerola, P. D.; Olson, J. M. A New Bacteriochlorophyll *a*-Protein Complex Associated with Chlorosomes of Green Sulfur Bacteria. *Biochim. Biophys. Acta* **1986**, *848*, 69–76.

(14) Montaño, G. A.; Wu, H.-M.; Lin, S.; Brune, D. C.; Blankenship, R. E. Isolation and Characterization of the B798 Light-Harvesting Baseplate from the Chlorosomes of *Chloroflexus aurantiacus*. *Biochemistry* **2003**, *42*, 10246–10251.

(15) Philipson, K. D.; Sauer, K. Exciton Interaction in a Bacteriochlorophyll–Protein from *Chloropseudomonas ethylica*. Absorption and Circular Dichroism at 77°K. *Biochemistry* **1972**, *11*, 1880–1885.

(16) Huh, J.; Saikin, S. K.; Brookes, J. C.; Valleau, S.; Fujita, R.; Aspuru-Guzik, A. Atomistic Study of Energy Funneling in the Light-Harvesting Complex of Green Sulfur Bacteria. *J. Am. Chem. Soc.* **2014**, *136*, 2048–2057.

(17) Bordignon, E.; Giacometti, G.; Carbonera, D. A Structural Model for the Assembly of the Reaction Centre and the B808-866 Complex in the Membranes of *Chloroflexus aurantiacus* Based on the Calculation of the Triplet Minus Singlet Spectrum of the Primary Donor. *Chemical Physics* **2003**, *294*, 267–275.